Title
Seismic Performance of Natural Gas Transmission Pipelines Affected by Ground Failure

Author
Bain, Christopher

Publication Date
2023

Peer reviewed|Thesis/dissertation

Seismic Performance of Natural Gas Transmission Pipelines Affected by Ground Failure

By

Christopher A. Bain

A dissertation submitted in partial satisfaction of the

requirements for the degree of

Doctor of Philosophy

in

Engineering – Civil and Environmental Engineering

in the

Graduate Division

of the

University of California, Berkeley

Committee in charge:

Professor Jonathan D. Bray, Chair
Professor Kenichi Soga
Professor Douglas S. Dreger

Spring 2023

ABSTRACT

Seismic Performance of Natural Gas Transmission Pipelines Affected by Ground Failure

by

Christopher A. Bain

Doctor of Philosophy in Engineering – Civil and Environmental Engineering

University of California, Berkeley

Professor Jonathan D. Bray, Chair

Natural gas transmission pipelines can be affected by earthquakes from traveling seismic waves and earthquake-induced ground failure from liquefaction or landslides. Case histories of earthquake effects to natural gas transmission pipelines in California show that ground failure poses the most acute risk as no modern gas pipelines in California have been shown to rupture due to seismic waves.

The *OpenSRA* (Open Seismic Risk Assessment) software tool has been developed through the contributions of several members of a large multidisciplinary research team to assess the seismic risk to natural gas infrastructure including below ground transmission pipelines. The tool implements the Pacific Earthquake Engineering Research (PEER) center's Performance Based Earthquake Engineering (PBEE) methodology for assessing risk. The PEER PBEE framework assesses seismic performance at the system level by probabilistically quantifying an intensity measure (IM), such as the peak ground acceleration (PGA), and the response of the system to the IM in terms of seismic displacement or other engineering demand parameters (EDP). The EDPs are used with fragility relationships to estimate the damage to the system in terms of longitudinal pipe strain or other damage measures (DM). The DMs are used to evaluate decision variables (DV) such as the probability of pipeline rupture.

Research performed through this study identified data and methods for assessing the seismic permanent ground displacement (PGD) EDP at the statewide to site-specific scales in the *OpenSRA* tool. Due to the differences in the types of data and methods available for estimating seismic displacement at the statewide versus the site-specific scale, four data and analysis levels were created:

- Level 1 analyses assess the seismic risk to natural gas transmission pipelines from ground failure using data available at a uniform resolution across the state of California. The Level 1 methods estimate potential liquefaction and landslide-induced displacements using proxies for geologic, geotechnical, and groundwater data and have very high aleatory variability (due to inherent randomness) and epistemic uncertainty (due to uncertainty that the model is correct).
- Level 2 analyses utilize data available at regional scales at higher resolution compared to Level 1 analyses including larger scale geologic maps, limited, generic subsurface geotechnical data, and better groundwater information. Level 2 analyses have high uncertainty, but it is less than at Level 1.

- Level 3 analyses utilize site-specific data including subsurface data from geotechnical borings or cone penetration tests (CPTs). The methods for estimating seismic displacement at the site-specific scale have less epistemic uncertainty and are more reliable compared to the methods utilized at Levels 1 and 2. Due to the higher quality and resolution of the data available at Level 3 and the reduced epistemic uncertainty of the Level 3 methods for estimating seismic displacement, Level 3 analyses have less uncertainty than Level 2 analyses.
- Level 4 analyses employ state-of-the-art numerical simulations and require advanced laboratory testing to calibrate the material constitutive models. Level 4 analyses are beyond the current scope of the *OpenSRA* project.

Due to a lack of suitable methods available in the literature for estimating liquefaction-induced lateral spread displacement at Level 2, research focused on developing a new method for probabilistically estimating potential lateral spread displacement at regional scales. The new method collects CPTs across a region and sorts them into distinct surficial geologic deposits. The lateral displacement index (LDI) is then calculated for 225 unique combinations for peak ground acceleration (PGA), earthquake moment magnitude (M_w), and depth to groundwater (GWT). Models conditioned on the surficial geology, PGA, M_w, and GWT are developed to estimate the probability that LDI is negligible (i.e., equals "zero," which is defined as LDI less than three) and the non-zero LDI and its uncertainty. LDI is assumed to be distributed as a mixed-random variable whereby there is a mass probability that LDI equals "zero" and a distribution of non-zero LDI. An estimated distribution of LDI is converted to a distribution of lateral spread displacement using correlations of LDI to lateral displacement conditioned on the topographic slope for gently sloping sites far from a free-face or the free-face ratio for sites near a free-face feature. The method is shown to estimate reasonably both the spatial extent and magnitude of lateral displacements for the 1989 M_w 6.9 Loma Prieta earthquake in the San Francisco Bay area of California and the 2010 M_w 7.1 Darfield and 2011 M_w 6.2 Christchurch earthquakes in the Christchurch area of New Zealand.

Other research of this study focused on the longitudinal strain response of the pipelines to the seismic PGD experienced at Balboa Boulevard in the San Fernando Valley of Southern California during the 1994 M_w 6.7 Northridge earthquake. Eight pipelines, including five natural gas transmission pipelines, a natural gas distribution line, and two pressurized water trunk lines crossed the liquefaction-induced ground deformation zone produced by the 1994 Northridge earthquake. The Old Line 120 natural gas transmission pipeline, the gas distribution line, and the Granada and Rinaldi Trunk Lines broke in both tension and compression during the 1994 Northridge earthquake. The New Line 120, Line 3000, and Line 3003 natural gas transmission pipelines and the Mobil Oil Line M70 crude oil transmission pipeline did not break in 1994. No PGD was observed and no pipelines failed at the site during the 1971 M_w 6.6 San Fernando earthquake. Evidence suggests the groundwater was lower in 1971 than in 1994, which reduced the likelihood of liquefaction-induced ground movements at Balboa Boulevard in 1971.

The longitudinal strains were assessed in a conventional manner using an analytical model typically used in engineering practice. The pipelines were analyzed with mean values for the soil-pipeline system properties, including: the steel yield strength, the shape of the steel stress-strain curves, the soil-pipeline interface shear stress, the pipe geometry, the length of the ground deformation zone, and the amount of seismic PGD. Critical strains for tensile rupture and compressive buckling were estimated. The results of this modeling show good agreement between the expected and observed performance of the pipelines. The pipelines that failed developed the

highest longitudinal strains and the pipelines that did not fail developed significantly lower strains. In the case of one pipeline (i.e., Line 3000), however, the longitudinal strain developed in it was estimated to be sufficient to cause buckling in the compressive deformation zone, but it did not fail.

There are several possible reasons for this discrepancy. The soil-pipeline interaction in the analytical model depends not only on the length of the soil block displacement, but also on the shear force conveyed to the pipeline by the adjacent soil. There is uncertainty in the soil-pipeline interface shear stress and small variations can significantly affect the strain estimate. The critical compressive strain plays an important role in predicting pipeline failure. Uncertainty in the critical strains was not evaluated in the conventional analysis. The longitudinal strain is also sensitive to the pipe steel yield stress, which was assumed to be equal to its specified minimum value, and the amount of ground displacement, for which there is significant uncertainty.

The longitudinal strain response of the pipelines at Balboa Boulevard was also assessed probabilistically in the manner in which *OpenSRA* assesses the seismic risk of natural gas pipelines. The aleatory variability and epistemic uncertainty for each of the soil-pipeline system parameters was estimated and Monte Carlo simulations of the longitudinal strain were calculated with the validated analytical model. New fragility functions for assessing tensile rupture and compressive buckling are developed, including their aleatory variability and epistemic uncertainty. Sampling the distributions for each of the system parameters allows for a distribution of the longitudinal strain to be estimated for each pipeline. Assessing the longitudinal strain distributions with the new fragility functions results in distributions for the probability of tensile rupture and the probability of compressive buckling for each pipeline. The results of this study show good agreement between the expected and observed performance of the pipelines. The probability of compressive buckling distribution for Line 3000, which was expected to fail in the conventional analysis, varies from low to high, demonstrating the significant uncertainty in the assessment of this line. The methodology employed in the *OpenSRA* software is judged to be reasonable in its application to assessing the seismic performance of buried pipelines.

To my very patient girlfriend, Lindsey

TABLE OF CONTENTS

LIST OF FIGURES

CHAPTER 2

CHAPTER 3

CHAPTER 4

CHAPTER 5

LIST OF TABLES

CHAPTER 2

CHAPTER 3

CHAPTER 4

CHAPTER 5

ACKNOWLEDGMENTS

I would like to sincerely thank my advisor, Professor Jonathan Bray, for his guidance and support over the past few years. Completing a doctorate is intellectually challenging and emotionally taxing and would not be possible without the support of an advisor who cares about the success and wellbeing of their student. Jon has been this and more. He pushed me to become a better student, spurred my development as a researcher, and encouraged me to grow into a leader. Furthermore, Jon has personally inspired me by his passion for earthquake engineering, his depth-of-knowledge, attention to detail, and his personable and unwaveringly positive and upbeat demeanor, qualities which I aspire to emulate.

I would also like to sincerely thank Dr. Thomas O'Rourke, who has been a mentor throughout the course of the doctorate program. Tom routinely provides insight, wisdom, and technical knowledge, gained from a lifetime of experience, that no university course or textbook could ever replicate. Working with and learning from him has been an immense pleasure and privilege.

Scott Lindvall was the resident geologist on the *OpenSRA* team and another mentor over the course of the doctorate program. Scott approaches problems from a different angle than the engineers on the team, and his unique perspective often unveiled solutions to challenging problems which were masked by my own limitations. His encouragement to think without reticence and his unyielding kindness set the standard for the ideal researcher and person. For that and more, I thank him.

Dr. Daniel Hutabarat has been a prodigious mentor and friend over the past five years. I have known Daniel from my early days at UC Berkeley when he was the graduate student instructor for Jon's geotechnical earthquake engineering class. From my days in the master's degree program all the way through the *OpenSRA* project, Daniel has helped me advance my skills and knowledge and I cannot thank him enough.

I also thank Professors Kenichi Soga, Douglas Dreger, Robert Kayen, and Shaofan Li, who served on my qualifying exam committee. Professors Soga and Dreger also served on my dissertation committee. Taking classes with each of these professors, as well as serving as the graduate student instructor for Professor Kayen's engineering geology class, were invaluable learning experiences. I sincerely thank them for serving on my committees and guiding me towards academic success.

The *OpenSRA* project was funded by the California Energy Commission (CEC). I thank the CEC and specifically, Yahui Yang, the CEC project manager, for supporting this research. Dr. Jennie Watson-Lamprey of Slate Geotechnical Consultants served as the *OpenSRA* project manager. I am grateful to her and to Dr. Barry Zheng and Micaela Largent, also of Slate, for their hard work and friendship during the project. I learned much from them and the *OpenSRA* project would not have been successful without Jennie's expert guidance, Barry's dedication to the code, and Micaela's coordination. I also thank Professor Norman Abrahamson for his help in building regression models and estimating model epistemic uncertainty for the *OpenSRA* project.

I thank Dr. Sjoerd van Ballegooy and Nathan McDougall of Tonkin + Taylor for their thoughtful comments regarding the development of the regional scale lateral spread displacement procedure and for providing several important datasets used in the modeling of the Christchurch area. I also thank Professor Katerina Ziotopoulou of University of California, Davis, and Dr. Craig Davis, formerly of Los Angeles Department of Water and Power, for sharing information and insights on their studies of the ground failure at Balboa Boulevard and the water trunk lines.

1 INTRODUCTION

1.1 OVERVIEW

Permanent ground deformation from liquefaction or slope displacement is the primary earthquake-induced hazard affecting modern natural gas transmission pipelines. Risk assessments of pipeline networks are currently performed using highly subjective and qualitative risk scoring approaches. These approaches do not properly account for all uncertainties, resulting in an incomplete and inaccurate assessment of the risk from seismic displacement. Assessing risk with consistent logic that properly accounts for all uncertainties at regional to site-specific scales can focus risk reduction efforts to where they will have the greatest impact.

The Open Seismic Risk Assessment (*OpenSRA*) software tool has been developed following the Pacific Earthquake Engineering Research (PEER) Center's Performance Based Earthquake Engineering (PBEE) methodology for assessing risk. The PEER PBEE framework assesses seismic performance at the system level by probabilistically quantifying an intensity measure (IM), such as the peak ground acceleration (PGA), and the response of the system to the IM in terms of seismic displacement or other engineering demand parameters (EDP). The EDPs are used with fragility relationships to estimate the damage to the system in terms of longitudinal pipe strain or other damage measures (DM). Finally, the DMs are used to evaluate decision variables (DV) such as the probability of pipeline rupture.

Research performed in this study for the *OpenSRA* project included creating a framework for performing seismic risk of pipelines due to ground failure at the statewide to site-specific scales, developing a new method for probabilistically assessing the liquefaction-induced lateral spread displacement hazard at regional scales, evaluating case histories of pipelines intersecting permanent ground deformation including at Balboa Boulevard, and developing fragility relationships for assessing the probability of leakage or rupture for pipes subjected to tensile or compressive strain.

1.2 DISSERTATION ORGANIZATION

The following chapters explore methods and data for assessing seismic displacement due to earthquake-induced ground failure at statewide to site-specific scales, describe a new method for estimating liquefaction-induced lateral spread displacement and its uncertainty at regional scales, and assesses the performance of the pipelines subjected to seismic displacement at Balboa Boulevard during the Northridge earthquake in conventional and probabilistic manners. This dissertation is organized into six chapters as follows:

- Chapter 2 describes the methods and data utilized in the *OpenSRA* software for assessing seismic displacement at statewide to site-specific scales. The uncertainty due to inherent randomness (aleatory variability) and lack of knowledge (epistemic uncertainty) are estimated for each method. Additionally, fragility relationships are developed to estimate the probability of leakage or rupture for pipelines subjected to tensile or compressive strain.
- Chapter 3 describes a new method for assessing the liquefaction-induced lateral spread displacement hazard at regional scales. The method utilizes cone penetration tests (CPTs) collected in a region, such as the San Francisco Bay area of California or the Christchurch area of New Zealand, to estimate a distribution of the lateral displacement index (LDI)

conditioned upon the surficial geology, peak ground acceleration, earthquake moment magnitude, and the depth to groundwater. A distribution of LDI is converted to a distribution of lateral spread displacement using existing topographic correlations and maps of topographic slope and free-face ratio.

- Chapter 4 presents a conventional analysis of the buried pipeline performance to the seismic displacement experienced at Balboa Boulevard during the 1994 Northridge earthquake. Ground failure did not occur at the site during the 1971 San Fernando earthquake. Detailed assessments of the pipe/soil interface shear strength and the characteristics of the pipelines are presented, and an analytical model is used to assess the pipe strain response to the seismic displacement. The best estimates for the pipe strains are presented and the expected performance of the pipelines based on their estimated strains is compared to the observed performance. The longitudinal strain response at the locations of pipe bends is also assessed.
- Chapter 5 presents a probabilistic analysis of the pipeline performance to the seismic displacement experienced at Balboa Boulevard during the Northridge earthquake. Ground failure did not occur at the site during the 1971 San Fernando earthquake. Uncertainties in the pipe/soil interface shear strength, characteristics of the pipelines such as the yield strength, the amount of ground displacement, and the length of the ground deformation zone are estimated. Monte Carlo simulations of the pipe strain were achieved with an analytical model. Distributions of the pipe strain and the probability of tensile rupture or pipe wall buckling are presented and compared to the observed performance of the pipelines.
- Chapter 6 summarizes key results from the presented research and provides recommendations for future research.

2 SEISMIC GROUND FAILURE HAZARD DEMANDS AFFECTING BURIED PIPELINE PERFORMANCE

2.1 INTRODUCTION

This study is part of a multi-year, multi-disciplinary project conducted by the Pacific Earthquake Engineering Research Center (PEER) with the Lawrence Berkeley National Laboratory (LBNL) and funded by the California Energy Commission (CEC). The overall project is titled "Performance-Based Earthquake Engineering Assessment Tool for Natural Gas Storage and Pipeline Systems," henceforth referred to as the "*OpenSRA* project." The overall goal of the *OpenSRA* project is to create an open-source research-based seismic risk assessment tool for natural gas infrastructure that can be used by utility stakeholders to better understand state-wide risks, prioritize mitigation, plan new gas infrastructure, and help focus post-earthquake repair work.

The probabilistic seismic risk tool developed in the *OpenSRA* project follows the widely accepted risk methodology of Cornell (1968). A seismic source characterization is used to develop a suite of earthquake scenarios with associated rates of occurrence to represent the seismic hazard. Fault ruptures and the resulting ground deformation are generated for each earthquake scenario to represent the seismic loading, which includes a map of ground motion parameters. This scenario-based seismic parameter map is overlaid on the infrastructure system and the seismic loading combined with the capacities of the infrastructure to calculate the seismic performance of the natural gas system for the scenario. By repeating the process for all the scenarios in the suite, the tool can evaluate the seismic risk to the system.

A user-driven research approach was used to develop *OpenSRA* to be easily used by regulators and utilities, and to include updated models and methods for the seismic demands and capacities that control the seismic risk for natural gas systems. The project includes several innovative approaches that improve the basic methodology and distinguish this project's approach from standard approaches currently used. Current risk studies developed by the utilities use risk scoring approaches that are highly subjective and qualitative. They do not properly incorporate the uncertainties in the seismic demand and in the fragility of the system and its components. Targeted research was conducted in this project to improve the characterization of uncertainty of key inputs to the seismic risk assessment tool. The seismic risk methodology employed in this project provides quantitative estimates of the probabilistic seismic risk. For risk-informed decision-making processes, the reliability of the risk estimates needs to be considered because this can be significant, particularly for large, rare earthquakes.

The project team includes researchers from UC Berkeley (which this study is part of), LBNL, UC San Diego, University of Nevada Reno, the PEER Center, the NHERI SimCenter, and Slate Geotechnical Consultants and its subcontractors Lettis Consultants International (LCI) and Dr. Thomas O'Rourke.

The scope of this chapter is to assess the ground deformation hazards posed to natural gas infrastructure in California from liquefaction-induced lateral spreading and vertical settlements and from earthquake-induced landslides. The analytical methods and data available in the literature are summarized and their implementation into *OpenSRA* is described. Uncertainties in the methods and data are estimated and described.

2.2 PROJECT APPROACH

This chapter assesses the earthquake-induced ground deformation hazard to natural gas infrastructure in California from liquefaction-induced lateral spreading and vertical settlement and from seismic slope displacement due to earthquake-induced landslides. A review of the procedures and data available in the literature is presented and gaps in the literature are identified. Updates or modifications to existing procedures resulting from targeted research are described in this chapter and a new method for assessing liquefaction-induced lateral spread displacements is described in detail in Chapter 3.

The *OpenSRA* project requires the analysis of seismic risk at the statewide to site-specific scales. To do this, data and procedures to evaluate geohazards are categorized into four levels (see Appendix A):

1. Level 1 analyses utilize data that are continuous at a uniform resolution over the entire state of California. With its lower level of resolution and without site-specific or subsurface data, the statewide data lead to very high uncertainty.
2. Level 2 analyses utilize data produced at regional scales collected at higher resolution than Level 1 data. Level 2 data are not necessarily geospatially continuous over the entire state of California. There is minimal, generic subsurface data or estimated engineering properties. Use of Level 2 data leads to high uncertainty, but less uncertainty than with Level 1 data.
3. Level 3 analyses utilize site-specific geologic and topographic mapping and includes subsurface data through CPTs, borings with SPT, and soil/rock index tests. Subsurface data can be used in performance-based liquefaction, lateral spreading, slope displacement, and settlement procedures. Level 3 data enables assessment with medium uncertainty, less than with Level 2 data.
4. Level 4 analyses utilize high-quality laboratory test data with the Level 3 site-specific geologic, topographic, and geotechnical data. Use of Level 4 data supports the performance of advanced numerical analyses. Level 4 analyses will have the least uncertainty in estimating the effects of earthquake-induced ground deformation on buried pipes. Due to the high level of data required they will not be employed commonly in making systemwide seismic risk assessments. Instead, they will be used on project-specific efforts. Level 4 analyses are beyond the current scope of the *OpenSRA* Project.

The qualitative descriptions of uncertainty at each data and analysis level (i.e., very high, high, and medium) are intended to communicate the decreasing amount of uncertainty possible as more robust data and analytical methods are employed. The uncertainties associated with these data and analyses levels for a liquefaction triggering assessment illustrate the ranges of uncertainty typically associated with these descriptions. Liquefaction triggering models are assumed to be lognormally distributed with aleatory variability (due to inherent randomness and denoted as β_r) on the order of $\beta_r \approx 0.8 – 1.0$ at Level 1, $\beta_r \approx 0.7 – 0.9$ at Level 2, and $\beta_r \approx 0.5 – 0.7$ at Level 3. When applicable, epistemic uncertainty (due to incomplete scientific knowledge leading to modeling uncertainty) is included and denoted as β_u. This chapter recommends data and procedures available in the literature for performing analyses at Levels 1 – 3. Chapter 3 introduces a new method developed for probabilistically assessing the liquefaction-induced lateral spread displacement hazard at regional scales.

2.2.1 Level 1 Liquefaction Triggering Models and Data

To enable Level 1 assessments of liquefaction triggering, the only models that can be applied at a uniform data resolution across the entire state of California come from Zhu et al. (2015) and Zhu et al. (2017). These regional-scale methods use inputs that are proxies for geotechnical, geologic, and groundwater conditions to quantitatively assess the probability of liquefaction triggering at the statewide scale. Zhu et al. (2015, 2017) claim their models capture general trends observed at the regional scale for a few earthquakes. They do not provide quantitative assessments of the performance of their models. As no subsurface data are used to inform the models, Level 1 liquefaction triggering assessments are judged to have very high uncertainty.

The inputs for the Zhu et al. (2015) model include peak ground acceleration (PGA), compound topographic index (CTI), and the time-averaged shear wave velocity in the upper 30-meters of the subsurface (V_{S30}). The inputs for the Zhu et al. (2017) models include the peak ground velocity (PGV), V_{S30}, the average annual precipitation ($precip$), nearest distance to the coast (d_c), nearest distance to a river (d_r), nearest distance to any water (d_w), and a depth to groundwater model (wtd). Statewide datasets of the model inputs are presented in Appendix A. The statewide Zhu et al. (2015) and Zhu et al. (2017) datasets shown in Appendix A are included in *OpenSRA* enabling Level 1 liquefaction triggering assessments to be performed across the entire state of California without additional inputs required from the user.

Zhu et al. (2017) updates the 2015 model by including case histories from 27 earthquakes in six countries, by including additional explanatory variables, and by developing separate models for different geomorphic environments. Zhu et al. (2017) formulates a coastal model, for use at sites that are located within coastal basins and are less than approximately 20 kilometers from the coast, and a non-coastal model, applicable to non-coastal events or for worldwide application. Zhu et al. (2017) show that either the coastal or non-coastal model performs better than the Zhu et al. (2015) model for all but six events.

The Zhu et al. (2015) global model is presented as Equation (2.1).

$$X = a_1 + a_2\, ln(PGA) + a_3 CTI + a_4\, ln(V_{S30}) \tag{2.1}$$

where X is an intermediate step to capture the probability, PGA is the peak ground acceleration (g), CTI is the compound topographic index (unitless), V_{S30} is the time-averaged shear wave velocity in the upper 30-meters of the subsurface in meters per second, and a_n are regression coefficients. Compound topographic index, sometimes called topographic wetness index, is a proxy for soil saturation and is calculated by taking the natural logarithm of the ratio of local upslope area draining through a point divided by the tangent of the slope of the point. As CTI is a function of the area upslope from a point, it tends to increase in broad, flat alluvial plains and decrease in narrow, steep areas.

The Zhu et al. (2017) coastal model is presented as Equation (2.2).

$$X = a_1 + a_2\, ln(PGV) + a_3\, ln(V_{S30}) + a_4 precip + a_5\sqrt{d_c} + a_6 d_r + a_7\left(d_r\sqrt{d_c}\right) \tag{2.2}$$

where X is an intermediate step to capture the probability, PGV is the peak ground velocity in centimeters per second, V_{S30} is the time-averaged shear wave velocity in the upper 30-meters of the subsurface in meters per second, $precip$ is the mean annual precipitation in millimeters, d_c is

the distance to the coast in kilometers, d_r is the distance to the nearest river in kilometers, and a_n are regression coefficients.

The Zhu et al. (2017) non-coastal model is presented as Equation (2.3).

$$X = a_1 + a_2\, ln(PGV) + a_3\, ln(V_{S30}) + a_4 precip + a_5 d_w + a_6 wtd \tag{2.3}$$

where d_w is the distance to the nearest water body (river, lake, or coast) in kilometers and wtd is the modeled depth to the water table in meters. The Zhu et al. (2015) and (2017) model regression coefficients are defined in Table 2.1.

The Youd et al. (2001) magnitude scaling factor (MSF), which is used to scale PGA prior to analysis using the Zhu et al. (2015) procedure, is presented as Equation (2.4).

$$MSF = 10^{2.24} / {M_w}^{2.56} \tag{2.4}$$

As described by Rashidian & Baise (2020), the USGS recommends a magnitude scaling factor (MSF), presented as Equation (2.5), that is multiplied by PGV before inserting the value of the ground motion parameter into the model.

$$MSF = \frac{1}{1 + e^{-2*(M_w - 6)}} \tag{2.5}$$

Once the model inputs are determined and X has been calculated, the probability of liquefaction triggering is calculated using Equation (2.6).

$$P(liq) = \begin{cases} \dfrac{1}{1 + e^{-X}}, & If\ PGV > 3\dfrac{cm}{s}\ AND\ PGA > 0.1\ g\ AND\ V_{S30} < 620\ \dfrac{m}{s} \\ 0, & Otherwise \end{cases} \tag{2.6}$$

In addition to the PGV, PGA, and V_{S30} thresholds in Equation (2.6), Rashidian & Baise (2020) also recommend capping the mean annual precipitation to 1700 mm. They found significant overprediction of the liquefaction hazard in areas with high annual precipitation without imposing this cap.

For statewide Level 1 analyses, V_{S30} comes from Wills et al. (2015), $precip$ comes from a published map of mean annual precipitation in California from 1981 – 2010 (California Department of Fish and Wildlife, n.d.), d_r was calculated using the flowline geometry in the USA Detailed Streams GIS layer (ESRI, 2019), d_c was calculated using the coastline geometry in the USA States GIS layer (ESRI, 2020), and d_w was calculated using both the USA Detailed Streams and USA States GIS layers (ESRI, 2019; ESRI, 2020). At Level 1, the depth to the groundwater table is estimated using a groundwater table model (250-m resolution) described by Fan & Miguez-Macho (2010). Estimating the depth to the groundwater table is a source of significant uncertainty when performing liquefaction potential studies. No other procedures could be found in the literature for estimating the depth to the groundwater table at Level 1. The statewide datasets input into *OpenSRA*, including the datasets for performing analyses with the Zhu et al. (2015) and Zhu et al. (2017) procedures, are shown in Appendix A.

Neither Zhu et al. (2015) nor Zhu et al. (2017) provide estimates for the aleatory variability or epistemic uncertainty associated with their models. For implementation into *OpenSRA*, the aleatory variability in the intermediate parameter (Equations (2.1) to (2.3)) is assumed to be lognormally distributed with $\beta_r = 0.90$ and the epistemic uncertainty is assumed to be lognormally distributed with $\beta_u = 0.50$.

2.2.2 *Level 1 Liquefaction-Induced Lateral Spreading and Vertical Settlement Models and Data*

Hazus (FEMA, 2020) methodology can be used at Level 1 to estimate lateral spread displacements and liquefaction-induced ground settlements. To use this method, liquefaction susceptibility must first be mapped, which is accomplished at the statewide level following the procedure of Zhu et al. (2017). Liquefaction susceptibility classes can be defined using either Equation (2.2) or Equation (2.3), but excluding the magnitude-scaled-PGV term from the calculation (i.e., setting $a_2 = 0$). The resulting dimensionless value, termed the susceptibility quantity, is classified according to Table 2.2.

The equation in Hazus (FEMA, 2020) for estimating lateral spread displacement is presented here as Equation (2.7).

$$D(inches) = K_\Delta * a \tag{2.7}$$

where a is calculated using Equation (2.8), and K_Δ is a magnitude dependent displacement correction factor calculated using Equation (2.9).

$$a = \begin{cases} 12r - 12 & for\ 1 < r \leq 2 \\ 18r - 24 & for\ 2 < r \leq 3 \\ 70r - 180 & for\ 3 < r \leq 4 \end{cases} \quad and\ r = \frac{PGA}{T_{PGA}} \tag{2.8}$$

$$K_\Delta = 0.0086(M_w)^3 - 0.0914(M_w)^2 + 0.4698(M_w) - 0.9835 \tag{2.9}$$

where T_{PGA} is the threshold value for PGA necessary to trigger liquefaction, found using Table 2.3. The procedure for calculating a is linearly extrapolated for $r > 4$.

According to Hazus (FEMA, 2020), the lateral spread displacement procedure was created by combining the liquefaction severity index (LSI) originally presented by Youd & Perkins (1987) with the attenuation relationship from Sadigh et al. (1986) as presented in Joyner & Boore (1988). LSI is a measure of differential ground failure displacement in inches (capped at 100 inches, as displacements of 100 inches or more are sufficient to cause severe damage to most engineered systems) and in Youd & Perkins (1987) is related to ground shaking using the horizontal distance from the source in kilometers and earthquake moment magnitude. Essentially, LSI is an estimate of the maximum possible ground displacement given distance to the seismic source and magnitude and is not correlated to site-specific conditions including topography.

Hazus (FEMA, 2020) modifies the relationship for LSI to use PGA in place of distance to the seismic source and normalizes it by T_{PGA} to attempt to account for the geotechnical conditions, represented by the liquefaction susceptibility classification assigned to a site, in a simplistic manner. The tri-linear relationship presented in Equation (2.8) with displacement converted to centimeters that Hazus (FEMA, 2020) uses to scale lateral spread displacement with PGA/T_{PGA} is plotted in Figure 2.1.

Lateral spreading is primarily a gravity driven process rather than an inertial process. Liquefied soils located on slightly sloping ground (~0.1 – 5.0%) or near a free-face may move gently downslope or towards the free-face due to in-situ static driving stresses, resulting in permanent ground deformation called lateral spreading. Figure 2.1 shows that the Hazus (FEMA, 2020) procedure estimates lateral spread displacement to increase more quickly with increasing

PGA/T_{PGA}, which is the inverse of the factor of safety against liquefaction triggering. This is the opposite to the trend that would be expected.

Lateral spread displacement has been correlated to several factors including the factor of safety of against liquefaction triggering (Zhang et al., 2004). As the factor of safety against liquefaction triggering decreases to near 1.0 (i.e., the excess pore pressure ratio increases and approaches 1.0) and liquefaction is triggered, shear strains accumulate in the soil and permanent ground displacements occur, the magnitude of the displacements being dependent on the relative density of the soil and topography at the site (Zhang et al., 2004). However, as the factor of safety against liquefaction triggering continues to decrease below 1.0 (i.e., PGA/T_{PGA} increases above 1.0), the rate of shear strain accumulation does not continuously increase. Rather, once the soil has liquefied and the factor of safety against liquefaction triggering is significantly less than 1.0, additional shear straining does not occur. Essentially, because lateral spreading is primarily a gravity driven process, once the shaking is strong enough to liquefy all the liquefiable layers, it is not expected that substantially larger displacements would occur with increasingly stronger shaking.

Neither the model aleatory variability nor epistemic uncertainty is specified in Hazus (FEMA, 2020). For implementation in *OpenSRA*, the aleatory variability is assumed to be lognormally distributed with $\beta_r = 0.90$. The epistemic uncertainty is assumed to be lognormally distributed with $\beta_u = 0.50$.

Liquefaction induced settlement is estimated in Hazus (FEMA, 2020) by assigning a displacement value based on the mapped susceptibility classification. Table 2.4 presents the liquefaction-induced settlement values from Hazus (FEMA, 2020), which has been modified by the authors such that sites with "very low" liquefaction susceptibility have non-zero settlement.

Uncertainty in the estimated displacements is assumed in Hazus (FEMA, 2020) to take the form of a uniform distribution with bounds of one-half to two times the mean values. For implementation in *OpenSRA*, the aleatory variability is assumed to be lognormally distributed with $\beta_r = 0.90$. The epistemic uncertainty is assumed to be lognormally distributed with $\beta_u = 0.50$.

2.2.3 Level 1 Seismic Slope Stability and Displacement Models and Data

At Level 1, the procedures available to assess seismic slope stability and potential slope displacements are robust and include Bray & Macedo (2019), Grant et al. (2016), and Jibson (2007). However, the data available to assess slope stability and potential displacements at the statewide level have very high uncertainty.

To assess seismic slope stability, the seismic yield coefficient (k_y) must be estimated. It is related to the slope's static factor of safety (FS). As presented in Grant et al. (2016), the form of the slope stability analysis depends on the material being assessed (i.e., rock or soil) and on the topographic slope as rotational slides and slumps tend to occur in moderately steep slopes (Grant et al., 2016 assume 20 – 35° slopes), infinite slope type disrupted soil slides can occur on moderate to steeply sloping terrain (Grant et al., 2016 assume 15 – 50° slopes), and rock slides and falls tend to occur on steeply sloping terrain (Grant et al., 2016 assume 50° or steeper slopes). Most seismically-induced landslides, including during California earthquakes, can be reasonably analyzed as infinite slope type failures; therefore, this is the only style of landsliding considered at Level 1.

The equation to estimate the static factor of safety for infinite slope type failures from Grant et al. (2016) is presented as Equation (2.10).

$$FS = \frac{c + c_r}{\gamma t \, sin(\beta)} + \frac{tan(\Phi)}{tan(\beta)} \tag{2.10}$$

where c is cohesion, c_r is root cohesion from vegetation, γ is the unit weight of the sliding mass, t is the thickness of the sliding mass, Φ is the friction angle of the sliding mass, and β is the topographic slope in degrees. Estimates for root cohesion vary significantly for different vegetation types and even within individual landslides and range from 0 kPa in unvegetated slopes to over 100 kPa in old growth forests (Schmidt et al., 2001). Given the uncertainty and near impossibility of accurately estimating root cohesion at the statewide level, it is ignored at Level 1, which introduces a very slight conservative bias. Seismically induced disrupted soil slides are typically shallow, usually 1 – 3 m thick (Grant et al., 2016) and can be reasonably modeled as a rigid Newmark (1965) sliding block.

Newmark (1965) estimates the yield coefficient as presented in Equation (2.11).

$$k_y = (FS - 1) \, sin(\beta) \tag{2.11}$$

The yield coefficient can also be estimated using Equation (2.12), which comes from Bray (2007).

$$k_y = tan(\Phi - \beta) + \frac{c}{\gamma t \, cos^2 \beta \, (1 + tan(\Phi) \, tan(\beta))} \tag{2.12}$$

where Φ is the friction angle of the sliding mass, c is cohesion of the sliding mass, γ is unit weight of the sliding mass, t is the thickness of the sliding mass, and β is the topographic slope.

For rigid sliding masses (i.e., the fundamental period of the sliding mass is $T_s = 0.0 \; s$), Bray & Macedo (2019) present Equation (2.13) to estimate the probability of "zero displacement" (defined as displacement less than 0.5 cm).

$$P(D = \text{"0"}) = 1 - \Phi\left(-2.46 - 2.98 \, ln(k_y) - 0.12(ln(k_y))^2 + 2.76 \, ln(PGA)\right) \tag{2.13}$$

"Non-zero" displacement for a rigid sliding block when $PGV \leq 115 \; cm/s$, which is the typical case, is estimated using Equation (2.14). "Non-zero" displacement for a rigid sliding block when $PGV > 115 \; cm/s$ is estimated using Equation (2.15).

$$\begin{aligned} ln(D) = {} & -4.551 - 2.491 \, ln(k_y) - 0.245(ln(k_y))^2 + 0.344 \, ln(k_y) \, ln(PGA) + 2.703 \, ln(PGA) \\ & - 0.089(ln(PGA))^2 + 0.607 M_w \pm \varepsilon\sigma \end{aligned} \tag{2.14}$$

$$\begin{aligned} ln(D) = {} & -4.551 - 2.491 \, ln(k_y) - 0.245(ln(k_y))^2 + 0.344 \, ln(k_y) \, ln(PGA) + 2.703 \, ln(PGA) \\ & - 0.089(ln(PGA))^2 + 0.607 M_w + ln(PGV) - 4.75 \pm \varepsilon\sigma \end{aligned} \tag{2.15}$$

where $\sigma = 0.74$ for Equations (2.14) and (2.15). Equation (2.13) is combined with Equation (2.14) or (2.15) using a mixed-random variable model to estimate the non-zero slope displacement distribution.

The equation from Jibson (2007) to estimate seismic slope displacement that does not consider earthquake magnitude is presented as Equation (2.16).

$$log(D_N) = 0.215 + log\left[\left(1 - \frac{k_y}{PGA/g}\right)^{2.341} \left(\frac{k_y}{PGA/g}\right)^{-1.438}\right] \pm 0.510 \tag{2.16}$$

where D_N is seismic slope displacement in centimeters and the model aleatory variability equals 0.510. The equation from Jibson (2007) that does consider earthquake magnitude is presented as Equation (2.17).

$$log(D_N) = -2.710 + log\left[\left(1 - \frac{k_y}{PGA/g}\right)^{2.335}\left(\frac{k_y}{PGA/g}\right)^{-1.478}\right] + 0.424M_w \pm 0.454 \quad (2.17)$$

where the terms are as previously described, and the model aleatory variability equals 0.454. Equation (2.17) is applicable for the magnitude range $5.3 \leq M_w \leq 7.6$. The Jibson (2007) equations apply only to rigid sliding masses, such as shallow infinite slope type failures and are stand-alone equations; they do not require an estimate for the probability of zero displacement.

For Level 1 statewide analyses, the geologic map comes from Wills et al. (2015) which is a compilation of published geologic map ranging in scale from 1:250,000 to 1:24,000, with the population centers of the San Francisco Bay area and the Los Angeles basin covered by the larger scale mapping.

This map contains a total of 17 mapped units including surface water, artificial dam fill, eight rock units, and seven alluvial units. The younger alluvium units are subdivided based on topographic slope. In areas mapped as young alluvium and sloping greater than 2%, the deposits are likely to be coarser-grained, slopes between 0.5% and 2% are likely to be composed of a mixture of sand, silty sand, and gravels, and slopes less than 0.5% are likely to be composed of finer sands, silts, and clays. The GIS mapping includes a single large polygon for the entire extent of the Sierra Nevada granite. Due to the significantly higher strength of the granite in the Sierras compared to crystalline rocks in some other parts of the state, such as the Bay Area, the map is altered to differentiate this unit. The Wills et al. (2015) geologic map is presented in Appendix B. A description of the units is provided in Table 2.5.

At Level 1, estimated distributions for friction angle and cohesion for each of the mapped units comes from the California Geological Survey database of shear strength tests (McCrink & Frost, 2021). Table 2.6 displays the estimated mean, median, and standard deviation for each of the mapped units.

The cohesion data are approximately lognormally distributed for each of the units. It is not clear if the friction angle data are normal or lognormal. The null hypothesis that the friction angle data are normally distributed is tested using the Lilliefors test, an update to the Kolmogorov-Smirnov (K-S) test. The null hypothesis could not be rejected for units Qi, Qoa, QT, Tsh/Tss, Tv, and crystalline rocks. The null hypothesis is however, rejected for units Qal, Qs, sp, Kss, and KJf. For consistency with the other analysis levels, the friction angle data are assumed to be lognormally distributed, a typical assumption for the engineering properties of geologic materials. The 5th and 95th percentiles from the respective friction angle and cohesion distributions for each unit were estimated as the minimum and maximum values, presented as Table 2.7.

2.2.4 Level 2 Liquefaction Triggering Models and Data

At Level 2, liquefaction triggering is analyzed using Youd & Perkins (1978) and Witter et al. (2006) type geologic based assessments in conjunction with Hazus (FEMA, 2020) methodology. Youd & Perkins (1978) and Witter et al. (2006) type analyses have been employed for decades to qualitatively assess the relative liquefaction hazard between mapped geologic deposits via susceptibility rankings (e.g., none, very low, low, moderate, high, very high). The Hazus (FEMA, 2020) methodology converts relative susceptibility rankings to a probability of

liquefaction estimate. Youd & Perkins (1978) correlated many geologic deposits of various ages to liquefaction susceptibility, as presented in Table 2.8. An example of applying Youd & Perkins (1978) methodology at a regional scale is the mapping in the San Francisco Bay area from Witter et al. (2006), presented in Figure 2.2.

Hazus (FEMA, 2020) converts liquefaction susceptibility to the probability of liquefaction using Equation (2.18).

$$P(Liquefaction_{SC}) = \frac{P(Liquefaction_{SC}|PGA = a)}{K_M K_W} * P_{ml} \quad (2.18)$$

where $P(Liquefaction_{SC}|PGA = a)$ is the conditional probability of liquefaction given a susceptibility class and specified PGA level, K_M is the moment magnitude correction factor, K_W is the groundwater correction factor, and P_{ml} is the proportion of the map unit that is susceptible to liquefaction. $P(Liquefaction_{SC}|PGA = a)$ is calculated using the formulas in Table 2.9.

The magnitude correction factor, K_M, is calculated using Equation (2.19), and the groundwater correction factor is calculated using Equation (2.20).

$$K_M = 0.0027 * {M_w}^3 - 0.0267 * {M_w}^2 - 0.2055 * M_w + 2.9188 \quad (2.19)$$

$$K_W = 0.022 * D_W + 0.93 \quad (2.20)$$

where D_W is the depth to groundwater in feet. Lastly, P_{ml} is found using Table 2.10.

2.2.5 Level 2 Liquefaction-Induced Lateral Spreading and Vertical Settlement Models and Data

At Level 2, the Hazus (FEMA, 2020) methodology can again be applied to estimate potential lateral spread displacement and vertical settlement due to liquefaction. However, given the better geologic mapping and groundwater data at Level 2, a new, probabilistic method for assessing potential lateral spread displacements at regional scales (Bain & Bray, 2023) has been developed and is presented in detail in Chapter 3 of this dissertation. An example of Level 2 groundwater data is shown in Figure 2.3 (USGS, 2021a).

2.2.6 Level 2 Seismic Slope Stability and Displacement Models and Data

At Level 2, the procedures used to evaluate potential seismic slope displacement are the same at Level 2 as at Level 1; the difference between Level 1 and Level 2 analyses are the resolution and quality of the input geological data. At Level 2, it is expected that the user will have collected geologic data at higher resolution than the statewide geologic map used for Level 1 analyses and may include GIS based geologic mapping at larger scale than the statewide map with estimates for engineering parameters from seismic hazard zone reports (SHZR) from CGS or other subsurface data collected at regional scales. The difference in resolution between Level 1 and Level 2 geologic maps is illustrated in Figure 2.4, which shows the significant detail gained moving from the small scale statewide geologic map (CGS, 2010) to the larger scale geologic map from Bedrossian et al. (2012). The red star denotes the location of the Balboa Boulevard site. The response of the pipelines at this to the seismic displacement experienced during the Northridge earthquake are evaluated in detail in Chapters 4 and 5.

In addition to larger scale geologic maps, Level 2 assessments can utilize the California landslide inventory curated by the California Geological Survey. The landslide inventory is incomplete at a statewide level, but many quadrangles in and near the population centers of the San Francisco Bay area and the Los Angeles Basin have been extensively mapped for landslides.

2.2.7 Level 3 Liquefaction Triggering Models and Data

At Level 3, liquefaction triggering is analyzed using CPT or Standard Penetration Test (SPT) based procedures, with CPT based procedures being preferred due to the improved repeatability and reliability of the CPT compared to the SPT.

Three probabilistic liquefaction triggering methods are available for the CPT: Moss et al. (2006), the Ku et al. (2012) probabilistic modification to the Robertson & Wride (1998) as updated by Robertson (2009) procedure, and the Boulanger & Idriss (2016) procedure. Each of these methods follows the simplified procedure for evaluating soil liquefaction potential originally outlined by Seed & Idriss (1971), which defines the factor of safety against liquefaction triggering as the ratio of the cyclic resistance ratio (CRR) to the cyclic stress ratio (CSR). These procedures differ in the calculation of both CRR and CSR and all evaluate liquefaction triggering probabilistically. A comparison of the median liquefaction triggering curves from these three methods is shown in Figure 2.6.

For the SPT, three procedures are again recommended to evaluate liquefaction triggering: the NCEER procedure described by Youd et al. (2001), the Idriss & Boulanger (2008) as updated by Boulanger & Idriss (2014) procedure, and Cetin et al. (2018). Of these methods, only the Cetin et al. (2018) procedure assesses liquefaction triggering probabilistically. The Cetin et al. (2018) liquefaction triggering curves are presented in Figure 2.5.

2.2.8 Level 3 Liquefaction-Induced Lateral Spreading and Vertical Settlement Models and Data

At Level 3, liquefaction induced lateral spreading and vertical settlement are assessed using the CPT following the procedures from Zhang et al. (2004) and Zhang et al. (2002). The Zhang et al. (2004) procedure computes the lateral displacement index (LDI), presented in Equation (2.21), which is related to lateral spread displacement through the topographic correlations presented in Equation (2.22) and Equation (2.23). The relationship between the maximum cyclic shear strain, γ_{max}, which is a function of soil relative density, and the factor of safety against liquefaction triggering as presented by Zhang et al. (2004), is shown in Figure 2.7.

$$LDI = \int_0^{z_{max}} \gamma_{max} dz \tag{2.21}$$

$$\frac{LD}{LDI} = S + 0.2 \quad (for\ 0.1\% < S < 5.0\%) \tag{2.22}$$

$$\frac{LD}{LDI} = 6 * \left(\frac{L}{H}\right)^{-0.8} \quad (for\ 1 < L/H < 50) \tag{2.23}$$

The Zhang et al. (2002) procedure estimates the post-liquefaction volumetric strain at level sites far from a free face using Equation (2.24).

$$S = \int_0^{z_{max}} \varepsilon_v \, dz \tag{2.24}$$

where ε_v is the post-liquefaction volumetric strain for the dz increment of soil, which is a function of normalized, clean sand equivalent CPT tip resistance and the factor of safety against liquefaction triggering, presented in Figure 2.8. Both the Zhang et al. (2004) and Zhang et al. (2002) procedures can be applied with any of the CPT based liquefaction triggering procedures.

At Level 3, the Youd et al. (2002) and Cetin et al. (2009) procedures can be used to estimate liquefaction-induced lateral spread displacements and vertical settlements using SPT data.
Youd et al. (2002) provides two multilinear regression equations to estimate lateral spread displacement for gently sloping sites and for sites near a free-face. Equation (2.25) estimates the lateral spread displacement (D_H) for gently sloping sites.

$$\begin{aligned} log\, D_H = {} & -16.213 + 1.532 * M_w - 1.406 * log\, R^* - 0.012 * R + 0.338 * log\, S + 0.540 \\ & * log\, T_{15} + 3.413 * log(100 - F_{15}) - 0.795 * log(D50_{15} + 0.1\, mm) \end{aligned} \tag{2.25}$$

where D_H is the estimated lateral spread displacement in meters, R is the horizontal distance from the site to the nearest bound of the seismic energy source in kilometers, S is the ground slope in percent, T_{15} is the cumulative thickness of saturated granular layers with corrected blow counts, $(N_1)_{60}$ less than 15, F_{15} is the average fines content for granular materials included within T_{15} in percent, $D50_{15}$ is the average mean grain size for granular materials within T_{15} in millimeters, and R^* is defined by Equation (2.26).

$$R^* = R + 10^{(0.89 * M_w - 5.64)} \tag{2.26}$$

Equation (2.27) estimates the lateral spread displacement for sites near a free-face.

$$\begin{aligned} log\, D_H = {} & -16.713 + 1.532 * M_w - 1.406 * log\, R^* - 0.012 * R + 0.592 * W + 0.540 * log\, T_{15} \\ & + 3.413 * log(100 - F_{15}) - 0.795 * log(D50_{15} + 0.1\, mm) \end{aligned} \tag{2.27}$$

where W is the free-face ratio (FFR). The Youd et al. (2002) method has two significant limitations. Firstly, the multilinear regression they employed is a statistical fitting to field case history data without an underlying mechanistic model. Hence, the mechanics of lateral spreading may not be entirely captured. Secondly, earthquake shaking intensity is characterized by the horizontal distance to the seismic source. Charactering the shaking intensity by only the horizontal distance to the seismic source does not capture the many variables that affect the intensity of ground shaking at a site that can be captured by sophisticated ground motion models (GMMs). For example, using the PGA estimated with a GMM would provide a more statistically robust estimate of ground shaking and the effects of local site conditions and the aleatory variability and epistemic uncertainty in the estimate would be considered.

The Cetin et al. (2009) procedure probabilistically assesses the volumetric strain potential of saturated, cohesionless soil using the closed-form solution presented in Equation (2.28).

$$\ln(\varepsilon_v) = \ln\left[1.879 * \ln\left[\frac{780.416 * \ln\left(CSR_{SS,20,1D,1\ atm}\right) - N_{1,60,CS} + 2442.465}{636.613 * N_{1,60,CS} + 306.732}\right] + 5.583\right] \pm 0.689 \tag{2.28}$$

$$lim\colon 5 \le N_{1,60,CS} \le 40, \quad 0.05 \le CSR_{SS,20,1D,1\ atm} \le 0.60$$

where CSR_{field} is converted to $CSR_{SS,20,1D,1\ atm}$ using Equation (2.29).

$$CSR_{SS,20,1D,1\ atm} = \frac{CSR_{field}}{K_{md} * K_{M_w} * K_\sigma} \quad (2.29)$$

where K_{md} is a multidirectional shaking effects correction factor found with Equation (2.30).

$$K_{md} = 0.361 * ln(D_R) - 0.579 \quad (2.30)$$

K_{M_w} is a magnitude correction factor found using Equation (2.31).

$$K_{M_w} = \frac{87.1}{{M_w}^{2.217}} \quad (2.31)$$

The confining effective stress correction factor is found using Equation (2.32).

$$K_\sigma = \left(\frac{\sigma'_{v,0}}{P_a}\right)^{f-1}, \quad f = 1 - 0.005 * D_R \quad (2.32)$$

Additionally, a linear depth weighting factor to 18 m, presented in Equation (2.33), is multiplied to the value calculated in Equation (2.28).

$$DF_i = 1 - \frac{d_i}{18\ m} \quad (2.33)$$

Therefore, the estimated volumetric strain of each sublayer of saturated, cohesionless soil is presented as Equation (2.34).

$$\varepsilon_{v,eqv} = \frac{\sum \varepsilon_{v,i} t_i DF_i}{\sum t_i DF_i} \quad (2.34)$$

The estimated settlement at the ground surface is presented as Equation (2.35).

$$s_{estimated} = \varepsilon_{v,eqv} * \sum t_i \quad (2.35)$$

Equation (2.28) through Equation (2.35) present a theoretical framework for assessing liquefaction induced ground settlements in the free field. This model is then calibrated against the case history database to assess its performance and uncertainty. The final model to assess liquefaction induced ground settlement, calibrated to the case history database, is presented as Equation (2.36).

$$ln(s_{estimated}) = ln(1.15 * s_{estimated}) \pm \varepsilon\sigma \quad (2.36)$$

where $\sigma = 0.64$.

2.2.9 Level 3 Seismic Slope Stability and Displacement Models and Data

Many natural gas transmission pipelines are installed in geologic materials that can be explored using the CPT. CPT tip resistance and sleeve friction can be correlated to soil strength parameters to evaluate slope stability and potential displacements. To evaluate the strength of clayey soils, it is useful to estimate the undrained shear strength ratio (s_u/σ'_{v0}), which is directly related to the overconsolidation ratio (OCR). Equation (2.37) is used to estimate the undrained shear strength ratio for normally consolidated clays from the CPT.

$$(s_u/\sigma'_{v0})_{NC} = \left[\frac{q_t - \sigma_{v0}}{\sigma'_{v0}}\right] * (1/N_{kt}) = (Q_t/N_{kt}) \tag{2.37}$$

where N_{kt} ranges from approximately 10 to 18, with a mean value of 14. Assuming that sleeve friction, f_s, is a direct measurement of the remolded undrained shear strength, the undrained shear strength ratio is presented as Equation (2.38).

$$(s_{u-remolded}/\sigma'_{v0}) = (f_s/\sigma'_{v0}) = \left[\frac{F * Q_t}{100}\right] \tag{2.38}$$

For mechanically overconsolidated soils, the undrained shear strength ratio is calculated using Equation (2.39).

$$(s_u/\sigma'_{v0})_{OC} = (s_u/\sigma'_{v0})_{NC} * (OCR)^{0.8} \tag{2.39}$$

where OCR can be calculated using Equation (2.40) from Robertson (2009) or Equation (2.41) from Kulhawy & Mayne (1990).

$$OCR = 0.25 * (Q_t)^{1.25} \tag{2.40}$$

$$OCR = k * \left[\frac{q_t - \sigma_{v0}}{\sigma'_{v0}}\right] = k * Q_t \tag{2.41}$$

where k ranges from 0.2 to 0.5, with a mean value of 0.33. According to Robertson & Cabal (2015), values in the higher end of the range are expected for aged, heavily overconsolidated clays.

Several relationships have been proposed to evaluate the friction angle of sandy soil. To estimate the peak friction angle for clean, rounded, uncemented quartz sands, Kulhawy & Mayne (1990) suggest Equation (2.42) based on high quality field data and Robertson & Campanella (1983) suggest Equation (2.43) based on calibration chamber tests.

$$\Phi' = 17.6 + 11 * \log(Q_{tn}) \tag{2.42}$$

$$\tan(\Phi') = \frac{1}{2.68} * \left[\log\left(\frac{q_c}{\sigma'_{v0}}\right) + 0.29\right] \tag{2.43}$$

Alternatively, Been & Jefferies (2006) present a relationship, presented here as Equation (2.44), to estimate the peak friction angle by relating the critical state friction angle of the soil, which is influenced by mineralogy, to the normalized, clean sand equivalent CPT tip resistance.

$$\Phi' = \Phi'_{cs} + 15.84 * \log\left(Q_{tn,cs}\right) - 26.88 \tag{2.44}$$

According to Robertson & Cabal (2015), Equation (2.44) is the best relationship for estimating the peak friction angle in predominantly non-quartz sands.

With the presented correlations, a distribution of the undrained shear strength or friction angle can be estimated from a profile of CPT measurements. After developing a distribution for the undrained shear strength or friction angle, a distribution for the yield coefficient can be estimated.

At Level 3, seismic slope displacements can be assessed using the previously presented Bray & Macedo (2019) or Jibson (2007) models if the sliding mass is rigid (i.e., the initial fundamental period of the sliding mass, $T_S = 0.0\ s$). For non-rigid sliding masses, the seismic slope displacement is estimated using the 5%-damped spectral acceleration at 1.3 times the initial fundamental period of the potential sliding mass (i.e., $S_a(1.3 * T_S)$) using the Bray & Macedo (2019) method.

The initial fundamental period of the potential sliding mass is estimated using the relationship of $T_S = 4H/V_S'$, where H is the height of the sliding mass and V_S' is its equivalent (average) shear wave velocity if the mass can be approximated as a 1D system. The relationship is $T_S = 2.6H/V_S'$ if the sliding mass is a triangular 2D system. The initial fundamental period of the sliding mass can be approximated for other cases using an effective height (H') using the relationship of $T_S = 4H'/V_S'$, as described in Bray & Macedo (2021). For simplicity in this application, at Level 3, where there is large uncertainty regarding the default values of the effective height and equivalent shear wave velocity of the potential sliding mass, $H' = 0.8H$, where $H = 12\ m$ is the estimated maximum thickness of the sliding mass, and $V_S' = 250\ m/s$, which results in $1.3T_S = 0.2\ s$.

The Bray & Macedo (2019) models to assess the probability of negligible displacement (i.e., seismic slope displacement less than 0.5 cm, which is termed "0") are presented as Equations (2.45) and (2.46).

$$P(D = \text{"0"}) = 1 - \Phi\left(-2.46 - 2.98\,ln(k_y) - 0.12(ln(k_y))^2 - 0.71T_S\,ln(k_y) + 1.69T_S + 2.76\,ln(S_a(1.3T_S))\right)\ for\ cases\ where\ T_S \le 0.7\ s \quad (2.45)$$

$$P(D = \text{"0"}) = 1 - \Phi\left(-3.40 - 4.95\,ln(k_y) - 0.30(ln(k_y))^2 - 0.33T_S\,ln(k_y) - 0.62T_S + 2.85\,ln(S_a(1.3T_S))\right)\ for\ cases\ where\ T_S > 0.7\ s \quad (2.46)$$

"Non-zero" displacement is estimated using Equation (2.47).

$$ln(D) = a1 - 2.491\,ln(k_y) - 0.245(ln(k_y))^2 + 0.344\,ln(k_y)\,ln(S_a(1.3T_S)) + 2.703\,ln(S_a(1.3T_S)) - 0.089(ln(S_a(1.3T_S)))^2 + a2T_S + a3(T_S)^2 + 0.607M_w + a4\ln(PGV) + a5 \pm \varepsilon\sigma \quad (2.47)$$

where $\sigma = 0.74$ for Equation (2.47). When $PGV \le 115\ cm/s$, which is the typical case, $a1 = -5.894$, $a2 = 3.152$, $a3 = -0.910$, $a4 = 0$, and $a5 = 0$ for systems with $T_S \ge 0.10\ s$, and $a1 = -4.551$, $a2 = -9.690$, $a3 = 0$, $a4 = 0$, and $a5 = 0$ for $T_S < 0.10\ s$ (i.e., the PGV term is not required). When $PGV > 115\ cm/s$, $a1 = -5.894$, $a2 = 3.152$, $a3 = -0.910$, $a4 = 1$, and $a5 = -4.75$ for systems with $T_S \ge 0.10\ s$, and $a1 = -4.551$, $a2 = -9.690$, $a3 = 0$, $a4 = 1$, and $a5 = -4.75$ for $T_S < 0.10\ s$.

2.3 PIPE STRAIN FRAGILITY RELATIONSHIPS

2.3.1 Tensile Pipe Strain Fragility Relationships

The most important performance goal for natural gas transmission pipelines is to maintain pressure integrity (i.e., prevent rupture). For continuous steel pipelines with high-quality, overmatched girth welds subjected to tensile strain caused by permanent ground deformation (PGD), the 1984 ASCE *Guidelines for the Seismic Design of Oil and Gas Pipeline Systems* permit longitudinal strains in the 3 – 5% range, the American Lifelines Alliance guidelines (ALA, 2001)

recommend a tensile strain limit of 4% to maintain pressure integrity, and 2004 Pipeline Research Council International (PRCI) *Guidelines for Gas and Liquid Hydrocarbon Pipelines* (Honegger & Nyman, 2004) suggest a tensile strain limit of 2 – 4% to maintain pressure integrity. For a natural gas pipeline risk assessment project in British Columbia, Canada, Wijewickreme et al. (2005) use 7% tensile strain as the median value to maintain pressure integrity, with the 90 and 10% probability of exceedance tensile strains assumed to be 3% and 10%, respectively. Wijewickreme et al. (2005) developed these values with the goal of not being overly conservative after a review of pipeline rupture criterion available at the time, including the ASCE (1984) guidelines.

To develop a realistic (not overly conservative) tensile rupture fragility relationship, this study assumes that the 4% pipe strain criterion suggested by ALA (2001) and Honegger & Nyman (2004) to maintain pressure integrity corresponds to a 30% probability of pipeline rupture. The typical recommended pipe strain limit of 4% likely corresponds to a small probability of rupture, as would be appropriate for regulatory guidelines. However, because the exact probability of rupture at 4% pipe strain is unknown, rupture is estimated to have 30% probability of occurrence at 4% pipe strain on the basis of expert judgement. The tensile rupture fragility function is presented as Equation (2.48).

$$Prob(Tensile\ Rupture) = 1 - \Phi\left(\frac{-\ln(\varepsilon_p) + \ln(4.68)}{0.3}\right) \tag{2.48}$$

ALA (2001) and Honegger & Nyman (2004) also recommend a tensile strain limit to maintain normal operability (i.e., prevent leakage). This performance goal is less understood than the pressure integrity performance goal. ALA (2001) recommends a tensile strain limit of 2% to maintain normal operability and the Honegger & Nyman (2004) guidelines recommend a range of 1 – 2% to maintain normal operability. It is assumed that the 2% strain limit corresponds to a 30% probability of tensile leakage on the basis of expert judgement. The tensile leakage fragility function is presented as Equation (2.49).

$$Prob(Tensile\ Leakage) = 1 - \Phi\left(\frac{-\ln(\varepsilon_p) + \ln(2.34)}{0.3}\right) \tag{2.49}$$

Figure 2.9 and Figure 2.10 present plots of Equation (2.48) and Equation (2.49). 10th and 90th percentiles are presented for the fragility functions assuming the epistemic uncertainty β_u = 0.20, a common assumption for structural systems. β_u represents the epistemic uncertainty in the mean or median value (i.e., uncertainty that the suggested models are the correct models). The aleatory variability is assumed to equal β_r = 0.30 and represents the inherent randomness in the loading conditions (e.g., eccentricities in the pipe alignment, nonuniform backfill soil conditions) and pipe properties (e.g., post-yield stress-strain behavior, weld quality, corrosion).

2.3.2 Compressive Pipe Strain Fragility Relationship

As stated in Wijewickreme et al. (2005), "The pipe wall response following the onset of compressive wrinkling is complex and it is not well understood in terms of specifying pressure integrity strain limits". Therefore, for continuous steel pipelines with high-quality, overmatched girth welds subjected to compressive strain caused by permanent ground deformation (PGD), buckling itself can be taken as the critical damage state because tearing of the pipe wall can occur during buckling and any further straining in the pipe that occurs from permanent ground deformation concentrates at the buckle, increasing the likelihood of pipe wall tearing or rupture.

Mohr (2003) collected the results of published laboratory compressive pipe tests. The results of the tests, which are plotted as the critical compressive pipe strain versus the pipe diameter to pipe wall thickness (D/t) ratio, are presented in Figure 2.11. These data correspond to the longitudinal pipe strain at the maximum compressive stress. According to Harris et al. (1957), buckling occurs at or just before the maximum load the pipe can resist.

The strain data in Figure 2.11 are transformed using the natural logarithm and found to be linear in natural log space. Figure 2.12 presents the strain data transformed by the natural logarithm and presented in log scale with a linear regression fit to the data. Equation (2.50) presents the linear regression to the compressive pipe strain laboratory test data.

$$\ln(\varepsilon_p) = -1.617 * \ln(D/t) + 1.709 + \varepsilon\sigma \tag{2.50}$$

where ε_p is the critical pipe strain in percent, D/t is the pipe diameter to wall thickness ratio, ε represents the number of standard deviations from the mean, and $\sigma = 0.407$, where σ is the standard deviation of the residuals in natural log space. The residuals are approximately normally distributed in natural log space.

The data presented in Figure 2.11 and Figure 2.12 are for pipes without internal pressure. In tension, the effect of internal pressure on the performance of pipelines is small and it is reasonable to ignore it; however, in compression, the stabilizing effect of internal pressure should be accounted for. Mohr (2003) recommends a correction factor to convert a pipe strain estimate to a zero-pressure-equivalent pipe strain, presented here as Equation (2.51).

$$\varepsilon_{p-eq} = \frac{\varepsilon_p}{1 + \sigma_h/\sigma_y} \tag{2.51}$$

where ε_{p-eq} is the zero-pressure-equivalent compressive longitudinal pipe strain, ε_p is the estimated compressive longitudinal pipe strain, σ_h is the pipe hoop stress, and σ_y is the pipe yield stress.

The data presented in Figure 2.11 and Figure 2.12 come from controlled laboratory experiments that would have less uncertainty than that of field conditions. To account for the greater uncertainty associated with field conditions, β_r is increased from 0.407 to 0.5. The resulting probability of compressive buckling or pipe wall wrinkling fragility function is presented as Equation (2.52).

$$Prob(Compressive\ Buckling) = 1 - \Phi\left(\frac{-\ln(\varepsilon_{p-eq}) - 1.617 * \ln(D/t) + 1.709}{0.5}\right) \tag{2.52}$$

where Φ is the standard normal cumulative distribution, ε_{p-eq} is the estimated zero-pressure-equivalent longitudinal pipe strain caused by permanent ground deformation, D/t is the pipe diameter to wall thickness ratio, and $\beta_r = 0.5$.

Pipelines can often sustain more axial strain after buckling or pipe wall wrinkling has occurred prior to the pipe wall tearing or rupturing. To convert Equation (2.52) to a probability of pipe rupture fragility function, the 50% probability of exceedance values are shifted up to the 20% probability of exceedance level. The resulting probability of compressive rupture fragility function is presented as Equation (2.53).

$$Prob(Compressive\ Rupture) = 1 - \Phi\left(\frac{-\ln(\varepsilon_{p-eq}) - 1.617 * \ln(D/t) + 2.130}{0.5}\right) \tag{2.53}$$

Equation (2.52) and the 95%, 84%, 50%, 16%, and 5% probability of exceedance percentiles of Equation (2.52) are plotted over the regressed range of D/t values on an arithmetic scale in Figure 2.13. Figure 2.13 also shows the critical compressive pipe strain laboratory test data compiled by Mohr (2003). Figure 2.14 shows the same data plotted on a log scale.

Equation (2.53) and the 95%, 84%, 50%, 16%, and 5% probability of exceedance percentiles of Equation (2.53) are plotted over the regressed range of D/t values in Figure 2.15. Figure 2.15 shows the probability of rupture percentiles shift upwards allowing for more strain relative to the probability of compressive pipe wall buckling percentiles presented in Figure 2.13.

The epistemic uncertainty in the mean can be estimated as the standard error of the intercept in Equation (2.52) (intercept = 1.709). From the regression statistics, the standard error of the intercept equals 0.22. In structural systems, β_u is commonly assumed to be 0.20 to 0.25. Given the limitations of the dataset, β_u is taken as 0.25. Figure 2.16 and Figure 2.17 display the compressive probability of rupture fragility function presented in Equation (2.53) for pipes with D/t ratios of 20, 40, 60, and 80 along with the 10^{th} and 90^{th} percentiles assuming $\beta_u = 0.25$.

2.4 CONCLUSIONS

This chapter summarizes the procedures implemented in *OpenSRA* for assessing liquefaction triggering, liquefaction-induced lateral spreading and ground settlement, and seismic slope instability and the resulting slope displacement. Estimates of ground displacement resulting from liquefaction-induced lateral spreading and settlement or from earthquake-induced landslides are required to assess the seismic vulnerability of buried natural gas pipelines.

To address the requirement by the CEC to assess natural gas systems at statewide, regional, and site-specific scales, four levels of available data and analytical methods were employed. The resolution of the data and the uncertainty of the estimates of ground displacement possible at each of these scales vary so these levels enable regulators and owners to evaluate the seismic risk at the natural gas pipeline system at the desired level.

Level 1 analyses utilize data that are geospatially continuous at a uniform resolution over the entire state of California. As a result, these data are at low resolution, so the uncertainty of the estimates made at Level 1 are very high. Level 2 analyses utilize data produced at regional scales collected at higher resolution than Level 1 data. These analyses may be informed by subsurface data or estimated engineering properties, so the uncertainty of the Level 2 estimates is reduced relative to Level 1 estimates, but Level 2 analyses are still considered to have high uncertainty. Level 3 analyses utilize site-specific data such as Cone Penetration Test (CPT) data or 1:24,000 scale or larger geologic mapping to evaluate geohazards or the response of natural gas infrastructure to shaking or ground deformation. Level 3 data enable assessment with medium uncertainty. Level 4 analyses utilize high-quality laboratory test data to support the performance of advanced numerical analyses of project-specific systems and components. Level 4 analyses are beyond the current scope of the *OpenSRA* project. The data and methods available at each of the first three levels are delineated in Appendix A. Limitations and reservations with some of the procedures and the evaluation of uncertainty are discussed, when appropriate.

The results of this study establish procedures and data to be incorporated in *OpenSRA* to assess liquefaction and seismic slope stability hazards at statewide, regional, and site-specific scales in California. A new procedure is developed for probabilistically assessing liquefaction-induced lateral spread displacement at the regional scale to fill a gap that existed at Level 2. This method is described in detail in Chapter 3. Methods and models to estimate ground displacement

due to liquefaction or earthquake-induced landslides with characterization in the uncertainty of the estimate enable more robust seismic risk assessments of natural gas pipelines to be performed.

The ultimate objective of the research presented in this chapter is to develop models and procedures for implementation into the *OpenSRA* software to estimate the demands to buried natural gas pipelines from ground deformation hazards. These ground deformation models and procedures estimate the probability and distribution of potential permanent ground deformations at statewide to site-specific scales.

These models and procedures can then be used to produce results that can be used in support of the development of fragility functions that assess the performance of buried pipeline systems undergoing permanent ground deformation. Post-earthquake reconnaissance surveys show that the primary cause of damage to buried natural gas pipeline systems is from seismically induced permanent ground deformation.

Regional scale liquefaction and landslide deformation models that represent better the spatial heterogeneity of ground deformation observed after major earthquakes are required to reduce the tendency of regional scale models to overestimate the pervasiveness of permanent ground deformation. These enhancements would enable more robust, mean-centered, less uncertain, estimates of ground deformations and their resulting effects on buried natural gas pipelines for scenario earthquake assessments. Moreover, liquefaction and liquefaction-induced displacement hazard assessments at regional to site-specific scales are highly sensitive to the depth to groundwater. Lowering or raising the groundwater table can “turn off” or “turn on” liquefaction triggering. Estimating the depth to groundwater with currently available data and methods is difficult, especially at regional scales, and therefore, the uncertainty of the depth of groundwater produces significant uncertainty in the estimation of liquefaction effects on natural gas infrastructure. However, techniques for measuring the depth to groundwater, including Distributed Acoustic Sensing (DAS), could be employed to reduce the uncertainty in the estimate of groundwater depth. Collecting these data would reduce the uncertainty in liquefaction hazard assessments. As there can be significant temporal variations in the groundwater level, additional measurements over several years would further reduce uncertainty and enhance the estimates of seismic risk due to ground deformation hazards.

This chapter also describes the fragility relationships developed to assess the probability of leakage or rupture for pipelines subjected to tensile strain or compressive strain. The tensile fragility relationships were developed on the basis of limited information with the goal of not being overly conservative. The compressive fragility relationship was developed using a database of high-quality laboratory test results.

Table 2.1: Regression Coefficients for the Level 1 Zhu et al. (2015, 2017) Liquefaction Triggering Models

Coefficient	Zhu et al. (2015)	Zhu et al. (2017) Model 1 (Coastal)	Zhu et al. (2017) Model 2 (Non-Coastal)
a_1	24.100	12.435	8.801
a_2	2.067	0.301	0.334
a_3	0.355	-2.615	-1.918
a_4	-4.784	5.556×10^{-4}	5.408×10^{-4}
a_5	-	-0.0287	-0.2054
a_6	-	0.0666	-0.0333
a_7	-	-0.0369	-

Table 2.2: Liquefaction Susceptibility Classification at Level 1 from Zhu et al. (2017)

Susceptibility Quantity (Unitless)	Liquefaction Susceptibility Class
-1.15 to 5.30	Very High
-1.95 to -1.15	High
-3.15 to -1.95	Moderate
-3.20 to -3.15	Low
-38.1 to -3.20	Very Low
less than -38.1	None

Table 2.3: Threshold PGA Values for Liquefaction Triggering at Level 1 (from FEMA, 2020)

Susceptibility Class	T_{PGA}
Very High	0.09 g
High	0.12 g
Moderate	0.15 g
Low	0.21 g
Very Low	0.26 g
None	N/A

Table 2.4: Liquefaction Induced Settlement at Level 1 (from FEMA, 2020)

Susceptibility Class	Settlement (in.)	Settlement (cm)
Very High	12	30
High	6	15
Moderate	2	5
Low	1	2.5
Very Low	0.5	1
None	0	0

Table 2.5: Mapped Units in the Statewide Geologic Map from Wills et al. (2015)

Unit	Description
adf	Artificial dam fill (Latest Holocene)
Qi	Intertidal mud, including mud around the San Francisco Bay and similar mud around the Sacramento/San Joaquin delta and Humboldt Bay (Quaternary)
af/Qi	Artificial fill over intertidal mud around the San Francisco Bay and similar areas (Latest Holocene over Quaternary)
Qal1	Quaternary (Holocene) alluvium in areas of very low slopes (less than 0.5%)
Qal2	Quaternary (Holocene) alluvium in areas of moderate slopes (0.5 – 2.0%)
Qal3	Quaternary (Holocene) alluvium in areas of steep slopes (>2%)
Qoa	Quaternary (Pleistocene) alluvium
Qs	Quaternary (Pleistocene) sand deposits, such as the Merritt Sand in the Oakland area
QT	Quaternary to Tertiary (Pleistocene to Pliocene) alluvial deposits, such as the Saugus Formation of Southern California, the Paso Robles Formation of the central Coast Ranges, and the Santa Clara Formation of the San Francisco Bay area
Tsh	Tertiary shale and siltstone units, such as the Repetto, Fernando, Puente, and Modelo Formations of the Los Angeles area
Tss	Tertiary shale and siltstone units, such as the Topanga Formation in the Los Angeles area and the Butano Formation in the San Francisco area
Tv	Tertiary volcanic units including the Conejo Volcanics in the Santa Monica Mountains and the Leona Rhyolite in the East Bay Hills
sp	Serpentinite
Kss	Cretaceous sandstone of the Great Valley Sequence in the central Coast Ranges
KJf	Franciscan complex rocks, including mélange, sandstone, shale, chert, and greenstone
crystalline	Crystalline rocks, including Cretaceous granitic rocks, Jurassic metamorphic rocks, schist, and Precambrian gneiss
crystalline2	Crystalline rocks including granites, granodiorites, and diorites in the Sierra Nevada

Table 2.6: Level 1 Engineering Properties for the Statewide Geologic Map from Wills et al. (2015)

Unit (MS48)	Subunits	Count	Mean ϕ' (°)	Median ϕ' (°)	COV ϕ' (°)	Mean c' (kPa)	Median c' (kPa)	COV c' (kPa)
adf	N/A	N/A	N/A	N/A	N/A	N/A	N/A	N/A
Qi	Qhym	11	17	19	52	15.8	12.0	52
af/Qi	N/A	N/A	N/A	N/A	N/A	N/A	N/A	N/A
Qal1, Qal2, Qal3	Qha	142	23	23	46	32.5	23.9	82
	Qal	18						
	Qhy	12						
Qoa	Qoa	67	29	30	37	33.1	23.9	106
	Qpa	258						
Qs	Qs	134	36	37	13	10.6	4.8	170
QT	Qts	348	26	26	42	43.3	35.9	79
Tsh, Tss	Tes	49	27	27	40	40.8	29.9	117
	Tmoes	2						
	Tmos	45						
	Tms	120						
	Tpas	2						
	Tpms	7						
	Toes	47						
Tv	Tmov	8	30	29	46	25.6	27.5	65
	Tpmv	4						
sp	Jsp	111	28	26	42	48.2	35.9	97
Kss	KJs	103	24	24	39	36.5	28.7	85
	Ks	119						
KJf	fsr	20	26	25	35	43.2	29.2	113
	Kfs	77						
	Kfv	3						
	KJf	43						
	KJfc	25						
	KJfm	103						
	KJfs	34						
	KJfv	12						
Crystalline	Ji	30	26	26	25	18.1	16.8	82
Crystalline2	N/A	N/A	40*	40*	25*	23.9*	23.9*	100*

* Estimated values without data

Table 2.7: Level 1 Engineering Properties for the Statewide Geologic Map from Wills et al. (2015)

Unit (MS48)	Subunits	Count	Min ϕ' (°)	Max ϕ' (°)	Min c' (kPa)	Max c' (kPa)
adf	N/A	N/A	N/A	N/A	N/A	N/A
Qi	Qhym	11	3	28	6.0	27.5
af/Qi	N/A	N/A	N/A	N/A	N/A	N/A
Qal1, Qal2, Qal3	Qha	142	8	44	2.0	82.8
	Qal	18				
	Qhy	12				
Qoa	Qoa	67	13	46	0.0	91.2
	Qpa	258				
Qs	Qs	134	28	42	0.0	43.1
QT	Qts	348	9	45	0.0	100.5
Tsh, Tss	Tes	49	11	44	2.3	111.8
	Tmoes	2				
	Tmos	45				
	Tms	120				
	Tpas	2				
	Tpms	7				
	Toes	47				
Tv	Tmov	8	15	44	5.5	43.5
	Tpmv	4				
sp	Jsp	111	13	48	2.4	149.6
Kss	KJs	103	8	40	1.1	101.6
	Ks	119				
KJf	fsr	20	12	43	2.9	106.8
	Kfs	77				
	Kfv	3				
	KJf	43				
	KJfc	25				
	KJfm	103				
	KJfs	34				
	KJfv	12				
Crystalline	Ji	30	13	38	0.0	42.7
Crystalline2	N/A	N/A	30*	50*	0.0*	35.9*

* Estimated values without data

Table 2.8: Relative Liquefaction Susceptibility of Various Geologic Deposits (from Youd & Perkins, 1978)

Type of Deposit	General Distribution of Cohesionless Sediments in Deposits	Likelihood that Cohesionless Sediments, when Saturated, would be Susceptible to Liquefaction (By Age of Deposit)			
		<500 yr	Holocene	Pleistocene	Pre-Pleistocene
Continental Deposits					
River Channel	Locally Variable	Very High	High	Low	Very Low
Flood Plain	Locally Variable	High	Moderate	Low	Very Low
Alluvial Fan and Plain	Widespread	Moderate	Low	Low	Very Low
Marine Terraces and Plains	Widespread	–	Low	Very Low	Very Low
Delta and Fan-Delta	Widespread	High	Moderate	Low	Very Low
Lacustrine and Playa	Variable	High	Moderate	Low	Very Low
Colluvium	Variable	High	Moderate	Low	Very Low
Talus	Widespread	Low	Low	Very Low	Very Low
Dunes	Widespread	Moderate	Low	Low	Very Low
Loess	Variable	High	High	High	Unknown
Glacial Till	Variable	Low	Low	Very Low	Very Low
Tuff	Rare	Low	Low	Very Low	Very Low
Tephra	Widespread	High	High	?	?
Residual Soils	Rare	Low	Low	Very Low	Very Low
Sebka	Locally Variable	High	Moderate	Low	Very Low
Coastal Zone					
Delta	Widespread	Very High	High	Low	Very Low
Esturine	Locally Variable	High	Moderate	Low	Very Low
Beach – High Wave Energy	Widespread	Moderate	Low	Very Low	Very Low
Beach – Low Wave Energy	Widespread	High	Moderate	Low	Very Low
Lagoonal	Locally Variable	High	Moderate	Low	Very Low
Fore Shore	Locally Variable	High	Moderate	Low	Very Low
Artificial					
Uncompacted Fill	Variable	Very High	–	–	–
Compacted Fill	Variable	Low	–	–	–

Table 2.9: Conditional Probability of Liquefaction Relationships at Level 2 (from FEMA, 2020)

Susceptibility Class	$P(Liquefaction_{SC}\|PGA = a)$
Very High	$0 \leq 9.09 * a - 0.82 \leq 1.0$
High	$0 \leq 7.67 * a - 0.92 \leq 1.0$
Moderate	$0 \leq 6.67 * a - 1.0 \leq 1.0$
Low	$0 \leq 5.57 * a - 1.18 \leq 1.0$
Very Low	$0 \leq 4.16 * a - 1.08 \leq 1.0$
None	0.0

Table 2.10: Proportion of the Land Area Assumed Susceptible to Liquefaction (from FEMA, 2020)

Susceptibility Class	Proportion of Map Unit
Very High	0.25
High	0.20
Moderate	0.10
Low	0.05
Very Low	0.02
None	0.00

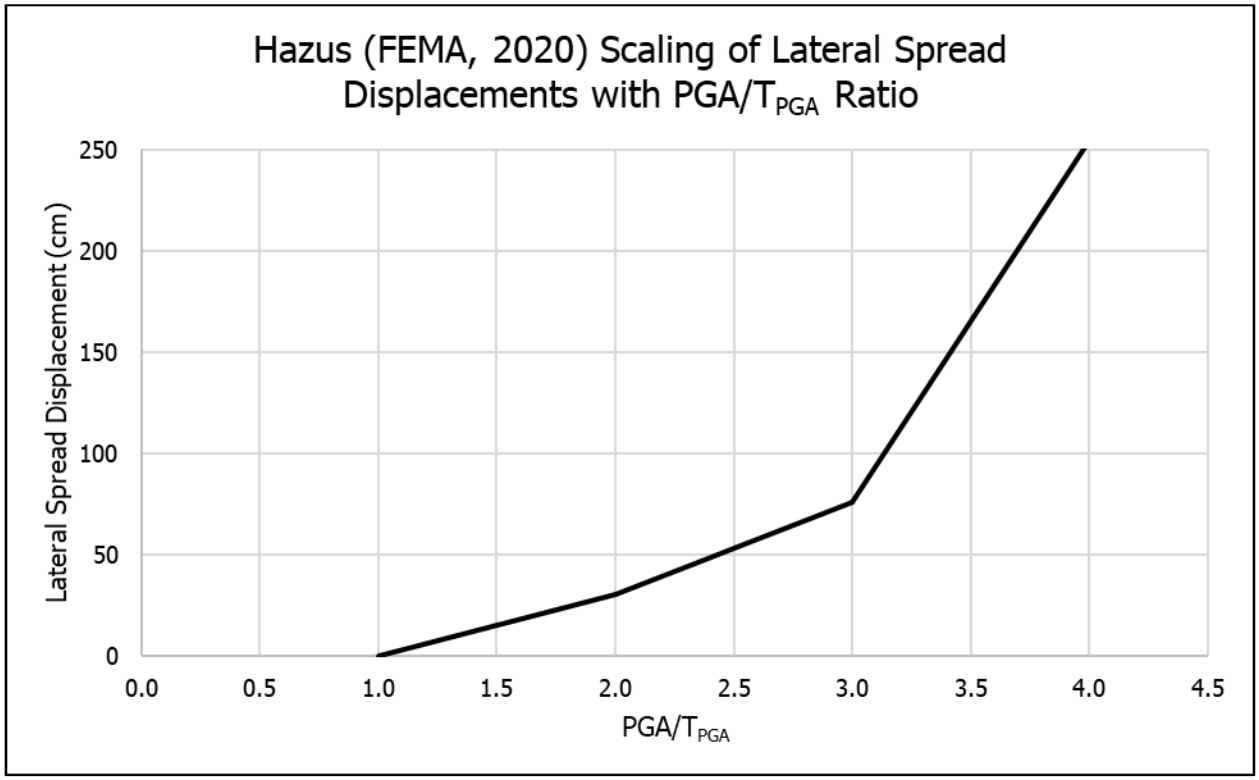

Figure 2.1: Scaling of Lateral Spread Displacements with PGA/T_{PGA} at Level 1 (from FEMA, 2020)

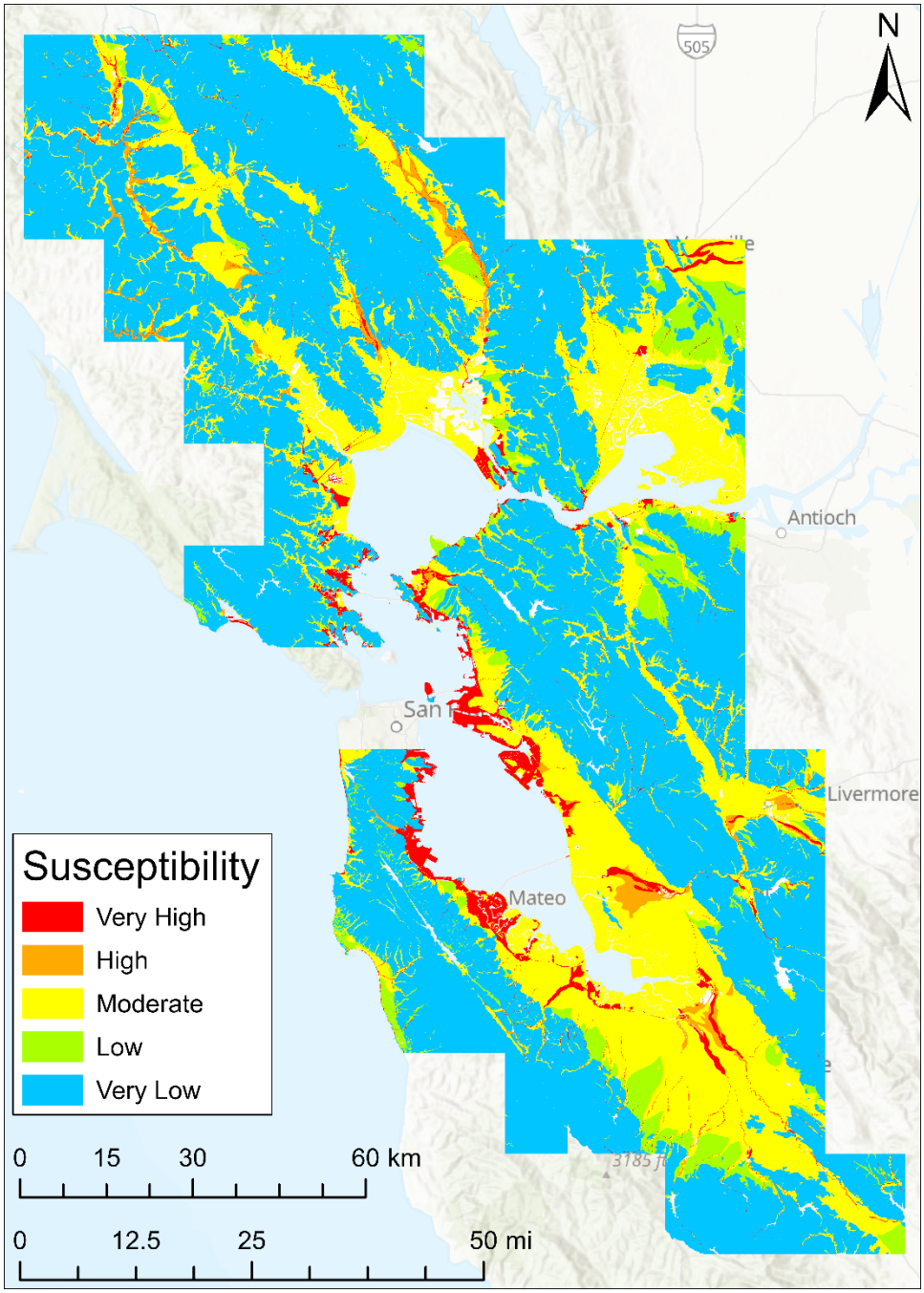

Figure 2.2: Relative Liquefaction Susceptibility in the San Francisco Bay Area (from Witter et al., 2006)

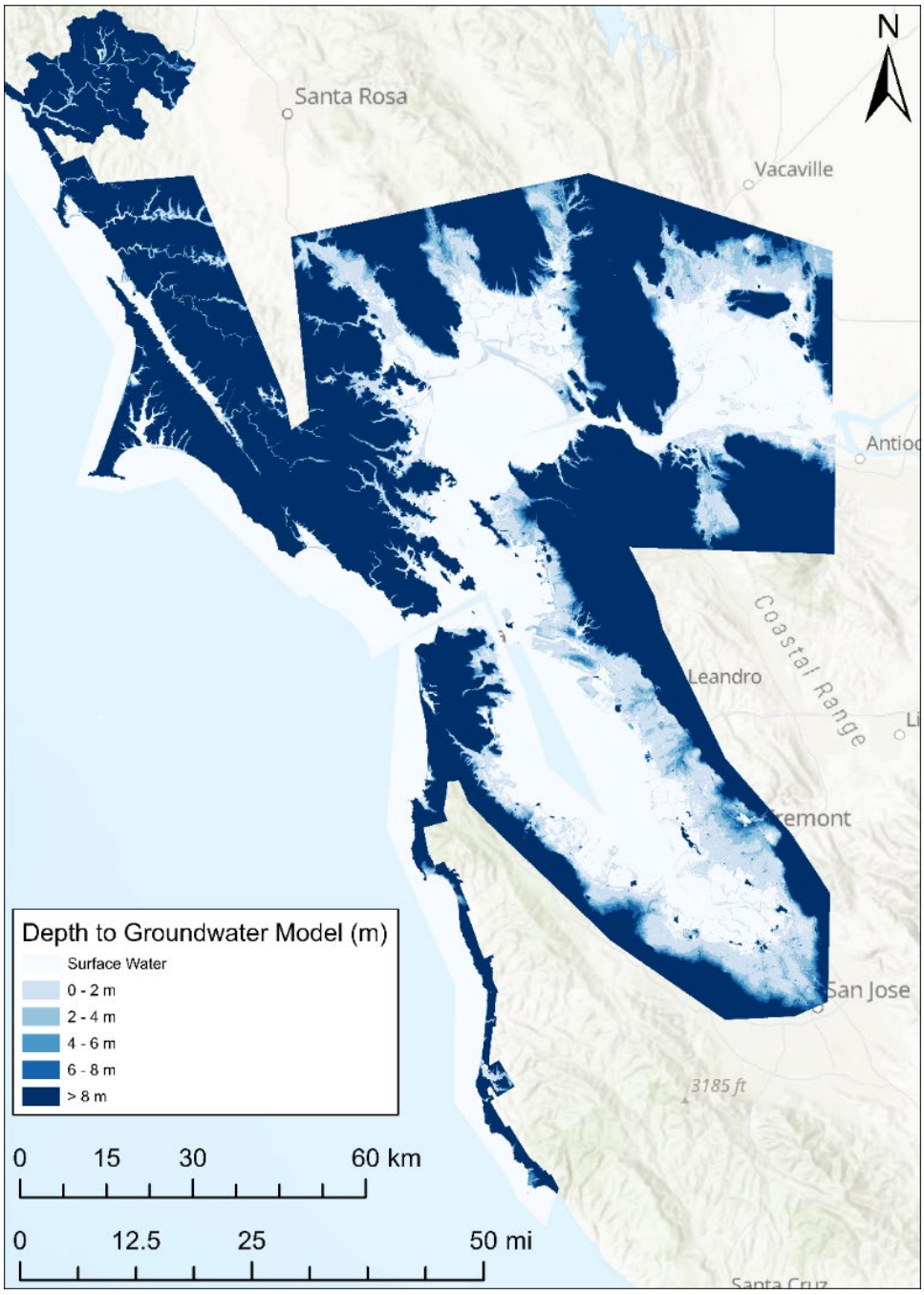

Figure 2.3: Level 2 Groundwater Model from the USGS CoSMoS Project (USGS, 2021a)

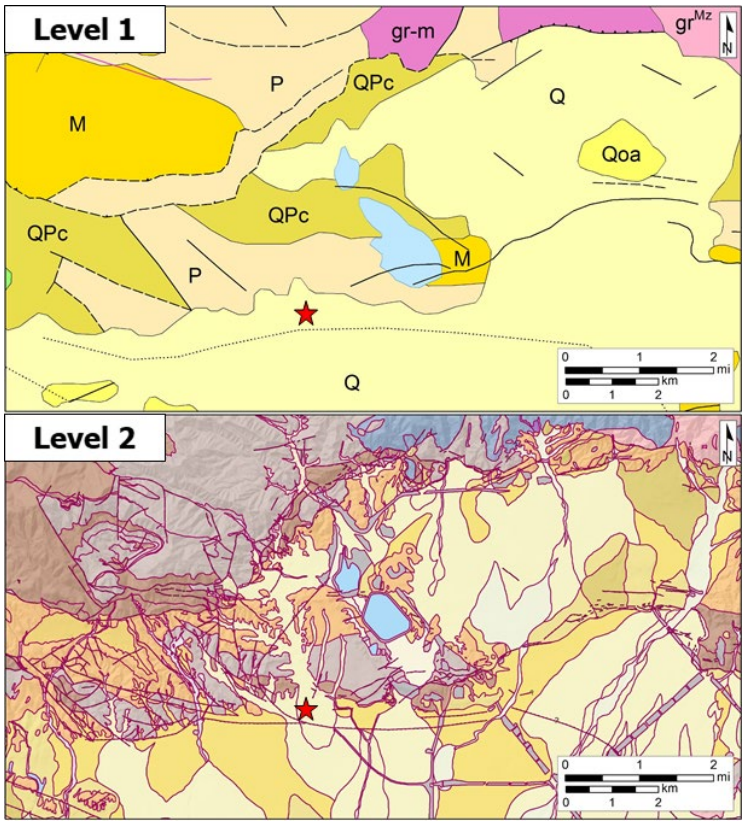

Figure 2.4: Comparison of Level 1 (1:750,000 Scale) Geologic Map from CGS (2010) and Level 2 (1:100,000 Scale) Geologic Map from Bedrossian et al. (2012)

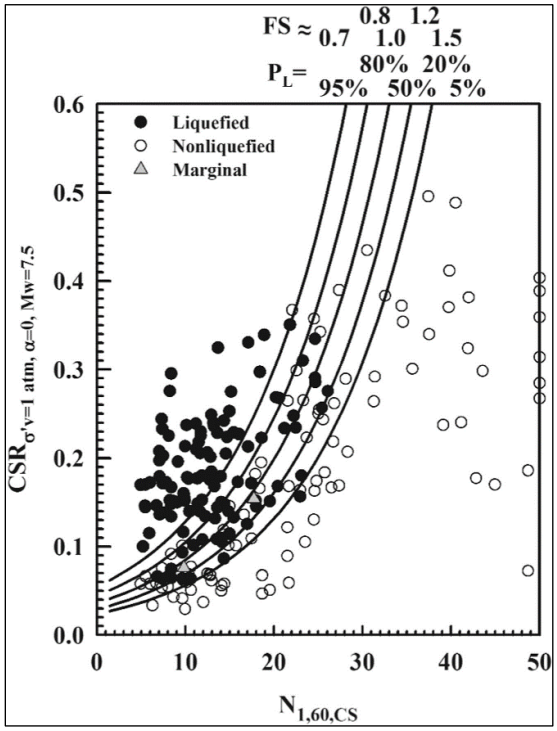

Figure 2.5: SPT Liquefaction Triggering Curves from Cetin et al. (2018)

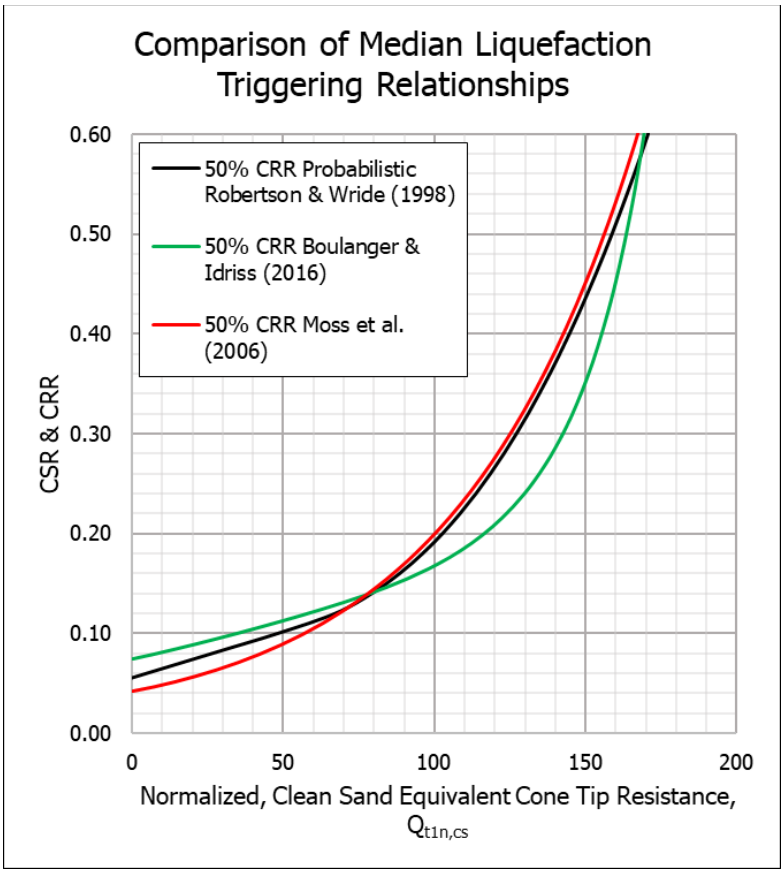

Figure 2.6: Comparison of Median CPT Liquefaction Triggering Relationships from Moss et al. (2006), Boulanger & Idriss (2016), and the Probabilistic Modification to the Robertson & Wride (1998) as Updated by Robertson (2009) Procedure from Ku et al. (2012)

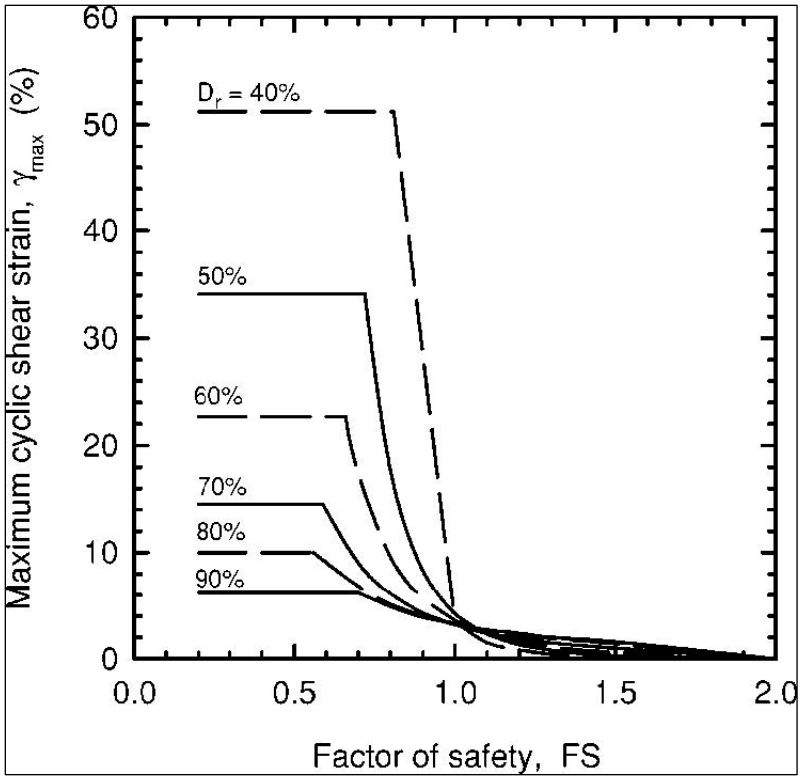

Figure 2.7: Relationships to Estimate the Maximum Cyclic Shear Strain from Zhang et al. (2004)

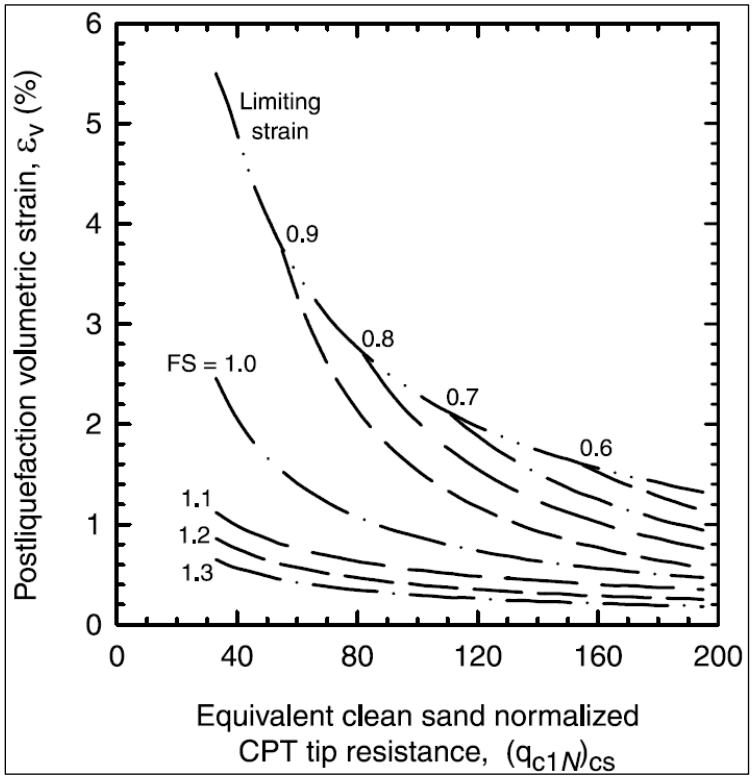

Figure 2.8: Relationships to Estimate the Post-Liquefaction Volumetric Strain from Zhang et al. (2002)

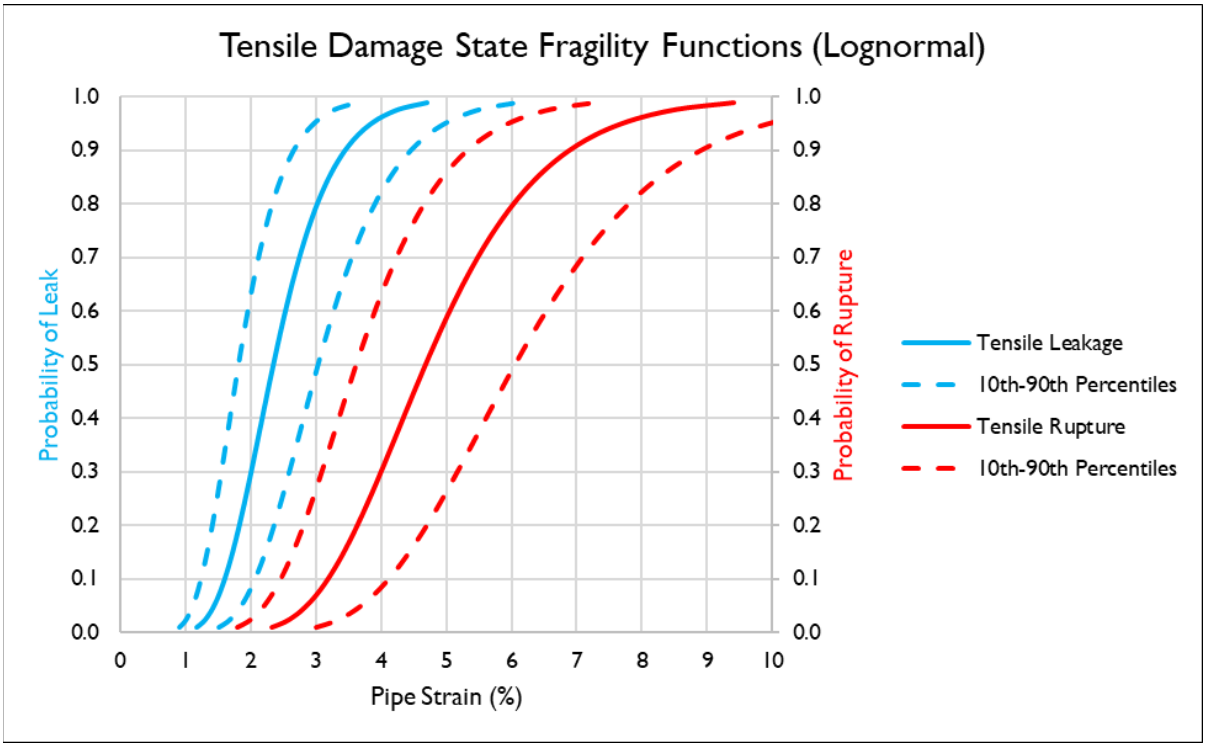

Figure 2.9: Lognormal Pipe Leakage and Rupture Fragility Functions (Arithmetic Scale)

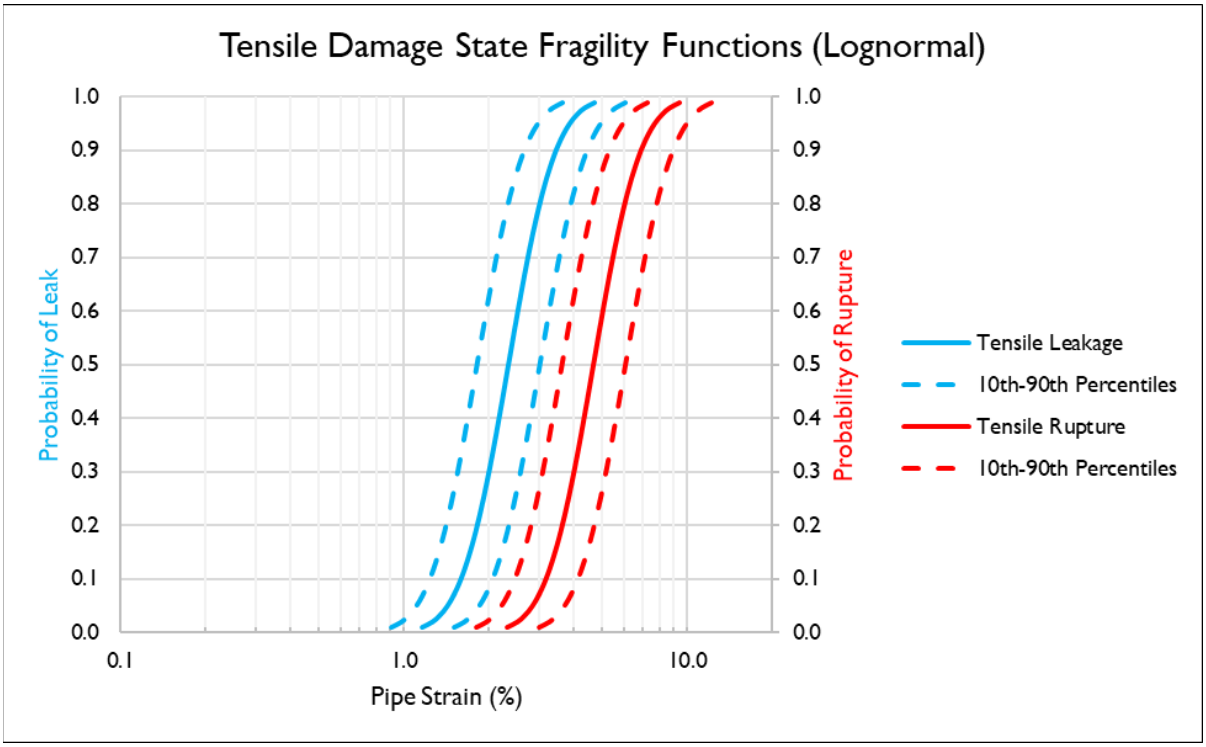

Figure 2.10: Lognormal Pipe Leakage and Rupture Fragility Functions (Log Scale)

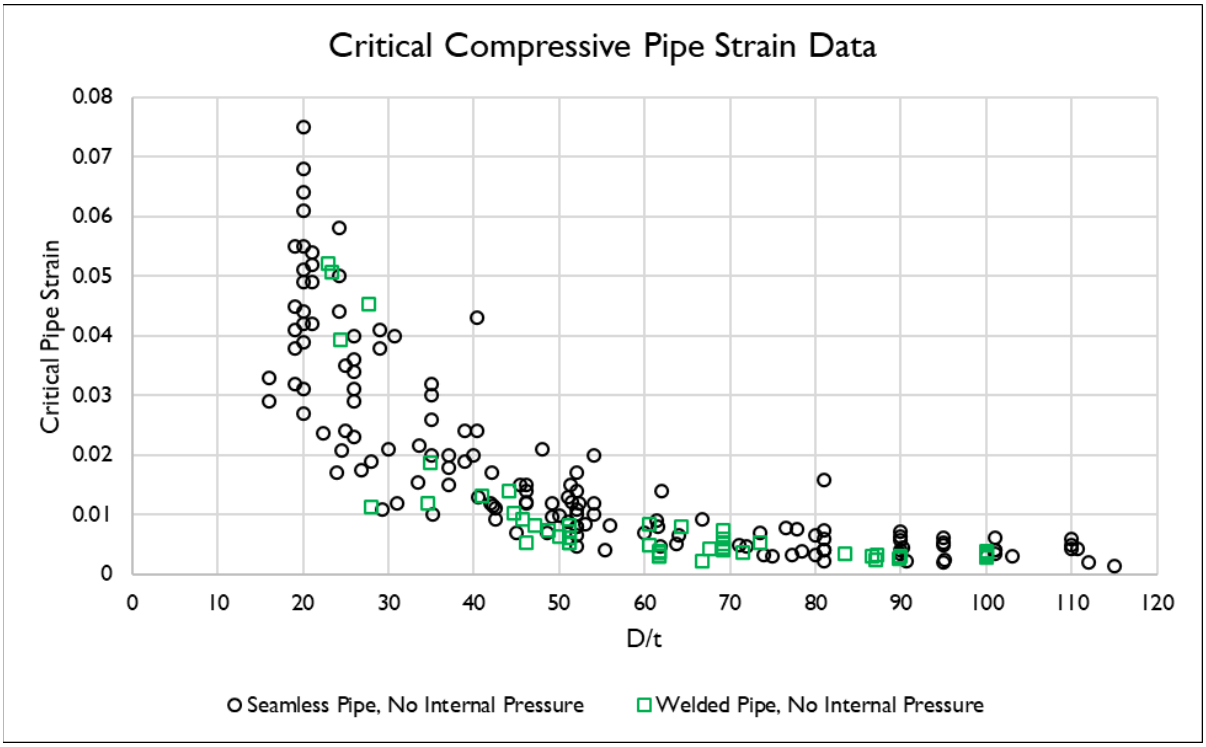

Figure 2.11: Critical Compressive Pipe Strain Laboratory Test Data Compiled by Mohr (2003)

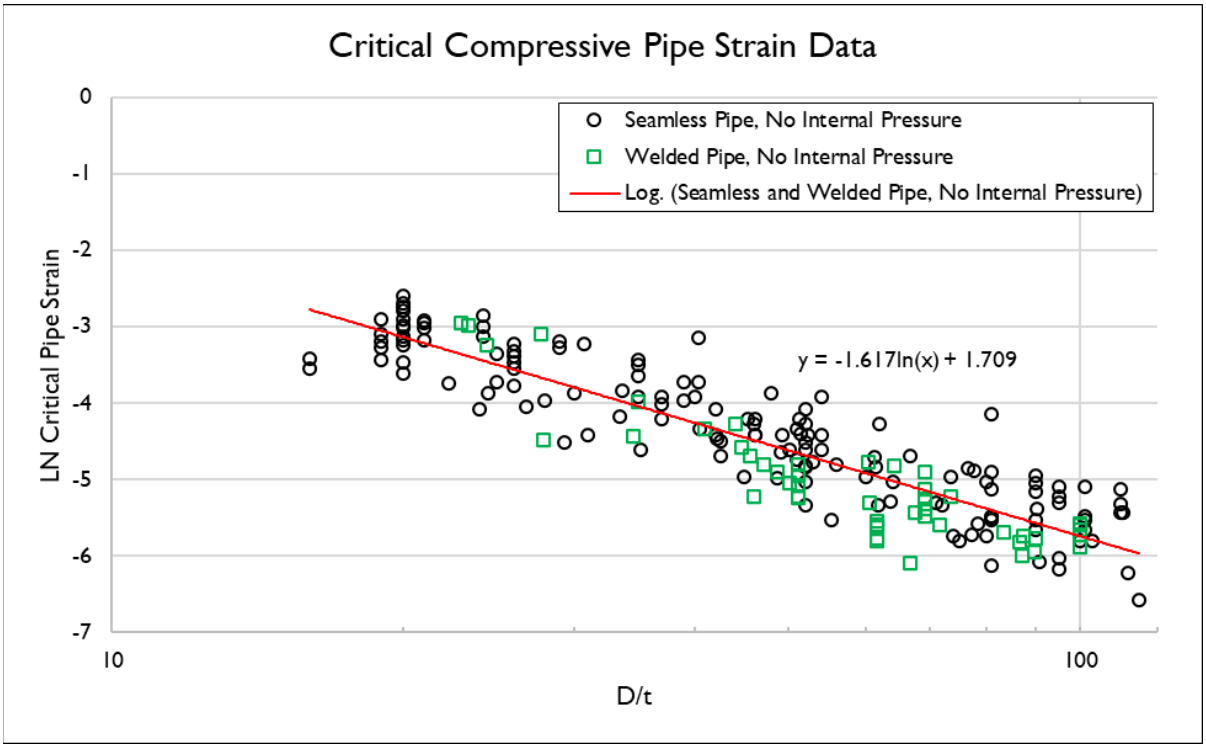

Figure 2.12: Natural Logarithm of Critical Compressive Pipe Strain Laboratory Test Data from Mohr (2003) with Linear Regression

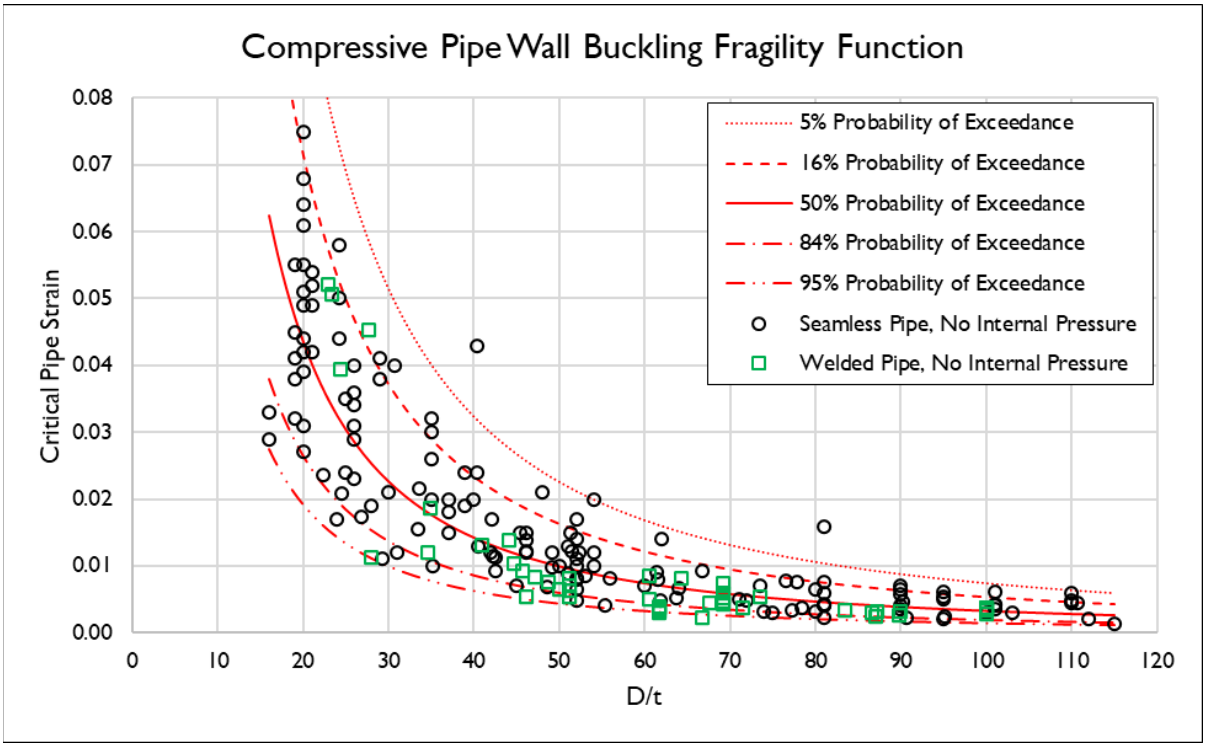

Figure 2.13: Compressive Pipe Wall Buckling Fragility Function, Equation (2.52), with the Critical Compressive Pipe Strain Laboratory Test Data Compiled by Mohr (2003) (Arithmetic Scale)

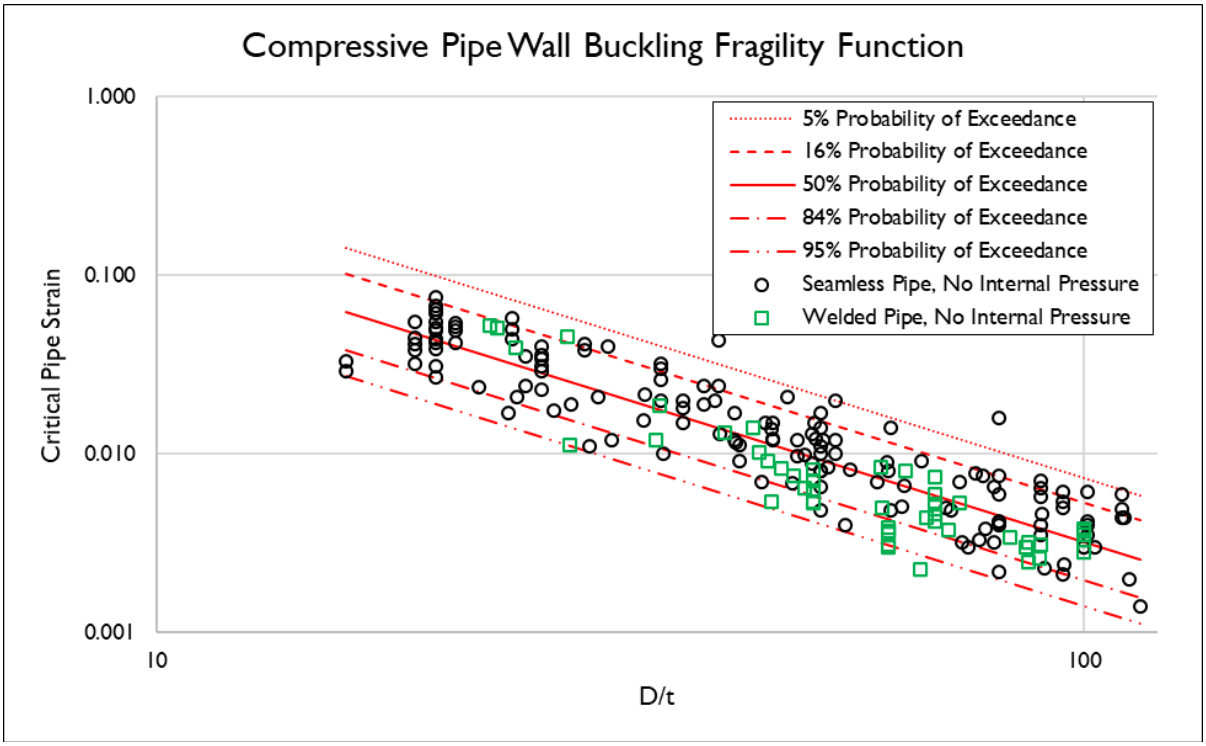

Figure 2.14: Compressive Pipe Wall Buckling Fragility Function, Equation (2.52), with the Critical Compressive Pipe Strain Laboratory Test Data Compiled by Mohr (2003) (Log Scale)

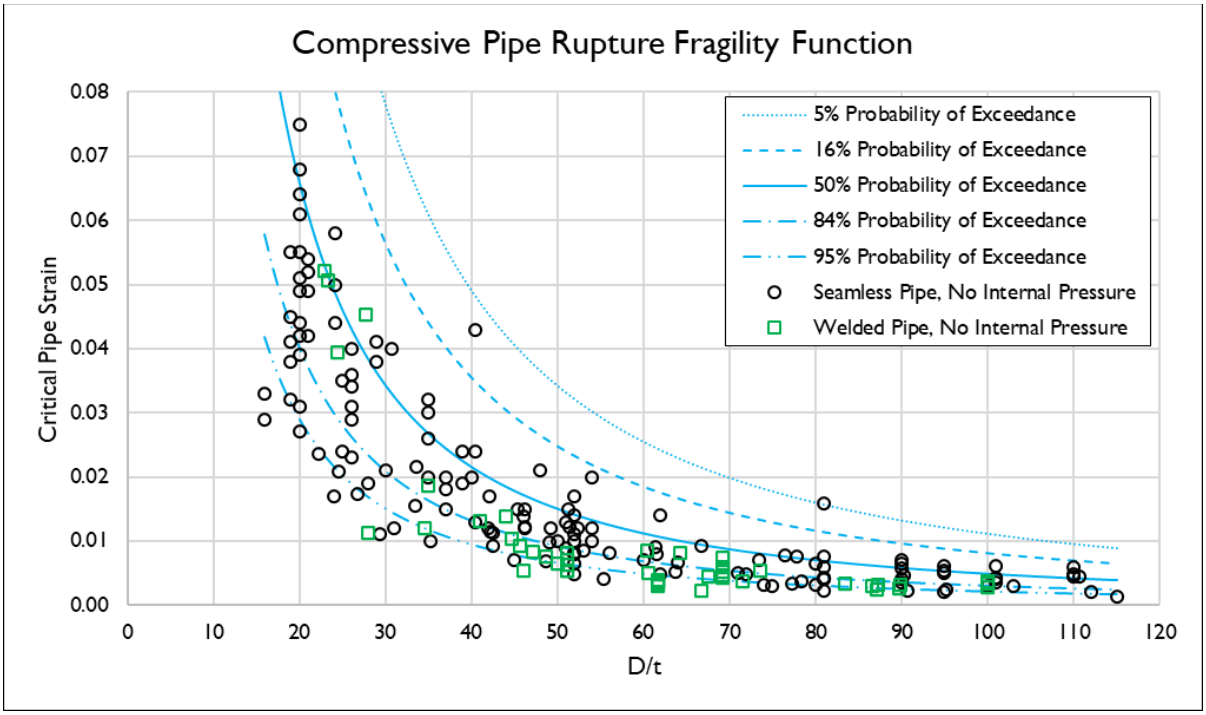

Figure 2.15: Compressive Pipe Rupture Fragility Function, Equation (2.53), with the Critical Compressive Pipe Strain Laboratory Test Data Compiled by Mohr (2003)

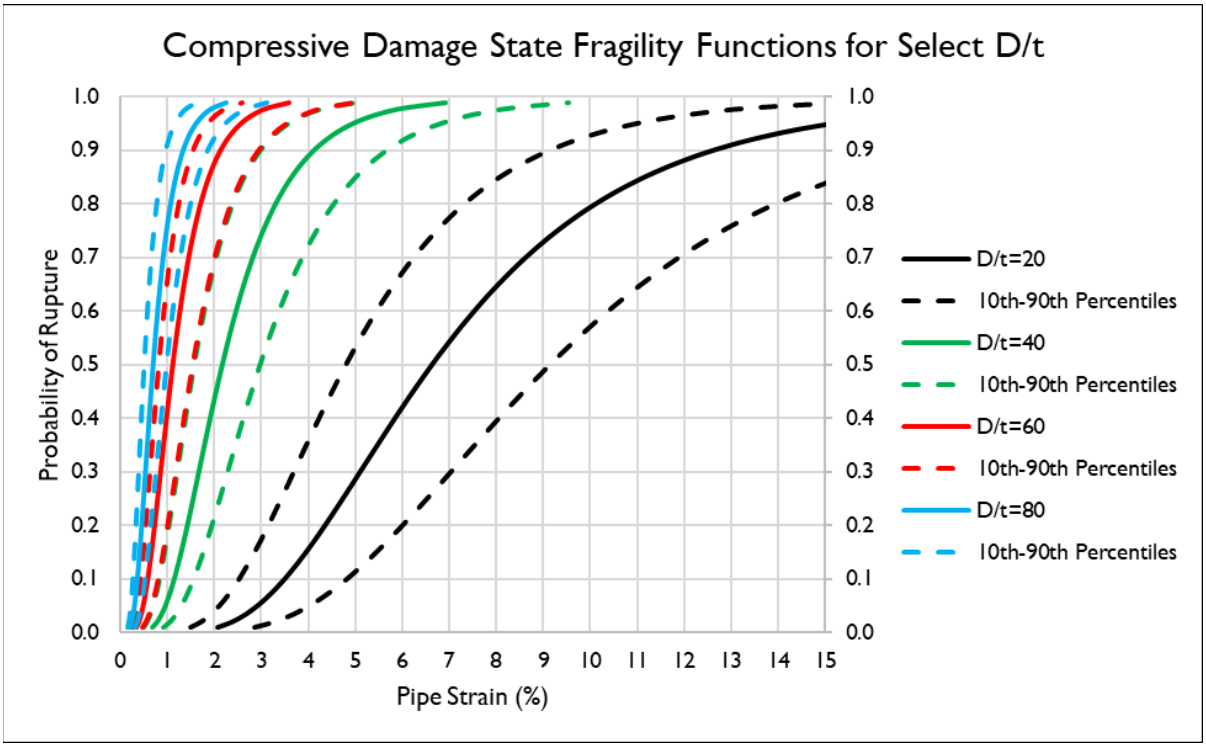

Figure 2.16: Probability of Compressive Rupture, Equation (2.53), for Select D/t Ratios (Arithmetic Scale)

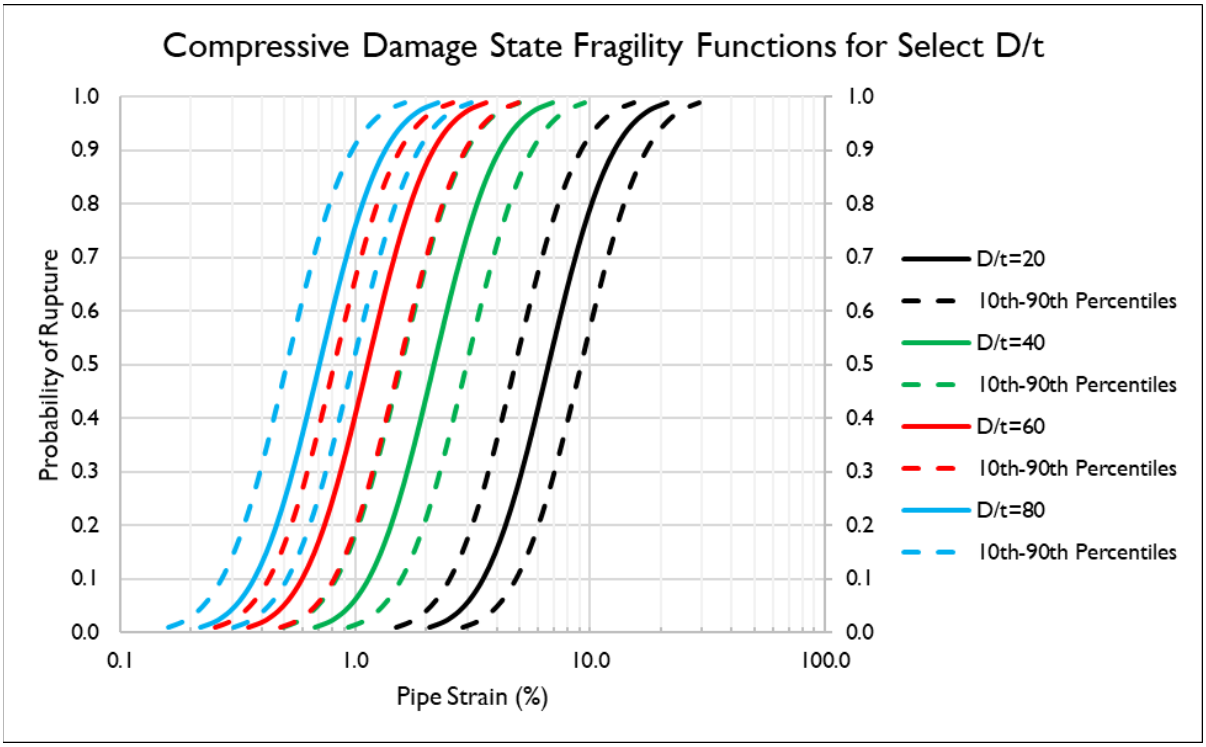

Figure 2.17: Probability of Compressive Rupture, Equation (2.53), for Select D/t Ratios (Log Scale)

3 REGIONAL SCALE PROBABILISTIC PROCEDURE FOR ESTIMATING LATERAL SPREAD DISPLACEMENTS

The contents of this chapter are based in large part on the material contained in a journal article published in the Soil Dynamics and Earthquake Engineering journal by Bain, C. A. and Bray, J. D. entitled: "Regional Scale Probabilistic Procedure for Estimating Lateral Spread Displacements," (Bain & Bray, 2023).

3.1 INTRODUCTION

Liquefaction-induced lateral spread displacement is a common mechanism of seismic displacement and often causes severe damage to port facilities and distributed infrastructure, such as buried pipelines. The lateral spread displacement hazard can be assessed at the site-specific scale using methods such as cone penetration tests (CPTs) or advanced numerical analysis techniques, but these methods are impractical for assessing potential lateral spread displacements across large, distributed infrastructure systems. Distributed infrastructure systems such as water and gas pipeline networks may include hundreds of kilometers of pipelines, and the liquefaction and lateral spread displacement hazard may vary significantly throughout the geographic area of these networks. To assess the lateral spread displacement hazard to lifeline systems, a need exists for improved regional scale analysis methods. This paper describes and illustrates the use of a new procedure to probabilistically assess potential liquefaction-induced lateral spread displacements at regional scales.

To develop the procedure, cone penetration test (CPT) data are collected in a region and are sorted by surficial geology. The lateral displacement index (LDI) is calculated for each CPT for 225 unique combinations of depth to groundwater (GWT), peak ground acceleration (PGA), and earthquake moment magnitude (M_w). The data are used to derive relationships to estimate the probability that LDI equals zero ($P_{LDI=0}$), where small values of LDI are assumed to be essentially zero, and the mean, non-zero LDI. The $P_{LDI=0}$ and mean, non-zero LDI relationships are combined using a mixed-random variable model whereby there is a mass probability that LDI equals zero (denoted LDI_0) and a continuous distribution of non-zero LDI. The distribution of non-zero LDI is then converted to a distribution of non-zero lateral spread displacement using existing topographic correlations of LDI to lateral spread displacement. Finally, to realistically model the spatial extent of lateral spreading, the modeled lateral displacements are scaled by the proportion of a surficial geologic unit estimated to be susceptible to surface liquefaction and a minimum displacement threshold is established. The modeling is shown to reasonably estimate both the spatial extent and severity of lateral spreading in the San Francisco Bay Area of California for the 1989 M_w 6.9 Loma Prieta earthquake and in Christchurch, New Zealand for the 2010 M_w 7.1 Darfield and 2011 M_w 6.2 Christchurch earthquakes.

3.2 AVAILABLE REGIONAL SCALE LIQUEFACTION TRIGGERING AND LATERAL SPREAD DISPLACEMENT PROCEDURES

Evaluating liquefaction triggering and potential lateral spread displacements at regional scales is challenging due to the variability and large uncertainty inherent to estimating geotechnical, groundwater, and topographic conditions as well as the earthquake shaking intensity.

The Zhu et al. (2015) and (2017) procedures use proxies for geotechnical and groundwater conditions, such as slope-based shear wave velocity in the upper 30 m (V_{S30}), compound topographic index (CTI), mean annual precipitation, and distance to the coast, nearest river, or nearest body of water, along with the PGA or peak ground velocity (PGV) to estimate the probability of liquefaction triggering. Given that these procedures use only proxies for subsurface conditions, their estimates are highly uncertain. Moreover, these methods do not quantify the aleatory variability (uncertainty due to inherent randomness) or epistemic uncertainty (uncertainty due to lack of data). Furthermore, Zhu et al. (2015) and (2017) do not attempt to quantify the potential consequences of liquefaction, such as lateral spread displacements.

Alternatively, Youd & Perkins (1978)-type geologic based assessments have been employed for decades to qualitatively assess the relative susceptibility of surficial geologic units to liquefaction triggering over regions with large-scale geologic mapping that differentiates quaternary units by age and depositional environment. Geologic-based maps of relative liquefaction susceptibility can be converted to quantitative estimates for the probability of liquefaction triggering and lateral spread displacement using the Hazus (FEMA, 2020) methodology. The Hazus (FEMA, 2020) method for estimating lateral spread displacement is based on the Youd & Perkins (1987) liquefaction severity index (LSI), which loosely correlates the severity of liquefaction to the distance to the seismic energy source (R) and the earthquake M_w. The Hazus method implicitly assumes that lateral spreading is only an inertia driven process, whereby the stronger the shaking, the greater the lateral spread displacement, and it does not consider topography in estimating displacements. This approach does not consider the potential mechanism for lateral spread displacement where earthquake shaking generates excess pore water pressure resulting in liquefaction and overlying, non-liquefied sediments move gently downslope or towards a free-face due largely to gravitational forces greater than the strength of the liquefied material at times with high excess pore water pressures. For these reasons, the Hazus method may not reliably characterize the lateral spread displacement hazard. In addition, Hazus does not estimate the aleatory variability or epistemic uncertainty in the lateral spread displacement estimate.

Another approach to evaluating liquefaction at regional scales is to calculate liquefaction vulnerability indices, such as the liquefaction potential index (LPI) (Iwaski et al., 1982) or the liquefaction severity number (LSN) (van Ballegooy et al., 2014a), at CPT locations or at soil exploratory borings with standard penetration test (SPT) blow counts, to then interpolate between investigation sites using kriging techniques, and lastly, to correlate the calculated vulnerability index to the probability of liquefaction triggering or potential consequences of liquefaction. This approach has validity but is limited to areas with many geotechnical investigations spaced relatively close together. It is difficult to apply these techniques in risk analyses, which may require evaluating thousands of ground shaking iterations, and it is difficult to track the uncertainty from dozens to thousands of individual geotechnical investigations.

In another approach that was the inspiration of this paper, Holzer et al. (2011) merged geologic based evaluations with subsurface geotechnical investigations to develop what they termed *Liquefaction Probability Curves for Surficial Geologic Deposits*. Holzer et al. (2011) collected CPTs in regions, sorted them by surficial geology, and calculated LPI for many different PGAs and for two groundwater depths (1.5 and 5 m). PGA was scaled by the magnitude scaling factor (MSF) from Youd et al. (2001) to generalize the relationships to all earthquake magnitudes and at each value of the magnitude-scaled PGA, the percentage of CPTs within a geologic unit with LPI > 5 is taken to be the probability of liquefaction. The threshold LPI value of 5 was selected because

Toprak & Holzer (2003) found that liquefaction is likely when LPI > 5. Logistic models were then fitted to the data to create relationships that estimate the probability of liquefaction triggering given magnitude-scaled PGA and depth to groundwater of 1.5 or 5 m.

While the Holzer et al. (2011) method was a significant contribution to advance regional scale modeling techniques, it is not without limitations. Holzer et al. (2011) presents models for two discrete groundwater depths (1.5 and 5 m) rather than modeling the depth to groundwater as a continuous variable. Holzer et al. (2011) also employs LPI, which has validity in estimating the likelihood of surface manifestations of liquefaction (i.e., ground failure), but LPI has not been correlated directly to lateral spread displacement (LD). Finally, Holzer et al. (2011) do not estimate aleatory variability or epistemic uncertainty with their method.

3.3 TOPOGRAPHIC DRIVERS OF LATERAL SPREADS AND THE LATERAL DISPLACEMENT INDEX

As discussed previously, lateral spread displacement is often driven by gravitational forces as non-liquefied soils overlying liquefied sediments move gently downslope or towards a free-face (e.g., river banks or the waterfront at port facilities). In other cases, inertial effects may also contribute to lateral spread displacements; however, the liquefaction of continuous soil layers is still a primary mechanism of lateral spreading in these cases. Methods for estimating potential lateral spread displacements typically require site-specific geotechnical investigations (e.g., Youd et al., 2002; Zhang et al., 2004; Faris et al., 2006; Gillins & Bartlett, 2018) and characterize in-situ static driving stresses using topographic slope or free-face ratio (*FFR*, which is the ratio of the distance to the bottom of a free-face feature, *L*, to the height of the free-face, *H*). The Zhang et al. (2004) procedure is one of the most commonly employed CPT-based methods in engineering practice. Its topographic correlations for converting LDI to LD are used in this study.

Zhang et al. (2004) correlates LDI to lateral spread displacement (LD) for gently sloping sites far from a free-face as Equation (3.1) and the correlation for sites near a free-face is presented as Equation (3.2).

$$\frac{LD}{LDI} = S + 0.2 \quad for\ 0.2\% < S < 3.5\% \tag{3.1}$$

$$\frac{LD}{LDI} = 6 * (FFR)^{-0.8} \quad for\ 4 < FFR < 40 \tag{3.2}$$

where S is the topographic slope in percent and FFR is the free-face ratio (L/H). LDI as defined by Zhang et al. (2004) is calculated using Equation (3.3) and is an index of the cumulative shear strain potential from all liquefiable layers in the subsurface.

$$LDI = \int_0^{z_{max}} \gamma_{max} dz \tag{3.3}$$

The maximum potential shear strain of a soil layer, γ_{max}, is a function of the relative density of the soil layer and the excess pore pressure ratio, represented by the factor of safety against liquefaction triggering (FS_{Liq}). For this study, the factor of safety against liquefaction triggering was estimated using the 50% probability of liquefaction cyclic resistance ratio (*CRR*) relationships from Boulanger & Idriss (2016) and the Ku et al. (2012) probabilistic modification to the Robertson & Wride (1998) as updated by Robertson (2009) procedure, giving equal weight to the two methods. As recommended by Holzer et al. (2011), soils in the San Francisco Bay Area with soil behavior type index $I_c \geq 2.4$ were considered not susceptible to liquefaction triggering.

For soils in Christchurch, soils with $I_c \geq 2.6$ were assumed to not be susceptible to liquefaction triggering, which is a typical assumption (e.g., Maurer et al. 2019). To evaluate liquefaction triggering using Boulanger & Idriss (2016), their relationship to estimate the fines content was used for soils in the San Francisco Bay Area while the relationship from Maurer et al. (2019) was used to estimate the fines content for soils in Christchurch. Relative density was estimated using the relationships from Idriss & Boulanger (2008), Jamiolkowski et al. (2001), and Kulhawy & Mayne (1990), giving weights of 0.4, 0.3, and 0.3, respectively. γ_{max} was calculated using the relationships from Zhang et al. (2004) and Idriss & Boulanger (2008), giving equal weight to the two methods.

The definition of LDI presented in Equation (3.3) assumes liquefaction at all depths contributes equally to lateral displacement at the ground surface, with the only recommended limitation from Zhang et al. (2004) being that liquefaction triggering should not be evaluated below a depth of 23 m. In the regions evaluated for this study, free-faces are generally small (typically a few meters) so estimating lateral spread displacement by considering liquefaction triggering to a depth of 23 m leads to significant overestimation of the lateral spread hazard for the free-face condition. Additionally, for the gently sloping ground condition, liquefaction at depths greater than about 10-15 m is unlikely to contribute to lateral displacement at the ground surface. For these reasons, a sensitivity study was performed to estimate an appropriate maximum depth for evaluating liquefaction triggering and to investigate potential depth weighting factors (DWFs) to limit the contribution of deep liquefiable layers to the lateral spread hazard.

LDI was calculated with no DWF to maximum depths of 10 m and 15 m, and using several forms of DWFs, which are presented in Figure 3.1. To evaluate the appropriateness of each of these assumptions, the procedure described in later sections of this paper was evaluated in the San Francisco Bay Area for the M_w 6.9 Loma Prieta earthquake and the results interrogated. It was found that evaluating LDI with no DWF leads to unacceptable overestimation of the spatial extent of lateral spreading and displacement magnitudes. DWF 1 (bolded red in Figure 3.1) reduces the overestimation of the lateral spread hazard at the regional scale to an appropriate degree for the San Francisco Bay Area dataset. DWF 1 also worked well for the Christchurch dataset, which will be discussed later. Accordingly, DWF 1 was employed, and the definition of LDI is modified for this study to that presented in Equation (3.4).

$$LDI = \int_0^{z_{max}} \gamma_{max} w(z) dz\,, \quad where: \quad w(z) = 1 - \sinh\left(\frac{z}{13.615}\right)^{2.5} \tag{3.4}$$

In addition to incorporating DWF 1 in the calculation of LDI, LDI was assumed to be zero for CPTs with less than 0.30 m of soil expected to liquefy (i.e., soil profile had less than 0.30 m with $FS_{Liq} < 1.0$). For lateral spreading to occur, liquefied soils must be continuous over a relatively large area, which is less likely when only thin layers of liquefied soil are present. The selected value of 0.3 m is still likely conservative as the thinnest liquefied layer in the case history database used by Youd et al. (2002) to develop their lateral spread displacement procedure was 1.0 m and the thinnest liquefied layer in the case histories used by Zhang et al. (2004) to develop their procedure was 0.6 m. LDI was calculated for each of the CPTs for every combination of PGA, M_w and GWT presented in Table 3.1 (225 unique combinations).

3.4 DATA SOURCES AND UNCERTAINTY

3.4.1 San Francisco Bay Area Datasets and Uncertainty

The implementation of the proposed regional scale liquefaction-induced lateral spread displacement procedure is illustrated through its use in two regions: the San Francisco Bay Area of California and the Christchurch area of New Zealand. In the San Francisco Bay Area, the CPT database comes from the United States Geological Survey (USGS, 2020a), the geologic map is the 1:24,000 scale mapping from Witter et al. (2006), and a groundwater table model assuming local mean sea level (LMSL) conditions comes from the USGS Coastal Storm Modeling System (CoSMoS) project (USGS, 2021a), who modeled the depth-to-groundwater in the coastal areas around the San Francisco Bay Area using the groundwater modeling program MODFLOW (USGS, 2022). Topographic slope and free-face ratio are derived from 10-m resolution digital elevation models (DEMs) of terrestrial elevations from the USGS (USGS, 2020b) and a 10-m resolution DEM with bathymetric elevations of the San Francisco Bay from the USGS (Fregoso et al., 2017). Geometry of free-face features in the Bay area comes from the Bay Area Aquatic Resources Inventory (BAARI) GIS database published by the San Francisco Estuary Institute and Aquatic Science Center (SFEI, 2017) and from a shapefile database of streams in the San Francisco Bay Area published by the Bay Area Open Space Council (Bay Area Open Space Council, 2008). The model is evaluated using the USGS *ShakeMap* estimates for the median PGA for the 1989 M_w 6.9 Loma Prieta Earthquake (USGS, 2021b) and observations of liquefaction primarily from the USGS (Holzer, 1998) study supplemented by those from the Seed et al. (1991) study.

The datasets used for modeling in the San Francisco Bay Area all have uncertainty. Most of the CPTs in this dataset are electric cones but some are mechanical cones. CPTs have uncertainty in the measured corrected tip resistance (q_t) and the measured sleeve friction (f_s). Kulhawy & Mayne (1990) estimate the coefficient of variation (COV) for tip resistance measurements collected with mechanical or electric cones is 10% and 5%, respectively. The COV for sleeve friction measurements collected with mechanical or electric cones is 20% and 10%, respectively. In addition to the uncertainty in the actual CPT tip resistance and sleeve friction measurements, interpreting CPT data introduces additional uncertainty into the assessment. For example, CPT measurements are used to estimate the fines content (FC) of potentially liquefiable sands in liquefaction triggering assessments with significant uncertainty. The variability in the tip resistance and sleeve friction measurements and the uncertainty associated with estimating fines content from CPT measurements were not considered in this study. Instead, measured values were used. However, a full probabilistic study could be performed with a logic tree approach to capture these sources of epistemic uncertainty.

The most significant potential uncertainty in the Witter et al. (2006) mapping is in the accuracy of the mapped units. There is the potential that the units indicated on the map may not always align with the geology at the site. For the purposes of this study, all mapped units are assumed to be accurate.

The depth to groundwater model used in this study from the USGS CoSMoS project (USGS, 2021a) has significant uncertainty which stems largely from the methods used to generate the model using MODFLOW (USGS, 2022). There is also uncertainty due to the inherent temporal variability in the groundwater table. According to Befus et al. (2020), the area's hydrogeology was modeled with uniform aquifer thickness along the coast with a horizontal impermeable layer at a depth of 50 m below sea level. Given that the properties of the aquifer are unknown, the aquifer

hydraulic conductivity (k) was assumed to be constant with values of 0.1, 1, and 10 m/day assumed to span the estimated range of aquifer hydraulic conductivities in the study region. Depth to groundwater models were generated by solving the steady-state groundwater flow equation at a 10-m resolution. Model depth to groundwater estimates were compared to well measurements in the study area with the model assuming k = 1 m/day producing results that adequately approximate mean depth to groundwater conditions with the assumption of local mean sea level (LMSL) conditions. The models assuming k = 0.1 and 10 m/day systematically bias the model to produce high and low depth to groundwater estimates, respectively. The steady-state depth to groundwater model residuals assuming LMSL and k = 1 m/day is estimated to have COV ≈ 41% and it is assumed to be approximately lognormally distributed. The form of the residual distribution was not investigated by Befus et al. (2020).

According to Wechsler (1999), DEMs may be subject to three types of errors: blunders associated with the data collection process, systematic errors associated with improperly calibrated equipment or data processing software, and random errors. The USGS can identify and remove blunders and systematic errors, but random errors persist in the published datasets. According to Stoker & Miller (2022), the uncertainty in the USGS 10-m DEMs is normally distributed with standard deviation equal to 0.82 m. This standard deviation was estimated using 10-m DEMs from all over the United States and may or may not accurately reflect the uncertainty of the 10-m DEMs in the Bay Area. These errors carry through the calculation of the topographic slope and the free-face ratio, but for the purposes of this study, the uncertainty in the calculated slope and free-face ratio resulting from the uncertainty in the DEM elevations was not considered.

ShakeMap provides estimates of the intensity of ground motions for the 1989 M_w 6.9 Loma Prieta earthquake as an uncertainty-weighted average of direct ground motion observations and estimates from ground motion models (GMMs). Total uncertainty is geospatially variable and is a function of the uncertainty obtained using a distance-to-observation spatial correlation function and the uncertainty of the GMMs. *ShakeMap* datasets for the Loma Prieta earthquake including uncertainty are available from the USGS (USGS, 2021b). For the purposes of this study, the lateral spread displacement model was evaluated using the median ground motion estimates and the sensitivity to the shaking intensity was interrogated by evaluating the model for the 16% and 84% probability of exceedance ground motion estimates.

The Witter et al. (2006) geologic map for the San Francisco Bay Area was simplified into three distinct groups: the artificial fill over Holocene estuarine mud (*afem*) deposits, latest Holocene alluvial fan levee (*Qhly*) and similar highly susceptible alluvial and fluvial deposits, and Holocene alluvial fan (*Qhl*) and similar moderately susceptible alluvial and fluvial deposits. The USGS CPT database (USGS, 2020a) does not contain enough CPTs in older deposits to attempt to estimate a distribution of LDI in those units. They are assumed to not be susceptible to liquefaction in this study. The USGS CPTs in the San Francisco Bay Area used in this study are overlaid on the simplified version of the Witter et al. (2006) geologic map in Figure 3.2. The number of CPTs in each evaluated deposit, including in New Zealand, is presented in Table 3.2. All CPT data are available from the USGS (2020a).

An innovative aspect of this method is the use of LDI calculated from CPT data representative of each geologic unit and then conversion of LDI distributions to distributions of lateral spread displacement using existing topographic correlations. To do this, free-face ratio and topographic slope are mapped in the Bay Area. Gently sloping areas with slopes less than 5 degrees are easily distinguished by calculating a slope map from the DEM but estimating free-face ratio at regional scales is more difficult. Figure 3.3 displays the process of deriving a map of free-face

ratio in a portion of the Bay Area around Oakland. Figure 3.3a displays a continuous 10-m raster DEM image with terrestrial and bathymetric elevations, and Figure 3.3b displays shapefiles of the free-face features and the calculated distance up to 250 m from the free-face features. Then, Figure 3.3c displays the resulting estimated heights of the free-face features. The height of a free-face feature was estimated by performing a focal statistics operation whereby the minimum elevation in a 250 m neighborhood around every cell was subtracted from the elevation of the center cell of the moving window. In the last step, free-face ratio, which is displayed in Figure 3.3d, was estimated by dividing the distance to the free-face features by the height of the free-face features. Figure 3.4 displays the other model inputs in the Bay area for the back-analysis of the 1989 M_w 6.9 Loma Prieta earthquake. Figure 3.4a displays median PGA contours from the USGS ShakeMap (USGS, 2021b), Figure 3.4b displays a groundwater table model in the Bay Area (USGS, 2021a), and Figure 3.4c displays locations of observed liquefaction (Holzer, 1998).

3.4.2 Christchurch, New Zealand Area Datasets and Uncertainty

Christchurch CPTs, DEMs, event-specific depth to groundwater models, and liquefaction observations and interpretations are provided in the New Zealand Geotechnical Database (NZGD, 2021) and papers by Bradley et al. (2020), Cubrinovski et al. (2012), Robinson et al. (2013), Cubrinovski & Robinson (2016), Rathje et al. (2017), and Toprak et al. (2018). This study relied primarily on the datasets provided in the NZGD (2021) and the Bradley et al. (2020) CPT dataset. The DEMs and groundwater models were provided in GIS raster and shapefile formats by Sjoerd van Ballegooy and Nathan McDougall from Tonkin + Taylor (van Ballegooy, personal communication, 2021).

Elevations contained in the 5-m resolution DEMs in the Christchurch area have less uncertainty relative to the USGS 10-m DEMs of the San Francisco Bay Area. Residuals for all DEMs are normally distributed with standard deviations generally on the order of 0.06 to 0.16 m (CERA, 2014). For the purposes of this report, uncertainties in the DEM elevations were not considered to investigate their impact on the modeled lateral spread hazard.

According to van Ballegooy et al. (2014b), uncertainty in the depth to groundwater models comes predominantly from two sources: temporal fluctuations in groundwater elevations caused by seasonal rainfall, short-term dewatering, or other natural or artificial events, and from geospatial modeling uncertainties from lidar-derived ground surface elevations, errors from interpolation, or errors from other sources. Uncertainty in the depth to groundwater models is geospatially variable and is a function of distance to the nearest monitoring well and the number of readings at that well. Four geospatial classes were created to communicate confidence in the modeled depth-to-groundwater: lowest (west of 4 m median groundwater contour), lower (groundwater table based on widely spread monitoring wells), medium, and higher (groundwater table surface based on closely spread monitoring wells with longer duration monitoring records). Uncertainty in the groundwater table for each of the described uncertainty classes is ±0.5 to ±1.0 m, ±0.4 m, ±0.2 m, and ±0.1 m, respectively. The areas investigated for the purposes of this study are in the medium and higher confidence classes with uncertainty less than ±0.2 m. The uncertainty in the depth to groundwater was not investigated in this study. The sensitivity to the uncertainty in the modeled depth to groundwater is expected to be small given the relatively low values of uncertainty in this dataset.

The western part of the Avon River floodplain was mapped using satellite imagery and LiDAR-based DEMs for this study. This study area was selected because significant lateral

spreading was observed during the Darfield and Christchurch earthquakes and although the geology could be refined further, it is generally similar enough within the mapped study area to permit reasonable regional assessments. Regional assessments should not be expected to capture the subsurface geotechnical conditions in as much detail as site-specific assessments. Two additional areas were mapped: a) an area near the coast with Christchurch Formation sands deposited in a high wave energy environment (termed "high energy deposits") and b) an area adjacent to the high energy deposits, but further inland, with Christchurch Formation sands deposited in a lower energy environment (termed "low energy deposits"). The high energy deposits experienced little to no surface liquefaction during both the Darfield and Christchurch earthquakes and the low energy deposits experienced significant liquefaction. The Avon River floodplain and the NZGD CPTs in that area are shown in Figure 3.5.

Free-face ratio in the Avon River floodplain in Christchurch was mapped in a similar manner to the process described previously for the San Francisco Bay Area and illustrated in Figure 3.3, except that the free-faces along the Avon River were mapped manually. Additionally, bathymetric data could not be located for the Avon River, therefore, based on cross-sections presented by Robinson (2013), it is assumed that the Avon River is a constant 3.5 m depth. As the Avon River is generally between 2 and 5 m depth, use of a constant depth of 3.5 m introduces additional epistemic uncertainty into the analysis.

Figure 3.6 displays the median PGA contours and liquefaction severity observations for the Darfield and Christchurch earthquakes in Christchurch. As described by Bradley & Hughes (2012), the estimated PGA and uncertainty contours (termed "conditional" PGA and "conditional" uncertainty) were estimated using a New Zealand-specific ground motion model (GMM) and conditioned on observations of ground motion intensity at recording stations. Conditional uncertainty is a function of distance to the nearest recording station; where ground motion is known exactly (i.e., at a recording station), the uncertainty in the shaking intensity is zero and at locations far from a recording station, the uncertainty in the shaking intensity increases to the uncertainty of the New Zealand-specific GMM.

3.5 MODEL FUNCTIONAL FORM AND MIXED RANDOM VARIABLE DISTRIBUTION

The LDI datasets calculated for each geologic deposit were evaluated to develop models to assess the probability that LDI equals "zero" (i.e., a negligible value), which is delineated as $P_{LDI=0}$. To estimate $P_{LDI=0}$, small values of LDI < 3 were assumed to be essentially zero and the percentage of CPTs with LDI < 3 at each depth to groundwater and each magnitude-scaled PGA was taken to equal $P_{LDI=0}$. The sensitivity of the results to using an LDI threshold of 3 was investigated and found to be minor, as discussed later.

Equation (3.5a) was fit to the data to estimate $P_{LDI=0}$.

$$Prob_{LDI=0} = 1 - \frac{1 + a_0 * GWT^{a_1}}{\left[1 + exp\left[(a_2 + a_3 * GWT) * \left(PGA/MSF - (a_4 + GWT^{a_5})\right)\right]\right]^{a_6}} \quad (3.5a)$$

where a_0, a_1, a_2, a_3, a_4, a_5, and a_6 are model fitting coefficients, GWT is the depth to the groundwater table, and the magnitude scaling function (MSF) is defined as (Idriss & Boulanger 2008):

$$MSF = 6.9 * exp\left(\frac{-M_w}{4}\right) - 0.058, \quad MSF \leq 1.8 \quad (3.5b)$$

The non-zero LDI data was transformed using the natural logarithm, and Equation (3.6a) was fit to the data to estimate the mean, non-zero *ln*(LDI).

$$if\ \frac{PGA}{MSF} \leq \left(\frac{PGA}{MSF}\right)_{min} \begin{cases} LDI = 0 \\ else, \quad \ln(LDI) = \dfrac{[b_0 + b_1 * GWT] * \left[\frac{PGA}{MSF} - \left(\frac{PGA}{MSF}\right)_{min}\right]}{[b_2 + b_3 * GWT] + \left[\frac{PGA}{MSF} - \left(\frac{PGA}{MSF}\right)_{min}\right]} \end{cases} \quad (3.6a)$$

where b_0, b_1, b_2, and b_3 are model fitting coefficients, and

$$\left(\frac{PGA}{MSF}\right)_{min} = 0.012 * GWT + 0.06 \quad (3.6b)$$

The threshold value of $LDI_0 = 3$ was selected after performing an analysis using the dataset calculated from the CPTs available in the *afem* geologic unit in the San Francisco Bay Area. Equation (3.5a) and Equation (3.6a) were fit to the data assuming different LDI_0 values of 1, 3, 5, and 10, and the sensitivity of the results to each of these potential threshold values was evaluated. Using the fitted models for the four potential LDI_0 values listed, the median LDI was evaluated for many scenarios consisting of different combinations of PGA, M_w, and GWT and were found to generally have low sensitivity to the selected LDI_0 threshold value.

The residuals for the mean, non-zero *ln*(LDI) models were tested for normality using the Lilliefors test, which is an improvement to the Kolomorgorov-Smirnov (K-S) test. The model residuals for each of the deposits were found to not be normal and were instead fit with skew-normal distributions, which requires shape (α), location (ξ), and scale (ω) fitting parameters. The skew-normal cumulative distribution function (CDF) cannot be solved using closed-form solutions in Excel but is easily solved using programming languages such as Python.

As employed by Bray & Travasarou (2007), Rodriguez-Marek & Song (2016), and Bray & Macedo (2019), the LDI data are distributed as a mixed random variable. A mixed random variable distribution separates a discrete, lumped mass probability that LDI equals zero from a continuous distribution for non-zero *ln*(LDI) so that meaningless differences in the relative values of low LDI values do not determine the uncertainty in the estimate of meaningful values of LDI when LDI is larger than a selected threshold LDI value (i.e., $LDI_0 = 3$).

3.6 GEOLOGIC BASED MODELS FOR SAN FRANCISCO BAY AREA DEPOSITS AND CHRISTCHURCH, NEW ZEALAND DEPOSITS

The $P_{LDI=0}$ data and the fit of Equation (3.5a) to these data and the mean, non-zero *ln*(LDI) data and the fit of Equation (3.6a) to these data for the *afem*, *Qhly*, and *Qhl* geologic units in the San Francisco Bay Area are shown in Figure 3.7. The $P_{LDI=0}$ data and the fit of Equation (3.5a) to these data and the mean, non-zero *ln*(LDI) data and the fit of Equation (3.6a) to these data for the Avon River floodplain, and Christchurch Formation low energy and high energy deposits of the Christchurch area are shown in Figure 3.8. The model regression coefficients for each of the evaluated deposits are presented in Table 3.3. Fitting parameters for the skew-normal residuals distributions for each of the evaluated deposits are presented in Table 3.4.

For each geologic deposit, the $P_{LDI=0}$ data show that at low magnitude-scaled PGA values, the $P_{LDI=0}$ equals or is close to one, which indicates lateral spread displacement is unlikely (i.e., LDI is likely negligible). The $P_{LDI=0}$ decreases as the magnitude-scaled PGA increases. At large

magnitude-scaled PGA values, the $P_{LDI=0}$ asymptotically approaches the percentage of evaluated CPTs within a particular geologic unit with LDI < 3.

The non-zero *ln*(LDI) data show that at magnitude-scaled PGA values less than the minimum magnitude-scaled PGA estimated in Equation (3.6a), the mean, non-zero *ln*(LDI) equals zero. As the magnitude-scaled PGA increases to an intensity greater than the minimum threshold value estimated for liquefaction triggering and lateral spreading to occur, the mean, non-zero *ln*(LDI) increases quickly before asymptotically approaching the average non-zero *ln*(LDI) value from all evaluated CPTs within a particular geologic unit.

This asymptotic behavior exhibited in both the $P_{LDI=0}$ and non-zero *ln*(LDI) data is mechanistically correct; as the shaking intensity increases, LDI should not increase in an unbounded manner because all saturated, liquefiable soils will eventually liquefy at sufficiently strong ground shaking levels, albeit with low strain potential for dense deposits. The model aleatory variability (inherent randomness) comes from the range of non-zero LDI calculated at each CPT within a particular geologic unit.

3.7 CONVERSION OF LDI DISTRIBUTION TO LATERAL SPREAD DISPLACEMENT DISTRIBUTION

The models presented in Figure 3.7 and Figure 3.8 are used to estimate distributions of LDI. An estimated distribution of LDI is converted to a distribution of potential lateral spread displacement using the topographic correlations from Zhang et al. (2004) presented as Equations (3.1) and (3.2). An example LDI distribution and conversion to a distribution of lateral spread displacement using Equation (3.2) for Avon River Floodplain deposits and several different values for the free-face ratio is presented as Figure 3.9.

To be consistent with the widely used CPT processing software *CLiq*, the model bounds for Equation (3.1) are modified from the values presented in Zhang et al. (2004) to slopes ranging from 0.1% < S < 5%. Areas far from free-faces with S ≤ 0.1% may experience level ground liquefaction with sand boils and ejecta, but these areas lack sufficient static driving stress to experience lateral spreading. The results are not sensitive to the selection of a threshold value of S = 0.1%. Areas with S ≥ 5% have deposits that are assumed to be too dense to experience lateral spreading. In areas with 3.5% ≤ S < 5%, S = 3.5% is applied in Equation (3.1) to limit excessive lateral spread displacement estimates.

The model bounds for Equation (3.2) are expanded in *CLiq* from the values presented in Zhang et al. (2004) to *FFR* (L/H) ranges of 1 < *FFR* < 50. This study adopts the increased upper bound of *FFR* = 50, but in areas with 1 < *FFR* ≤ 4, *FFR* = 4 is applied in Equation (3.2) to limit excessive lateral spread displacement estimates. Lateral spreading due to proximity to a free-face is considered to a maximum of 250 m from a free-face feature.

In areas with gently sloping ground and near a free-face feature with *FFR* < 50, the lateral spread displacement is taken as the maximum value estimated using both the sloping ground displacement estimated from Equation (3.1) and the free-face displacement estimated from Equation (3.2). This is advantageous because it is not always clear which condition controls (i.e., sloping ground or free-face). By allowing the model to make this determination automatically, strict, artificial transitions between the two models are avoided.

Liquefaction case histories in California and worldwide indicate that although large areas are often mapped as being susceptible to liquefaction in regional scale studies, only a small proportion of the total land area experience the surface effects of liquefaction and an even smaller

proportion experience lateral spread displacement. To limit overestimation of the liquefaction hazard, Hazus (FEMA, 2020) estimates the proportion of land area that is susceptible to liquefaction according to the liquefaction susceptibility class mapped using Youd & Perkins (1978) methodology as summarized in Table 3.5. In addition to overestimating the spatial extent of surface liquefaction, regional assessments also typically overestimate the liquefaction severity. Lateral spread displacements estimated using the described procedure are multiplied by the proportion of land area estimated to be susceptible to liquefaction using the values presented in Table 3.5. Testing of the presented models to estimate LDI and lateral displacements across the study regions without scaling by the factors presented in Table 3.5 results in significant overestimation of the spatial extent of lateral spreading and the lateral spread severity. In the Bay area, both the *afem* and *Qhly* deposits were estimated by Witter et al. (2006) to be very highly susceptible to liquefaction and the *Qhl* deposits were estimated by Witter et al. (2006) to be moderately susceptible to liquefaction. In the Christchurch area, the Avon River Floodplain and the low depositional energy Christchurch Formation sands are estimated to be very highly susceptible to liquefaction and the high depositional energy Christchurch Formation sands are estimated to have low liquefaction susceptibility.

3.8 ILLUSTRATIVE CASE HISTORY ASSESSMENTS

3.8.1 San Francisco Bay Area during the 1989 M_w 6.9 Loma Prieta Earthquake

The 1989 M_w 6.9 Loma Prieta earthquake caused significant liquefaction of the sandy artificial fill over estuarine mud (*afem*) deposits along the margins of the San Francisco Bay, especially around Oakland and Alameda, Treasure Island, and the Marina District. Locations of observed surface effects of liquefaction in the Bay area are presented in Figure 3.4c. Lateral spread displacements for the Loma Prieta earthquake were modeled using the proposed procedure with the simplified version of the Witter et al. (2006) geologic map presented in Figure 3.2, the groundwater table model from the USGS CoSMoS project (USGS, 2021a), and the USGS ShakeMap estimates for median PGA (USGS, 2021b) shown in Figure 3.4a. The study focused on the Oakland and San Jose areas, where the USGS (2020a) CPT data were available.

Figure 3.10 displays the spatial distribution of the estimated $Prob_{LDI=0}$ parameter and Figure 3.11 shows the estimated 84%, 50%, and 16% probability of exceedance LDI in the San Francisco Bay Area. This proposed procedure estimates that LDI is highest in the artificial fill deposits around the margins of the Bay and in the youngest Holocene alluvial fan levee deposits in the San Jose area, which is consistent with the observed locations of liquefaction in these areas in the post-earthquake reconnaissance (e.g., Holzer, 1998). The proposed procedure estimates the $Prob_{LDI=0}$ to be less than one (though typically greater than 0.5) in the Holocene alluvial deposits. The $Prob_{LDI=0}$ in these areas is higher (i.e., lateral spreading is less likely) compared to the artificial fill and youngest Holocene alluvial fan levee deposits. This is consistent with expectations for these deposits which were mapped as moderately susceptible to liquefaction by Witter et al. (2006) compared to very high susceptibility for the artificial fill and youngest Holocene alluvial fan levee deposits. Liquefaction was not observed in the Holocene alluvial fan deposits (Holzer, 1998).

Figure 3.12 shows the estimated 84%, 50%, and 16% probability of exceedance lateral spread displacements in the Bay Area. At the 50% probability of exceedance level, the proposed procedure estimates the largest lateral displacements near significant free-faces in the artificial fill

deposits around the margins of the Bay and in the youngest Holocene alluvial fan levee deposits in the San Jose area near major tributaries such as the Guadalupe River at the 16% probability of exceedance level. Lateral spread displacements estimated as a function of LDI are an index for both the likelihood of liquefaction occurrence and the severity of potential displacements. Estimated lateral spread displacements less than or equal to 5 cm are considered to be negligible, because these areas are unlikely to experience surface manifestations of liquefaction or noticeable lateral spreading. The proposed procedure focuses only on areas where the estimated lateral displacement exceeds 5 cm, which reduces the tendencies for regional scale liquefaction ground failure hazard models to overestimate the spatial distribution and severity of the liquefaction hazard. Comparison of the lateral spread displacement estimates will be discussed further in Section 9 of this paper.

To evaluate the sensitivity to the PGA, the proposed procedure is evaluated in the Bay Area with the 84% and 16% probability of exceedance ground motions. Figure 3.13 and Figure 3.14 show the estimated lateral spread displacements with the 84% and 16% probability of exceedance PGA, respectively. This assessment shows that the estimated spatial extent of lateral spreading and magnitude of displacements decreases significantly with the 84% probability of exceedance PGA as the shaking intensity is insufficient to trigger liquefaction in some areas. The estimated spatial extent and magnitude of displacements increases modestly with the 16% probability of exceedance PGA.

3.8.2 Christchurch Area during the 2010 M_w 7.1 Darfield and 2011 M_w 6.2 Christchurch Earthquakes

The 2010 M_w 7.1 Darfield and 2011 M_w 6.2 Christchurch earthquakes caused severe, widespread liquefaction in Christchurch, New Zealand with the Christchurch earthquake causing significantly more liquefaction-induced damage due to its closer proximity to most of the urban area of Christchurch. Figure 3.15 shows the estimated $Prob_{LDI=0}$ parameter and the 84%, 50%, and 16% probability of exceedance estimated LDI values in the Avon River floodplain deposits for the Darfield and Christchurch earthquakes. This proposed procedure estimates the $Prob_{LDI=0}$ is significantly higher during the Darfield earthquake compared to the Christchurch earthquake, which is consistent with field observations of liquefaction severity (e.g., NZGD, 2021; Cubrinovski et al. 2012; Robinson et al. 2013; Cubrinovski & Robertson 2016; Rathje et al. 2017; and Toprak et al. 2018). Correspondingly, the estimated LDI values are much higher for the Christchurch earthquake compared to the Darfield earthquake, which is also consistent with observations (NZGD, 2021). Figure 3.16 displays the estimated 84%, 50%, and 16% probability of exceedance lateral spread displacements in the Avon River Floodplain deposits for the Darfield and Christchurch earthquakes, which will be discussed further in Section 9 of the paper.

Figure 3.17 displays the estimated ProbLDI=0 in the low and high depositional energy Christchurch Formation deposits for the Darfield and Christchurch earthquakes. The $Prob_{LDI=0}$ for the low energy deposits is much lower compared to the high energy deposits and the non-zero LDI is much greater. Correspondingly, the low energy deposits are estimated to have greater LD, as shown in Figure 3.18, which is consistent with observations (NZGD, 2021).

3.9 DISCUSSION OF ILLUSTRATIVE CASE HISTORY ASSESSMENTS

The reasonableness of the lateral spread displacement estimates using the proposed procedure can be quantitatively assessed in the Christchurch area due to the extensive high quality LiDAR ground displacement vectors available (NZGD, 2021). The uncertainty of the LiDAR-derived estimates of lateral spread displacements is generally about twice the uncertainty of the vertical measurements of the LiDAR survey. Most of the areas studied for the purposes of this report have vertical accuracy of ±0.2 m meaning that the LiDAR derived estimates for lateral displacements generally have accuracy of ±0.4 m.

Figure 3.19 shows the median estimated lateral spread displacements compared to the measured lateral spread displacements from LiDAR in the Avon River Floodplain deposits and the low depositional energy Christchurch Formation deposits for the Christchurch Earthquake. In the Avon River Floodplain deposits, 62% of median estimated lateral spread displacements for the Christchurch Earthquake are greater than the measured displacements from Lidar indicating the median performance of the proposed procedure is biased slightly high, but the overall magnitude of displacements is captured well for the Christchurch earthquake. Additionally, 54% and 75% of the estimated lateral spread displacements are within a factor of two and within a factor of three, respectively, of the lateral ground displacement measurements from LiDAR. In the low energy deposits, 59% of estimated lateral spread displacements are greater than the measured ground displacements from LiDAR and 48% and 68% of the estimated lateral spread displacements are within a factor of two and within a factor of three, respectively, of the LiDAR ground displacement measurements. The lack of significant LD in the high energy deposits is captured well by the proposed procedure.

In both the Avon River Floodplain deposits and the low energy deposits, the proposed procedure does not capture well the lateral displacements measured from LiDAR during the Darfield Earthquake at the median performance level. The magnitude scaled PGA is near the threshold for liquefaction triggering and the proposed models estimate $P_{LDI=0}$ to be slightly greater than 0.5 (~0.55) in many parts of the evaluated units, leading to zero displacement. The proposed procedure captures the measured lateral displacements from LiDAR well at the 16% probability of exceedance performance level.

In the San Francisco Bay Area, the performance of the proposed procedure is evaluated qualitatively based on the estimated spatial extent of lateral spreading and a comparison of the estimated lateral spread displacements to the reported lateral displacements in select areas. Holzer (1998) reports cracks approximately 30 cm wide in the main runway and adjacent taxiway at Oakland International Airport, and he reports 50 to 70 cm of lateral spread displacement along the west perimeter dike at Oakland International Airport. Additionally, Holzer (1998) reports 10-cm wide cracks at the Alameda Naval Air Station, fissures approximately 30 cm wide near the approach to the Bay Bridge, and several meters of lateral spread displacement in the Seventh Street Marine Container Terminal and Matson Terminal at the Port of Oakland where a perimeter dike wall failed. Minor lateral spreading with cracks generally less than 3 cm were reported along Interstate Highway 80, south of the University Avenue exit from Interstate Highway 80 and the frontage road west of the highway (Holzer, 1998). The 84% to 16% probability of exceedance range of lateral spread displacements estimated by the proposed procedure in these areas generally capture the observed lateral spread displacement, except for the area where the perimeter dike wall failed. The 84% to 16% probability of exceedance lateral spread displacement estimate range underestimates the reported displacement of several meters in this area. Overall, the observed

lateral spread displacements in the Oakland/Alameda area are captured reasonably well by the proposed procedure.

Holzer (1998) reports that no significant lateral spreading was observed in the San Jose area. Minor lateral spreading resulted in slight ground cracking at the San Jose International Airport along the east bank of the Guadalupe River. No lateral spreading was observed along Coyote Creek. The 84% to 16% probability of exceedance modeled lateral spread displacements in these areas generally capture the reported amount and distribution of lateral spread displacements in the San Jose area. Overall, the spatial extent and severity of lateral spread displacements are estimated well in the San Francisco Bay Area.

The performance of the proposed procedure in the Christchurch area and in the San Francisco Bay Area is judged to be good to outstanding for a regional scale liquefaction-induced lateral spread displacement procedure. Both the geospatial extent of lateral spreading and the severity of lateral spreading are estimated reliably for the investigated field case histories. Furthermore, the estimated lateral spread displacements are not biased excessively high or low as demonstrated with the Christchurch earthquake data. Regional scale models tend to overestimate both the spatial extent of liquefaction and liquefaction severity. This is not the case with the proposed procedure.

An analysis by Russell et al. (2017) compared the estimated lateral spread displacements using the Zhang et al. (2004) method at individual CPTs within approximately the same area of Christchurch of this study and found that 77% of the lateral spread displacement estimates are higher than the displacement measurements for the Christchurch earthquake and 57% of the estimates plot within a factor of two of the displacement measurements. Even when assessing the lateral spread hazard at individual CPTs, the Russell et al. (2017) analysis demonstrates the inherent difficulty in estimating lateral spread displacements using simplified procedures. The performance of the proposed regional scale procedure introduced in this study is about as reliable as the site-specific CPT-based lateral spread procedures widely used in engineering practice. Thus, its performance for the Christchurch earthquake at the regional scale is satisfactory.

3.10 LIMITATIONS

The proposed procedure has several limitations. Firstly, the proposed procedure is only as good as the input geospatial datasets, which all have epistemic uncertainty. GIS-based geologic maps have uncertainty in the accuracy of the linework and in the mapped deposit (i.e., the geologic map may be incorrect). Additionally, surficial geologic maps do not communicate information regarding subsurface conditions, and it is common, especially in alluvial fan environments, for different types of deposits to overlap in the subsurface (e.g., sheet flood deposits may overlap fluvial deposits). Groundwater levels are inherently difficult to map as there is significant uncertainty due to temporal variability in groundwater levels in the rainy season versus the dry season, tidal variations, and local variability due to local groundwater drawdown or recharge and local variations in the hydraulic conductivity of the geologic units. Additionally, long-term climatic trends such as prolonged droughts or a series of exceedingly wet winters will influence the depth to groundwater. Each of these uncertainties vary in time and space and are difficult to assess. Similarly, DEMs have uncertainty from the LiDAR measurements and conversion to bare earth topography.

Another source of uncertainty comes from the way free-face ratio is mapped at regional scales. Free-face ratio is defined as the distance to the bottom of the free-face divided by the height

of the free-face. To map free-face ratio in the San Francisco Bay Area and around the Avon River in Christchurch, the lateral distance was estimated to the edge of the free-face features, which likely does not correspond to the location of the bottom of the free-face feature. This systemically underestimates the distance to the free-face feature, resulting in systemically slightly higher free-face ratio values. Additionally, Euclidean distance to the free-face features is calculated on a grid which creates uncertainty in the distance estimate, with the maximum uncertainty from the grid resolution issue estimated to equal one half the resolution of the grid.

Additionally, lateral spread displacements estimated with the Zhang et al. (2004) method are typically assumed to only be accurate within a factor of two of the mean estimate. Moreover, the Zhang et al. (2004) topographic equations used in the proposed procedure are intended for free-field sites, and it is unlikely that sites with free-field conditions can be easily distinguished from sites that have retaining walls that buttress the soil and prevent lateral spreading or have other, non-free-field conditions at regional scales.

3.11 CONCLUSIONS

A new regional scale procedure is presented for probabilistically estimating the lateral spread displacement hazard. The proposed procedure combines subsurface data from CPTs with surficial geologic mapping, groundwater data, the earthquake magnitude, and the earthquake shaking intensity to estimate a distribution of LDI, which is converted to a distribution of lateral spread displacement using the topographic correlations of LDI to lateral displacement presented by Zhang et al. (2004).

The proposed procedure produces reasonable results for the 1989 M_w 6.9 Loma Prieta earthquake in the San Francisco Bay Area and the 2010 M_w 7.1 Darfield and 2011 M_w 6.2 Christchurch earthquakes in Christchurch, New Zealand. For both investigated regions, the models estimate reasonably both the spatial extent and severity of liquefaction. In the Christchurch area, the modeling is quantitatively shown to estimate lateral spread displacements in an unbiased manner. Moreover, the median estimate of lateral spread displacement for the Christchurch Earthquake captures most of the measured lateral spread displacement within a factor of two, and this regional scale method performs as well as site-specific CPT-based methods in Christchurch. In the San Francisco Bay Area, the proposed procedure estimates the largest displacements near significant free-faces in the artificial fills along the Bay, particularly in the Oakland/Alameda area, which is consistent with post-earthquake reconnaissance observations.

The proposed procedure advances the state-of-the-art of regional scale liquefaction and lateral spread displacement modeling through several innovations. Firstly, the proposed procedure capitalizes on the innovative liquefaction probability curves approach developed by Holzer et al. (2011). As discussed, regional scale models typically employ either proxies for geotechnical, geologic, and groundwater conditions (e.g., Zhu et al., 2017 uses V_{S30} as a proxy for geotechnical conditions) or they use kriging techniques to interpolate the liquefaction hazard between widely spaced CPTs or soil exploratory borings. Holzer et al. (2011) combined subsurface data from CPTs in the form of the liquefaction potential index (LPI) with surficial geologic mapping, a reliable means for characterizing the liquefaction potential at regional scales (Youd & Perkins, 1978). Holzer et al. (2011) show that the probability of surface liquefaction can be estimated reasonably as the proportion of CPTs in a geologic unit with LPI > 5 for given PGA, M_w, and GWT.

This study extends the Holzer et al. (2011) framework in an innovative manner by characterizes surficial geologic units using the lateral displacement index (LDI), which is

commonly used in site-specific methods to estimate lateral spread displacement but has not been used in regional scale methods. Models are developed to estimate a distribution of LDI for geologic units, which are conditioned on surficial geology, PGA, M_w, and GWT. The lateral spread displacement is then estimated based on LDI using topography estimated from DEMs.

Another innovative aspect of this work is how topography is characterized and used in this regional scale procedure. Most lateral spreads occur near a free-face condition and have been characterized by Youd et al. (2002) and Zhang et al. (2004), among others, using the ratio of the distance to the bottom of the free-face to the height of the free-face (i.e., the free-face ratio). As such, to estimate reasonably the locations and severity of lateral spreading at regional scales, it is important to estimate reasonably the free-face ratio of potential lateral spread areas across the region being studied. As illustrated in Figure 3.3, the proposed procedure can estimate reliably the free-face ratio using data commonly available over large regions. For example, free-face ratio had not been mapped previously over areas as large as the entirety of the San Francisco Bay Area.

Additional validation studies with the proposed procedure are warranted. For example, the performance of the proposed procedure for other earthquakes, such as the 2014 M_w 6.0 South Napa earthquake, which produced only limited amounts of minor liquefaction, could be interrogated. The South Napa earthquake produced limited amounts of minor liquefaction in part because it occurred in August at the height of the dry season, and it occurred in the midst of a severe, multi-year drought during which groundwater and stream flows were much lower than historical measurements. Additionally, it would be informative to perform forward modeling for several earthquake scenarios in the San Francisco Bay Area. For example, in 2017 the USGS released the results of their *HayWired* study (USGS, 2017), which hypothesized a M_w 7.0 earthquake on the Hayward Fault and modeled the potential ground shaking intensity in the Bay Area. Using the modeled ground shaking intensity, the lateral spread displacement hazard can be estimated and compared if the earthquake occurs during the dry season or the rainy season. Additionally, investigating the effect of potential sea level rise on the lateral spread hazard would be an interesting application of the proposed procedure.

This study demonstrates that liquefaction-induced lateral spreading can be modeled reasonably at regional scales and provides a framework for performing regional scale lateral spread assessments. The San Francisco Bay Area and Christchurch are unique in the quantity and quality of geotechnical, geologic, groundwater, and topographic data that are available. It is hoped that this study motivates organizations to collect the data required to enable the proposed regional scale lateral spread procedure, as well as other procedures, to be performed in other important regions, such as in Los Angeles, Salt Lake City, or Seattle.

Table 3.1: Range of Investigated Parameters

Parameter	Range of Values
PGA (g)	0.1, 0.15, 0.2, 0.3, 0.4, 0.5, 0.6, 0.8, 1.0
M_w	6.0, 6.5, 7.0, 7.5, 8.0
GWT (m)	0.5, 1.5, 3.0, 5.0, 7.0

Table 3.2: Number of CPTs in Each Investigated Surficial Geologic Deposit

Area	Surficial Geologic Deposit	Number of CPTs
San Francisco Bay Area	Artificial Fill over Estuarine Mud Deposits (*afem*)	89
	Latest Holocene Alluvial Fan Levee Deposits (*Qhly*)	41
	Holocene Alluvial Fan Deposits (*Qhl*)	177
Christchurch	Avon River Floodplain Deposits	442
	Christchurch Formation: Low Energy Deposits	150
	Christchurch Formation: High Energy Deposits	46

Table 3.3: Model Coefficients for the San Francisco Bay Area and Christchurch Area Deposits

Surficial Geologic Deposit	$P_{LDI=0}$ Model Coefficients						
	Parameter						
	a_0	a_1	a_2	a_3	a_4	a_5	a_6
afem	-0.081	1.01	-28.8	2.32	-0.98	0.012	15
Qhly	-0.142	0.55	-14.6	0.34	-1.16	0.018	112
Qhl	-0.270	0.50	-14.0	0.84	-1.01	0.019	13
Avon River	-0.0003	3.63	-29.0	2.15	-0.93	0.033	5.7
Low Energy	-0.005	0.30	-31.9	1.70	-1.11	0.012	1340
High Energy	-0.044	0.59	-19.1	0.73	-0.82	0.045	2.7

Surficial Geologic Deposit	Mean Non-Zero *ln*(LDI) Model Coefficients			
	Parameter			
	b_0	b_1	b_2	b_3
afem	4.43	-0.212	0.018	0.001
Qhly	3.89	-0.096	0.011	0.002
Qhl	3.53	-0.159	0.006	0.0001
Avon River	5.03	-0.148	0.010	0.005
Low Energy	4.83	-0.078	0.018	0.013
High Energy	3.42	0.035	0.035	0.018

Table 3.4: Skew-Normal Residuals Distribution Fitting Parameters for the San Francisco Bay Area and Christchurch Area Deposits

Surficial Geologic Deposit	Skew-Normal Distribution Fitting Parameters		
	Parameter		
	Shape, α	Location, ξ	Scale, ω
afem	0.00	0.01	0.80
Qhly	-5.72	1.26	1.56
Qhl	1.72	-0.72	1.15
Avon River	-3.88	1.04	1.31
Low Energy	-3.03	0.75	0.93
High Energy	-1.90	0.60	1.02

Table 3.5: Proportion of the Land Area Assumed Susceptible to Liquefaction (after FEMA, 2020)

Liquefaction Susceptibility Class	Proportion of Class Susceptible to Liquefaction
Very High	0.25
High	0.20
Moderate	0.10
Low	0.05
Very Low	0.02
None	0.00

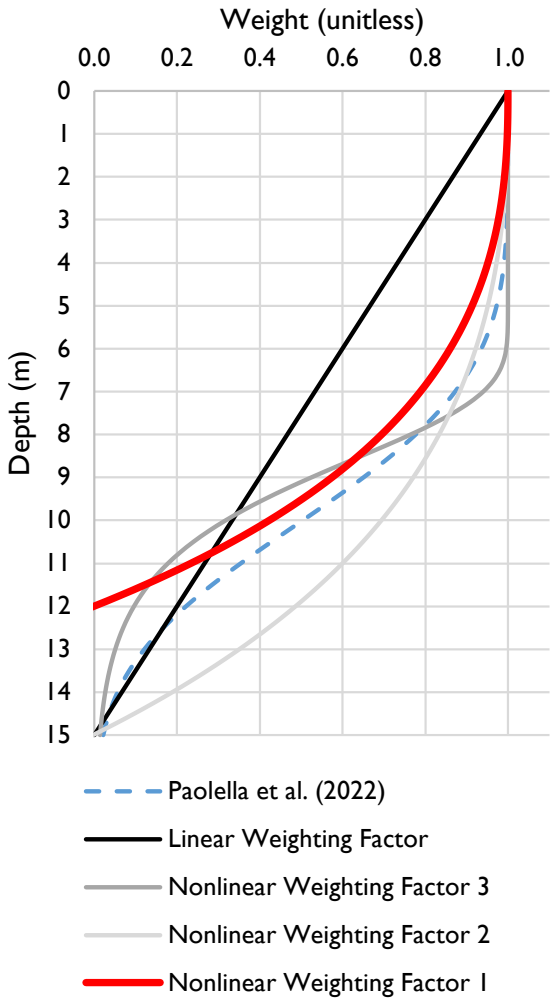

Figure 3.1: Investigated Depth Weighting Factors (DWFs) with Selected DWF in Red

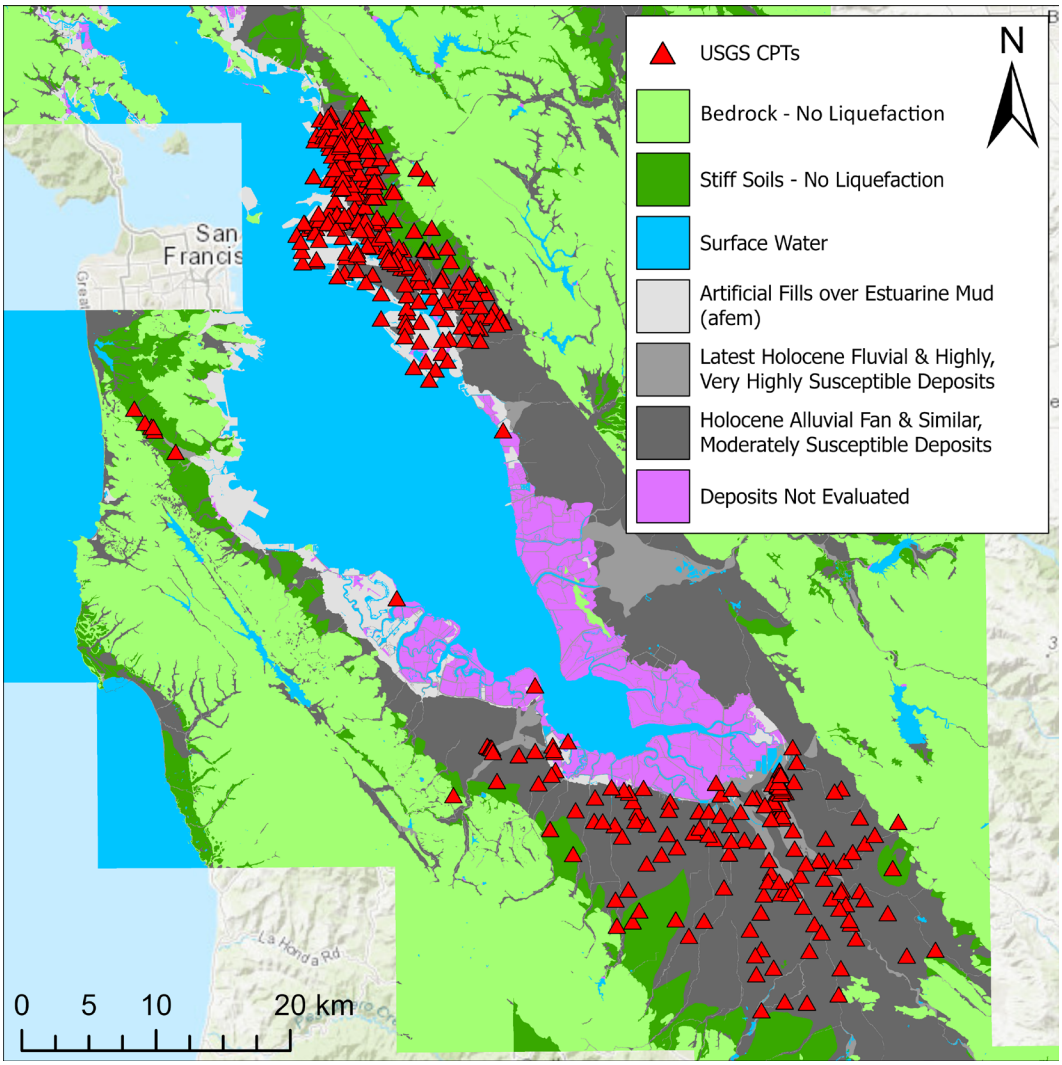

Figure 3.2: Locations of USGS CPTs in the San Francisco Bay Area Overlaid on Simplified Version of Witter et al. (2006) Geologic Map

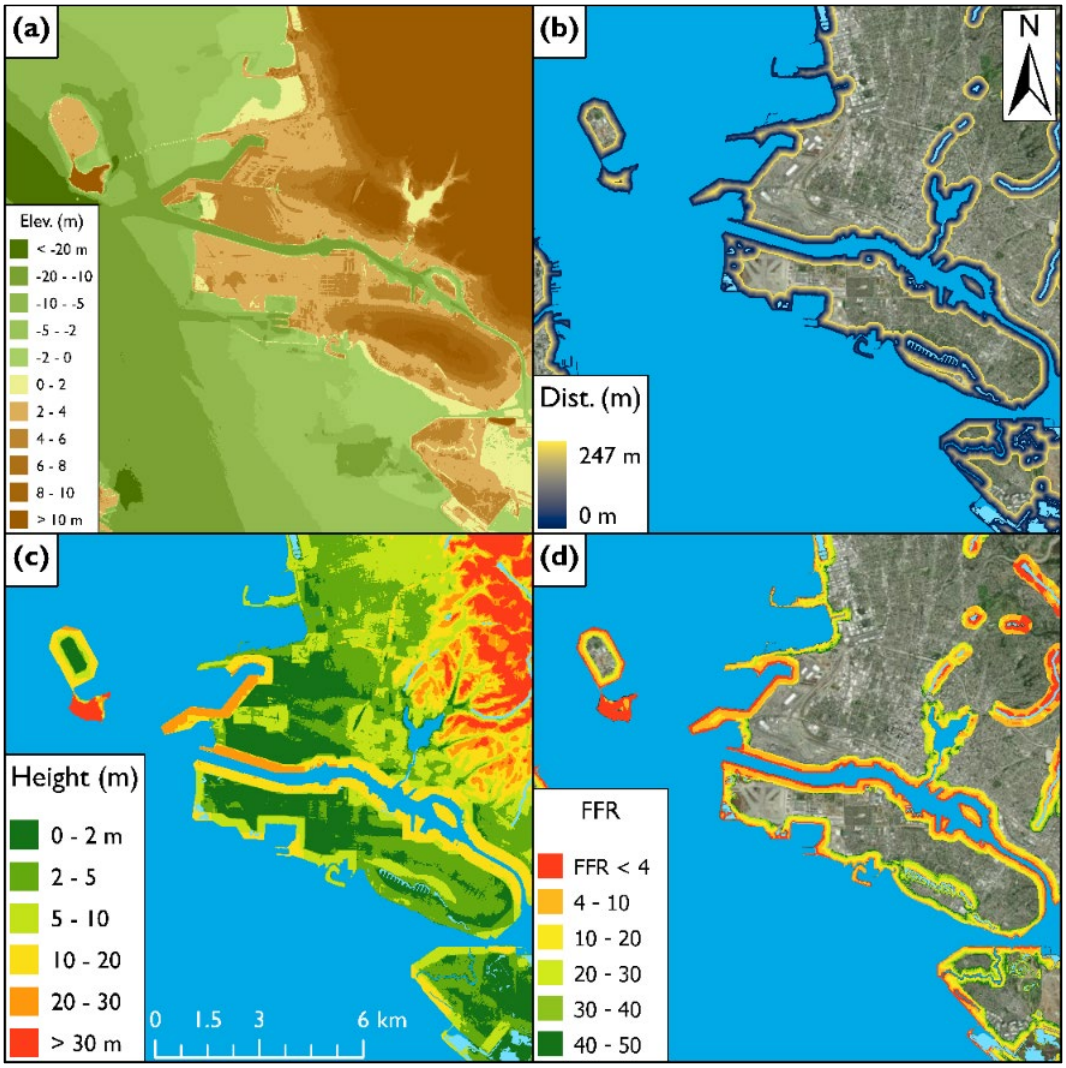

Figure 3.3: Process for Mapping Free-face Ratio in Bay Area (a) Continuous 10 m Resolution DEM with Terrestrial and Bathymetric Elevations, (b) Shapefiles of Free-face Features with Calculated Distance to Features up to 250 m, (c) Estimated Height of Free-face Features, and (d) Resulting Free-face Ratio Map in Bay Area

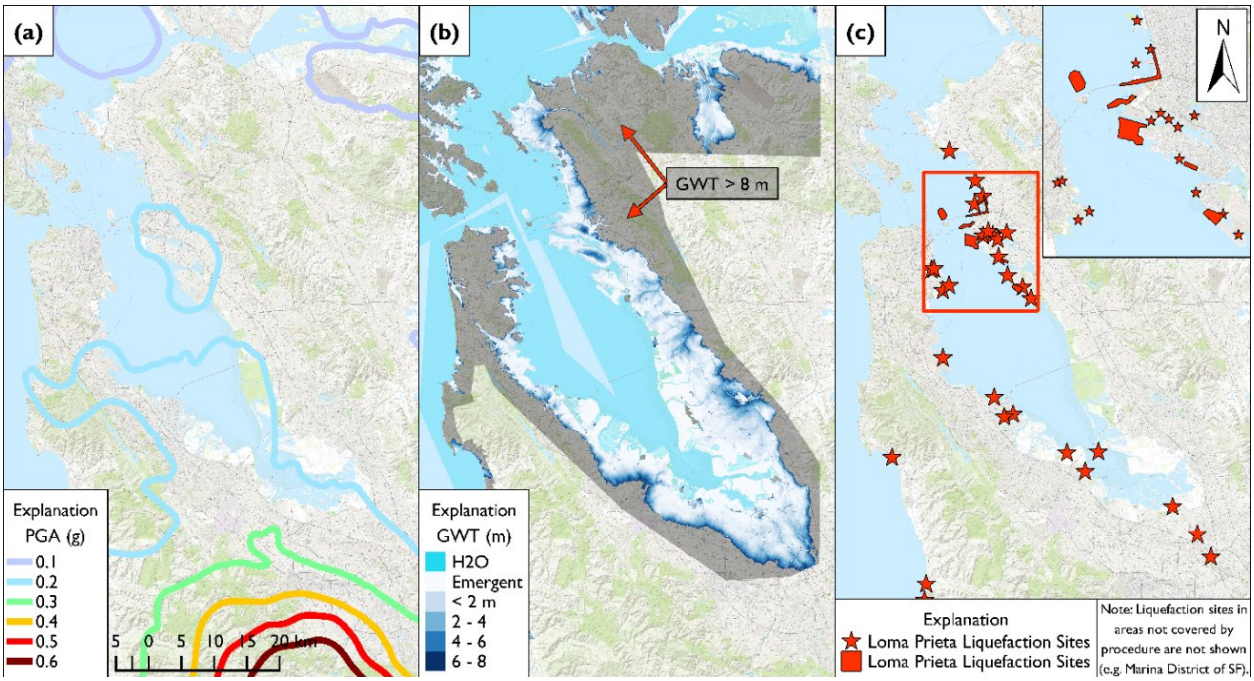

Figure 3.4: Datasets in Bay Area for Back-Analysis of M_w 6.9 Loma Prieta Earthquake (a) Median PGA Contours, (b) GWT Model, and (c) Locations of Observed Liquefaction

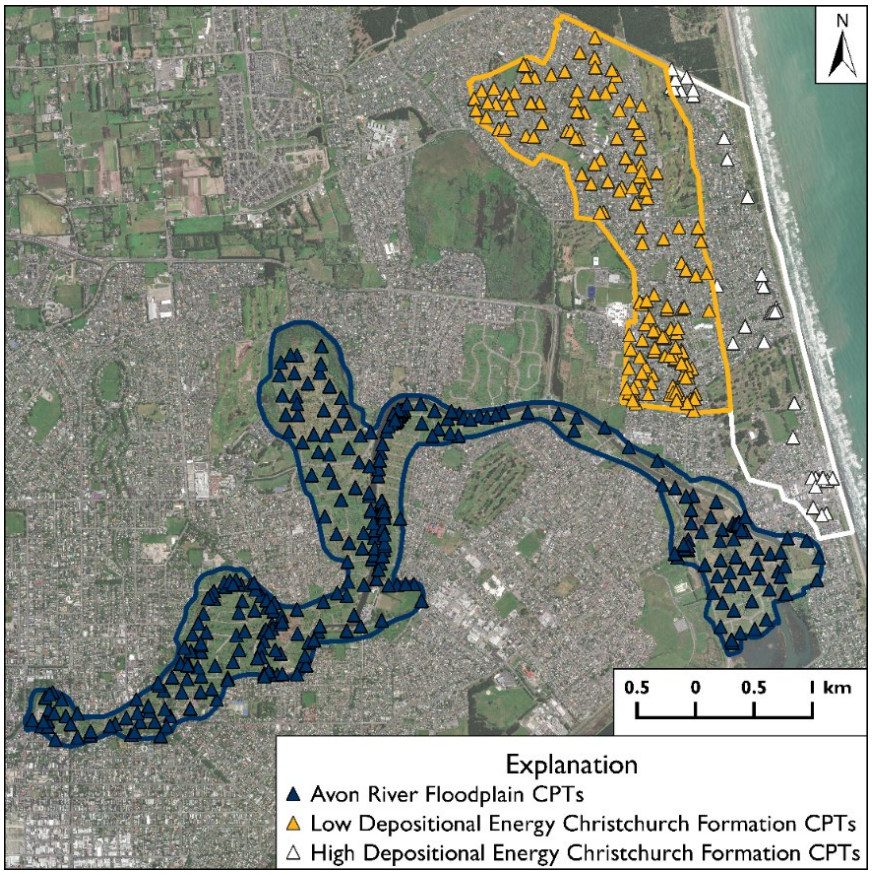

Figure 3.5: Investigated Regions of Christchurch with Locations of NZGD CPTs

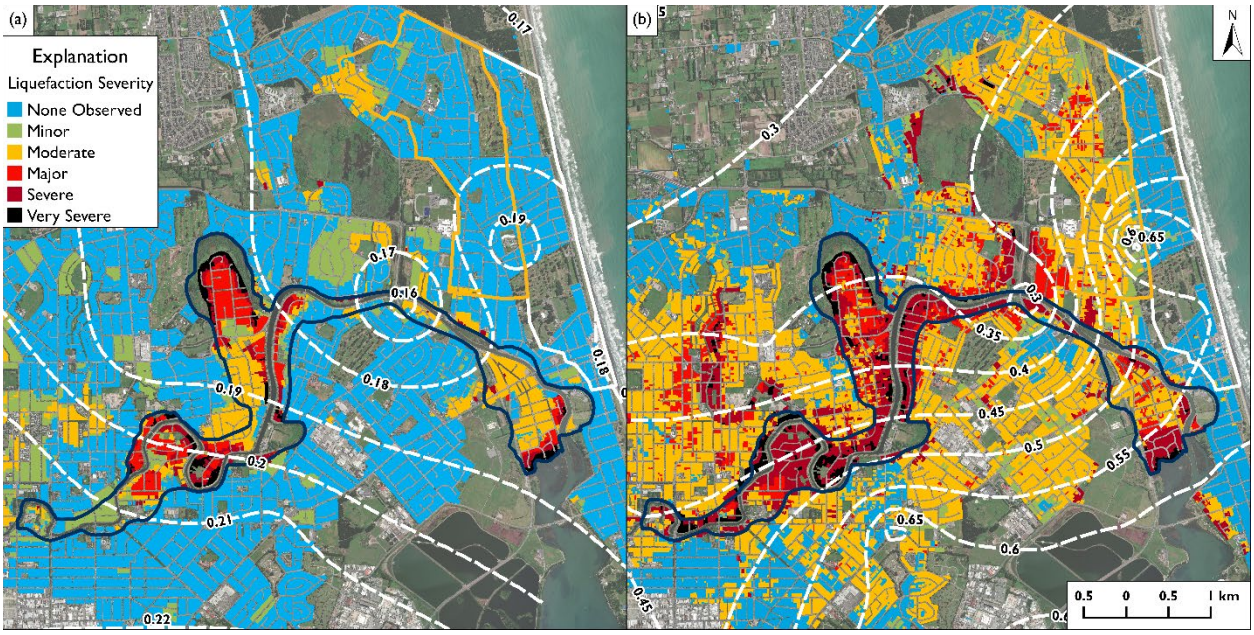

Figure 3.6: Conditional Median PGA Contours and Liquefaction Severity Observations for (a) 2010 M_w 7.1 Darfield earthquake and (b) 2011 M_w 6.2 Christchurch Earthquake (Bradley & Hughes (2012)

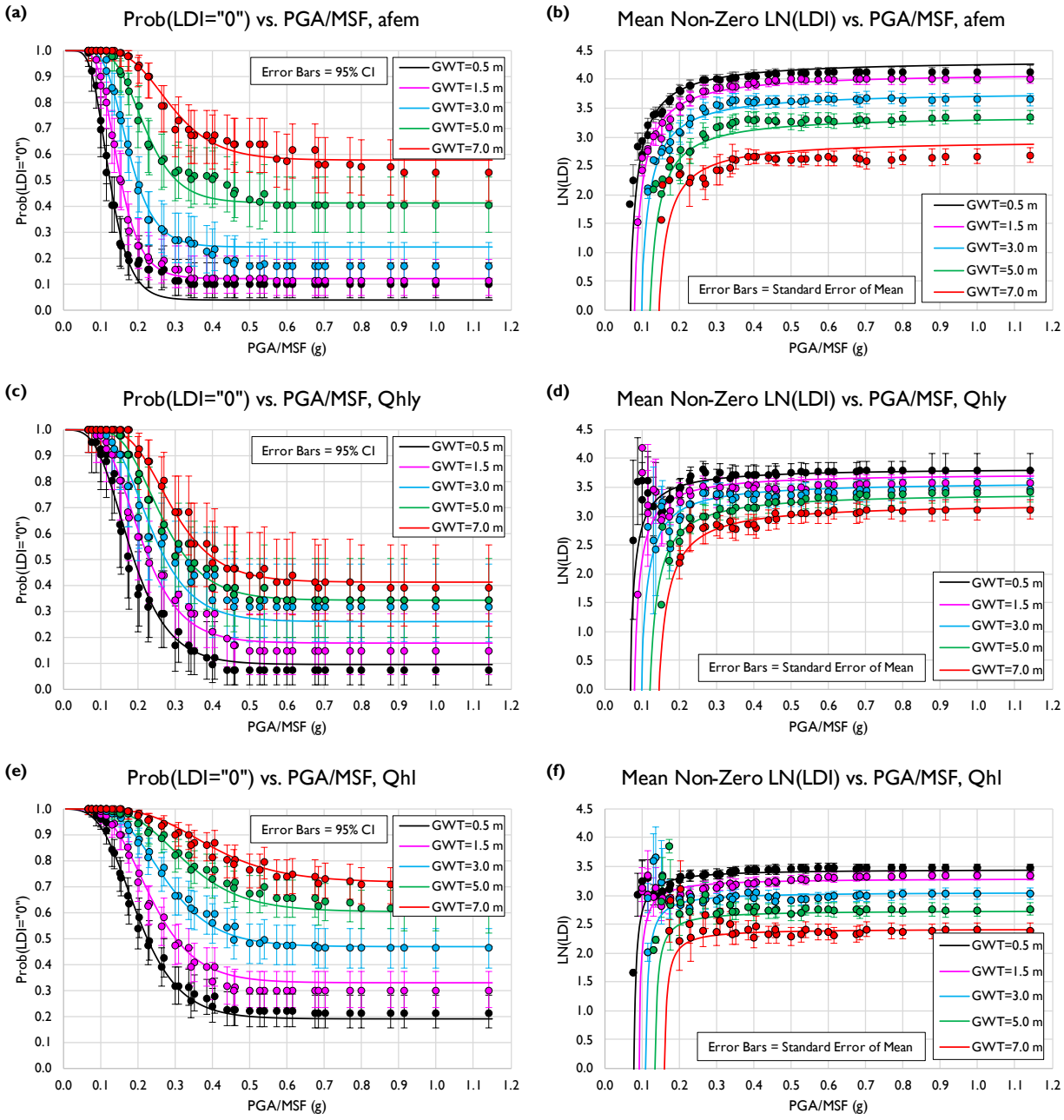

Figure 3.7: ProbLDI=0 and Mean, Non-Zero *ln*(LDI) Models Fit to Data for: (a) and (b) *afem* Deposits, (c) and (d) *Qhly* Deposits, and (e) and (f) *Qhl* Deposits

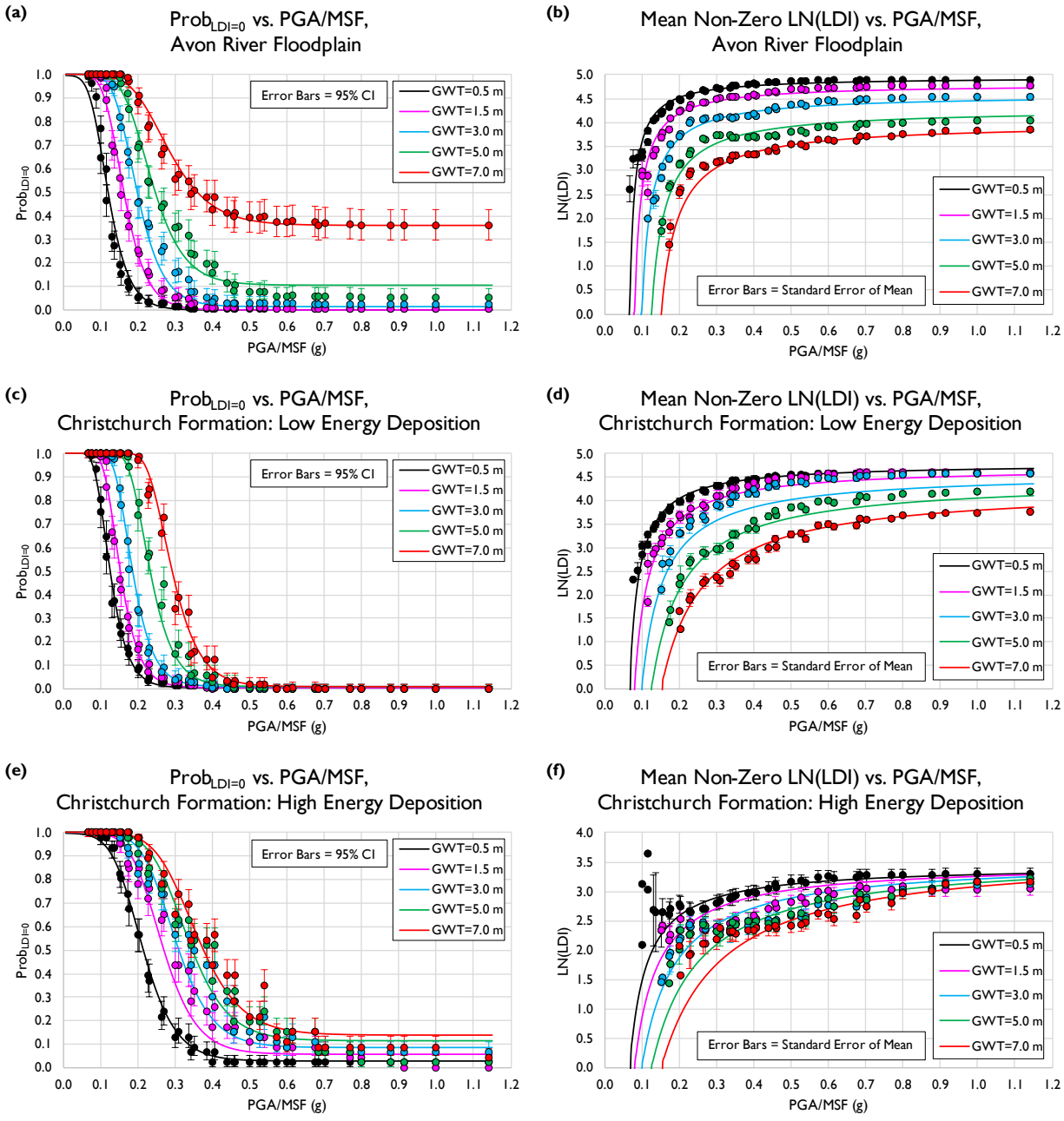

Figure 3.8: ProbLDI=0 and Mean, Non-Zero *ln*(LDI) Models Fit to Data for: (a) and (b) Avon River Floodplain Deposits, (c) and (d) Christchurch Formation: Low Energy Deposits, and (e) and (f) Christchurch Formation: High Energy Deposits

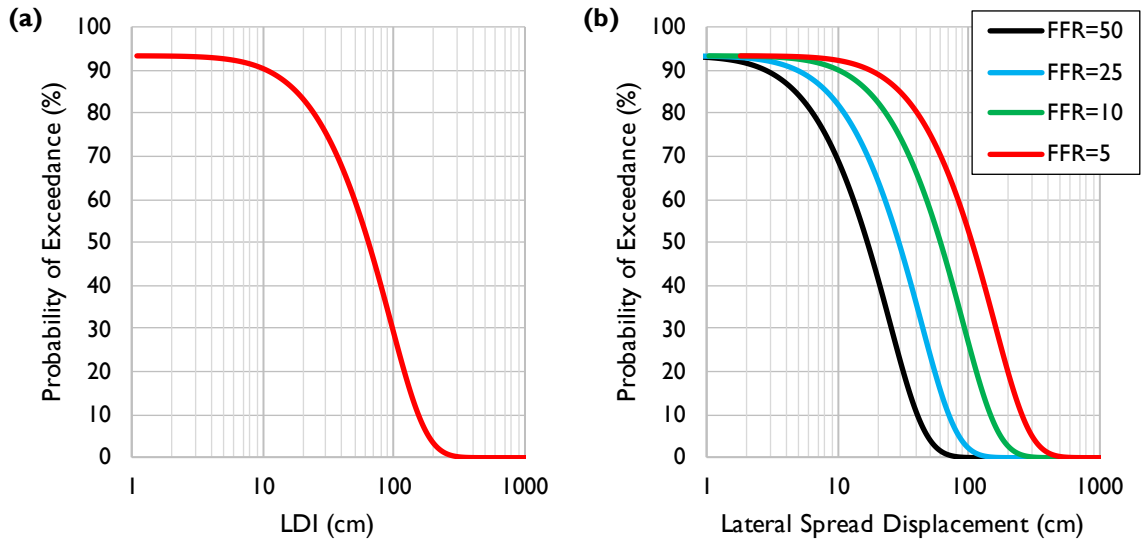

Figure 3.9: (a) Example LDI Distribution for Avon River Floodplain Deposits, GWT=2.5 m, PGA=0.41 g, M_w=6.2 and (b) Conversion of LDI Distribution to Lateral Spread Displacement Distribution for Free-face Ratios of 50, 25, 10, and 5

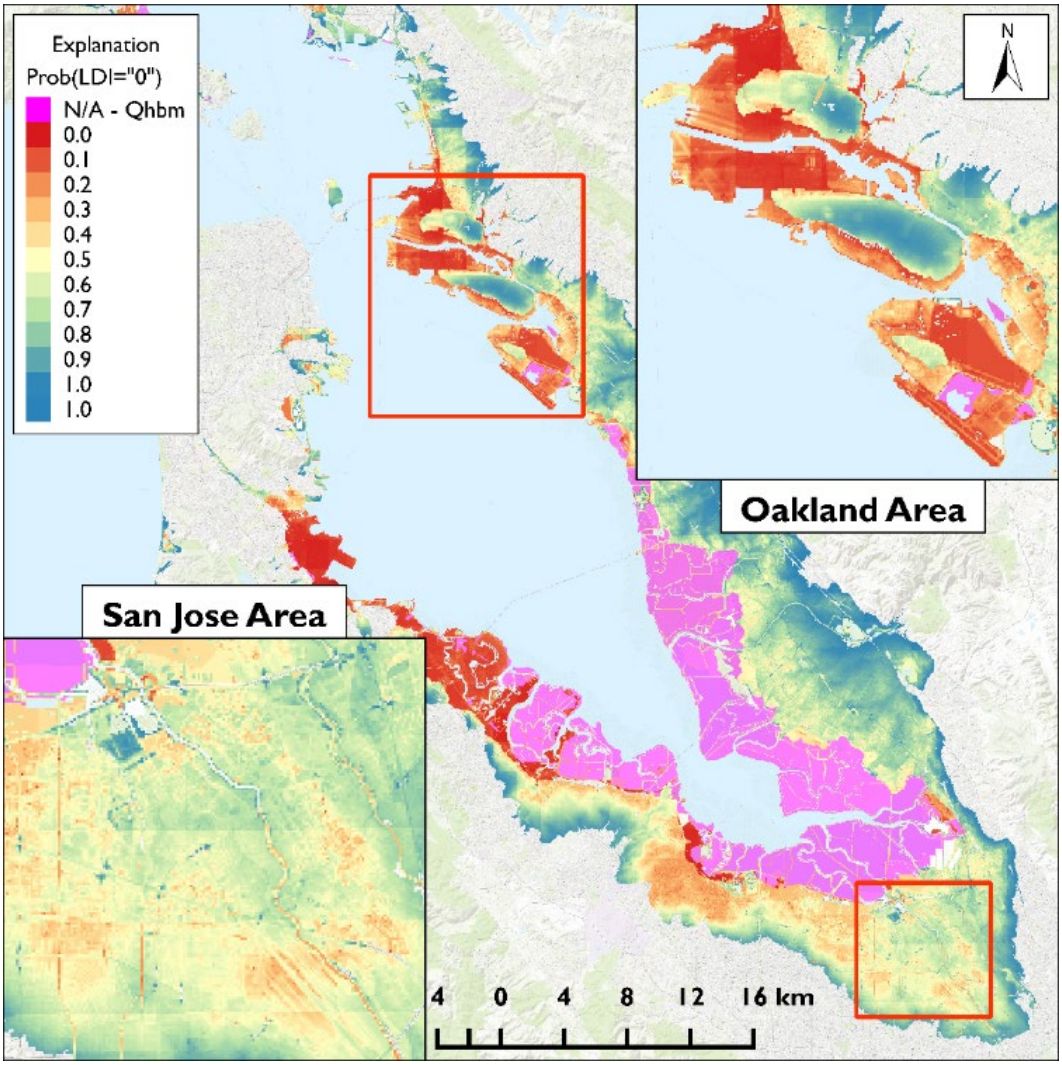

Figure 3.10: Modeled $Prob_{LDI=0}$ in the San Francisco Bay Area for the 1989 M_w 6.9 Loma Prieta Earthquake

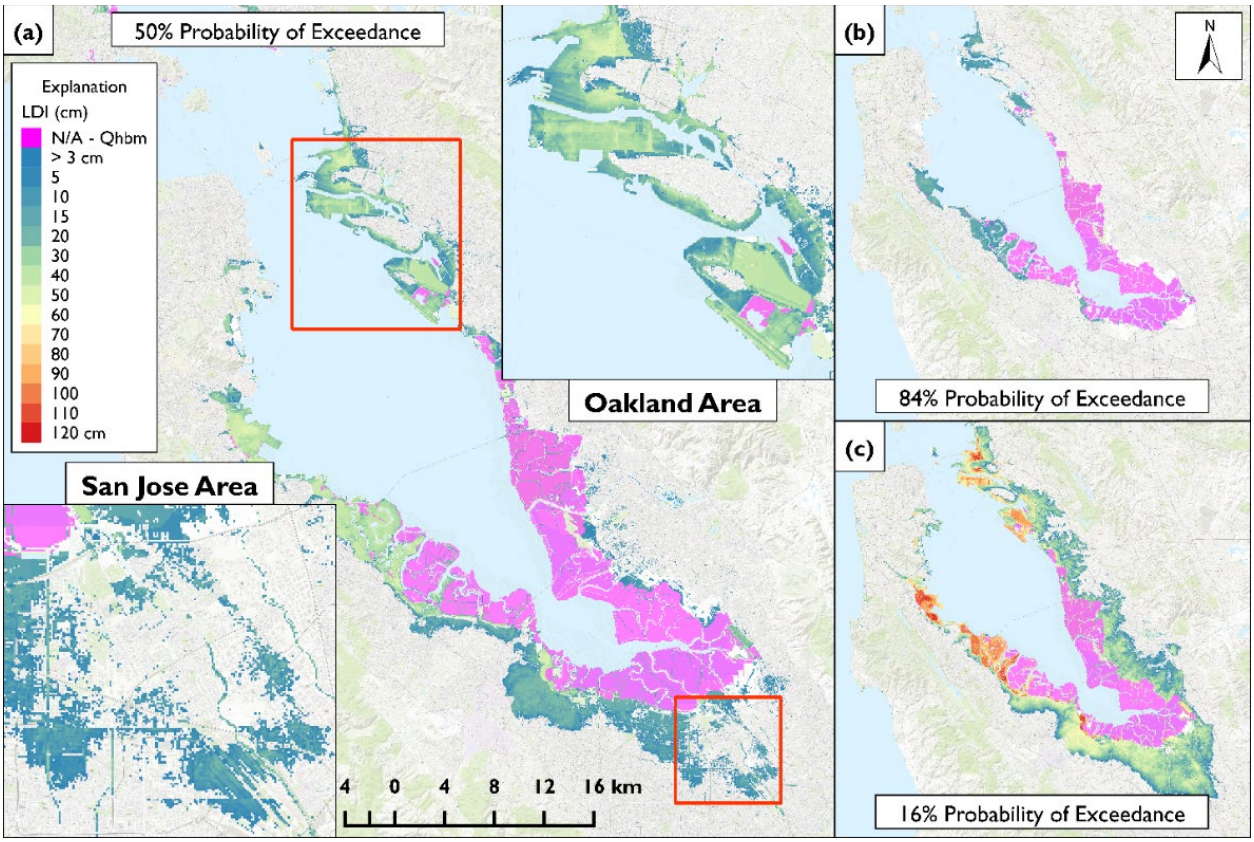

Figure 3.11: Modeled LDI in the San Francisco Bay Area for the 1989 M_w 6.9 Loma Prieta Earthquake (a) Modeled 50% Probability of Exceedance LDI, (b) Modeled 84% Probability of Exceedance LDI, and (c) Modeled 16% Probability of Exceedance LDI

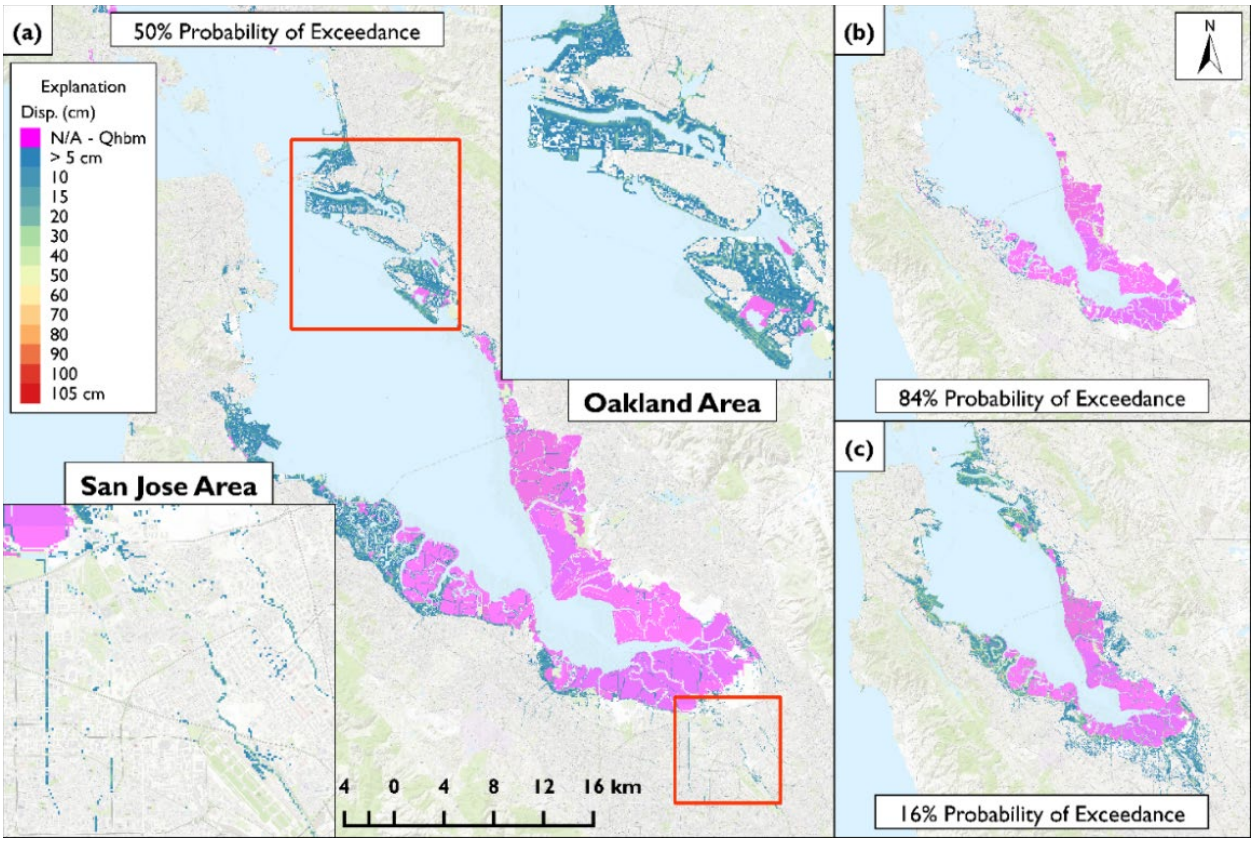

Figure 3.12: Modeled Lateral Spread Displacements (LD) in the San Francisco Bay Area for the 1989 M_w 6.9 Loma Prieta Earthquake Median PGA (a) Modeled 50% Probability of Exceedance LD, (b) Modeled 84% Probability of Exceedance LD, and (c) Modeled 16% Probability of Exceedance LD

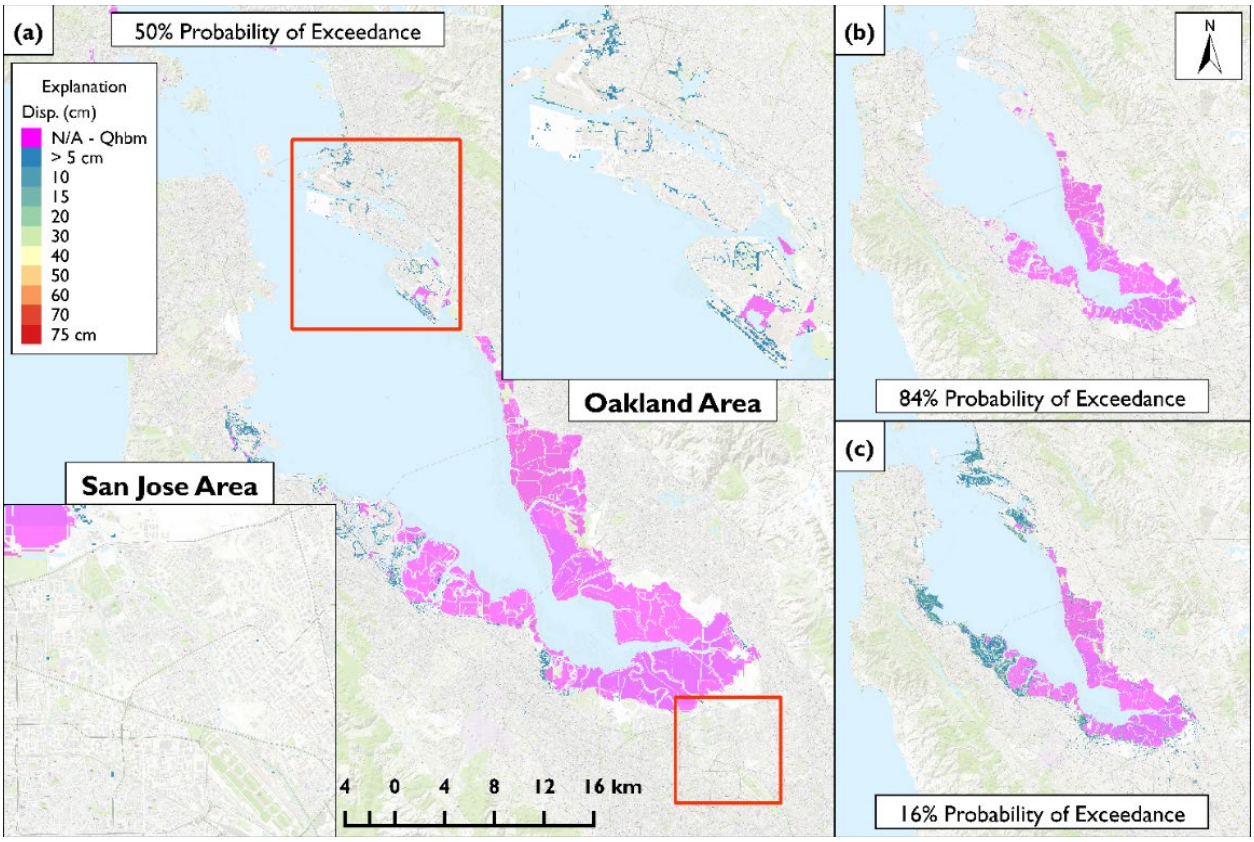

Figure 3.13: Modeled Lateral Spread Displacements (LD) in the San Francisco Bay Area for the 1989 M_w 6.9 Loma Prieta Earthquake 84% Probability of Exceedance PGA (a) Modeled 50% Probability of Exceedance LD, (b) Modeled 84% Probability of Exceedance LD, and (c) Modeled 16% Probability of Exceedance LD

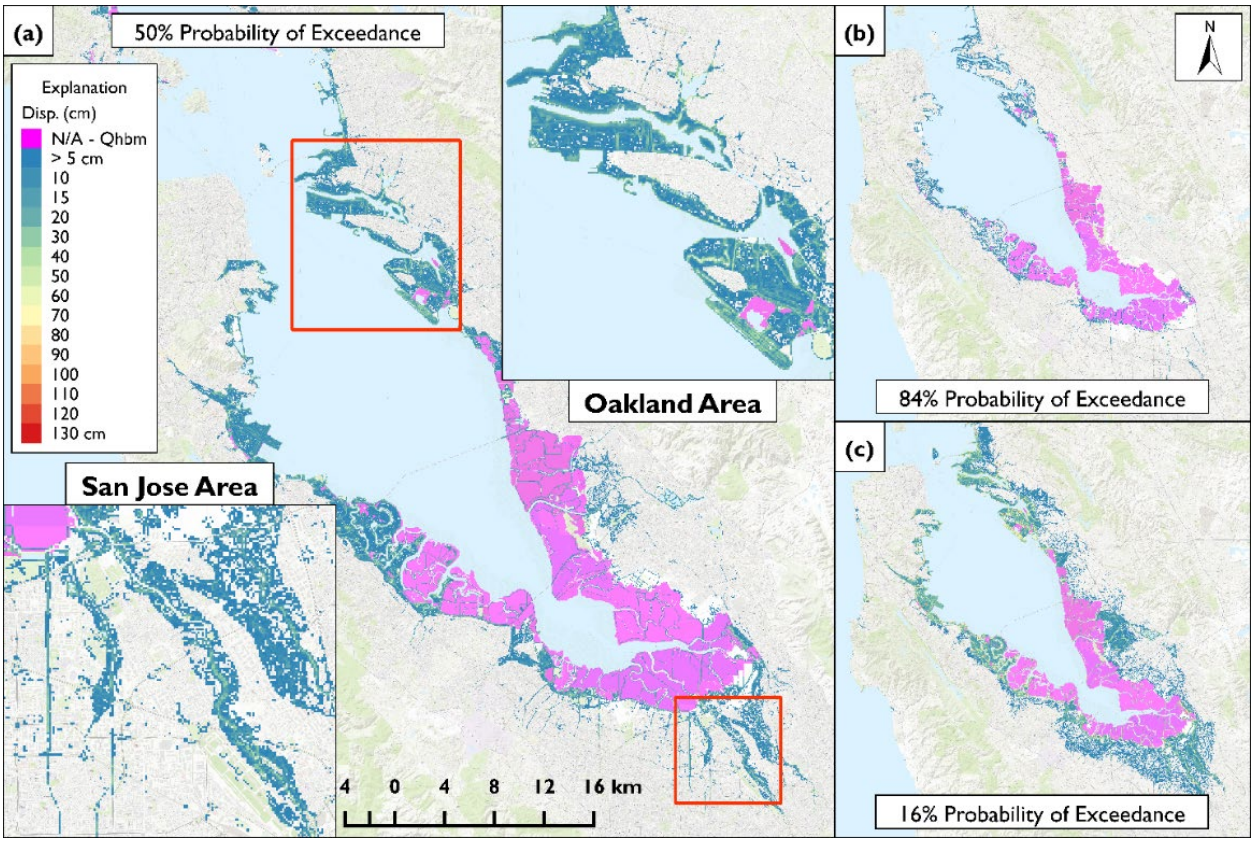

Figure 3.14: Modeled Lateral Spread Displacements (LD) in the San Francisco Bay Area for the 1989 M_w 6.9 Loma Prieta Earthquake 16% Probability of Exceedance PGA (a) Modeled 50% Probability of Exceedance LD, (b) Modeled 84% Probability of Exceedance LD, and (c) Modeled 16% Probability of Exceedance LD

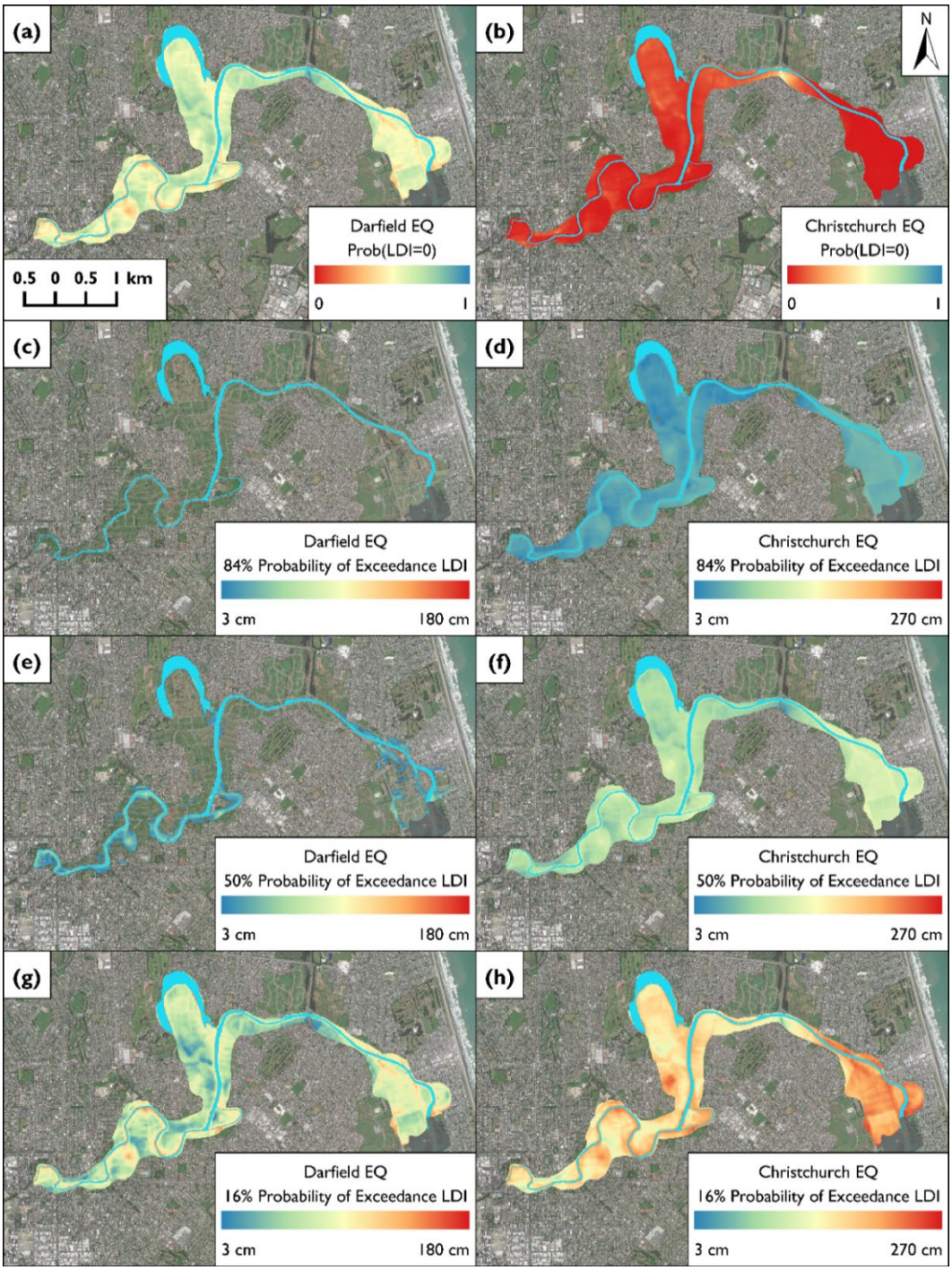

Figure 3.15: Avon River Floodplain Deposits: (a) $Prob_{LDI=0}$ for the Darfield Earthquake, (b) $Prob_{LDI=0}$ for the Darfield Earthquake, (c) 84% Probability of Exceedance LDI for the Darfield Earthquake, (d) 84% Probability of Exceedance LDI for the Christchurch Earthquake, (e) 50% Probability of Exceedance LDI for the Darfield Earthquake, (f) 50% Probability of Exceedance LDI for the Christchurch Earthquake, (g) 16% Probability of Exceedance LDI for the Darfield Earthquake, and (h) 16% Probability of Exceedance LDI for the Christchurch Earthquake

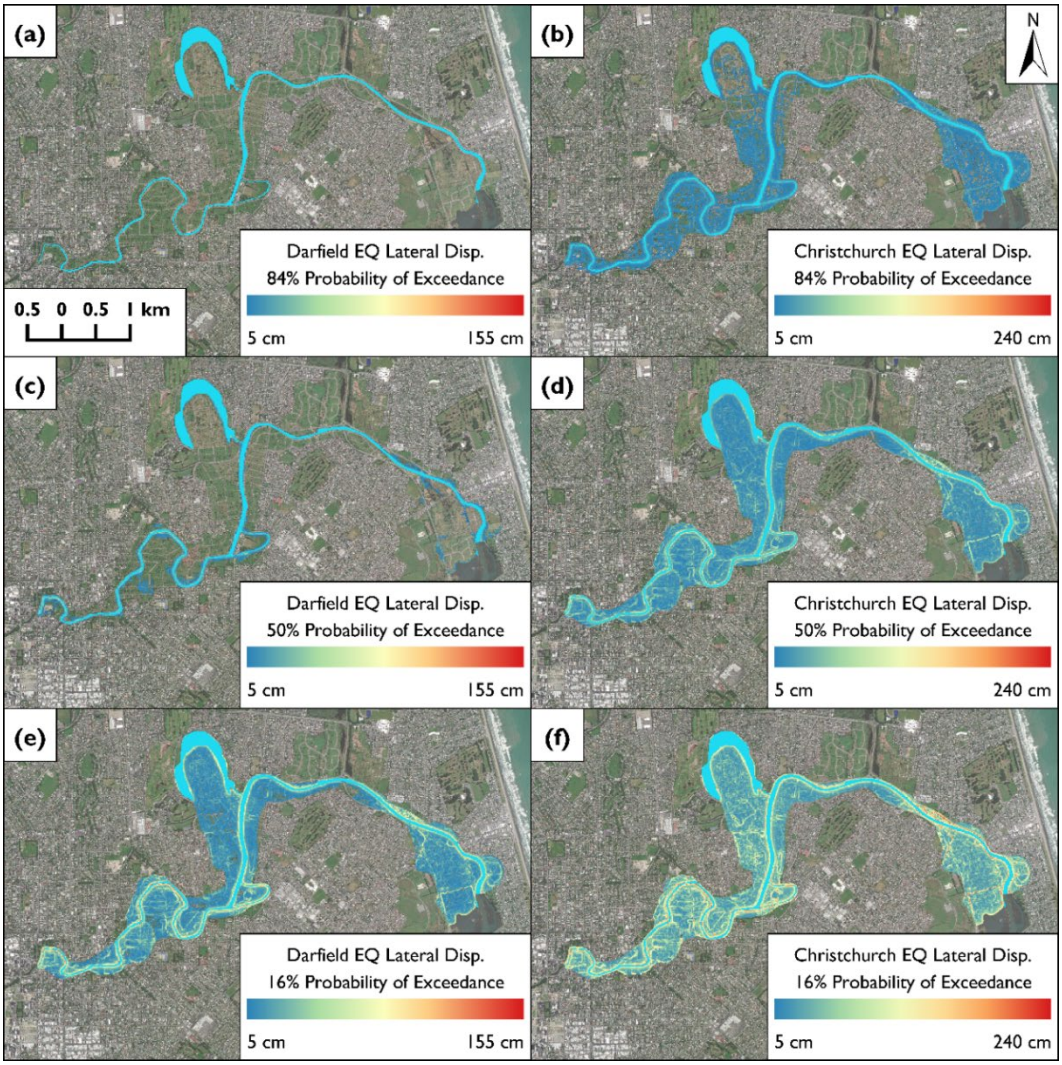

Figure 3.16: Avon River Floodplain Deposits: (a) Modeled 84% Probability of Exceedance LD for the Darfield Earthquake, (b) Modeled 84% Probability of Exceedance LD for the Christchurch Earthquake, (c) Modeled 50% Probability of Exceedance LD for the Darfield Earthquake, (d) Modeled 50% Probability of Exceedance LD for the Christchurch Earthquake, (e) Modeled 16% Probability of Exceedance LD for the Darfield Earthquake, and (f) Modeled 16% Probability of Exceedance LD for the Christchurch Earthquake

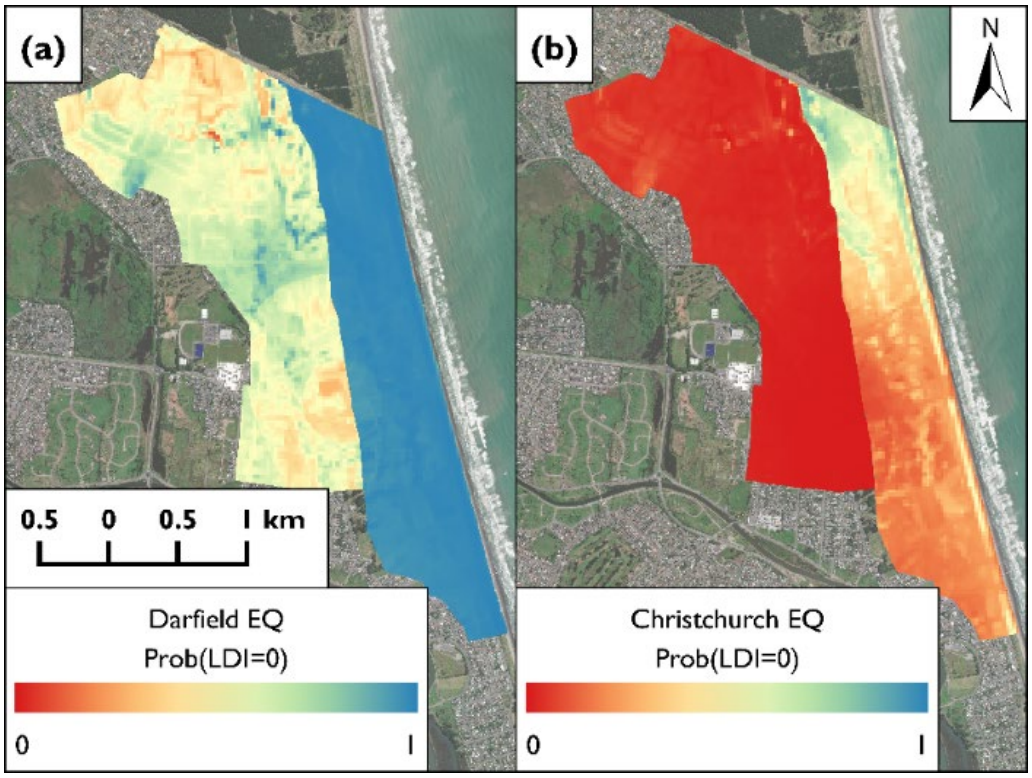

Figure 3.17: Modeled $Prob_{LDI=0}$ in the Low and High Energy Christchurch Formation Deposits for: (a) Darfield Earthquake and (b) Christchurch Earthquake

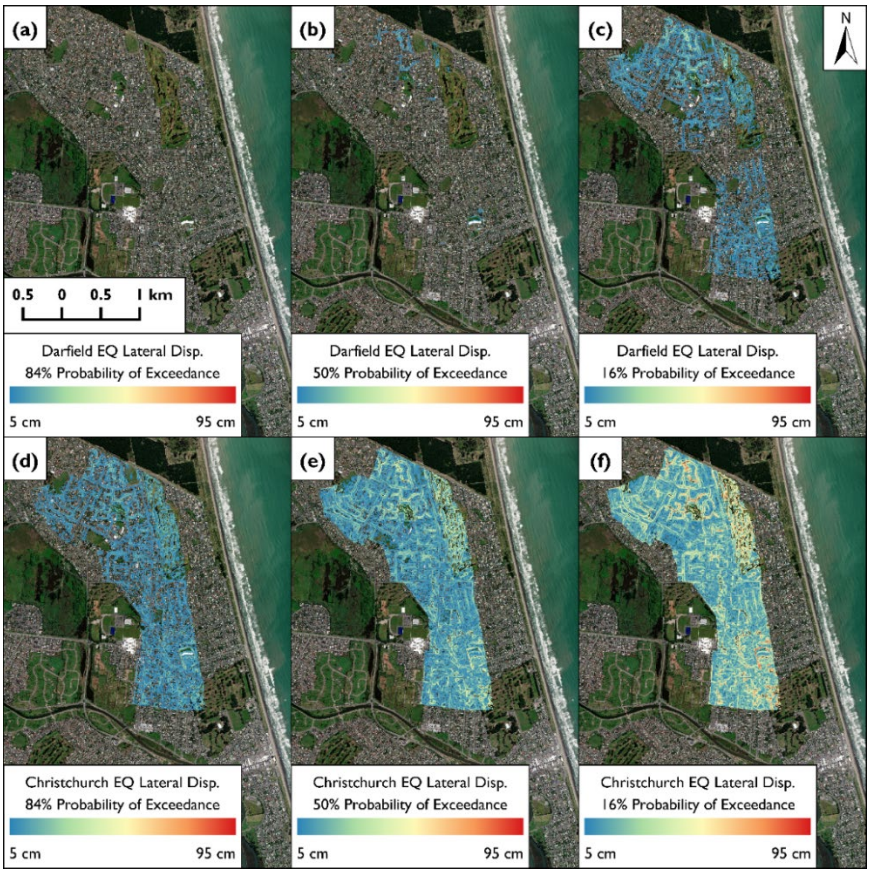

Figure 3.18: Low and High Energy Christchurch Formation Deposits: (a) Modeled 84% Probability of Exceedance LD for the Darfield Earthquake, (b) Modeled 50% Probability of Exceedance LD for the Darfield Earthquake, (c) Modeled 16% Probability of Exceedance LD for the Darfield Earthquake, (d) Modeled 84% Probability of Exceedance LD for the Christchurch Earthquake, (e) Modeled 50% Probability of Exceedance LD for the Christchurch Earthquake, (f) Modeled 16% Probability of Exceedance LD for the Christchurch Earthquake

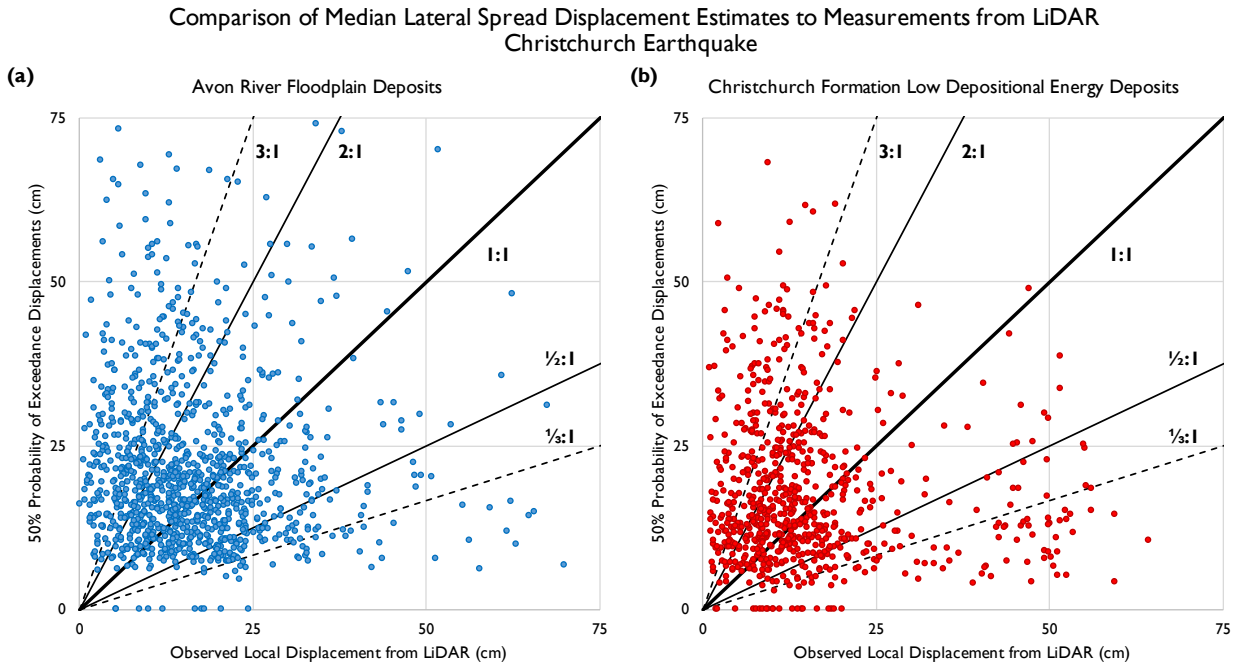

Figure 3.19: Comparison of Lateral Spread Displacements Measured with Lidar from Christchurch Earthquake to (a) 50% Probability of Exceedance Lateral Spread Displacement Estimates in the Avon River Floodplain Deposits and (b) 50% Probability of Exceedance Lateral Spread Displacement Estimates in the Low Depositional Energy Christchurch Formation Sands for Median PGA Values

4 PIPELINE RESPONSE TO SEISMIC DISPLACEMENT AT BALBOA BOULEVARD DURING THE 1994 NORTHRIDGE EARTHQUAKE

The contents of this chapter are based in large part on the material contained in a journal article under review by Bain, C. A., O'Rourke, T. D., and Bray, J. D. entitled: "Pipeline Response to Seismic Displacement at Balboa Boulevard during the 1994 Northridge Earthquake," (Bain et al., 2023a).

4.1 INTRODUCTION

Balboa Boulevard between Lorillard and Rinaldi Streets is situated in the northern San Fernando Valley of Southern California. A general location map for the site is presented in Figure 4.1. During the 1994 M_w 6.7 Northridge earthquake, this site experienced significant seismic ground displacement that ruptured a natural gas transmission pipeline, natural gas distribution pipeline, and two pressurized water trunk lines. Three other natural gas transmission pipelines and an oil transmission pipeline were not damaged. As shown in Figure 4.2, escaping natural gas from a ruptured transmission pipeline was ignited, causing an explosion which destroyed five houses.

This paper presents measurements of the seismic ground displacement at the site using several procedures. The reliability of these procedures is discussed. The geologic, geotechnical, and groundwater data available at the site are presented and past studies that have investigated the seismic displacement mechanism during the Northridge earthquake (e.g., Pretell et al., 2021) are summarized. The geometric and engineering properties of the pipelines and the soil-pipeline interface, including data previously unpublished in the public domain, are presented. Ramberg-Osgood parameters for modeling the stress-strain behavior of the steel pipelines are estimated using tensile coupon tests when available. An analytical model is used to estimate the longitudinal strain in each pipeline caused by seismic ground displacement that occurred during the Northridge earthquake. The modeled pipe strains are compared to the estimated critical strains to test for agreement between the expected and observed pipeline performance.

4.2 GROUND DEFORMATION AT BALBOA BOULEVARD

No significant seismic ground displacement was documented at the Balboa Boulevard site during the 1971 M_w 6.6 San Fernando earthquake even though the ground shaking was intense (i.e., ShakeMap 50% PGA = 0.50 g; 16%–84% PGA = 0.33–0.77 g [USGS, 2023a]). Conversely, a broad zone of seismic deformation and ground failure, approximately 600 m long by 600 m wide, formed to the north of Rinaldi Street (Stewart et al., 1996) during ground shaking from the 1994 Northridge earthquake (i.e., ShakeMap 50% PGA = 0.80 g; 16%–84% PGA = 0.56–1.14 g [USGS, 2023b]). Along Balboa Boulevard, a block-slide type displacement moved downslope in a south-southeast direction subparallel to Balboa Boulevard. A zone of maximum extensional deformation formed approximately 275 to 300 m upgradient of a zone of maximum compressional deformation. The ground movement is similar to the displacement of a soil block that translates downslope between the zones of tensile and compressive ground deformation (O'Rourke & Palmer, 1994; SoCalGas & PG&E, 2000). The zone of maximum tensile deformation had numerous transverse

ground cracks, whereas tented blocks of pavement were observed in the zone of maximum compressive deformation (Stewart et al., 1996). All the natural gas transmission and distribution pipeline ruptures and the most severe damage to the water trunk lines occurred at the zones of maximum tensile and compressional deformation. Figure 4.3 presents a map showing the approximate locations of the zones of maximum extensional and compressional deformation as shown by O'Rourke & Palmer (1994) with the locations of repairs to the Granada and Rinaldi Trunk Lines as presented by Ziotopoulou et al. (2022).

Seismic ground displacement at Balboa Boulevard was measured by several investigators: 1) the Los Angeles Bureau of Engineering (LABE) performed field surveys and measured approximately 50 cm of maximum lateral displacement (LABE, 1995), 2) Holzer et al. (1999) reports approximately 50 cm of aggregate displacement in both the extensional and compressional deformation zones based on street centerline surveys, 3) Sano (1998) used air photos taken before and after the Northridge earthquake to show lateral movements similar to those measured by LABE with an approximate average of 50 cm, and 4) Hecker et al. (1995) estimates the maximum lateral displacements to range from approximately 33 to 54 cm in extension and 27 to 42 cm in compression. Horizontal displacements across individual cracks were generally a few centimeters or less (Holzer et al. 1999); however, the Granada Trunk Line pulled apart at the location of a Dresser mechanical coupling an estimated 46 ± 5 cm, as reported by Ziotopoulou et al. (2022). If one assumes the Dresser coupling provided negligible pullout resistance, the displacement at the Dresser coupling is approximately equal to the block displacement of 50 cm, which is consistent with the other measurements and field observations.

The field survey measurements from LABE (1995) are compared to the measurements from aerial photographs from Sano (1998) in Figure 4.4. In general, the field survey measurements collected at the site (LABE, 1995; Holzer et al. 1999; Hecker et al. 1995) compare favorably to the measurements from aerial photographs by Sano (1998). As indicated in Figure 4.4, the measurements from the aerial photographs have a relatively large standard deviation of approximately 20 cm. Vertical displacements at the site were reported by Hecker et al. (1995) to be mostly less than a few centimeters, with occasional cracks showing as much as 25 cm of vertical displacement. Vertical displacements in the maximum tensile and compressive deformation zones were downward and upward, respectively, consistent with a block-slide type deformation.

4.3 SUBSURFACE SOIL AND GROUNDWATER CONDITIONS AND THE SEISMIC DISPLACEMENT MECHANISM AT BALBOA BOULEVARD

In April 1995, the USGS initiated a geotechnical investigation at Balboa Boulevard in an unnamed alleyway approximately 40 m west of and parallel to Balboa Boulevard. Soil conditions in the alleyway are considered representative of the soil conditions along Balboa Boulevard. The geotechnical investigation included collecting 17 cone penetration test (CPT) soundings, of which 13 were paired with drilled borings with standard penetration test (SPT) blow counts, field vane tests up to 6.4 m depth, Shelby tube samples, and groundwater monitoring wells. In addition to the USGS investigations, SoCalGas & PG&E (2000) contracted for six CPT soundings and five borings with SPT measurements and soil samples. Additionally, two seismic CPTs were performed to estimate shear wave velocity profiles. The USGS CPT locations are displayed in Figure 4.3.

Bennet et al. (1998) and Holzer et al. (1999) divide the soil underlying Balboa Boulevard into four units from the surface, down: A, B, C, and D. Bennett et al. (1998) describes unit A as an approximately 1-meter-thick artificial fill consisting of road and agricultural soils. Unit B

consists of late Holocene sheet flood and debris flow deposits typical to alluvial fans, which were actively aggregating prior to human intervention to channelize and control stormwater runoff. Unit C is described as late Pleistocene to middle Holocene fluvial deposits. Holzer et al. (1999) identified the saturated portion of unit C as the critical unit because CPT measurements and SPT blow counts suggest that portions of this unit liquefied during the Northridge earthquake. Unit D is described as Pleistocene age dense and firm sand, silt, and clay fluvial deposits, but may be a part of the Saugus formation. The transition from Holocene to Pleistocene sediments is evident by a significant increase in CPT tip resistance and SPT blow counts.

At the time of the Northridge earthquake, groundwater at the Balboa Boulevard site was perched north of a concealed fault structure. According to Bennett et al. (1998) and Holzer et al. (1999), although no fault plane was directly observed by the USGS, fault evidence includes an abrupt decrease in the depth to groundwater of approximately 8.3 m between borings BAL-13.5 and BAL-16 (located approximately 160 m apart) and the presence of an organic-rich sandy lens at the south end of the profile, which is thought to be a sag pond deposit that formed adjacent to a Pleistocene fault scarp. Bennett et al. (1998) observe that zones of maximum tensile and compressive deformation correspond to the intersection of the groundwater table with soil unit C. No parts of units A or B were saturated.

Bennett et al. (1998) measured the depth to the water table using piezometers installed in seven standpipes in July 1995 and again in March, June, and December 1996 and found the water table to be stable. This stability suggests that the reported depths are representative of the groundwater conditions at the time of the January 17, 1994, Northridge earthquake. Additionally, Holzer et al. (1999) reports that the saturated sediments in unit C were a darker color compared to the unsaturated sediments in unit C. The darker color indicates reducing conditions and suggests that the measured water table is a long-term hydrologic feature. The geologic cross section, CPT measurements, and water table at the site are shown in Figure 4.5 after Holzer et al. (1999) and Pretell et al. (2021).

Holzer et al. (1999) present CPT soundings and corrected SPT blow counts that indicate that the saturated sediments in unit C were liquefiable and would be expected to liquefy at the shaking intensity experienced during the Northridge earthquake (i.e., $FS_{Liq} < 1.0$). Due to the strong evidence for liquefaction, they attribute the seismic displacement primarily to liquefaction-induced lateral spreading. Pretell et al. (2021) also examined the seismic displacement mechanism and the seismic performance of the soil deposits at the site through nonlinear deformation analyses (NDAs) implemented in the finite difference software FLAC. They simulated the seismic behavior of the soils using the PM4Sand version 3.1 (Ziotopoulou & Boulanger, 2016; Boulanger & Ziotopoulou, 2017) and PM4Silt version 1.0 (Boulanger & Ziotopoulou, 2018; Boulanger & Ziotopoulou, 2019) constitutive models.

In summarizing the results of their study, Pretell et al. (2021) conclude: "*The seismic performance of Balboa Boulevard using NDAs accurately reproduced observed ground deformation patterns, with the results suggesting liquefaction of sand-like soils together with cyclic softening and shear failure of clay-like soils as the failure mechanism leading to ground deformations at this site*." Both sand-like and clay-like behavior contributed to the ground deformation observed on site, although the liquefaction of sand-like material was the dominant mechanism. However, Pretell et al. (2021) point out their analyses also recognize clay-like soil deformation, which is typically overlooked when assessing lateral displacements at sites with soil liquefaction. Additionally, Pretell et al. (2021) show that high shear stresses associated with near-fault forward directivity effects (i.e., ground motion velocity pulse) appear to have triggered or

exacerbated nonlinear behavior of soils and ground deformations at Balboa Boulevard and caused shear failure of clay-like soils.

Evidence suggests the water table was lower during the 1971 San Fernando earthquake than during the 1994 Northridge earthquake. If the water table was at the same elevation during the San Fernando earthquake as it was during the Northridge earthquake, similar lateral spread displacements would be estimated. It is hypothesized that the sediments in unit C were not saturated at the time of the 1971 San Fernando earthquake, so they did not liquefy during this event. With the water table in 1971 assumed to be 2 m lower than in 1994, liquefaction is not triggered, and no lateral spreading occurs, which is consistent with post-earthquake observations for the San Fernando earthquake.

4.4 PIPELINES AT BALBOA BOULEVARD

4.4.1 Characteristics, Engineering Properties, and Performance of the Pipelines at Balboa Boulevard

There are no reports of buried pipeline damage at Balboa Boulevard in 1971. However, several buried pipelines failed during the 1994 Northridge earthquake. Detailed data exist for eight pipelines on Balboa Boulevard between Lorillard and Rinaldi Streets: the Old Line 120, New Line 120, Line 3000, and Line 3003 natural gas transmission pipelines, a natural gas distribution pipeline, the Line M70 Mobil Oil crude oil transmission pipeline, and the Granada and Rinaldi Water Trunk Lines (GTL and RTL, respectively). Breaks in the GTL and RTL caused flooding and severe erosional damage to Balboa Boulevard. Rupture and the subsequent explosion of Old Line 120 caused the most acute damage. Important aspects of the pipelines are summarized in Table 4.1. The approximate locations of the pipelines at the Balboa Boulevard site are shown in Figure 4.6.

The Old Line 120 was constructed in 1930 with API 5L Grade B steel (specified minimum yield stress, SMYS = 241 MPa) using a belled-end pipe and chill ring design joined with an early shielded electric arc welding technique (SoCalGas & PG&E, 2000). A chill ring is a steel ring that fits inside the pipe and provides a backing for the weld. Chill rings help the welder achieve full root penetration by supporting the weld root during welding and accelerating solidification of the weld pool. The pipe had an outside diameter of 560 mm and wall thickness of 7.1 mm. The pipeline was coated in coal tar enamel and buried in native clayey soils with 1.2 m cover to the top of the pipe at each failure location. At the time of the Northridge earthquake, it was operating at a pressure of 1.34 MPa. Old Line 120 failed at full circumferential girth welds in the tensile and compressive ground deformation zones, located approximately 275 m apart. At the tensile deformation zone there was approximately 250 mm of separation; at the compressive deformation zone, measurements of the buckled segment (shell buckling) showed that the pipeline compressed approximately 340 mm (SoCalGas & PG&E, 2000). According to SoCalGas & PG&E (2000), the pipe failures showed evidence of cyclic loading.

The results of a tensile coupon test for Old Line 120 pipe steel are provided by SoCalGas & PG&E (2000) in Figure 4.7. This tensile coupon test shows a linear response until the Lüders plateau at 47,200 psi (approximately 325 MPa). At 325 MPa the tensile strain is 0.16%. After attaining a stress of 325 MPa, there is virtually no tensile resistance from 0.16% strain to approximately 1.25% strain, after which the steel stiffens with additional strain until reaching an

ultimate tensile stress of about 450 MPa when the specimen fails. This figure also shows a Ramberg-Osgood relationship fit through the Lüders plateau, which will be discussed later.

Inspection of the tensile girth weld failure in Old Line 120 by SoCalGas & PG&E (2000) indicates that the fracture started at a weld start/stop point superimposed on a small weld flaw. Despite the fracture initiating at the weld and the presence of other flaws in the weld, the crack propagated primarily through the heat affected zone adjacent to the weld, rather than through the weld itself. The tensile coupon tests show slightly lower yield strength of the heat affected zone, with an average 313 MPa for weld specimens collected 9 m north of Lorillard Street. SoCalGas & PG&E (2000) observe that tensile coupon tests of small portions of the weld, which may contain flaws, would overstate the influence of flaws on the strength of the pipeline.

The API 5L Grade B steel in Old Line 120 had a SMYS of 241 MPa. As can been seen from the test results, the actual yield strength of the pipe steel (e.g., Figure 4.7) is significantly larger, including the yield strength of the heat affected zone adjacent to the welds. Unless a stress-strain plot has been acquired explicitly for the pipe steel, its yield strength must be inferred from the SMYS in the specification. Because this is a minimum specification, the inferred strength of the pipe steel will be a lower bound.

New Line 120 was constructed to replace 10 km of Old Line 120 just before the Northridge earthquake. It was pressurized to 1.3 MPa at the time of the Northridge earthquake (SoCalGas & PG&E, 2000). The portion of New Line 120 replacing Old Line 120 between Lorillard and Rinaldi Streets was constructed on McLennan Avenue one block east of Balboa Boulevard. SoCalGas & PG&E (2000) and Hecker et al. (1995) show ground displacements and transverse cracks on McLennan Avenue similar to those observed on Balboa Boulevard.

New Line 120 is 610 mm in diameter, has 6.4 mm thick walls, and was constructed with API 5L X-60 steel, with SMYS 414 MPa. The pipe was joined using modern shielded electric arc welding techniques, coated with fusion-bonded epoxy, and is assumed to be buried with 1.2 m cover to the top of the pipe. The pipe trench was backfilled with sand to allow 15 cm of sand cover while the remainder of the trench was backfilled with native soil. Following the Northridge earthquake, portions of New Line 120 were excavated to inspect the pipe exterior for damage and no damage was observed (SoCalGas & PG&E, 2000).

The natural gas distribution line at Balboa Boulevard was constructed in 1957 with API-5L Grade B or X-42 steel (SMYS=241 MPa for Grade B or SMYS=290 for X-42) with oxyacetylene girth welds. It is 168 mm in diameter, has 4.8 mm thick walls, and was backfilled with native clayey soil with an assumed 1.2 m cover to the top of the pipe. The pipe was covered with a tape wrap (SoCalGas & PG&E, 2000) and operated at approximately 0.30 MPa (O'Rourke & Palmer, 1994). During the Northridge earthquake, the gas distribution line failed in both the tensile and compressive ground deformation zones. In the tensile deformation zone, the pipe broke at an 8-degree miter weld joint, and in the compressive deformation zone, the pipe failed in the pipe body (SoCalGas & PG&E, 2000). According to SoCalGas & PG&E (2000), the pipe failures showed evidence of cyclic loading.

No flaws were observed in the ruptured weld in the tensile deformation zone (SoCalGas & PG&E, 2000). Strength tests performed on a section of the line indicated it had yield and ultimate strengths of approximately 390 MPa and 480 MPa, respectively (SoCalGas & PG&E, 2000). The yield strength was measured at 0.5% strain and the ultimate strength was measured at 5% strain. Based on these strength tests, the gas distribution line is assumed to be X-42 steel.

Lines 3000 and 3003 were constructed in 1956 and 1958, respectively, with API 5L X-52 steel (SMYS = 359 MPa) using modern shielded electric arc welding techniques. They are 762

mm in diameter, have 9.5 mm thick walls, and were coated with coal tar enamel. Both are assumed to be backfilled with the native clayey soil (SoCalGas & PG&E, 2000). At the time of the Northridge earthquake, both lines were operational with maximum allowable operating pressure (MAOP) of 4.48 MPa (SoCalGas & PG&E, 2000). Line 3000 crosses underneath the Rinaldi Water Trunk Line in the tensile deformation zone with 5.2 m of soil cover to the top of the pipe. Line 3000 crosses the compressive deformation zone with 2.4 m of soil cover. Line 3003 crosses the tensile deformation zone with 2.4 m of soil cover, but exits Balboa Boulevard to the west along Halsey Street without crossing the compressive deformation zone (see Figure 4.6). Lines 3000 and 3003 were excavated in several places to inspect the pipe exterior for damage, and no damage was observed (SoCalGas & PG&E, 2000).

Mobil Oil Line M70 was constructed in 1991 with API 5L X-52 steel (SMYS = 359 MPa) using modern shielded electric arc welding techniques. It is 406 mm in diameter and has 9.5 mm thick walls. The pipeline has a smooth, factory applied polyethylene coating and is assumed to be buried with 1.2 m cover to the top of the pipe. The pipeline trench was backfilled clean sand to provide 30 cm of cover followed by a one-sack cement slurry (i.e., flowable fill or structured backfill) to the pavement. Line M70 typically operates at 3.45 MPa (SoCalGas & PG&E, 2000). Mobil Oil Corporation inspected Line M70 for wrinkling, out-of-roundness, or other signs of damage using a pipeline inspection device and found no damage (SoCalGas & PG&E, 2000). O'Rourke & O'Rourke (1995) describe two prominent cracks 50 to 75 mm wide in the cement slurry backfill cover in the tensile deformation zone.

The GTL was constructed in 1956 using ASTM A283 Grade C steel (SMYS = 205 MPa) joined primarily with welded slip joints. Dresser mechanical couplings were used at some connections to accommodate small, post-construction movements in the pipeline (Ziotopoulou et al., 2022). According to Davis (1999), the average yield and ultimate strengths of the GTL from 21 mill test results and 52 reports on steel weld tests equal 275 MPa and 424 MPa, respectively. Th GTL is 1257 mm in diameter, has 6.4 mm thick walls, and is coated with coal tar enamel overlain with a 2.54 cm thick cement mortar lining (Ziotopoulou et al., 2022). The inside of the pipe is lined with cement mortar. The pipeline is buried in native clayey soil with about 1 to 1.2 m of cover to the top of the pipe. The design static head elevation for the GTL is 457 m (Ziotopoulou et al., 2022). At the time of the Northridge earthquake the pipeline was operating at about 1.1 MPa.

The GTL pulled out in the maximum tensile deformation zone approximately 46 ± 5 cm at the location of a Dresser mechanical coupling, as shown in Figure 4.8a. This type of coupling provides essentially no resistance to pullout. It also experienced approximately 25 cm of shortening in the compressive deformation zone, causing telescoping and a longitudinal tear in the shell, as shown in Figure 4.8b.

The RTL was constructed in 1978 using ASTM A283 Grade C or D steel (SMYS = 205 MPa for Grade C or SMYS = 230 MPa for Grade D) joined with welded slip joints. There is no evidence of Dresser couplings at the Balboa Boulevard site. It is 1727 mm in diameter, has 9.5 mm thick walls, and is coated with a 2.54 cm thick cement mortar lining (Ziotopoulou et al., 2022). The inside of the pipe is lined with cement mortar. The pipeline was buried in native clayey soil with about 1.5 m of cover to the top of the pipe. The design static head elevation for the RTL is 386 m (Ziotopoulou et al. 2022). At the time of the Northridge earthquake the pipeline was operating at about 0.4 MPa. The RTL failed in the tensile and compressive ground deformation zones.

4.4.2 Estimated Ramberg-Osgood Parameters for the Pipelines at Balboa Boulevard

Stress-strain curves of various pipe steels often use the Ramberg-Osgood model, which defines a power law relationship, for the shape of the curve. The Ramberg-Osgood model is defined as Equation (4.1).

$$\varepsilon_P = \frac{\sigma}{E} * \left[1 + \frac{n}{1+r} * \left(\frac{\sigma}{\sigma_y}\right)^r\right] \quad (4.1)$$

where ε_P is the pipe strain, σ is the applied stress, E is the Young's Modulus of the pipe steel, σ_y is the yield stress of the pipe steel, and n and r are Ramberg-Osgood model fitting parameters.

For this study, a yield strength of 313 MPa for the heat affected zone from a weld collected 9 m north of Lorillard Street is assumed to be representative of the steel in Old Line 120. Ramberg-Osgood parameters of $n = 8$ and $r = 50$ were fit to the stress-strain curve for Old Line 120, as shown in Figure 4.7. The Young's Modulus (E) was assumed to be 200 GPa, which applies for all pipelines at Balboa Boulevard.

According to Mason (2006), a Lüders plateau to about 1.5% strain is often observed in tensile coupon tests for pipelines constructed for the Los Angeles Department of Water and Power (LADWP). For the GTL, this study adopts Ramberg-Osgood parameters of $\sigma_y = 275$ kPa, $n = 8$, and $r = 50$. For the RTL, a yield strength equal to the SMYS was assumed, resulting in Ramberg-Osgood parameters of $\sigma_y = 205$ kPa, $n = 8$, and $r = 50$.

For the gas distribution line, the stress-strain characteristics of X-42 steel were assumed based on tensile coupon tests. Ramberg-Osgood parameters of $\sigma_y = 390$ kPa, $n = 25$, and $r = 10$ were fit to the stress-strain test data. For other X-grade steel pipelines, including New Line 120 and Lines 3000, 3003, and M70, the yield strength was assumed to equal their respective SMYS. The Ramberg-Osgood n and r parameters were taken directly from the recommendations of O'Rourke & Liu (2012), as summarized in Table 4.2.

4.4.3 Critical Tensile Strain Limits for the Pipelines at Balboa Boulevard

The most important performance goal for all pipelines is to maintain pressure integrity (i.e., prevent rupture). New Line 120, Lines 3000 and 3003, and Mobil Oil Line M70 are composed of X-grade steels with rounded stress-strain curves and circumferential, overmatched girth welds. For these pipelines, to maintain pressure integrity, limiting tensile strains are recommended as follows: 1) ASCE (1984) guidelines suggest 3 – 5%, 2) ALA (2001) guidelines suggest a 4% limit, and 3) PRCI (2004) guidelines suggest 2 – 4%. Wijewickreme et al. (2005) assumed 10%, 50% (median), and 90% probability of tensile pipe rupture at 3%, 7%, and 10% strains, respectively. In this study, the tensile critical strain limit for X-grade steels with overmatched, full circumferential girth welds is taken as 4%, which is consistent with recommended strain limits to maintain pressure integrity.

SoCalGas & PG&E (2000) indicate that the gas distribution line was constructed with oxyacetylene girth welds. Given the poor penetration often associated with oxyacetylene welds, the tensile capacity of the gas distribution line is assumed to be half that of the pipelines constructed using modern, shielded electric arc welding techniques. Accordingly, a 2% tensile strain limit for pipe rupture is assumed for the gas distribution line.

Old Line 120 had weld flaws at the location of tensile failure as well as a Lüders plateau for the stress-strain curve of the pipe steel (see Figure 4.7). The pipe strain at the end of the Lüders plateau is approximately 1.25%, from which a simplified tensile strain limit of 1% was assumed for maintaining pressure integrity.

Large pipelines, like the GTL and RTL, are welded in the field over a larger circumferential distance, which requires more than one welder. Given multiple welders per weld and alignment eccentricities associated with field construction, the tensile strain limit for pipe rupture was taken as half the recommended limit for pipelines with high quality, full circumferential girth welds, or 2% for these lines.

The ALA (2001) and PRCI (2004) guidelines also define a tensile strain limit criterion corresponding to a normal operability performance goal which PRCI (2004) states, "provides a high level of confidence of no significant pipeline damage". To maintain normal operability, ALA (2001) and PRCI (2004) set tensile strain limits below 2% and in the 1 – 2% range, respectively.

For New Line 120 and Lines 3000, 3003, and M70, the normal operability tensile strain limit is 2%. For the gas distribution line and the GTL and RTL, the tensile strain limit for normal operability is 1%. For Old Line 120, the strain at the start of the Lüders plateau is approximately 0.16%, which was simplified to a 0.15% tensile strain limit for normal operability.

4.4.4 Critical Compressive Strain Limits for the Pipelines at Balboa Boulevard

Tensile strain limits are based on the pipe capacity to stretch without compromising internal pressure, and compressive strain limits are based on pipe behavior as a thin-walled pressure vessel that can buckle when subjected to compressive loads. Critical compressive strain test data that correspond to the onset of pipe wall wrinkling for both seamless and welded pipe are plotted in Figure 4.9. The test data in Figure 4.9 were compiled by Mohr (2003) and are plotted against the pipe outside diameter to wall thickness (D/t) ratio. The data in Figure 4.9 are for zero internal pressure. Because the absence of pressure increases the buckling capacity by only a small amount, no modification of the data from pressure effects is included in the figure.

O'Rourke & Liu (2012) provide a simplified relationship, which estimates the critical compressive strain corresponding to the onset of wall wrinkling for pipelines with full circumferential girth welds, presented here as Equation (4.2).

$$\varepsilon_{cr} = 0.35 * \frac{t}{D} \tag{4.2}$$

where ε_{cr} is the estimated critical compressive strain corresponding to the onset of wall wrinkling, t is the pipe wall thickness, and D is the outside pipe diameter. Equation (4.2) is plotted against the test data in Figure 4.9.

Although a pipe may be able to accommodate additional strain after wrinkling starts, the development of a wrinkle or buckle is often taken as a critical damage state because any further displacement imposed on the pipeline concentrates strain rapidly at the buckle. For New Line 120, Lines 3000 and 3003, Mobil Oil Line M70, and the gas distribution line, the critical compressive strains associated with pipe wall wrinkling were estimated from Equation (4.2) and Figure 4.9 as 0.37%, 0.44%, 0.44%, 0.82%, and 1.00%, respectively.

Chill rings at the welds in Old Line 120 provided reinforcement against inward shell buckling. Thus, compressive wrinkling would not be expected at the joints, but could occur unimpeded in the body of the pipe. Using Equation (4.2) and Figure 4.9, the critical compressive strain is 0.44%.

Figure 4.10 from Mason et al. (2010) presents data to estimate the compressive capacity of welded slip joints. For the GTL (wall thickness, D/t, and yield stress equal to 6.4 mm, 196, and 275 MPa, respectively), the limiting compressive stress is approximately 0.52 times the yield stress, or 143 MPa. The critical compressive pipe strain limit for pressure integrity, calculated as the ratio of the yield stress and Young's Modulus, is 0.072%. For the RTL (wall thickness, D/t, and yield stress equal to 9.5 mm, 182, and 205 MPa, respectively), the limiting compressive stress is approximately 0.45 times the yield stress, or 92 MPa. The critical compressive pipe strain limit for pressure integrity, calculated as the ratio of the yield stress and Young's Modulus, is 0.046%. The estimated tensile and compressive strain limits for each pipeline are presented in Table 4.3.

4.5 SOIL MOVEMENT AND PIPE STRAIN MODEL

O'Rourke & Liu (2012) present a model for estimating the strain for pipelines subjected to longitudinal permanent ground displacement using the Ramberg-Osgood stress-strain model for pipe steel. This block-slide model is well suited for the one-dimensional soil and pipeline displacement conditions at Balboa Boulevard. Pipe strain has two possible cases in which the length of the ground deformation zone is comparatively short for Case I and long for Case II relative to the length of the soil block movement required for the pipeline and ground displacement to be equal. Case I and Case II of the idealized block displacement model are illustrated in Figure 4.11a and Figure 4.11b, respectively. In Case I, the maximum pipe displacement is less than the ground displacement and the pipe strain is controlled by the length of the block displacement. In Case II, the maximum pipe displacement near the center of soil block movement is equal to the ground displacement and that part of the pipe experiences no axial force or strain.

Pipe displacement for the idealized block model is calculated using Equation (4.1).

$$\delta(x) = \frac{\beta_p x^2}{2E} * \left[1 + \frac{2}{2+r} * \frac{n}{1+r} * \left(\frac{\beta_p x}{\sigma_y}\right)^r\right] \tag{4.3}$$

where $\delta(x)$ is the pipe displacement at distance x from point A in Figure 4.11a or Figure 4.11b, β_p is termed the pipe burial parameter and defined as the shear force per unit length of pipeline (t_u) divided by the pipe cross-section area (A), E is the Young's Modulus of the pipe steel, σ_y is the yield stress of the pipe steel, and n and r are the Ramberg-Osgood parameters.

In Figure 4.11b, the distance L_e is termed the embedment length and is the length of buried pipe over which the pipe slips relative to the soil. By setting the distance x in Equation (4.1) equal to L_e, and the pipe displacement, $\delta(x)$, equal to one half of the ground displacement (pipe displacement equals one half the ground displacement at distance L_e from point A in Figure 4.11b), the value of L_e can be calculated using mathematical software. This is shown in Equation (4.4), where PGD is the permanent ground displacement of the soil block.

$$\delta(L_e) = \frac{PGD}{2} = \frac{\beta_p {L_e}^2}{2E} * \left[1 + \frac{2}{2+r} * \frac{n}{1+r} * \left(\frac{\beta_p L_e}{\sigma_y}\right)^r\right] \tag{4.4}$$

The appropriate case for the idealized block displacement model is determined with Equation (4.5).

$$L^* = min\begin{cases} L/2 & - \quad Case\ 1 \\ L_e & - \quad Case\ 2 \end{cases} \tag{4.5}$$

The maximum longitudinal pipe strain, ε_P, is equal to the first derivative of Equation (4.1), and is calculated with Equation (4.6).

$$\varepsilon_P = \frac{\beta_p L^*}{E} * \left[1 + \frac{n}{1+r} * \left(\frac{\beta_p L^*}{\sigma_y}\right)^r\right] \quad (4.6)$$

4.6 SOIL-PIPELINE INTERFACE SHEAR RESISTANCE

Old Line 120, the gas distribution line, Lines 3000 and 3003, and the GTL and RTL are buried in horizon B clayey soils identified by Bennett et al. (1998) as native sheet flood and debris flow deposits. For these lines, the maximum shear resistance force per unit length of pipe (t_u) is estimated using Equation (4.7).

$$t_u = \alpha * s_u * \pi * D \quad (4.7)$$

where α is an adhesion factor, s_u is the undrained shear strength of the backfill (assumed to be constant along the length of the pipeline), and D is the outside pipe diameter. Horizon B soils are primarily low plasticity clays with measured peak undrained shear strengths ranging generally ranging from about 50 to 100 kPa (Bennett et al., 1998), with preference given to the low end of the measured range to account for soil disturbance next to the pipelines. The adhesion factor can be estimated using data summarized by Tomlinson (1957). Assuming the undrained shear strength equals 50 kPa, Tomlinson (1957) shows an average adhesion factor of about 0.7, resulting in an adhesive strength of approximately 35 kPa.

SoCalGas & PG&E (2000) performed pull-out tests on a section of Old Line 120 at Balboa Boulevard. Figure 4.12 presents the results of these pipe jacking tests, for which the soil-pipe interface shear stress is plotted as a function of the relative displacement between the pipe and the soil. The maximum shear stress is 680 psf ≈ 33 kPa, which is close to the value of 35 kPa estimated with the Tomlinson adhesion factor previously discussed. Using the pull-out test results, the soil-pipe interface shear strength is taken as 33 kPa.

New Line 120 and the Mobil Oil Line were backfilled with sand extending 15 and 30 cm, respectively, above the pipelines. A one-sack cement slurry was placed from the top of the sand backfill to the pavement (SoCalGas & PG&E, 2000). The maximum shear force per unit length of pipe is estimated using Equation (4.8).

$$t_u = \gamma\left(H_c + \frac{D}{2}\right)\left(\frac{1+K_0}{2}\right)\tan\left[\Phi'_{ds} * \frac{\delta}{\Phi'_{ds}}\right]\pi D \quad (4.8)$$

where H_c is the cover to the top of the pipe, D is the outside pipe diameter, K_0 is the coefficient of earth pressure at rest, assumed equal to 1 for compacted sandy backfill, $\Phi'_{ds} = 42°$ is the direct shear friction angle of dense sandy backfill, and δ is the soil-pipeline interface friction angle.

New Line 120 and Mobil Oil Line M70 were coated with fusion-bonded epoxy and smooth polyethylene, respectively. The sand-pipe interface friction angle ratio, δ/Φ'_{ds}, is approximately 0.60 for the pipeline coatings (O'Rourke et al., 1990). Table 4.4 summarizes the cover to top of pipe and the soil-pipe interface shear strength per unit length of pipe for the pipelines at Balboa Boulevard.

4.7 PIPE STRAIN FROM PGD ASSOCIATED WITH ELBOWS AND BENDS

The idealized block displacement model described in Section 5 applies to pipelines with no bends, thrust blocks, or other anchor points that restrain pipe movement. As shown in Figure 4.6, New Line 120, Lines 3000 and 3003, and the Mobil Oil Line M70 have bends near the displaced block. Old Line 120, the gas distribution line, and the GTL and RTL do not have bends near the sliding block.

Figure 4.13 from O'Rourke & Liu (2012) shows how an elbow near the compressive margin of a block displacement affects the distribution of axial force in a pipe at the tensile and compressive deformation zones. For Case I (Figure 4.13a), an elbow near a block displacement unequally distributes the maximum axial force in a pipe between the compressive and tensile deformation zones. In Figure 4.13a, L_0 is the distance from the compressive margin of the block PGD to the elbow. L_1 is the distance from the compressive margin of the soil block to the point of zero axial force in the portion of the pipe within the PGD zone. There is an axial force, F, at the elbow. O'Rourke & Liu (2012) explain that the block displacement imposes an axial force in the direction of ground movement. This axial force is resisted at an elbow or bend, which is assumed to act as an anchor. As shown in the figure, $F = t_u\ (L_1 - L_0)$.

In contrast to Case I, an elbow near the compressive margin of a block displacement in Case II does not affect the maximum axial force in a pipe at the margins of the PGD zone. In Figure 4.13b, L_0 is the distance from the compressive margin of the block displacement to the elbow. L_1 is the distance from the compressive margin of the block PGD to the point of zero axial force in the portion of the pipe within the PGD zone. In the figure, $L_1 = L_2 = L_e$, where L_e is the embedment length (shown in Figure 4.11b), and $F = t_u\ (L_1 - L_0)$.

The situation illustrated in Figure 4.13 of an elbow near the compressive margin of soil block displacement can be generalized to the case of elbows near both the tensile and compressive margins of a soil block. When a pipeline bend or elbow is located near the tensile ground deformation margin, the modeling is similar to that shown in Figure 4.13. The elbow near the compressive margin in Figure 4.13a or Figure 4.13b is replaced by an elbow near the tensile margin. For this condition, the axial force and displacement plots are mirror images of what is presented in Figure 4.13. When modeling elbows near both the tensile and compressive margins of a block displacement, one would combine the tensile and compressive effects to evaluate axial forces, stresses, and strains in the pipeline. The process to estimate pipe strain caused by soil block deformation is as follows:

1. If there are no elbows near the block PGD, solve for the embedment length, L_e, using Equation (4.1), and determine the appropriate analysis case with Equation (4.5). The strain at the tensile and compressive deformation zones is calculated with Equation (4.6) and the analysis is complete. If there are elbows near the margins of the block PGD, proceed to Step 2.
2. If there are elbows near the soil block, the axial forces at the margin of the block displacement and at the elbows are determined by solving the system of equations presented as Equation (4.9). To satisfy equilibrium of forces, the tensile and compressive forces acting on the pipeline must be equal, which is conveyed by the last expression in Equation (4.9). This study assumes that a bend or elbow acts as an anchor with no displacement.

$$\begin{cases} F_{B-T} = [(L - L_{1C}) - L_{0T}] * t_u \\ F_{B-C} = -(L_{1C} - L_{0C}) * t_u \\ F_T = (L - L_{1C}) * t_u \\ F_C = -(L_{1C} * t_u) \\ 0 = F_{B-T} + F_{B-C} + F_T + F_C \end{cases} \quad (4.9)$$

where F_{B-T} and F_{B-C} are the axial forces at the elbows near the tensile and compressive margins of the soil block, respectively; L is the length of the soil block; L_{1C} is the distance from the compressive margin of the soil block to the point of zero axial force in the portion of the pipe within the soil block; L_{0T} and L_{0C} are the distances to the elbows near the tensile and compressive margins of the soil block, respectively; F_T and F_C are the axial forces at the tensile and compressive margins of the block, respectively; and t_u is the soil-pipe interface shear force per unit length of pipe. In Equation (4.9), L, L_{0T}, L_{0C}, and t_u are known values and the system of equations can be solved for the unknown values (F_{B-T}, F_{B-C}, F_T, F_C, and L_{1C}) using mathematical software.

1. Next, solve for the embedment length, L_e, using Equation (4.1) and determine the appropriate analysis case with Equation (4.10), where $L_{1T} = L - L_{1C}$.

$$\begin{cases} IF\ L_e > L_{1T}\ AND\ L_e > L_{1C} & - & Case\ 1 \\ IF\ L_e < L/2 & - & Case\ 2 \\ IF\ L_e > L_{1T}\ OR\ L_e > L_{1C} & - & Transitional\ Case \end{cases} \quad (4.10)$$

3. If Case I of the model is applicable, the maximum longitudinal strains at the tensile and compressive deformation zones are calculated with Equation (4.6), where $L^* = L_{1T}$ at the tensile deformation zone and $L^* = L_{1C}$ at the compressive deformation zone. The axial stress at the bends is calculated with Equation (4.11).

$$\begin{aligned} \sigma_{B-T} &= F_{B-T}/A = [(L_{1T} - L_{0T}) * t_u]/A \\ \sigma_{B-C} &= F_{B-C}/A = [(L_{1C} - L_{0C}) * t_u]/A \end{aligned} \quad (4.11)$$

where σ_{B-T} and σ_{B-C} are the axial stresses at the elbows near the tensile and compressive margins of the block PGD, respectively, and A is the pipe cross-sectional area. The axial strain at the elbows is calculated using Equation (4.1).

4. If Case II of the model is applicable, the maximum longitudinal strain at the margins of the soil block is determined with Equation (4.6) where $L^* = L_e$. Elbows near the block PGD do not affect the axial force at the tensile and compressive deformation zones. The axial stress and strain at the elbows is calculated with Equation (4.12) and Equation (4.1), respectively.

$$\begin{aligned} \sigma_{B-T} &= F_{B-T}/A = [(L_e - L_{0T}) * t_u]/A \\ \sigma_{B-C} &= F_{B-C}/A = [(L_e - L_{0C}) * t_u]/A \end{aligned} \quad (4.12)$$

5. The transitional case in Equation (4.10) arises when the embedment length is greater than either L_{1T} or L_{1C}, but not both. For Case I (Figure 4.13a), the location of the zero-force point is at distance L_{1C} from the compressive margin of the soil block displacement. When $L_e = L/2$, the model is at the transition point between Case I and Case II and the zero-force point is at the center of the soil block. The special case occurs as the zero-force point shifts from distance L_{1C} to distance $L/2$ from the compressive margin of the soil block (i.e., the model transitions from Case I to Case II). The transitional case only applies to a pipeline with bends or elbows because the zero-force point is in the center of the soil block

if there are no bends or elbows. Equation (4.13) adjusts the distances from the tensile or compressive margins of the soil block L_{1T} and L_{1C}, respectively, to the zero-force point.

$$\begin{cases} IF\ L_e > L_{1T}\ AND\ L_e < L_{1C}\ THEN\ L_{1T,mod} = L_{1T} + (L_{1C} - L_e) \\ \\ IF\ L_e > L_{1C}\ AND\ L_e < L_{1T}\ THEN\ L_{1C,mod} = L_{1C} + (L_{1T} - L_e) \end{cases} \tag{4.13}$$

where $L_{1T,mod}$ and $L_{1C,mod}$ are the adjusted distances from the tensile and compressive margins of the soil block, respectively, to the zero-force point. The strain at the tensile and compressive deformation zones, ε_{P-T} and ε_{P-C}, respectively, are calculated with Equation (4.14) and Equation (4.15).

$$IF\ L_e > L_{1T}\ AND\ L_e < L_{1C} \begin{cases} \varepsilon_{P-T} = \dfrac{\beta_p(L_{1T,mod})}{E} * \left[1 + \dfrac{n}{1+r} * \left(\dfrac{\beta_p(L_{1T,mod})}{\sigma_y}\right)^r\right] \\ \\ \varepsilon_{P-C} = \dfrac{\beta_p(L_e)}{E} * \left[1 + \dfrac{n}{1+r} * \left(\dfrac{\beta_p(L_e)}{\sigma_y}\right)^r\right] \end{cases} \tag{4.14}$$

$$IF\ L_e > L_{1C}\ AND\ L_e < L_{1T} \begin{cases} \varepsilon_{P-T} = \dfrac{\beta_p(L_e)}{E} * \left[1 + \dfrac{n}{1+r} * \left(\dfrac{\beta_p(L_e)}{\sigma_y}\right)^r\right] \\ \\ \varepsilon_{P-C} = \dfrac{\beta_p(L_{1C,mod})}{E} * \left[1 + \dfrac{n}{1+r} * \left(\dfrac{\beta_p(L_{1C,mod})}{\sigma_y}\right)^r\right] \end{cases} \tag{4.15}$$

Figure 4.14 shows the block and pipeline displacement and the axial force, stress, and strain distributions for Old Line 120, the gas distribution line, and the GTL and RTL. The figure shows L_e is less than $L/2$ for these lines such that Case II of the block displacement model is applicable. The figure also shows the maximum tensile and compressive longitudinal strains are estimated to be greater than 10% for Old Line 120 and the GTL and RTL. For the gas distribution line, the maximum tensile and compressive longitudinal strains are estimated to be about 3.4%.

Figure 4.15 shows the block and pipeline displacement and the axial force, stress, and strain distributions for New Line 120, and Lines 3000, 3003, and M70. The figure shows that Case II is applicable to Lines 3000 and 3003 and Case I is applicable to New Line 120 and Mobil Oil Line M70. New Line 120 has 90-degree elbows approximately 90 m north and 40 m south of the tensile and compressive deformation zones, respectively. Line M70 has two 90-degree elbows in the tensile deformation zone where it crosses from one side of Balboa Boulevard to the other and a 90-degree elbow approximately 140 m south of the compressive deformation zone. For New Line 120, $\varepsilon_{P-T} = 0.17\%$, $\varepsilon_{P-C} = 0.14\%$, $\varepsilon_{P-BT} = 0.07\%$, and $\varepsilon_{P-BC} = 0.09\%$. For Line M70, $\varepsilon_{P-T} = \varepsilon_{P-BT} = 0.07\%$, $\varepsilon_{P-C} = 0.12\%$, and $\varepsilon_{P-BC} = 0.02\%$.

Lines 3000 and 3003 both have two 45-degree elbows within the tensile deformation zone where they cross from one side of Balboa Boulevard to the other. Line 3000 also has a 90-degree elbow approximately 120 m south of the compressive deformation zone. Line 3003 exits Balboa Boulevard along Halsey Street without crossing the compressive deformation zone. For Lines 3000 and 3003, $\varepsilon_{P-T} = \varepsilon_{P-BT} = 1.36\%$ and for Line 3000, $\varepsilon_{P-C} = 1.36\%$ and $\varepsilon_{P-BC} = 0.01\%$.

Table 4.5 summarizes the longitudinal strains at the margins of the block displacement where the maximum tensile and compressive ground deformation is located. The table shows that the pipelines buried in the native clayey soil (Old Line 120, gas distribution line, GTL, RTL, Line 3000, and Line 3003) are estimated to have significantly higher strains than the pipelines buried

in sandy backfill (New Line 120, Line M70). Table 4.6 summarizes the longitudinal strains at the pipeline bends. The table shows that the strains at bends located away from the margins block displacement are less than the strains at the tensile and compressive deformation zones. Conversely, the strains do not differ from those presented in Table 4.5 when a bend is located in the tensile or compressive deformation zone. Table 4.5 and Table 4.6 also present the transient longitudinal strains from seismic waves, which are discussed next.

4.8 ESTIMATED PIPE STRAIN FROM PROPAGATING SEISMIC WAVES

The pipelines at Balboa Boulevard underwent transient strains from seismic waves as well as permanent ground displacement. In the near field, transient strains are caused primarily by propagating s-waves. As shown by Pretell et al. (2021), the closest recording of the Northridge earthquake was at the Rinaldi Receiving Station (RSS), which is located approximately 2.2 km from the Balboa Boulevard site. The RSS has free-field conditions, and the ground motion recording was not affected by nonlinear soil response (e.g., liquefaction). The 228° component recorded peak ground velocity (PGV) of 150 cm/s in tension and 100 cm/s in compression.

As presented by several investigators (e.g., Argyrou et al., 2018), the ground strain parallel to the pipeline, ε_g, is estimated with Equation (4.16).

$$\varepsilon_g = \frac{V_a}{C_a}, where\ V_a = V\cos(\gamma_i)\ \ and\ C_a = \frac{C}{\sin(\gamma_i)} \tag{4.16}$$

V_a and C_a are the ground velocity and apparent wave propagation velocity, respectively, in the horizontal plane along the longitudinal axis of the pipeline. V is the ground velocity and γ_i is the angle of incidence in the horizontal plane between the longitudinal axis of the pipeline and the propagation direction of the s-wave. The maximum ground strain occurs at $V = \text{PGV}$ and $\gamma_i = 45°$. C is the apparent wave propagation velocity in the horizontal plane, calculated with Equation (4.17).

$$C = \frac{V_s}{\sin(\gamma_s)} \tag{4.17}$$

where V_s is the s-wave velocity of the surface soils and γ_s is the angle of incidence in the vertical plane between the s-wave propagation direction and the vertical. As explained by O'Rourke & Liu (2012), the small angle between the s-wave propagation direction and the vertical causes out-of-phase motion and longitudinal strain along the pipeline. For crustal earthquakes in California, C is assumed to be about 2.5 km/s. Simplifying Equation (4.16) gives the ground strain parallel to the longitudinal axis of the pipeline as Equation (4.18).

$$\varepsilon_g = \frac{V\sin(2\gamma_i)}{2C} \tag{4.18}$$

The pipelines are oriented at an azimuth of 0°. The 228° RRS recording is oriented such that the intersection angle is close to 45°. Using PGV = 150 cm/s and PGV = 100 cm/s, the maximum tensile and compressive transient ground strains are estimated as 0.03% and 0.02%, respectively. Using the criteria presented by O'Rourke et al. (2004), it is shown that the ground strain parallel to a pipeline is equal to the pipeline longitudinal strain (i.e., $\varepsilon_g = \varepsilon_p$).

The maximum strains from both transient and permanent ground movements may not occur at the same time. For example, the PGV and corresponding transient strain occurs at the beginning

of the RRS record from a near-fault pulse. The maximum strain from PGD may occur later when liquefaction is triggered. Assuming both strains occur at the same time is conservative. Even with this assumption, adding the maximum tensile and compressive transient strains of 0.03% and 0.02%, respectively, to the appropriate soil block deformation strain does not have a significant effect on the results. The transient longitudinal strains and the strains from soil block deformation in the tensile and compressive deformation zones and at the pipeline bends are presented and summed in Table 4.5 and Table 4.6, respectively. The estimated maximum pipe strain is largely due to the permanent ground displacement mechanism.

4.9 ESTIMATED STRAINS AND PIPELINE PERFORMANCE

The longitudinal strains estimated for Old Line 120, the gas distribution line, and the GTL and RTL are much greater than their respective tensile and compressive critical strains. As such, these lines would be expected to fail in tension and compression, which is consistent with observations during the Northridge earthquake. For Line 3003, New Line 120, and Mobil Oil Line M70, the modeled strains are less than their respective critical strains. As such, these lines would not be expected to fail. These results are also consistent with observations during the Northridge earthquake. The compressive longitudinal strain estimated for Line 3000, however, is greater than its critical compressive strain so it would be expected to fail. Line 3000 did not experience any failures. Its expected performance in the compressive deformation zone is inconsistent with its observed performance.

The soil-pipeline interaction in this model depends not only on the length of block displacement, but on the shear force conveyed to a pipeline by adjacent soil. Lines 3000 and 3003 are assumed to be backfilled with native clayey soil (SoCalGas & PG&E, 2000). If this assumption is incorrect and Line 3000 was backfilled with sandy soil, the strain in the compressive ground deformation zones increases to about 1.82%, much greater than the critical strain of 0.44%. This is due to the relatively deep burial depth and interface friction angle ratio of 0.9 for coal tar enamel in sand (O'Rourke & Liu, 2012). New Line 120 and Line M70 were buried at shallower depths and had low interface friction angle coatings, which significantly reduced the shear force conveyed to the pipelines and were responsible for the low strains in these lines.

Assuming that clayey backfill for Line 3000 is correct, different values for the interface shear strength were tested to determine their effect on the pipe strain. For all values of the interface shear strength greater than the assumed value of 33 kPa ($t_u = 79.0\ kN/m$), the longitudinal strains at the tensile and compressive deformation zones increase. Conversely, for all values of t_u less than 33 kPa, the longitudinal strains at the tensile and compressive deformation zones decrease. For example, assuming the interface shear strength is 25 kPa ($t_u = 59.8\ kN/m$), $\varepsilon_{P-T} = 0.23\%$ and $\varepsilon_{P-C} = 0.90\%$. For the extreme case when $t_u = 0.0\ kN/m$, there is no longitudinal strain.

The critical compressive strain, ε_{cr}, plays an important role in predicting pipeline failure. Equation (4.2) does not convey the uncertainty in the test data, from which $\varepsilon_{cr} = 0.44\%$ for D/t = 80. As presented in Figure 4.9, the data show that ε_{cr} was as high as 1.60% for D/t = 80. This strain exceeds the analytical compressive strain of 1.36% by about 18% and would confirm the field observation of no failure. Similarly, for the example with interface shear strength of 25 kPa, 1.60% strain exceeds the analytical compressive strain of 0.90% by 78%.

The longitudinal strain is also sensitive to the pipe steel yield stress and the amount of ground displacement. Because there are no tensile coupon tests for Line 3000, the yield stress is

assumed to equal the SMYS of 359 MPa, consistent with X-52 grade steel. Tests on samples from Old Line 120, the gas distribution line, and the GTL, however, indicate that the true yield stress may be much greater than its SMYS. There is also uncertainty in the amount of ground displacement, which may significantly affect the strain calculation. Increasing the yield strength or decreasing the amount of ground displacement both decrease the longitudinal strain.

Pipeline bends and elbows have been shown by previous investigations (e.g., Timoshenko, 1976) to magnify bending strains because longitudinal flexure will cause a thin-walled cylinder, like a pipeline, to flatten. It is of considerable interest, therefore, that the Balboa Boulevard pipeline failures were predominantly in the pipe barrel, and not in the many bends and elbows that were attached to the pipelines. The only exception to this trend was failure in a single miter bend of the gas distribution pipeline in the tensile ground deformation zone. If a bend or elbow does not act as an anchor, there will be axial pipeline movement in the soil block displacement zone, which tends to reduce both the axial force and bending moment in the bend or elbow. The analytical models used in this study replicate field conditions in which axial pipe strains control performance in lieu of axial force and moment at elbows and bends.

4.10 CONCLUSIONS

The performance of buried pipelines at Balboa Boulevard to transient strains from seismic waves and permanent ground displacement during the 1994 M_w 6.7 Northridge earthquake is evaluated. The PGD pattern during the Northridge earthquake was similar to a block-slide. It is characterized by a zone of maximum tensile deformation upslope from a zone of maximum compressive deformation. This study extends the O'Rourke & Liu (2012) model for block-slide displacement to represent transitions from Case I to Case II (Figure 4.13a and Figure 4.13b, respectively), which only occur when the pipeline has bends or elbows. The maximum transient longitudinal strains were evaluated and added to the strains from PGD. The transient longitudinal strains were generally minor compared with the strains from PGD.

The analytical results of this study were in good agreement with the observed pipeline performance. These results apply to eight different pipelines in both tensile and compressive ground deformation zones. The analytical models correctly capture the four observed failures as well as the absence of failure for four pipelines, which were not damaged by the ground movement. Only in one case did the analytical model indicate failure when none was observed. This discrepancy may be due to several factors, including the estimates of the interface shear force, the critical compressive strain, the pipe steel yield stress, and the amount of ground displacement. The critical compressive strain plays an important role in evaluating pipeline performance. The experimental data for shell buckling indicate it could be as high as 1.60% for pipe with similar D/t to Line 3000. This strain exceeds the estimated earthquake-induced compressive strain by 18% and would confirm the field observations of no failure.

Importantly, the Balboa Boulevard pipeline failures were predominantly in the pipe barrel, and not in the many bends and elbows that were attached to the pipelines. The analytical models used in this study replicate field conditions in which axial pipe strains control performance relative to the effects of moment at elbows and bends.

The tensile and compressive strain limits adopted in this study are derived from recommendations in the technical literature, comparative assessments, and expert judgement. They are intended for a general assessment of strains leading to the loss of pressure integrity. The assessment of critical strains and calculation of analytical strains are often based on conservative

assumptions of SMYS relative to the actual stress-strain characteristics, and are based on a lower bound relationship between critical compressive strain and D/t. Improvements in the evaluation of pipeline strains can be achieved by finite element simulations of the compressive and tensile deformation of welded slip joints and chill ring welds in addition to using the actual stress-strain relationships of pipe steel from tensile coupon tests.

Follow up work is being performed to estimate the aleatory variability (due to inherent randomness) and epistemic uncertainty (due to lack of knowledge) in the soil-pipeline system parameters and the critical strains. The pipelines will be assessed with Monte Carlo simulations to evaluate the total uncertainty in the strain response and the expected performance.

Table 4.1: Summary of the Buried Pipelines at Balboa Boulevard

Pipeline Name (Installation Date)	Material & Welds	Outside Diameter, Wall Thickness (mm)	Specified Minimum Yield Stress, SMYS (MPa)	Coating
Old Line 120 (1930)[1]	Grade B Steel with Early SEAW	560, 7.1	241	Coal Tar Enamel
New Line 120 (1994)[1]	X-60 Steel with Modern SEAW	610, 6.4	414	Fusion Bonded Epoxy
Natural Gas Distribution Line (1957)[1]	X-42 Steel with Oxyacetylene Girth Welds	168, 4.8	290	Tape Wrap
Line 3000 (1956)[1]	X-52 Steel with Modern SEAW	762, 9.5	359	Coal Tar Enamel
Line 3003 (1958)[1]	X-52 Steel with Modern SEAW	762, 9.5	359	Coal Tar Enamel
Granada Water Trunk Line (1956)[2]	Grade C Steel with Welded Slip Joints & Mechanical Coupling	1257, 6.4	205	2.54 cm Cement Mortar over Coal Tar Enamel
Rinaldi Water Trunk Line (1978)[2]	Grade C or D Steel with Welded Slip Joints	1727, 9.5	205 – 230	2.54 cm Cement Mortar over Coal Tar Enamel
Mobil Oil Line M70 (1991)[1]	X-52 Steel with Modern SEAW	406, 9.5	359	Polyethylene

SEAW = Shielded Electric Arc Welds

[1] Information for Pipeline from SoCalGas & PG&E (2000)

[2] Information for Pipeline from Ziotopoulou et al. (2022)

Table 4.2: Estimated Ramberg-Osgood Parameters for the Pipelines at Balboa Boulevard

Pipeline Name	Yield Stress (MPa)	Ramberg-Osgood Parameter	
		n	r
Old Line 120	313	8	50
New Line 120	414	10	12
Distribution Line	390	25	10
Line 3000	359	9	10
Line 3003	359	9	10
GTL	275	8	50
RTL	205	8	50
Line M70	359	9	10

Table 4.3: Estimated Tensile and Compressive Strain Limits for the Pipelines at Balboa Boulevard

Pipeline Name	Critical Tensile Strain (%)	Critical Compressive Strain (%)
Old Line 120	1	0.44
New Line 120	4	0.37
Distribution Line	2	1.00
Line 3000	4	0.44
Line 3003	4	0.44
GTL	2	0.072
RTL	2	0.059
Line M70	4	0.82

Table 4.4: Estimated Soil-Pipe Interface Shear Force per Unit Length of Pipe for the Pipelines at Balboa Boulevard

Pipeline Name	Cover to the Top of Pipe, H_c (m)	Soil-Pipe Interface Shear Force per Unit Length of Pipe (kN/m)
Old Line 120	1.2	58.1
New Line 120	1.2	25.8
Distribution Line	1.2	17.4
Line 3000	5.2 m in Tensile Zone 2.4 m in Compressive Zone	79.0
Line 3003	2.4	79.0
GTL	1.0 – 1.2	130.3
RTL	1.5	179.0
Line M70	1.2	16.0

Table 4.5: Estimated Maximum Longitudinal Strains at the Tensile and Compressive Deformation Zones and at the Bends Near the Tensile and Compressive Deformation Zones During the 1994 Northridge Earthquake

Pipeline Name	Maximum Pipe Strain (%) at the Tensile Margin of the Block Displacement Zone			Maximum Pipe Strain (%) at the Compressive Margin of the Block Displacement Zone		
	PGD	Transient	SUM[1]	PGD	Transient	SUM[1]
Old Line 120	12.88	0.03	**12.9**	12.88	0.02	**12.9**
New Line 120	0.17	0.03	**0.2**	0.14	0.02	**0.2**
Distribution Line	3.39	0.03	**3.4**	3.39	0.02	**3.4**
Line 3000	1.36	0.03	**1.4**	1.36	0.02	**1.4**
Line 3003	1.36	0.03	**1.4**	N/A		
GTL	17.57	0.03	**17.6**	17.57	0.02	**17.6**
RTL	16.40	0.03	**16.4**	16.40	0.02	**16.4**
Line M70	0.07	0.03	**0.1**	0.12	0.02	**0.1**

[1] Sum of transient strain and strain from PGD rounded to nearest tenth percent
N/A – Pipe does not cross the compressive deformation zone

Table 4.6: Estimated Maximum Longitudinal Strains at the Pipeline Bends During the 1994 Northridge Earthquake

Pipeline Name	Maximum Pipe Strain (%) at the Bend Near the Tensile Margin of the Block Displacement Zone			Maximum Pipe Strain (%) at the Bend Near the Compressive Margin of the Block Displacement Zone		
	PGD	Transient	SUM[1]	PGD	Transient	SUM[1]
New Line 120	0.07	0.03	**0.1**	0.09	0.02	**0.1**
Line 3000	1.36	0.03	**1.4**	0.01	0.02	**0.0**
Line 3003	1.36	0.03	**1.4**	N/A		
Line M70	0.07	0.03	**0.1**	0.03	0.02	**0.1**

[1] Sum of transient strain and strain from PGD rounded to nearest tenth percent
N/A – Pipe does not cross the compressive deformation zone

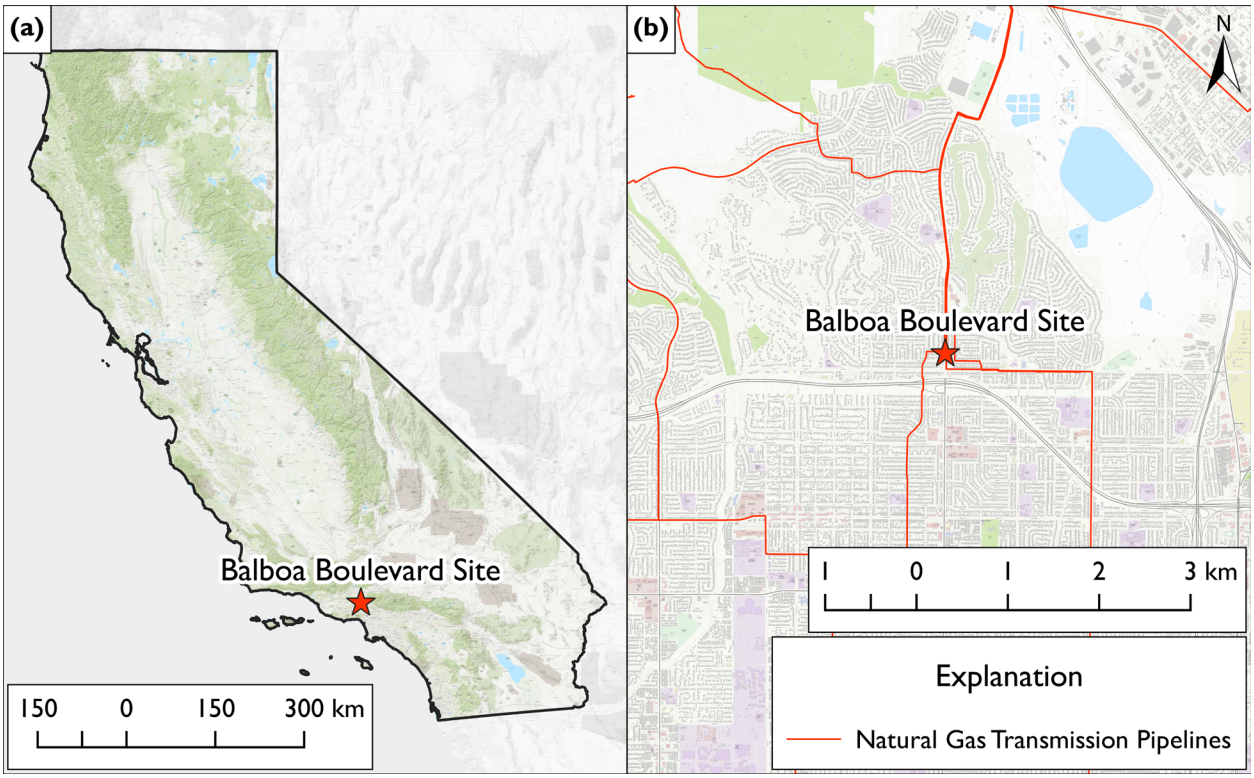

Figure 4.1: (a) General Location of the Balboa Boulevard Site in California and (b) Location of the Balboa Boulevard Site in the San Fernando Valley

Figure 4.2: (a) Explosion of Old Line 120 (from Blevins, 2010) and (b) Destroyed Houses on Balboa Boulevard (from Los Angeles Daily News, 2019)

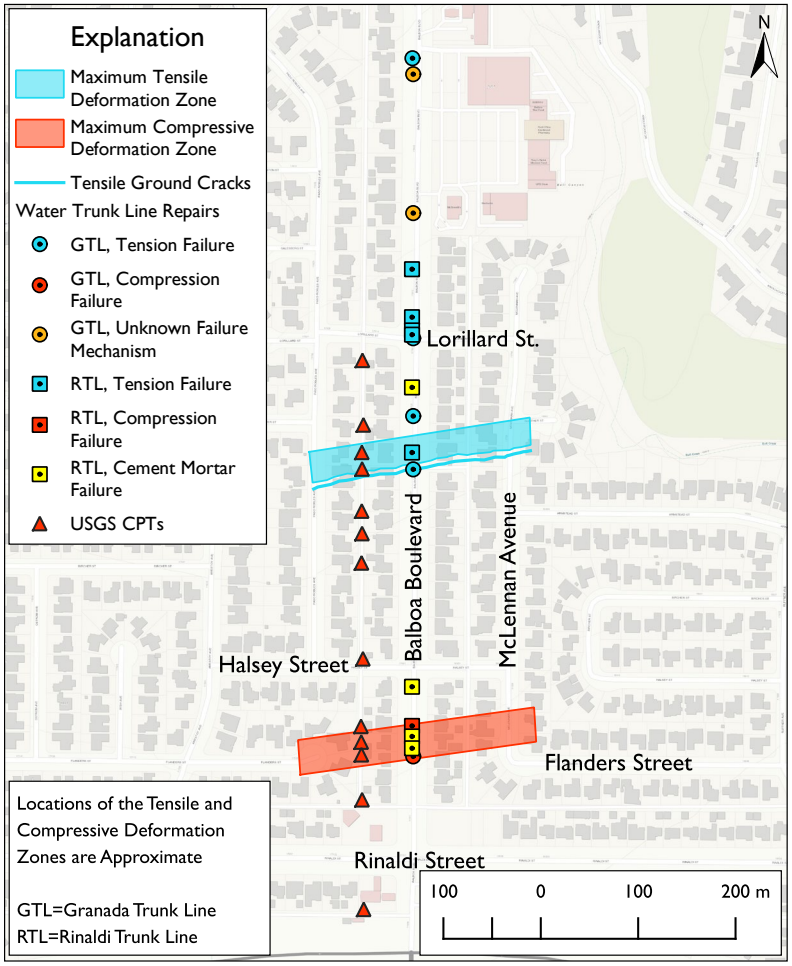

Figure 4.3: Map of the Tensile and Compressive Deformation Zones as Presented by O'Rourke & Palmer (1994) and GTL and RTL Failures from Ziotopoulou et al. (2022)

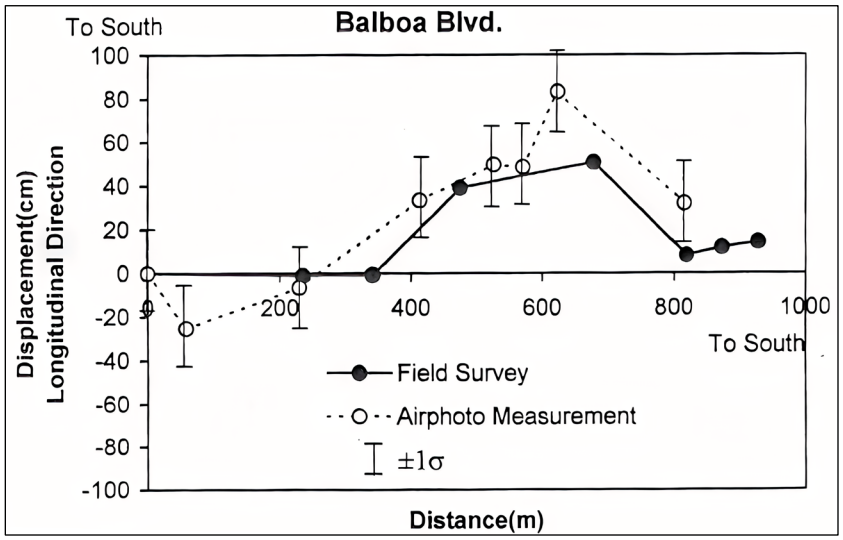

Figure 4.4: Comparison of Ground Displacement Measurements from the LABE Field Survey and from Aerial Photographs (from Sano, 1998)

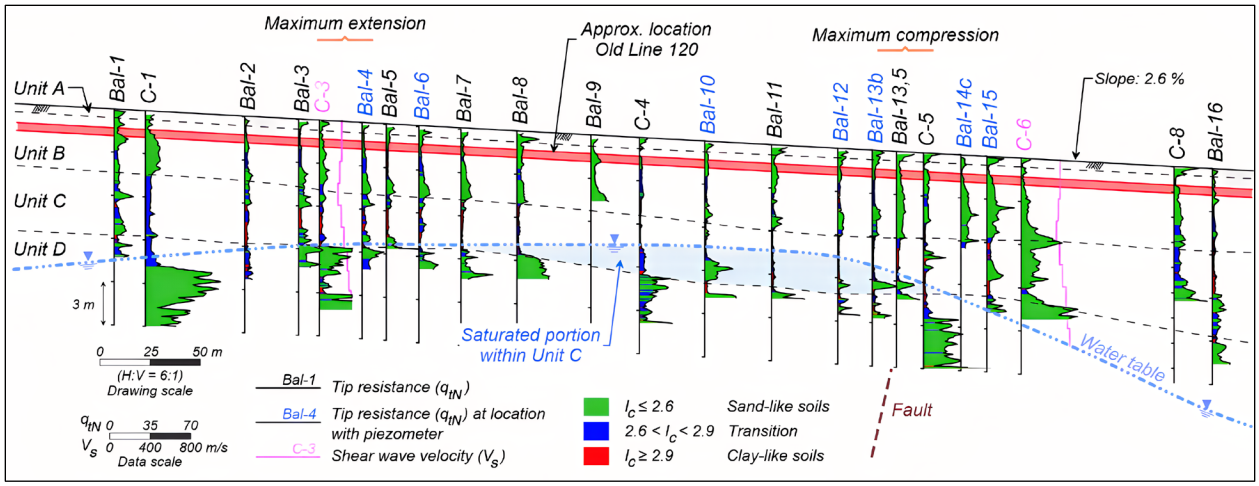

Figure 4.5: Geologic Cross Section, CPTs, and Water Table from Holzer et al. (1999) as presented by Pretell et al. (2021)

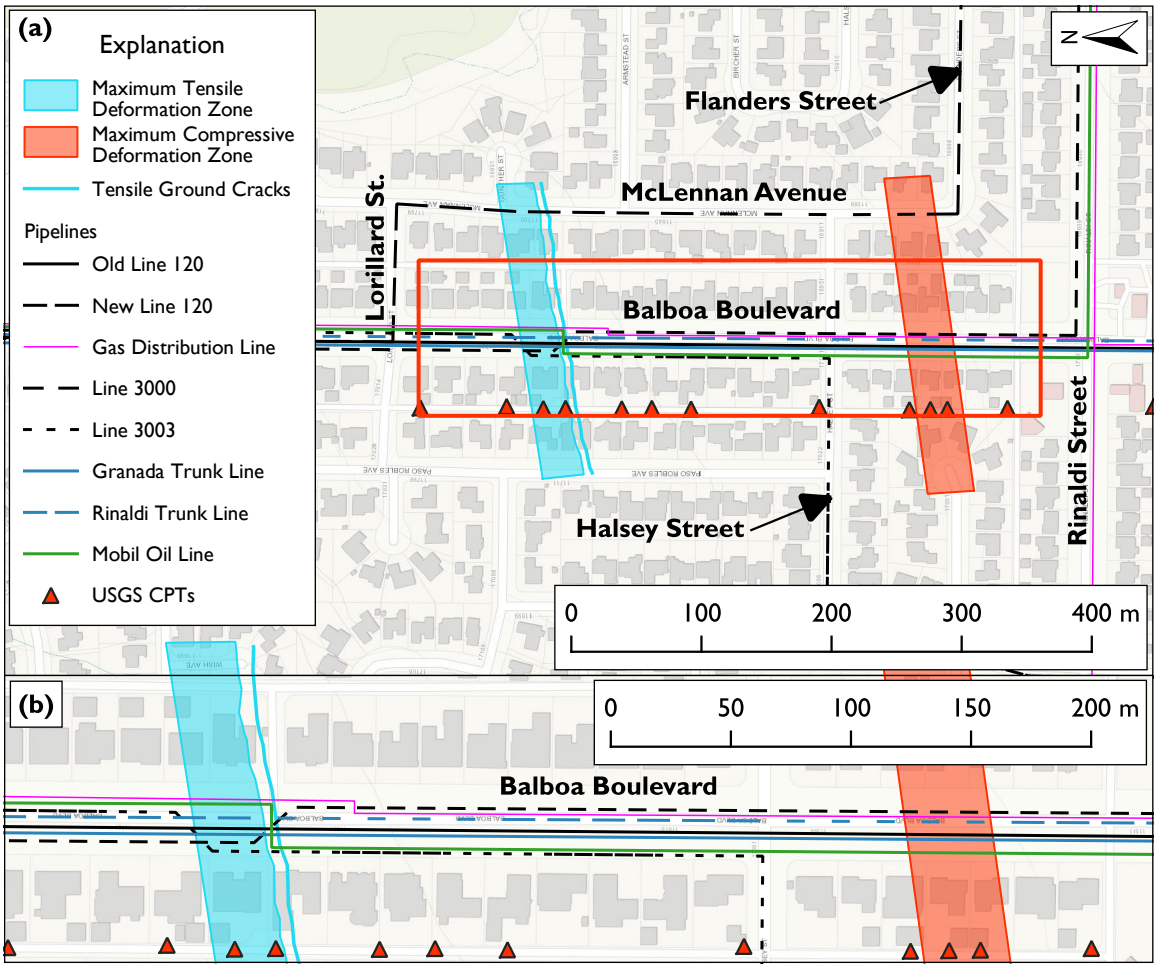

Figure 4.6: Approximate Locations of the Pipelines Along Balboa Boulevard with the Tensile and Compressive Deformation Zones as shown by O'Rourke & Palmer (1994)

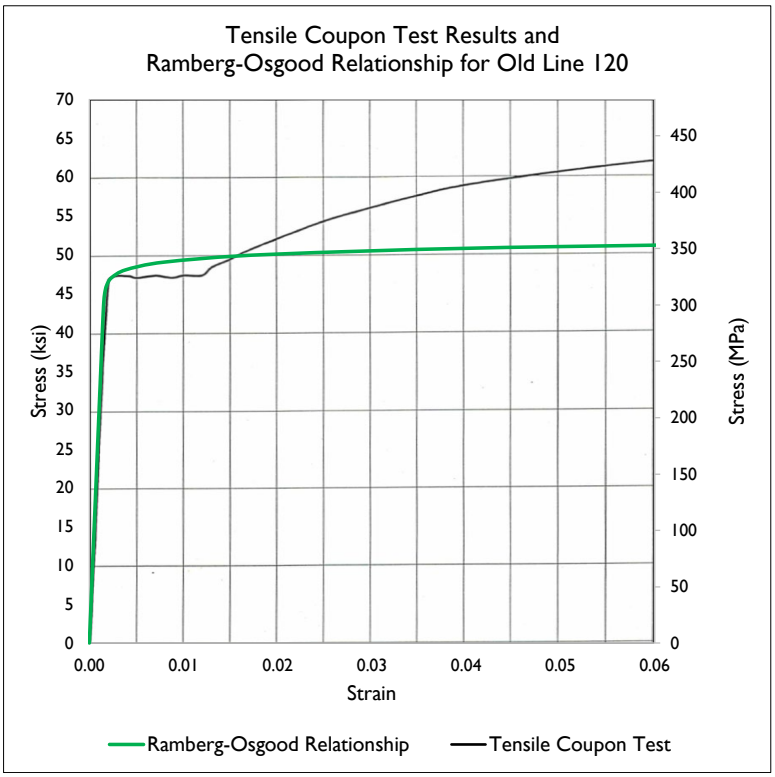

Figure 4.7: Tensile Coupon Test Results for Old Line 120 from SoCalGas & PG&E (2000) with a Ramberg-Osgood Model Fit Through the Lüders Plateau

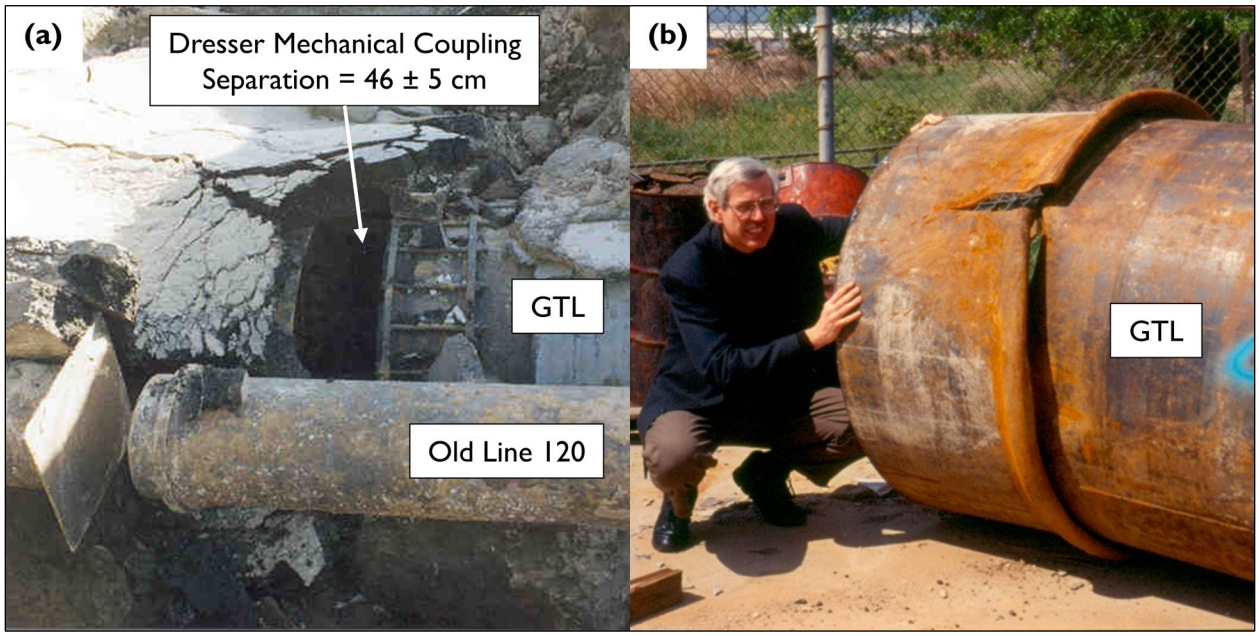

Figure 4.8: Granada Trunk Line (GTL) Failures: (a) Pullout of a Dresser Mechanical Coupling 46 ± 5 cm in the Tensile Deformation Zone and (b) Compressive Failure of a Welded Slip Joint in the Compressive Deformation Zone

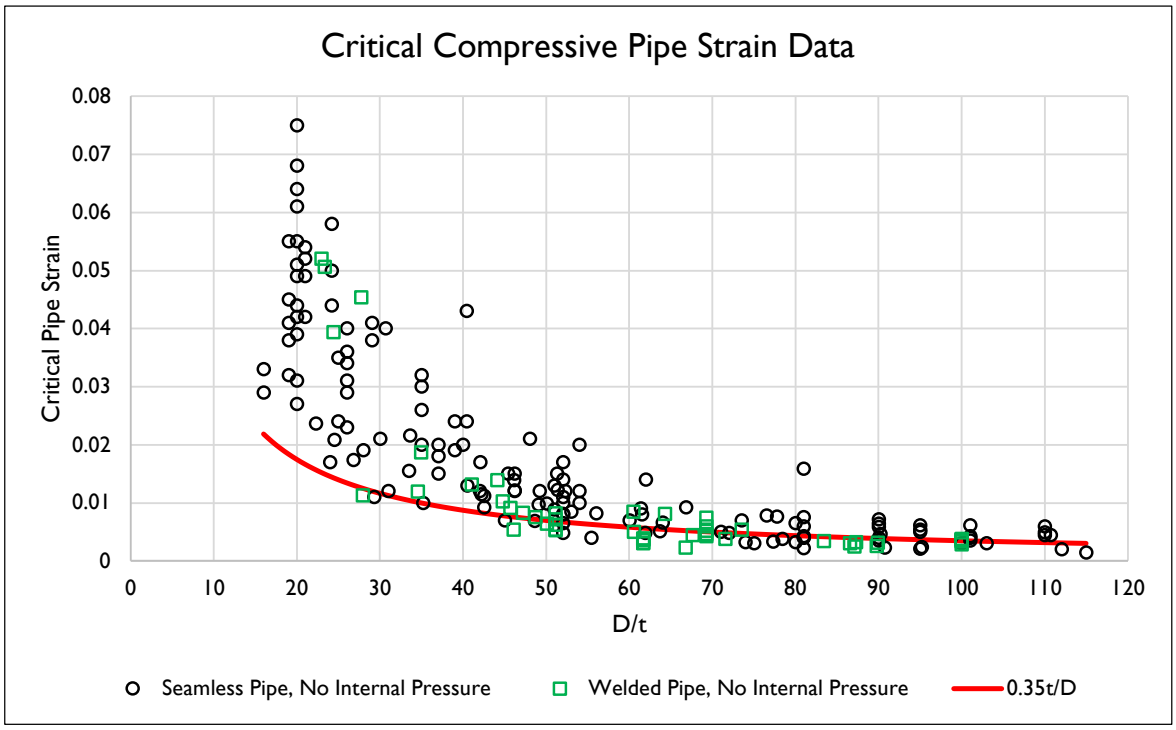

Figure 4.9: Critical Compressive Strain Data Corresponding to the Onset of Pipe Wall Wrinkling Plotted Against the Pipe Outside Diameter to Wall Thickness (D/t) Ratio (Data Compiled by Mohr, 2003; Equation from O'Rourke & Liu, 2012)

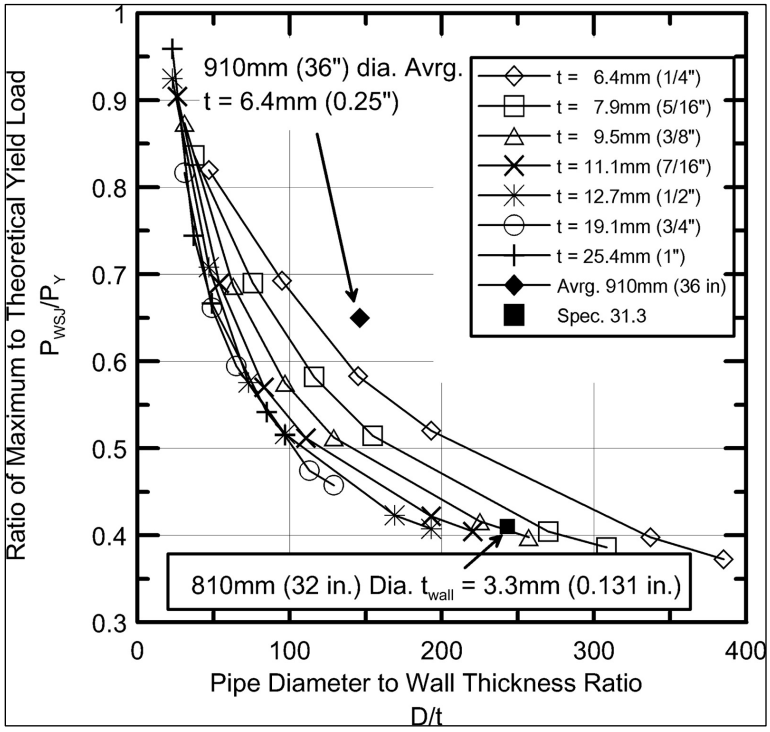

Figure 4.10: Design Chart to Estimate the Capacity of Welded Slip Joints with Internal Welds (from Mason et al., 2010)

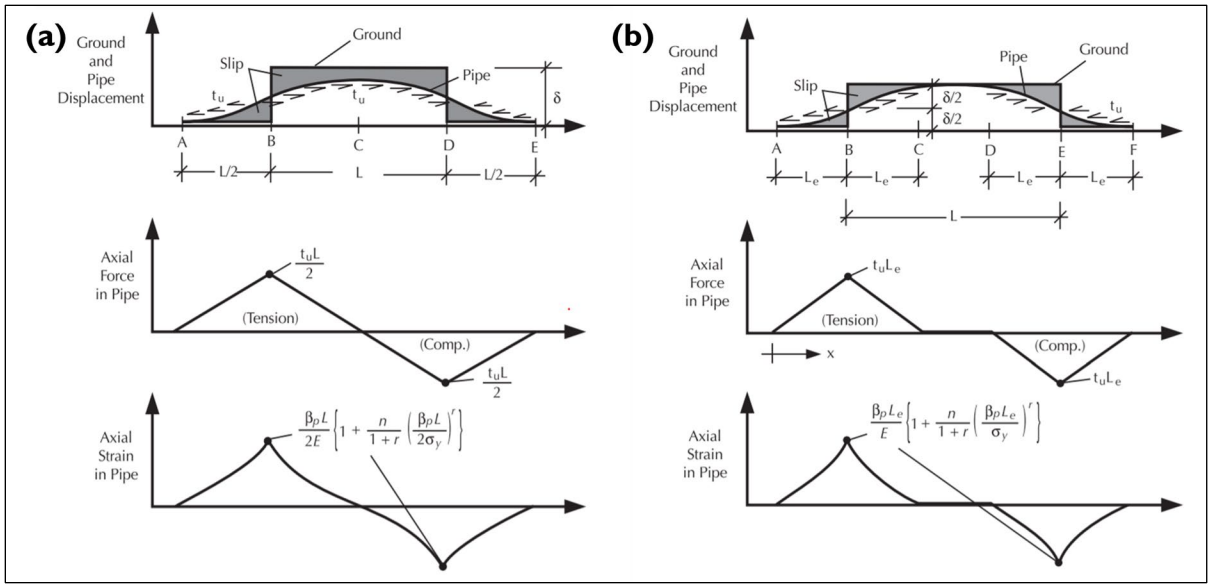

Figure 4.11: (a) Idealized Block Displacement Pattern – Case I, and (b) Idealized Block Displacement Pattern – Case II (from O'Rourke & Liu, 2012)

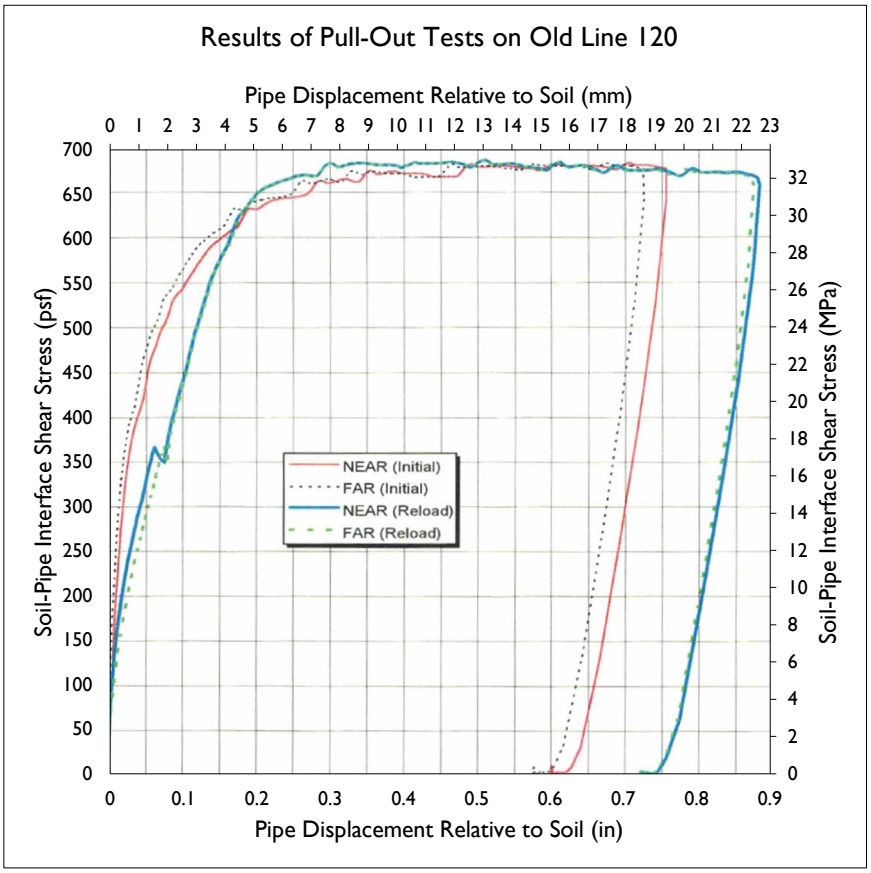

Figure 4.12: Results of Pull-Out Tests on Old Line 120 at Balboa Boulevard (from SoCalGas & PG&E, 2000)

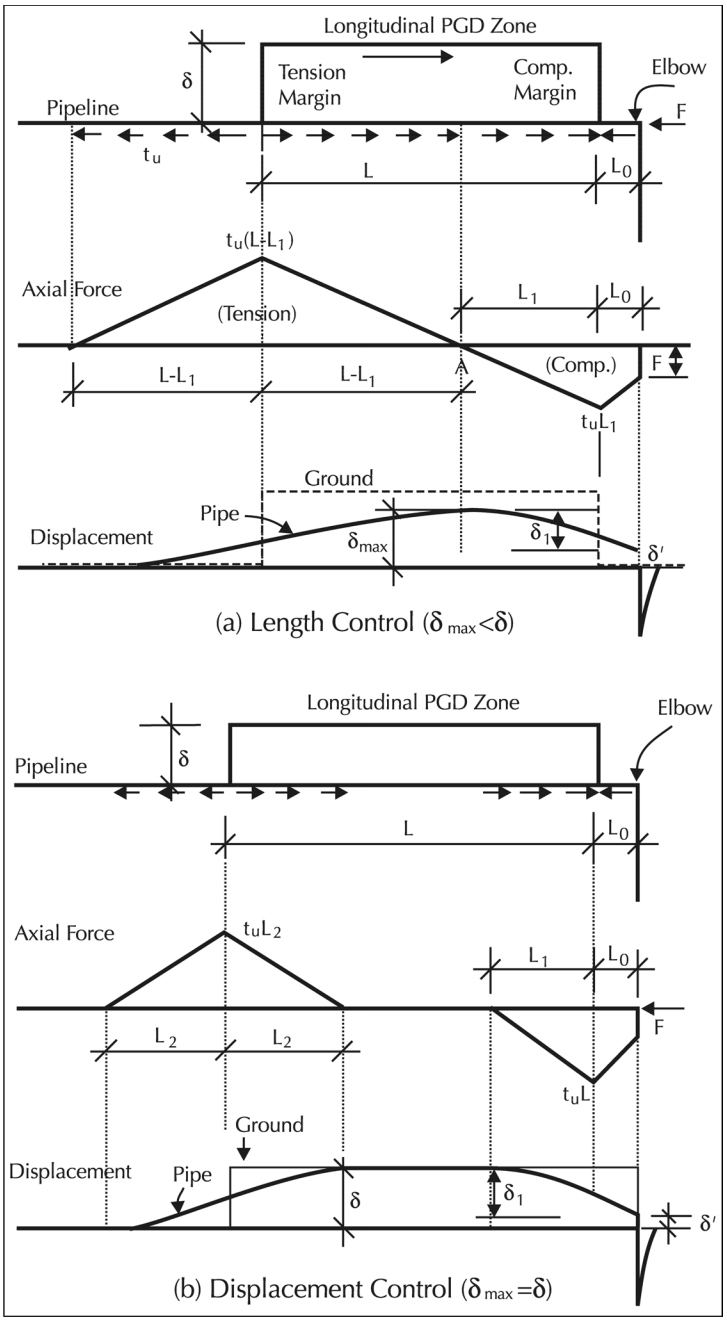

Figure 4.13: Effect of Elbow Located Close to a Block Displacement (a) Case I and (b) Case II (from O'Rourke & Liu, 2012)

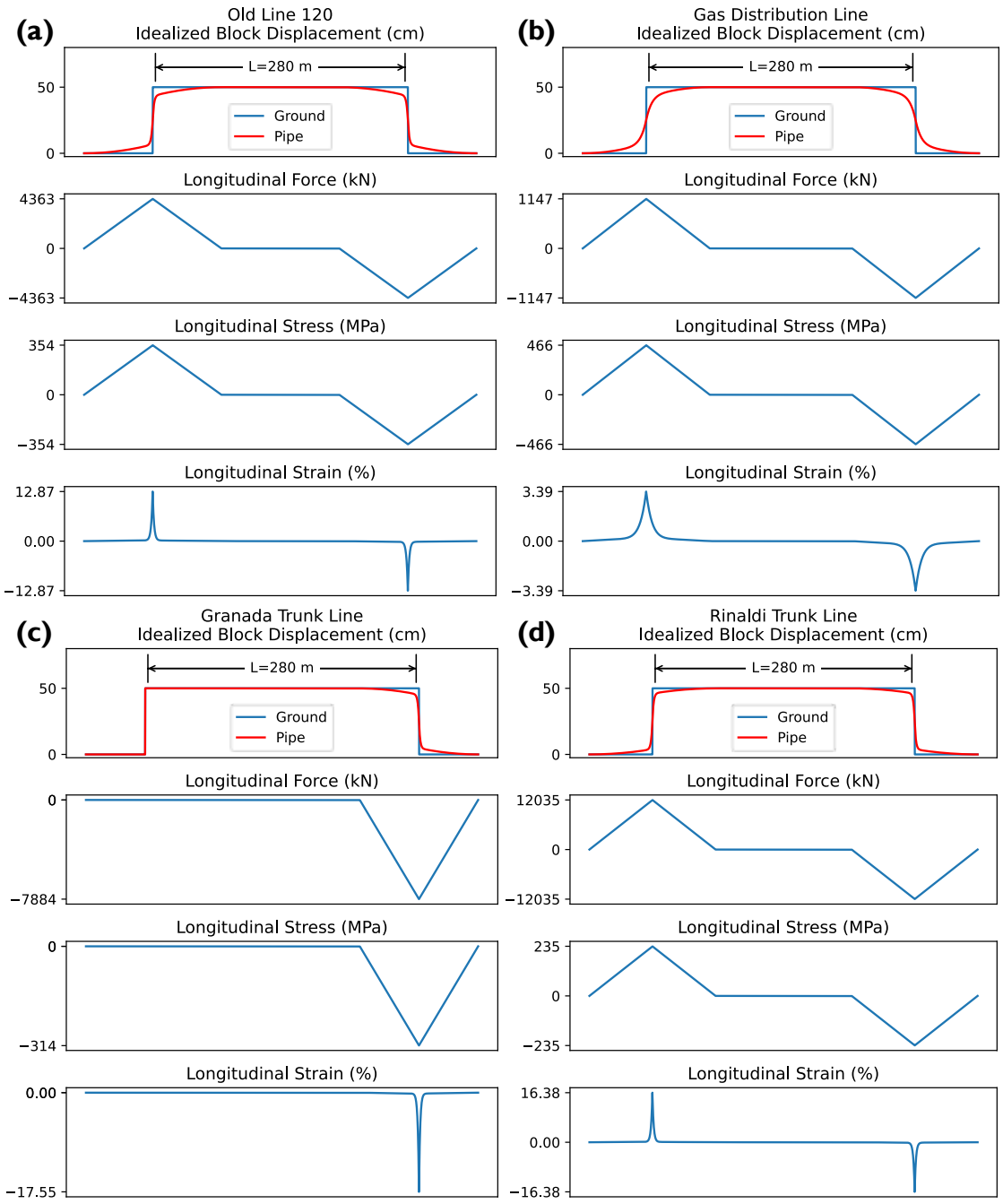

Figure 4.14: Modeled Pipeline Response for (a) Old Line 120, (b) Gas Distribution Line, (c) the Granada Trunk Line, and (d) the Rinaldi Trunk Line

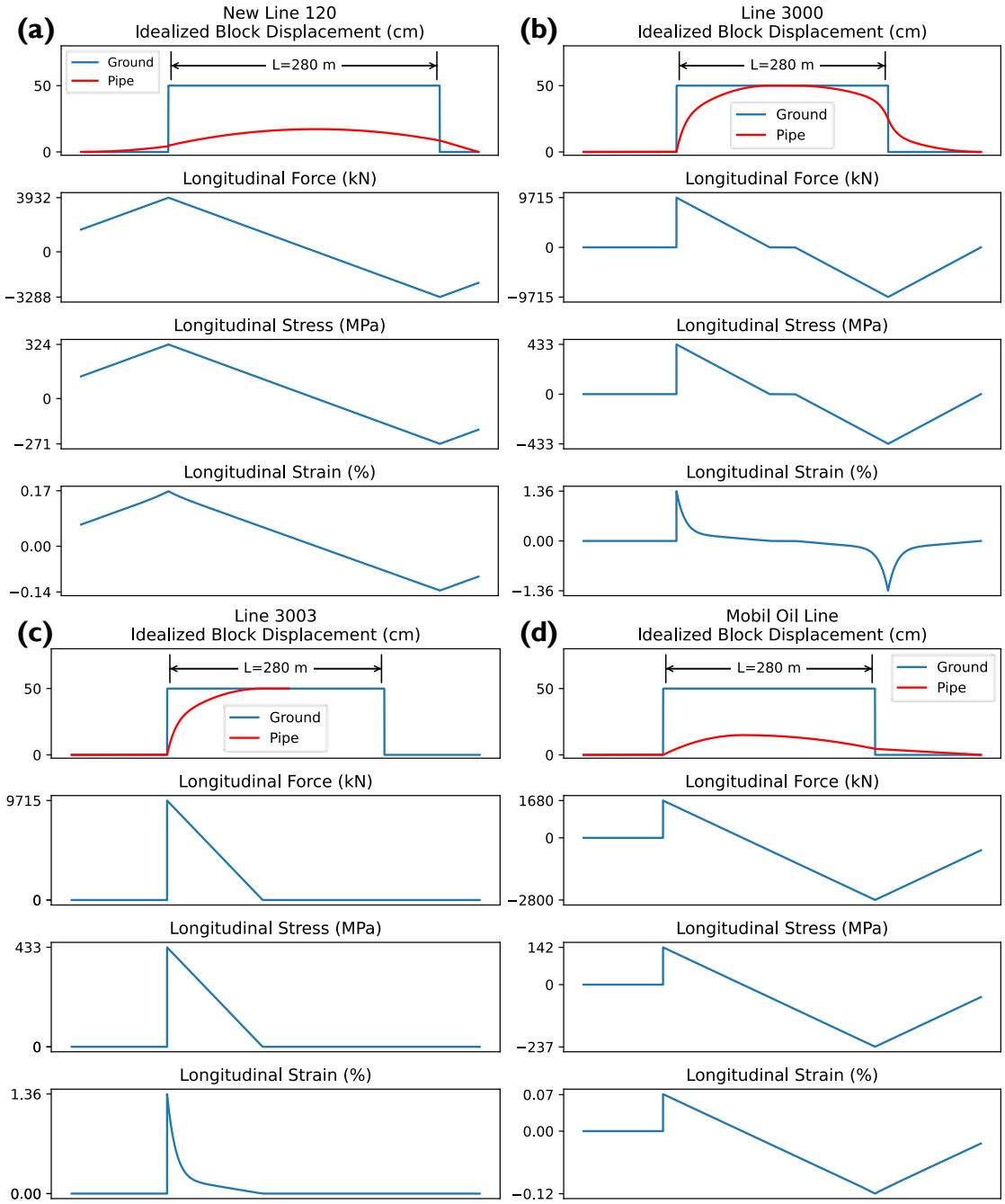

Figure 4.15: Modeled Pipeline Response for (a) New Line 120, (b) Line 3000, (c) Line 3003, and (d) Mobil Oil Line M70

5 PROBABILISTIC ASSESSMENT OF THE PIPELINE RESPONSE TO SEISMIC DISPLACEMENT AT BALBOA BOULEVARD DURING THE 1994 NORTHRIDGE EARTHQUAKE

The contents of this chapter are based in large part on the material contained in a journal article in preparation by Bain, C. A., O'Rourke, T. D., and Bray, J. D. entitled: "Probabilistic Assessment of the Pipeline Response to Seismic Displacement at Balboa Boulevard during the 1994 Northridge Earthquake," (Bain et al., 2023b).

5.1 INTRODUCTION

Balboa Boulevard between Lorillard and Rinaldi Streets is situated in the northern San Fernando Valley of Southern California. A general location map for the site is presented in Figure 5.1. During the 1994 M_w 6.7 Northridge earthquake, this site experienced significant seismic ground displacement which ruptured a natural gas transmission pipeline, a natural gas distribution pipeline, and two pressurized water trunk lines. Three other natural gas transmission pipelines and an oil transmission pipeline were not damaged. Figure 5.2 displays a map of the pipelines at Balboa Boulevard.

This work complements a paper that covers conventional analyses in which pipeline strains are evaluated by an analytical model and compared with critical strains estimated to preserve pressure integrity in each line (Bain et al., 2023a). The salient features of the ground deformation measurements, pipeline characteristics, and modeling approach are covered with emphasis on the uncertainty associated with these parameters. The reader is referred to Bain et al. (2023a) for additional details.

This study probabilistically evaluates the pipeline response to the seismic ground displacement during the Northridge earthquake using the Pacific Earthquake Engineering Research (PEER) Center's Performance Based Earthquake Engineering (PBEE) methodology. The PEER PBEE methodology has been employed in the Open Seismic Risk Assessment (*OpenSRA*) software recently developed by PEER for assessing risk to natural gas infrastructure including buried pipelines (https://peer.berkeley.edu/opensra, accessed May 2023). A full risk analysis utilizing PEER's PBEE methodology assesses risk at the system level by probabilistically quantifying an intensity measure (IM), such as the peak ground acceleration (PGA). The response of the system to the IM is quantified in terms of an engineering demand parameter (EDP), such as the seismic ground displacement. The damage to infrastructure caused by the EDP is assessed in terms of a damage measure (DM), such as the longitudinal pipe strain. Finally, the consequences of the DM are quantified in terms of a decision variable (DV), such as the probability of pipe rupture.

A forward analysis of a site such as Balboa Boulevard would require probabilistically assessing the IM using scenario ShakeMaps (https://earthquake.usgs.gov/data/shakemap/, accessed May 2023) or ground motion models (GMMs). The response of the soils to the IM would then be assessed using models to estimate the seismic ground displacement EDP and its uncertainty from liquefaction or slope instability. These two steps introduce significant uncertainty that would exceed that for the back-analysis of the Balboa Boulevard site described in this study.

For the back-analysis of the Balboa Boulevard site for the PGD experienced during the Northridge earthquake, the IM is not estimated and the seismic ground displacement EDP and its uncertainty is estimated using measurements collected after the earthquake from several investigators. The uncertainty in the other soil-pipeline system parameters is estimated, including the length of the seismic ground displacement zone, the soil-pipeline interface shear stress, the pipe steel yield strength, and the shape of the pipe steel stress-strain curves. Monte Carlo simulations of the longitudinal strain response are performed with an analytical model, which provides a distribution of the longitudinal strain DM for each pipeline.

New fragility relationships to assess the performance of a pipeline in response to tensile or compressive strain are proposed. These relationships are applied to the estimated longitudinal strains to develop distributions for the probability of tensile rupture or compressive buckling DVs. The resulting probabilities of failure compare well to the observed pipeline performance.

5.2 UNCERTAINTY IN THE GROUND DEFORMATION MEASUREMENTS AT BALBOA BOULEVARD

No significant seismic ground displacement occurred at the Balboa Boulevard site during the 1971 M_w 6.6 San Fernando earthquake. Conversely, a block-slide type displacement moved downslope in a south-southeast direction subparallel to Balboa Boulevard during the 1994 M_w 6.7 Northridge earthquake. Bain et al. (2023) estimated mean seismic ground displacement of 50 cm using measurements from several investigators (LABE, 1995; Holzer et al., 1999; Sano, 1998; Hecker et al., 1995). Pullout of the Granada Trunk Line (GTL) an estimated 46 ± 5 cm (Ziotopoulou et al., 2022) at the location of a Dresser mechanical coupling is approximately equal to the block displacement. Figure 5.3 compares the permanent ground deformation measurements from the field survey (LABE, 1995) and from air photos (Sano, 1998).

This study estimates the maximum seismic ground displacement and its uncertainty using two measurements from the field survey (LABE, 1995), four measurements from the air photos (Sano, 1998), and the measured pullout of the GTL (Ziotopoulou et al., 2022). The mean displacement from these seven data points is 50 cm with $\beta_r = 0.29$. The arithmetic displacements and the displacements transformed using the natural logarithm both indicate that the null hypothesis of normality cannot be rejected using the Lilliefors test. Although the form of the distribution is unclear, the seismic ground displacement is assumed to be lognormally distributed.

The aleatory variability in the seismic ground displacement measurements is excessive. A single measurement from the air photos shows displacement of about 84 cm, about 30 cm greater than the maximum measurement collected on the ground. Excluding this point, $\beta_r = 0.19$. Therefore, this study assumes the mean seismic ground displacement is 50 cm and $\beta_r = 0.19$. The distribution is truncated at lower and upper limits of 30 and 65 cm, respectively.

As discussed previously, the uncertainty in the seismic ground displacement EDP is relatively small for the back analysis of the site for the 1994 Northridge earthquake. For a forward analysis of this or another site, the uncertainty would be larger.

O'Rourke & Palmer (1994) and SoCalGas & PG&E (2000) indicate that the tensile and compressive deformation zones are approximately 280 to 300 m apart, respectively. The locations of the water trunk line repairs from Ziotopoulou et al. (2022) confirm these observations. The tensile rupture of the Rinaldi Trunk Line is located about 279 m upslope of the compressive rupture and the tensile rupture of the Granada Trunk Line is located about 293 m upslope of the compressive rupture. SoCalGas & PG&E (2000) indicates that the tensile and compressive

ruptures to the Old Line 120 natural gas transmission pipeline were located about 275 m apart. Given this data, the mean length of the block displacement is assumed to be 285 m and is uniformly distributed from 270 to 300 m. As will be shown in a forthcoming section, the strain analyses are not sensitive to this parameter.

5.3 UNCERTAINTY IN THE PIPELINE PROPERTIES AT BALBOA BOULEVARD

5.3.1 Uncertainty in the Geometric and Strength Parameters for the Pipelines at Balboa Boulevard

The Bain et al. (2023) study presents detailed data for eight pipelines on Balboa Boulevard between Lorillard and Rinaldi Streets: Old Line 120, New Line 120, Line 3000, and Line 3003 natural gas transmission pipelines, a natural gas distribution pipeline, the Mobil Oil Line M70 crude oil transmission pipeline, and the Granada and Rinaldi Water Trunk Lines (GTL and RTL, respectively). This subsection examines the uncertainty in the pipe outside diameter, wall thickness, and yield strength. The next subsection examines the stress-strain curves for the pipe steel.

The yield strength was measured for three pipelines: Old Line 120, the gas distribution line, and the GTL. The GTL was constructed in 1956 using ASTM A283 Grade C steel (specified minimum yield strength, SMYS = 205 MPa) joined primarily with welded slip joints. Dresser mechanical couplings were employed at some connections to accommodate small, post-construction movements in the pipeline (Ziotopoulou et al., 2022). According to Davis (1999), the average yield and ultimate strengths of the GTL from 21 mill test results and 52 reports on steel weld tests are 275 MPa and 424 MPa, respectively. The average yield strength is about 34% greater than the SMYS. The aleatory variability from the 21 mill tests (Craig Davis, personal communication, 2022) is $\beta_r = 0.04$ and the minimum and maximum values are 249 and 294 MPa, respectively. The yield strength data are not normally or lognormally distributed. This parameter is assumed to be lognormally distributed in the *OpenSRA* software. For this reason, this study assumes uncertainty in the yield strength is lognormally distributed with a mean of 275 MPa. The distribution is truncated at lower and upper limits of 245 and 300 MPa, respectively.

Old Line 120 was constructed in 1930 with API 5L Grade B steel (SMYS = 241 MPa) using a belled-end pipe and chill ring design joined with an early shielded electric arc welding technique (SoCalGas & PG&E, 2000). The results of a tensile coupon test for Old Line 120 pipe steel are provided by SoCalGas & PG&E (2000) in Figure 5.4. The figure also shows two possible Ramberg-Osgood models fit to the data, which will be discussed in a forthcoming section. This tensile coupon test shows the yield strength for Old Line 120 steel away from a weld is about 47,200 psi (325 MPa). This yield strength is about 35% greater than its SMYS. Tensile coupon tests of an intact weld retrieved 9 m north of Lorillard Street showed slightly lower yield strength in the heat affected zone adjacent to the weld, with an average of 313 MPa. This yield strength is about 30% greater than its SMYS. Uncertainty in the yield strength for Old Line 120 is assumed to be lognormally distributed with a mean of 313 MPa. The aleatory variability for the yield strength of this line is unknown. Due to the lack of test data, the aleatory variability is estimated assuming a base uncertainty equal to that of the GTL, $\beta_r = 0.04$, plus an additional 0.03. Taking the sum of the squares, $\beta_r = 0.05$ $\left(\sqrt{0.04^2 + 0.03^2} = 0.05\right)$. The distribution is truncated at lower and upper limits of 241 MPa (equal to the SMYS) and 325 MPa, respectively.

The natural gas distribution line at Balboa Boulevard was constructed in 1957 with API-5L X-42 steel (SMYS = 290 MPa) and oxyacetylene girth welds. Strength tests performed on a section of the line indicated it had yield and ultimate strengths of approximately 390 MPa and 480 MPa, respectively (SoCalGas & PG&E, 2000). The yield strength was measured at 0.5% strain and the ultimate strength was measured at 5% strain. This yield strength is about 34% greater than its SMYS. The yield strength for the gas distribution line is assumed to be lognormally distributed with a mean of 390 MPa. Like Old Line 120, the aleatory variability is assumed to equal $\beta_r = 0.05$. The distribution is truncated at a lower limit of 290 MPa (equal to the SMYS) and 435 MPa (equal to the SMYS plus fifty percent).

The Rinaldi Trunk Line (RTL) was constructed in 1978 using ASTM A283 Grade C or D steel (SMYS = 205 MPa for Grade C or SMYS = 230 MPa for Grade D) joined with welded slip joints. There is no evidence of Dresser couplings at the Balboa Boulevard site. The Bain et al. (2023) study assumes the RTL is Grade C steel.

The tensile coupon tests of samples from Old Line 120, the gas distribution line, and the GTL show that the yield strength is likely much greater than the SMYS. Additional data from Mason (2006), who provide six tensile coupon tests for 914 mm pipelines constructed for Los Angeles Department of Water and Power (LADWP), support a yield strength for the RTL greater than the SMYS. The average yield strength of these tests is about 263 MPa, about 28% greater than the SMYS assuming Grade C steel.

This study assumes the mean yield strength of the RTL is 266 MPa, 30% greater than the SMYS. Due to the lack of tensile coupon tests, the aleatory variability is taken as $\beta_r = 0.05$ and the distribution is truncated at a lower limit of 205 MPa (equal to the SMYS of Grade C steel) and an upper limit of 308 MPa (equal to the SMYS plus 50%).

New Line 120 was constructed to replace 10 km of Old Line 120 just before the Northridge earthquake. It was fabricated with API 5L X-60 steel (SMYS = 414 MPa). Lines 3000 and 3003 and the Mobil Oil Line M70 were constructed in 1956, 1958, and 1991, respectively, with API 5L X-52 steel (SMYS = 359 MPa). The yield strength of these lines is unknown but are all likely to be much greater than their SMYS. This study assumes the mean yield strength for these lines is 30% greater than their respective SMYS. For New Line 120, the mean yield strength is assumed to equal 538 MPa and for Lines 3000, 3003, and M70, the mean yield strength is assumed to equal 467 MPa. Because there are no tensile coupon tests for these lines, the aleatory variability is assumed to be $\beta_r = 0.06$. For New Line 120, the distribution is truncated at a lower limit of 414 MPa (equal to its SMYS) and an upper limit of 621 MPa (equal to the SMYS plus 50%). For Lines 3000, 3003, and M70, the distribution is truncated at a lower limit of 359 MPa (equal to their SMYS) and an upper limit of 539 MPa (equal to their SMYS plus 50%).

Mason (2006) provides 12 tensile coupon tests for 305-, 813-, and 914-mm pipelines constructed for LADWP. These tests show mean Young's Modulus (E) of about 208 GPa, with minimum and maximum values of about 191 and 219 GPa, respectively. Mason (2006) carefully measured the Young's Modulus from the steel's proportional limit (the point on the stress-strain curve where the deformation becomes nonlinear) rather than from the 0.2% offset yield stress. The arithmetic values of the Young's Modulus and the values of the Young's Modulus transformed using the natural logarithm both indicate that the null hypothesis of normality is rejected using the Lilliefors test. Even though the form of the distribution is unclear, this study assumes the Young's Modulus is lognormally distributed with mean E of 208 GPa and $\beta_r = 0.04$. Due to the limited data, the distribution is truncated at lower and upper limits of 180 and 230 GPa, respectively. As will be shown in a forthcoming section, the uncertainty in the Young's Modulus has a small effect on the

strain analysis. The uncertainty in the yield strength and Young's Modulus for the pipelines at Balboa Boulevard are summarized in Table 5.1.

There is uncertainty in the outside pipe diameter (D) and the pipe wall thickness (t) due to inherent variability during manufacturing. Small variations in D have a negligible effect on the strain estimate while small variations in t have a greater, though still small, effect. The uncertainty in D and t is estimated to be normally distributed with coefficients of variation ($COV = \sigma/\mu$) equal to 0.2% and 4%, respectively. API 5L specifies manufacturing tolerances that are applied to truncate the distributions. These tolerances depend on the specified D and t of a pipe. The tolerances for the RTL and GTL are unknown but are assumed to be consistent with the API 5L standards. The estimated aleatory variability for D and t for the pipelines at Balboa Boulevard is summarized in Table 5.2.

Old Line 120, New Line 120, and Line M70 have typical operating pressures of 1.34 MPa, 1.30 MPa, and 3.45 MPa, respectively (SoCalGas & PG&E, 2000). The operating pressure of the gas distribution line is assumed to be 0.3 MPa (O'Rourke & Palmer, 1994). Lines 3000 and 3003 have maximum allowable operating pressure (MAOP) equal to 4.48 MPa. At the time of the Northridge earthquake the GTL and RTL were operating at about 1.1 and 0.4 MPa, respectively.

There are no data to estimate the variability in the pipeline operating pressure during the Northridge earthquake. Small variations from the mean have a negligible effect on the evaluation, and for the purposes of this report, one can reasonably assume there is no uncertainty.

5.3.2 Uncertainty in the Ramberg-Osgood Parameters for the Pipelines at Balboa Boulevard

The stress-strain curves of various pipe steels often use the Ramberg-Osgood model, which defines a power law relationship, for the shape of the curve. The Ramberg-Osgood model is defined as Equation (5.1).

$$\varepsilon_P = \frac{\sigma}{E} * \left[1 + \frac{n}{1+r} * \left(\frac{\sigma}{\sigma_y}\right)^r\right] \tag{5.1}$$

where ε_P is the pipe strain, σ is the applied stress, E is the Young's Modulus of the pipe steel, σ_y is the yield stress of the pipe steel, and n and r are Ramberg-Osgood model fitting parameters.

The uncertainty in the shape of the stress-strain curve (i.e., the Ramberg-Osgood parameters) is difficult to estimate due to a lack of test data. The data from Mason (2006) for the 914 mm pipeline show a Lüders plateau to about 1.5% strain, similar to Old Line 120 (Figure 5.4). These tests show little variation in the shape of the stress-strain curve for Lüders plateau steel.

Two Ramberg-Osgood models are considered for Lüders plateau steel: 1) the stress-strain curve to the end of the Lüders plateau is modeled with Ramberg-Osgood parameters of $n = 8$ and $r = 50$, and 2) the stress-strain curve after the Lüders plateau is modeled with Ramberg-Osgood parameters of $n = 30$ and $r = 6$. The first relationship accurately models the longitudinal strain to the end of the Lüders plateau but may significantly overestimate the strain after the Lüders plateau. The second relationship slightly overestimates the longitudinal strain before the end of the Lüders plateau, but accurately models the strain after the Lüders plateau. The potential Ramberg-Osgood models for Lüders plateau steel are shown in Figure 5.4.

The uncertainty in the shape of the Ramberg-Osgood model for Lüders plateau steel is epistemic (i.e., uncertainty that the selected model is the correct model, denoted as β_u). The

epistemic uncertainty is treated with a logic tree approach with weights of 0.5 and 0.5 for the first and second models, respectively. These models apply for Old Line 120 and the GTL and RTL.

Ramberg-Osgood parameters of $n = 25$, and $r = 10$ are fit to the stress-strain test data for the gas distribution line. The Ramberg-Osgood parameters for New Line 120 and Lines 3000, 3003, and M70, are taken directly from the recommendations of O'Rourke & Liu (2012), summarized in Table 5.3. For these pipelines, the shape of the stress-strain curve has a small effect on the evaluation and this study assumes no uncertainty in their Ramberg-Osgood parameters.

5.4 PIPELINE FRAGILITY FUNCTIONS

5.4.1 Tensile Pipe Strain Fragility Functions

The most important performance goal for all pipelines is to maintain pressure integrity (i.e., prevent rupture). New Line 120, Lines 3000 and 3003, and Mobil Oil Line M70 are composed of X-grade steels with rounded stress-strain curves and circumferential, overmatched girth welds. For these pipelines, to maintain pressure integrity, limiting tensile strains are recommended as follows: 1) ASCE (1984) guidelines suggest 3 – 5%, 2) ALA (2001) guidelines suggest 4%, and 3) PRCI (2004) guidelines suggest 2 – 4%. Wijewickreme et al. (2005) assumed 10%, 50% (median), and 90% probability of tensile pipe rupture at 3%, 7%, and 10% strains, respectively.

To develop a tensile rupture fragility function, it is assumed that at 4% tensile strain, there is a 30% probability of rupture (i.e., loss of pressure integrity). This assumption was made on the basis of expert judgement with the realization that strain limits recommended in guidelines likely correspond to a low probability of failure, though the exact probability is unknown. The developed tensile strain fragility function for pipe rupture is presented as Equation (5.2).

$$Prob(Tensile\ Rupture) = 1 - \Phi\left(\frac{-\ln(\varepsilon_p) + \ln(4.68)}{0.3}\right) \tag{5.2}$$

where Φ is the standard normal cumulative distribution and ε_p is the tensile longitudinal pipe strain. The aleatory variability due to inherent randomness in the loading conditions (e.g., eccentricities in the pipe alignment, nonuniform soil conditions) and pipe properties (e.g., post-yield stress-strain behavior, weld quality, corrosion) is estimated as $\beta_r = 0.3$. The tensile longitudinal strains corresponding to 10%, 50%, and 90% probability of pipe rupture are about 3.2%, 4.7%, and 6.9%, respectively. The epistemic uncertainty in the mean or median strain at which pressure integrity is lost (i.e., uncertainty that Equation (5.2) is the correct model), is estimated as $\beta_u = 0.2$. This is a typical value for structural systems (Norman Abrahamson, personal communication, 2022).

Equation (5.2) applies to steel pipelines with rounded stress-strain curves and circumferential, overmatched girth welds. Old Line 120 was constructed with a belled-end pipe and chill ring design joined using an early shielded electric arc welding technique. Old Line 120 also has a Lüders plateau. These design and construction methods, the characteristics of the pipe steel, and the presence of weld flaws (SoCalGas & PG&E, 2000) warrant lower tolerable strain limits. For Old Line 120, the median tensile strain associated with the loss of pressure integrity is estimated to occur at about 1.25%, coinciding with the end of the Lüders plateau. For Old Line 120, Equation (5.2) is modified as shown in Equation (5.3).

$$Prob(Tensile\ Rupture) = 1 - \Phi\left(\frac{-\ln(\varepsilon_p) + \ln(1.25)}{0.3}\right) \quad (5.3)$$

SoCalGas & PG&E (2000) indicate that the gas distribution line was constructed with oxyacetylene girth welds. Given the poor penetration often associated with oxyacetylene welds, the tensile capacity is assumed to be half that of pipelines constructed using modern, shielded electric arc welding techniques. Accordingly, the median tensile strain associated with the loss of pressure integrity is assumed to be 2.34% for the gas distribution line.

Large pipelines, like the GTL and RTL, are welded in the field over a large circumferential distance, which requires more than one welder. Given multiple welders per weld and alignment eccentricities associated with field conditions, the tensile strain capacity for pipe rupture is taken as half the recommended limit for pipelines with high quality, full circumferential girth welds. The median tensile strain for pipe rupture is also assumed to be 2.34% for these lines. For the gas distribution line and the GTL and RTL, Equation (5.2) is modified as shown in Equation (5.4).

$$Prob(Tensile\ Rupture) = 1 - \Phi\left(\frac{-\ln(\varepsilon_p) + \ln(2.34)}{0.3}\right) \quad (5.4)$$

The epistemic uncertainty for Equations (5.3) and (5.4) is also estimated as β_u = 0.2. Equations (5.2), (5.3), and (5.4) and their 10% and 90% epistemic percentiles are plotted on an arithmetic scale in Figure 5.5 and a logarithmic scale in Figure 5.6.

The ALA (2001) and PRCI (2004) guidelines also define a tensile strain limit criterion corresponding to a normal operability performance goal which PRCI (2004) states, "provides a high level of confidence of no significant pipeline damage". To maintain normal operability, ALA (2001) and PRCI (2004) set tensile strain limits below 2% and in the 1 – 2% range, respectively. Only the pressure integrity performance goal is evaluated in this study.

5.4.2 Compressive Pipe Strain Fragility Function

Tensile strain limits are based on a pipe's capacity to stretch without compromising internal pressure, and compressive strain limits are based on pipe behavior as a thin-walled pressure vessel that can buckle when subjected to compressive loads. Critical compressive strain test data that correspond to the onset of pipe wall wrinkling for both seamless and welded pipe are plotted in Figure 5.7. The test data were compiled by Mohr (2003) and are plotted against the pipe outside diameter to wall thickness (D/t) ratio. A regression fit to the data is presented as Equation (5.5). Equation (5.5) is plotted against the test data in Figure 5.7.

$$\ln(\varepsilon_{p-cr}) = -1.617 * \ln(D/t) + 1.709 + \varepsilon\sigma \quad (5.5)$$

where ε_{p-cr} is the critical compressive pipe strain corresponding to the onset of pipe wall wrinkling or buckling, D/t is the pipe outside diameter to wall thickness ratio, ε represents the number of standard deviations from the mean, and $\sigma = 0.407$ is the standard deviation of the residuals in natural log space. Figure 5.7 also shows an empirical relationship ($\varepsilon_{p-cr} = 0.35t/D$) from O'Rourke & Liu (2012) for estimating the critical compressive strain. This relationship was used by Bain et al. (2023) to estimate the critical compressive strains for the conventional analyses.

Separate regressions were fit to the seamless and welded pipe datasets. For the two regressions, neither the slopes nor the intercepts differ to a statistically significant degree.

Therefore, a single regression (Equation (5.5)) was fit to the entire dataset, providing a more statistically robust relationship.

The data presented in Figure 5.7 are for pipes with zero internal pressure. In tension, the effect of internal pressure is negligible, and it is reasonable to ignore it. In compression, internal pressure has a stabilizing effect that should be accounted for. Mohr (2003) recommends Equation (5.6) to convert the compressive pipe strain into the zero-pressure-equivalent pipe strain.

$$\varepsilon_{p-eq} = \frac{\varepsilon_p}{1 + \sigma_h/\sigma_y} \tag{5.6}$$

where ε_{p-eq} is the zero-pressure-equivalent compressive longitudinal pipe strain, ε_p is the estimated compressive longitudinal pipe strain, σ_h is the pipe hoop stress, and σ_y is the pipe yield stress. The pipe hoop stress is calculated with Equation (5.7).

$$\sigma_h = \frac{OP * D}{2 * t} \tag{5.7}$$

where OP is the pipeline operating pressure, D is the outside pipe diameter, and t is the pipe wall thickness.

The data presented in Figure 5.7 come from carefully controlled laboratory experiments that would have less uncertainty than that of field conditions. To account for the greater uncertainty associated with field conditions, the aleatory variability is increased from $\beta_r = 0.407$ to $\beta_r = 0.5$. The resulting fragility relationship to estimate the probability of compressive buckling or pipe wall wrinkling is presented as Equation (5.8).

$$Prob(Compressive\ Buckling) = 1 - \Phi\left(\frac{-\ln(\varepsilon_{p-eq}) - 1.617 * \ln(D/t) + 1.709}{0.5}\right) \tag{5.8}$$

where Φ is the standard normal cumulative distribution, ε_{p-eq} is the zero-pressure-equivalent compressive longitudinal pipe strain, D/t is the pipe outside diameter to wall thickness ratio, and $\beta_r = 0.5$. Figure 5.8 and Figure 5.9 show the 95%, 84%, 50%, 16%, and 5% probability of exceedance percentiles of Equation (5.8) plotted against the test data on arithmetic and logarithmic scales, respectively.

The epistemic uncertainty can be estimated as the standard error of the intercept in Equation (5.5). From the regression statistics, the standard error of the intercept equals 0.22. Given the limitations of the dataset, $\beta_u = 0.25$.

To illustrate the effect of the D/t ratio on the probability of compressive buckling, Equation (5.8) is plotted for D/t ratios of 80, 60, 40, and 20 on arithmetic and logarithmic scales in Figure 5.10 and Figure 5.11, respectively. The figures show that a pipe with D/t = 80 would be expected to buckle at strain about 10 times less than a pipe with D/t = 20. The figures also show the 10^{th} to 90^{th} epistemic percentiles.

Equation (5.8) was developed for $16 \leq D/t \leq 115$ and extrapolation beyond this range is cautioned. The GTL and RTL have D/t of about 196 and 182, respectively, and the compressive capacity of the pipes is controlled by the welded slip joints. Figure 5.12 from Mason et al. (2010) presents data to estimate the compressive capacity of welded slip joints. For the GTL, the limiting compressive stress is approximately 0.52 times the yield stress. For the RTL, the limiting compressive stress is approximately 0.45 times the yield stress. The data in Figure 5.12 was developed with numerical simulations and shown to compare favorably to full-scale laboratory test data. The figure does not indicate the uncertainty in these data. For this study, the compressive

fragility function for the GTL and RTL welded slip is a delta function; that is, if the ratio of the stress to the Young's Modulus is less than 0.52 or 0.45 times, respectively, the yield stress, the welded slip joint has 0% probability of compressive failure. Conversely, if the ratio of the stress to the Young's Modulus is greater than 0.52 or 0.45 times the yield stress, respectively, the welded slip joint has 100% probability of compressive failure.

5.5 SOIL MOVEMENT AND PIPE STRAIN MODEL EPISTEMIC UNCERTAINTY

O'Rourke & Liu (2012) present a model for estimating pipe strain for pipelines subjected to longitudinal permanent ground displacement using the Ramberg-Osgood stress-strain model for pipe steel. The idealized block displacement of O'Rourke & Liu (2012) best represents the seismic displacement at Balboa Boulevard. The model accounts for the soil-pipeline interface shear stress for pipelines in either clayey or sandy backfill and nonlinear pipeline steel stress-strain behavior using the Ramberg-Osgood model. The model can be modified to account for the effects of bends or elbows in the pipeline, which are assumed to act as anchors that do not move. The reader is referred to Bain et al. (2023a) for a detailed treatment of this model both with and without bends.

Old Line 120, the gas distribution line, and the GTL and RTL have bends near the soil block. New Line 120 has 90-degree elbows approximately 90 m north and 40 m south of the tensile and compressive margins of the soil block, respectively. The Mobil Oil Line M70 has two 90-degree elbows at the tensile deformation zone and a 90-degree elbow approximately 140 m south of the soil block. Lines 3000 and 3003 have two 45-degree bends at the tensile deformation zone and Line 3000 has a 90-degree elbow approximately 120 m south of the soil block.

The epistemic uncertainty of the soil-block model is unknown. The model makes two simplifying assumptions that affect the strain calculation: 1) the soil-pipeline interface shear stress is fully mobilized with zero relative slip between the pipeline and surrounding soil, and 2) the model simplifies the soil displacement pattern as a block displacement with abrupt displacements in the tensile and compressive ground deformation zones.

The first assumption introduces a small, conservative bias. This bias may be greater for pipelines buried in clayey backfill compared to pipelines buried in frictional backfill due to the greater relative slip necessary to fully mobilize the interface shear strength. The second assumption may also introduce a bias, the degree of which has not been studied. SoCalGas & PG&E (2000) indicate that about 30 cm of extension was concentrated in a zone approximately 12 m wide, about 40 cm of compression was concentrated in a zone approximately 30 m wide, and the remainder of the approximately 50 cm of seismic ground displacement was distributed throughout the soil block.

Assuming a base epistemic uncertainty of $\beta_u = 0.23$ typical for structural systems and adding an additional 0.2, the sum of the squares gives epistemic uncertainty for the soil-block model of $\beta_u = 0.30$.

5.6 SOIL-PIPELINE INTERACTION AND UNCERTAINTY

Old Line 120, the gas distribution line, Lines 3000 and 3003, and the GTL and RTL are buried in soils identified by Bennett et al. (1998) as native sheet flood and debris flow deposits. These soils are primarily low plasticity clays. For these lines, the maximum shear resistance force per unit length of pipe, t_u, is estimated using Equation (5.9).

$$t_u = \alpha * s_u * \pi * D \quad (5.9)$$

where α is an adhesion factor, s_u is the undrained shear strength of the backfill, and D is the outside pipe diameter. t_u is assumed to be constant along the length of the pipeline.

Bennett et al. (1998) summarizes the results of geotechnical investigations performed along Balboa Boulevard by the USGS following the 1994 Northridge earthquake. For soils less than 6 m depth, which are in the depth range of the pipelines at Balboa Boulevard, these investigations include 101 laboratory and 30 field vane shear strength tests. These tests show mean and median peak s_u about 4.25 (natural log units). Cone penetration test (CPT) measurements at the site show similar values. As t_u is assumed to be constant along a pipeline, it is appropriate to use an average value of s_u. Therefore, for the Balboa Boulevard site, the uncertainty in s_u is taken as the uncertainty in the median value. This is calculated as $\beta_u = \beta_r/\sqrt{N} = 0.43/\sqrt{131} = 0.04$, where β_u is the epistemic uncertainty in the average value of s_u, β_r is the aleatory variability of the undrained shear strength tests, and N is the number of tests.

There are many tests of the undrained shear strength at Balboa Boulevard to estimate the average value. For a site without this data, generic values of the undrained shear strength would be used. For example, one dataset of clays from Phoon & Kulhawy (1999) show mean undrained shear strength of about 112 kPa and the aleatory variability is described by a coefficient of variation ($COV = \sigma/\mu$), COV = 32%. This strength is much higher than the average value estimated at Balboa Boulevard and has much greater uncertainty. Using this mean and uncertainty would greatly increase the range of interface shear strength values compared to using the site-specific data. Consequently, this would increase the range of longitudinal strain estimates.

The adhesion factor, α, can be estimated using the dataset from Tomlinson (1957). The mean relationship for all data in the Tomlinson (1957) dataset is approximated with Equation (5.10), which has aleatory variability β_r = 0.47. This amount of variability is considered to be excessively high due to the wide variety of the ground and test conditions in this worldwide dataset. The native soils on Balboa Boulevard are well characterized with small epistemic uncertainty in the average undrained shear strength due to the many vane shear tests and CPTs. Assuming the Tomlinson (1957) database includes an additional uncertainty of 0.35, the β_r for the α parameter taking the sum of the squares is estimated to be only 0.3 for a buried pipeline in one ground condition undergoing longitudinal deformation.

$$\alpha = 5 * 10^{-5} * {s_u}^2 - 0.0139 * s_u + 1.2762, for\ s_u \leq 144\ kPa \quad (5.10)$$

SoCalGas & PG&E (2000) performed pullout tests on a section of Old Line 120 at Balboa Boulevard. Figure 5.13 presents the results of these pipe jacking tests, for which the soil-pipe interface shear stress is plotted as a function of the relative displacement between the pipe and the soil. The maximum shear stress is 680 psf ≈ 33 kPa.

The soil-pipeline interface shear stress calculated using the average s_u of the backfill soil with α from Tomlinson (1957) and the measured interface shear stress from the pullout tests on Old Line 120 represent epistemic uncertainty. The measured interface shear strength is assigned a weight of 0.75 and the interface shear strength estimated using the alpha method is assigned a weight of 0.25.

New Line 120 and the Mobil Oil Line were backfilled with sand extending 15 and 30 cm, respectively, above the pipelines. A one-sack cement slurry was placed from the top of the sand backfill to the pavement (SoCalGas & PG&E, 2000). The maximum shear force per unit length of pipe is estimated using Equation (5.11).

$$t_u = \gamma \left(H_c + \frac{D}{2}\right)\left(\frac{1+K_0}{2}\right)\tan\left[\Phi'_{ds} * \frac{\delta}{\Phi'_{ds}}\right]\pi D \quad (5.11)$$

where H_c is the soil cover to the top of the pipe, D is the outside pipe diameter, K_0 is the coefficient of earth pressure at rest, Φ'_{ds} is the direct shear friction angle of the sandy backfill, and δ is the soil-pipeline interface friction angle. $K_0 = 0.45$ based on soil stress measurements from full-scale axial pipe pullout tests (O'Rourke & Druschel, 1989).

Phoon & Kulhawy (1999) show a mean friction angle for sand of 42° with COV = 9% and minimum and maximum values of 37° and 53°, respectively. The type of laboratory test used to collect these measurements was not specified and may reflect triaxial rather than direct shear friction angle data. Duncan et al. (2014) indicates that triaxial strengths are greater than direct shear strengths. Duncan (2004) also presents data for the triaxial friction angle of sands and gravels which are lognormally distributed with $\beta_r \approx 0.07$. For this study, the mean friction angle is assumed to equal 42°, the aleatory variability is assumed to be lognormally distributed with $\beta_r = 0.07$, and the minimum and maximum values are taken as 35° and 55°, respectively. As will be shown in a forthcoming section, the estimated strains for New Line 120 and Line M70 are low, even for high values of the friction angle, resulting in low probabilities of tensile and compressive failure.

New Line 120 and Mobil Oil Line M70 were coated with fusion-bonded epoxy and smooth polyethylene, respectively. The mean sand-pipe interface friction angle ratio, δ/Φ'_{ds}, is 0.60 for these pipeline coatings (O'Rourke et al., 1990). O'Rourke et al. (1990) indicate that δ/Φ'_{ds} consistently ranged from 0.55 to 0.65 for three types of sand placed at different densities. The aleatory variability is assumed to be normally distributed with $\sigma = 0.04$ and the distribution is truncated at lower and upper limits of 0.5 and 0.7, respectively, to account for nonuniform soil and other field conditions.

New Line 120 and Line M70 have mean soil cover to the top of pipe of about 1.2 m. Since the value of t_u is assumed to be constant along the pipeline, it is appropriate to use an average value and estimate its epistemic uncertainty, which is likely small. This study assumes the epistemic uncertainty in the cover to the top of pipe is normally distributed with COV = 5% and is truncated at ±10%.

The mean soil unit total weight is estimated to equal 19.0 kN/m^3 with $\beta_r = 0.06$. The distribution is truncated at lower and upper limits of 18.0 and 21.0 kN/m^3, respectively.

5.7 ESTIMATED STRAINS AND PIPELINE PERFORMANCE

Monte Carlo simulations of the pipe strain response were performed using the soil block displacement model from O'Rourke & Liu (2012). One-hundred thousand simulations for each pipeline provide a distribution for the longitudinal strain response at the tensile and compressive deformation zones and at pipeline bends. Bends near the block displacement were modeled as anchors with no displacement.

Table 5.4 summarizes the longitudinal strain percentiles at the margins of the soil block and at the pipeline bends near the soil block. Table 5.4 shows the largest strains for the pipelines that failed during the Northridge earthquake (Old Line 120, the gas distribution line, and the GTL and RTL) and smaller strains for the pipelines that did not fail (New Line 120, Line M70, and Line 3003). The compressive strains for Line 3000 range from relatively small to large, indicating significant uncertainty in its response to PGD. Line 3000 did not fail. Table 5.4 also shows small strains for the pipeline bends away from the soil block displacement. The strain at pipeline bends

located at the tensile deformation zone are equal to those at the margin of the soil block. For presentation in this study, all longitudinal strains are rounded to the nearest tenth percent.

Figure 5.14 through Figure 5.16 show the distributions of the modeled pipe strain at the tensile and compressive deformation zones for the pipelines. Figure 5.14 shows the strain distribution (tensile and compressive) for Old Line 120, the gas distribution line, and the GTL and RTL. Figure 5.15 and Figure 5.16 show the distribution of tensile and compressive strain, respectively, for New Line 120, Line 3000, Line 3003, and Mobil Oil Line M70. Note the particularly low strains estimated for New Line 120 and Line M70. These low strain estimates are due primarily to the low interface shear stress developed at the interface of the sand backfill and the polythene pipeline coating. Even for large values of the friction angle, the longitudinal strain is very low.

Table 5.5 summarizes the probability of tensile rupture and compressive buckling percentiles at the margins of the soil block and at the pipeline bends. Table 5.5 shows the highest probabilities of tensile and compressive failure for Old Line 120 and the GTL and RTL. This analysis shows a wider range for the gas distribution line, but the mean probabilities of tensile rupture and compressive buckling for this line are still high (77.7% and 79.1%, respectively). Table 5.5 also shows very low probability of tensile rupture and compressive buckling for New Line 120 and Line M70. The probability of compressive rupture for Line 3000 ranges from low to high (5^{th} to 95^{th} percentiles range from 3.6 to 99.1%).

Figure 5.17 through Figure 5.20 show the distributions for the probability of tensile rupture and compressive pipe wall buckling for the pipelines. Figure 5.17 and Figure 5.18 show that Old Line 120, the gas distribution line, and the GTL and RTL have high probability of tensile failure, consistent with their observed performance. The other pipelines have very low probabilities of tensile rupture. Figure 5.19 and Figure 5.20 show that Old Line 120, the gas distribution line, and the GTL and RTL have high probabilities of compressive buckling and New Line 120 and Line M70 have low probabilities of compressive buckling, consistent with their observed performance. Line 3003 did not cross the compressive deformation zone. Figure 5.20 also shows the significant uncertainty in the compressive performance of Line 3000.

5.8 SENSITIVITY ANALYSIS

The estimated probabilities of tensile rupture and compressive buckling show good agreement with the observed performance of the pipelines at Balboa Boulevard. Line 3000 shows the most uncertainty in its performance. Therefore, a sensitivity analysis of Line 3000 is performed to determine which variables affect the strain calculation most. Figure 5.21 presents a tornado plot for Line 3000. A tornado plot shows the sensitivity of the analysis to each of the independent variables. The bars represent the sensitivity for each variable; the longer the bar, the greater the sensitivity to that variable. The longest bar is shown on top with progressively shorter bars below.

Figure 5.21 shows that the estimated strain response for Line 3000 is most sensitive to the alpha factor, which determines the shear force conveyed to the pipeline by the adjacent soil, followed by the permanent ground deformation, the model epistemic uncertainty, and the pipe steel yield strength. Additionally, the performance of Line 3000 in the compressive deformation zone is sensitive to the critical compressive strain, which has significant uncertainty. Taken together, these four variables account for about 99% of the total variance in the strain estimates for this line. Considering the uncertainty in each of these parameters described previously, as well

as the model epistemic uncertainty, the 16th to 84th percentile probabilities of compressive buckling for Line 3000 range from 19.7 to 94.9%. The 5th to 95th percentiles range from 3.6 to 99.1%.

The uncertainty in the compressive performance of Line 3000 could be reduced most by performing additional pipe pullout tests along Balboa Boulevard to better characterize the interface shear stress. Additionally, tensile coupon tests on samples of X-52 steel would reduce the uncertainty in the pipe steel yield strength.

5.9 CONCLUSIONS

This study probabilistically evaluates the performance of the pipelines at Balboa Boulevard to the seismic permanent ground displacement (PGD) during the 1994 M_w 6.7 Northridge earthquake. The PGD during the Northridge earthquake is modeled as a block-slide characterized by a zone of maximum tensile deformation upslope from a zone of maximum compressive deformation. The average seismic ground displacement calculated from field survey and air photo measurement as well as the offset of the GTL at the location of a Dresser mechanical coupling is 50 cm. The approximate locations of the tensile and compressive deformation zones and the distances between pipe breaks were compared to estimate the length of the block displacement between 270 and 300 m. Eight pipelines crossed the PGD zone. The Old Line 120 natural gas transmission pipeline, the gas distribution line, and the Granada and Rinaldi Trunk Lines experienced tensile and compressive ruptures. Four pipelines were undamaged. No buried pipelines experienced failures during the 1971 San Fernando earthquake because there was no PGD for this event.

One-hundred thousand Monte Carlo simulations of the longitudinal strain and the probabilities of tensile rupture and compressive buckling were assessed for each pipeline. The pipelines that experienced tensile and compressive ruptures in 1994 are shown to have high probabilities of tensile and compressive failure. Conversely, the pipelines that did not experience ruptures in 1994 are shown to have lower probabilities of failure. The performance of Line 3000 in the compressive ground deformation zone has the greatest uncertainty with the probability of compressive buckling ranging from low to high. The Bain et al. (2023) conventional analysis estimated compressive strain for Line 3000 sufficient to cause buckling at the compressive deformation zone.

This study demonstrates the effectiveness of the PEER PBEE methodology for assessing the performance of buried pipelines subjected to PGD. By estimating the range of possible longitudinal strains and probabilities of tensile and compressive failure, probabilistic analyses give a sense of the epistemic uncertainty in the performance of each pipeline at Balboa Boulevard. This is a significant advantage over conventional analyses, which do not show epistemic uncertainty in the performance of the pipelines.

Table 5.1: Estimated Pipe Yield Strength (γ) and Young's Modulus (E) Uncertainty

Pipeline Name	Yield Strength (MPa)				Young's Modulus (GPa)			
	Mean	β_r	Minimum	Maximum	Mean	β_r	Minimum	Maximum
Old Line 120	313	0.05	241	325	208	0.04	180	230
New Line 120	538	0.06	414	621	208	0.04	180	230
Distribution Line	390	0.05	290	435	208	0.04	180	230
Line 3000	467	0.06	359	539	208	0.04	180	230
Line 3003	467	0.06	359	539	208	0.04	180	230
GTL	275	0.04	205	308	208	0.04	180	230
RTL	266	0.06	205	308	208	0.04	180	230
Line M70	467	0.06	359	539	208	0.04	180	230

N/A – No upper limit for distribution

Table 5.2: Estimated Pipe Outside Diameter (D) and Wall Thickness (t) Uncertainty

Pipeline Name	Outside Pipe Diameter (mm)				Pipe Wall Thickness (mm)			
	Mean	COV (%)	Minimum	Maximum	Mean	COV (%)	Minimum	Maximum
Old Line 120	560	0.2	-3.2 mm	+3.2 mm	7.1	4	-0.1t	+0.1t
New Line 120	610	0.2	-3.2 mm	+3.2 mm	6.4	4	-0.1t	+0.1t
Distribution Line	168	0.2	-0.0075D	+0.0075D	4.8	4	-0.5 mm	+0.5 mm
Line 3000	762	0.2	-4.0 mm	+4.0 mm	9.5	4	-0.1t	+0.1t
Line 3003	762	0.2	-4.0 mm	+4.0 mm	9.5	4	-0.1t	+0.1t
GTL	1257	0.2	-4.0 mm	+4.0 mm	6.4	4	-0.1t	+0.1t
RTL	1727	0.2	-4.0 mm	+4.0 mm	9.5	4	-0.1t	+0.1t
Line M70	406	0.2	-0.0075D	+0.0075D	9.5	4	-0.1t	+0.1t

Table 5.3: Estimated Ramberg-Osgood Parameters for the Pipelines at Balboa Boulevard

Pipeline Name	Ramberg-Osgood Parameters					
	n	r	Weight	n	r	Weight
Old Line 120	8	50	0.5	30	6	0.5
New Line 120	10	12	1.0	N/A		
Distribution Line	25	10	1.0	N/A		
Line 3000	9	10	1.0	N/A		
Line 3003	9	10	1.0	N/A		
GTL	8	50	0.5	30	6	0.5
RTL	8	50	0.5	30	6	0.5
Line M70	9	10	1.0	N/A		

Table 5.4: Estimated 5th, 16th, 50th, 84th, and 95th Percentiles of the Maximum Longitudinal Strains at the Tensile and Compressive Deformation Zones During the 1994 Northridge Earthquake

Pipeline Name	Maximum Pipe Strain (%) at the Tensile Margin of the Block PGD						Maximum Pipe Strain (%) at the Compressive Margin of the Block PGD					
	5th	16th	50th	84th	95th	Mean	5th	16th	50th	84th	95th	Mean
Old Line 120	4.2	5.4	7.9	11.4	14.5	8.4	4.2	5.4	7.9	11.4	14.5	8.4
New Line 120	0.1	0.1	0.1	0.1	0.2	0.1	0.1	0.1	0.1	0.1	0.2	0.1
Distribution Line	1.9	2.4	3.5	5.0	6.3	3.7	1.9	2.4	3.5	5.0	6.3	3.7
Line 3000	0.2	0.3	0.6	1.1	1.6	0.7	0.4	0.5	0.6	1.1	1.6	0.9
Line 3003	0.2	0.3	0.6	1.2	1.8	0.7	N/A					
GTL	5.6	7.1	10.4	14.9	18.8	11.0	5.6	7.1	10.4	14.9	18.8	11.0
RTL	3.5	4.6	6.8	9.8	12.5	7.2	3.5	4.6	6.8	9.8	12.5	7.2
Line M70	0.0	0.0	0.0	0.1	0.1	0.0	0.0	0.1	0.1	0.1	0.1	0.1
Pipeline Name	**Maximum Pipe Strain (%) at the Elbow Near the Tensile Margin of the Block PGD**						**Maximum Pipe Strain (%) at the Elbow Near the Compressive Margin of the Block PGD**					
	5th	**16th**	**50th**	**84th**	**95th**	**Mean**	**5th**	**16th**	**50th**	**84th**	**95th**	**Mean**
New Line 120	0.0	0.0	0.0	0.1	0.1	0.0	0.0	0.0	0.1	0.1	0.1	0.1
Line 3000	0.2	0.3	0.6	1.1	1.6	0.7	0.0	0.0	0.0	0.1	0.1	0.0
Line 3003	0.2	0.3	0.6	1.1	1.6	0.7	N/A					
Line M70	0.0	0.0	0.0	0.1	0.1	0.0	0.0	0.0	0.0	0.0	0.0	0.0

N/A – Line 3003 did not cross the compressive deformation zone

Table 5.5: Estimated 5th, 16th, 50th, 84th, and 95th Percentiles of the Probability of Tensile Rupture and Pipe Wall Buckling at the Tensile and Compressive Deformation Zones During the 1994 Northridge Earthquake

Pipeline Name	Probability of Tensile Rupture (%) at the Tensile Margin of the Block PGD						Probability of Compressive Buckling (%) at the Compressive Margin of the Block PGD					
	5th	16th	50th	84th	95th	Mean	5th	16th	50th	84th	95th	Mean
Old Line 120	100	100	100	100	100	99.9	99.9	100	100	100	100	99.9
New Line 120	0.0	0.0	0.0	0.0	0.0	0.0	0.0	0.0	0.0	1.1	5.0	1.0
Distribution Line	15.6	46.5	90.6	99.7	100	77.7	20.9	52.9	90.3	99.1	99.9	79.1
Line 3000	0.0	0.0	0.0	0.0	0.1	0.1	3.6	19.7	67.6	94.9	99.1	60.5
Line 3003	0.0	0.0	0.0	0.0	0.1	0.1	N/A					
GTL	99.0	100	100	100	100	99.9	100	100	100	100	100	100
RTL	87.1	98.2	100	100	100	97.7	100	100	100	100	100	100
Line M70	0.0	0.0	0.0	0.0	0.0	0.0	0.0	0.0	0.0	0.0	0.0	0.0
Pipeline Name	**Probability of Tensile Rupture (%) at the Elbow Near the Tensile Margin of the Block PGD**						**Probability of Compressive Buckling (%) at the Elbow Near the Compressive Margin of the Block**					
	5th	**16th**	**50th**	**84th**	**95th**	**Mean**	**5th**	**16th**	**50th**	**84th**	**95th**	**Mean**
New Line 120	0.0	0.0	0.0	0.0	0.0	0.0	0.0	0.0	0.0	0.1	0.9	0.2
Line 3000	0.0	0.0	0.0	0.0	0.1	0.1	0.0	0.0	0.0	0.0	0.2	0.1
Line 3003	0.0	0.0	0.0	0.0	0.1	0.1	N/A					
Line M70	0.0	0.0	0.0	0.0	0.0	0.0	0.0	0.0	0.0	0.0	0.0	0.0

N/A – Line 3003 did not cross the compressive deformation zone

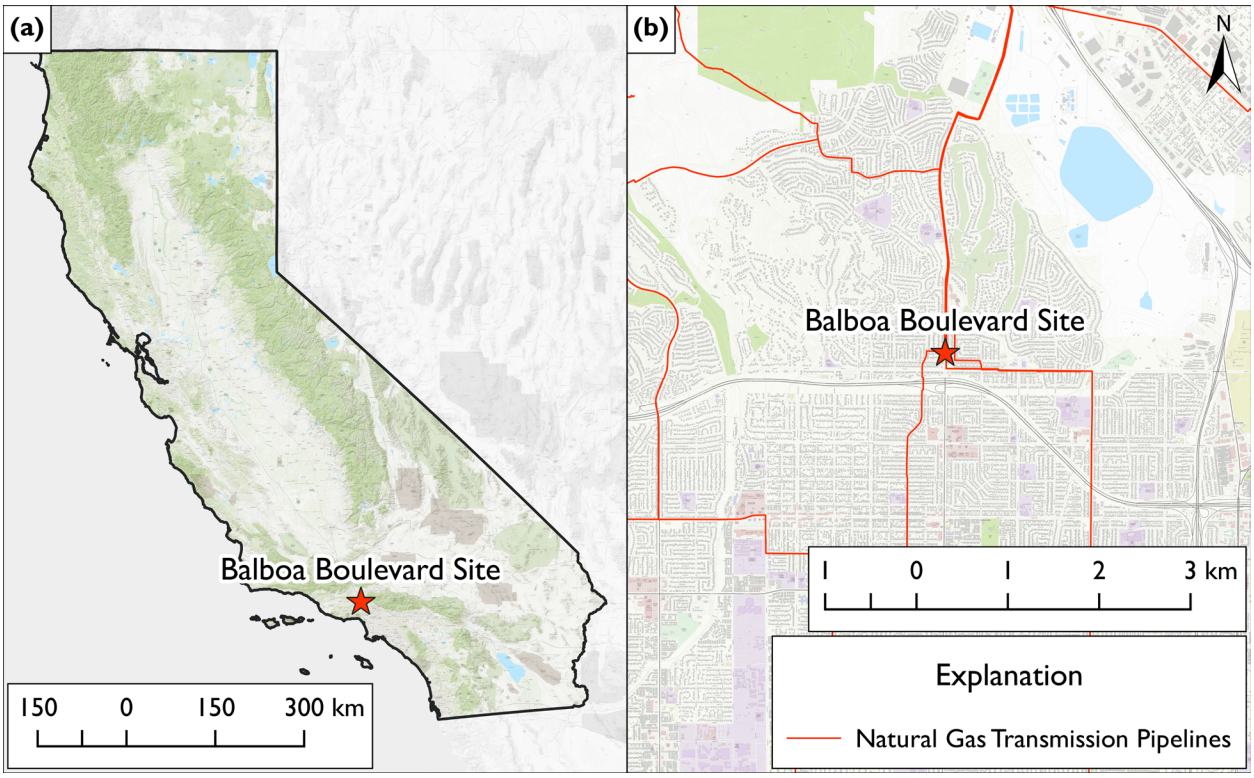

Figure 5.1: (a) General Location of the Balboa Boulevard Site in California and (b) Location of the Balboa Boulevard Site in the San Fernando Valley

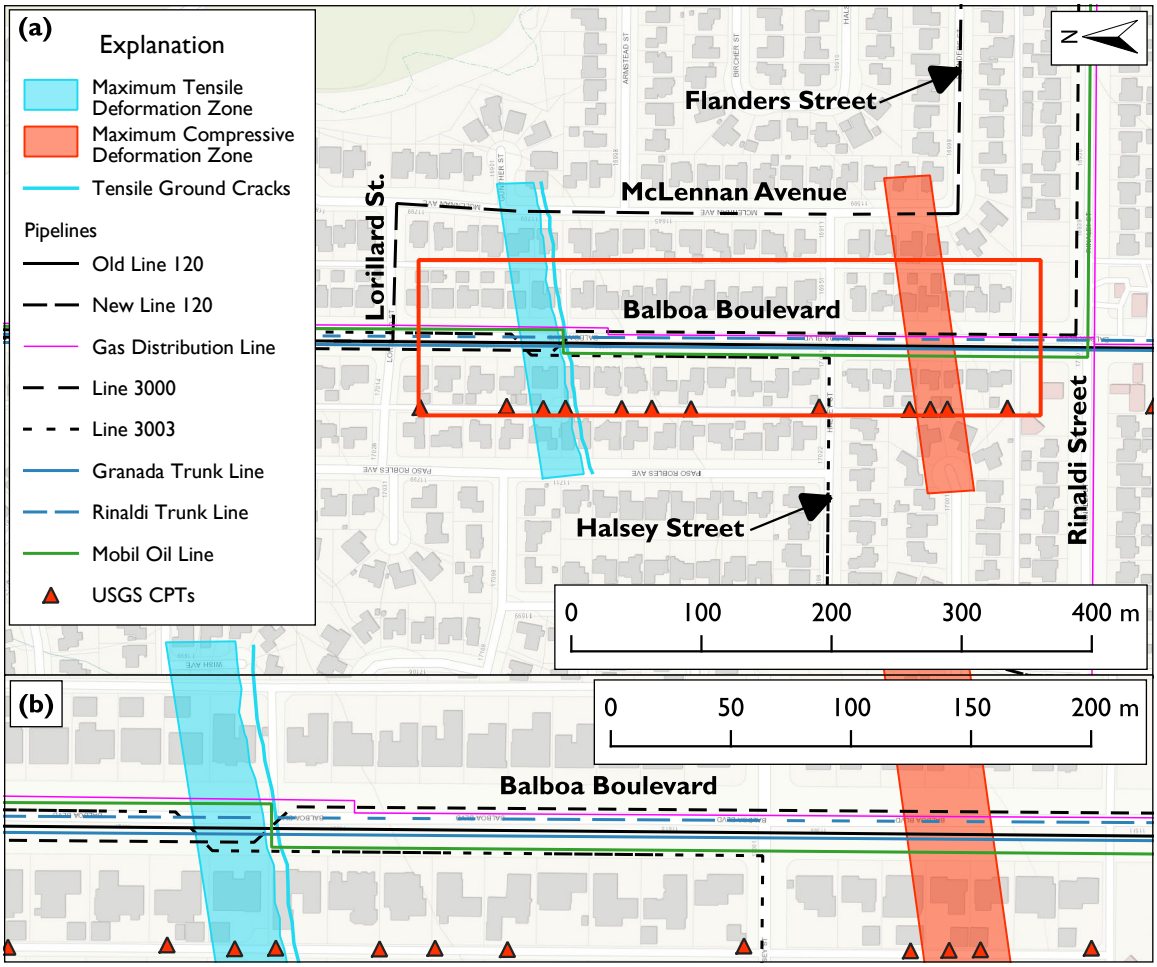

Figure 5.2: Approximate Locations of the Pipelines Along Balboa Boulevard with the Maximum Tensile and Compressive Deformation Zones as shown by O'Rourke & Palmer (1994)

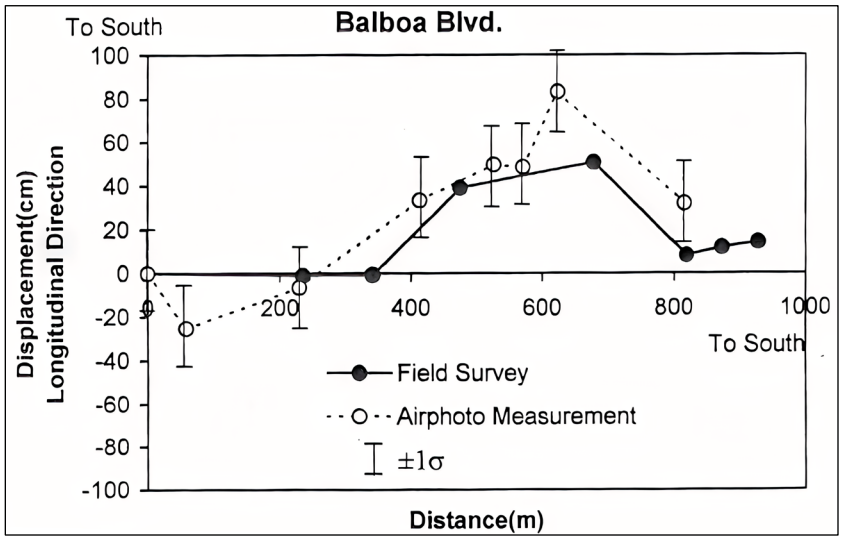

Figure 5.3: Comparison of Los Angeles Bureau of Engineering Ground Displacement Measurements Along Balboa Boulevard (LABE, 1995) to the Measurements from Aerial Photographs from Sano (1998)

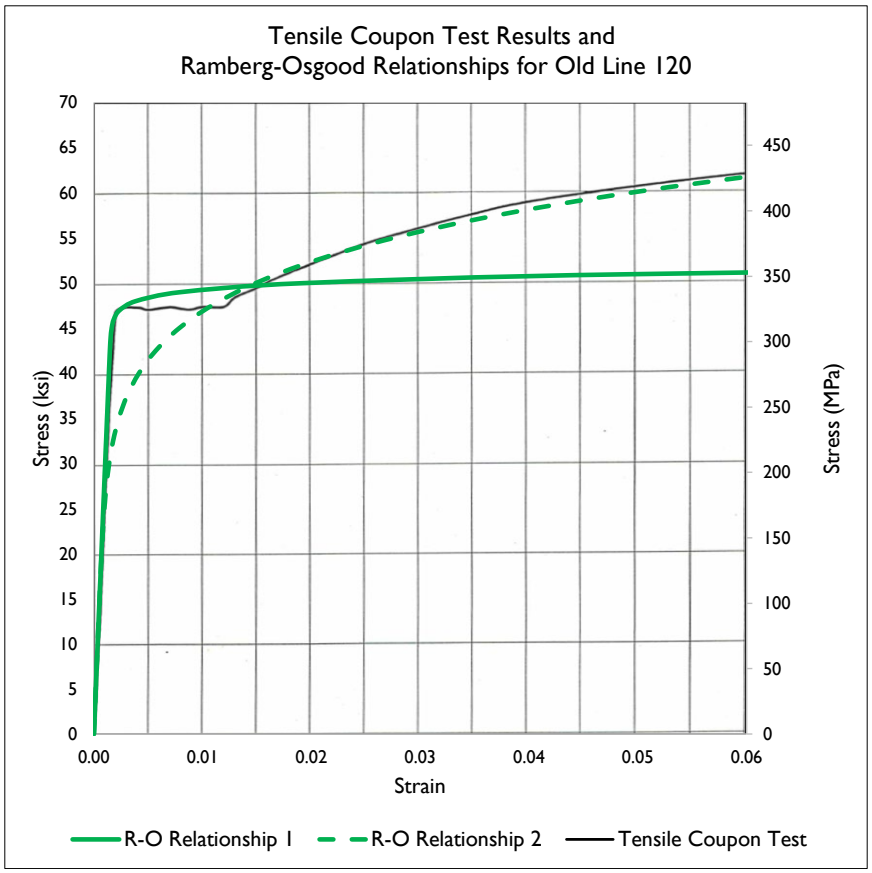

Figure 5.4: Tensile Coupon Test Results for Old Line 120 from SoCalGas & PG&E (2000) with Two Possible Ramberg-Osgood Relationships

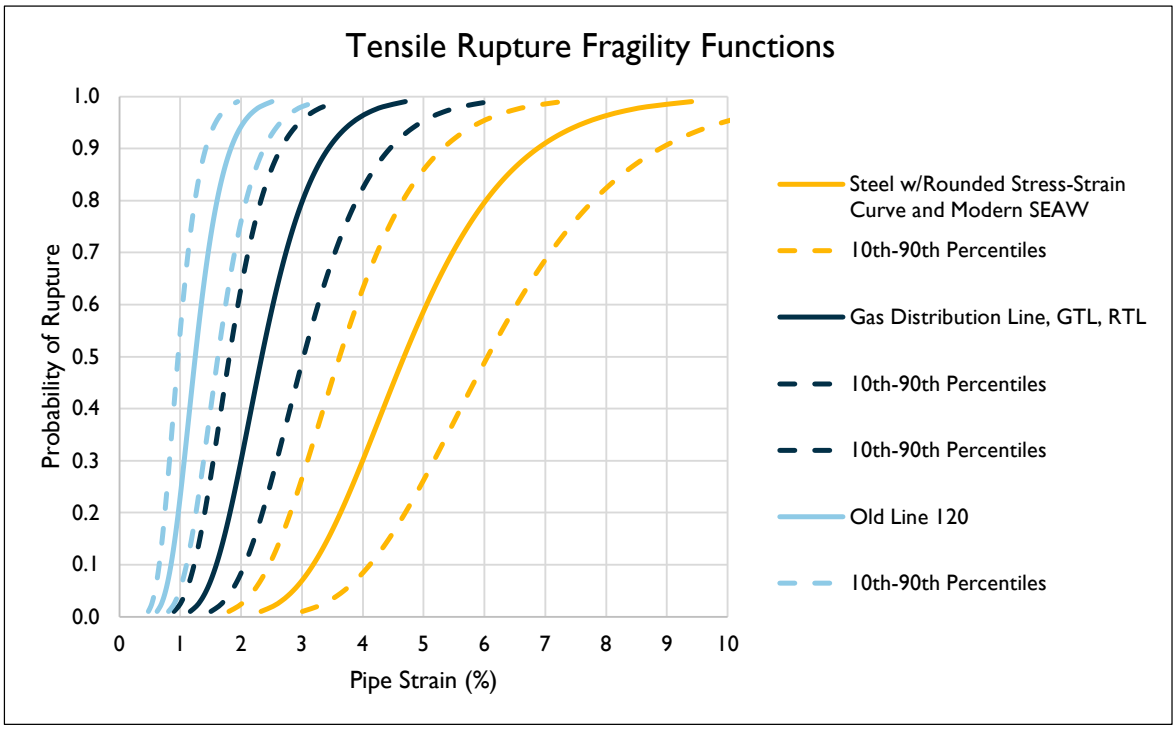

Figure 5.5: Tensile Rupture Fragility Functions (Equation (5.2), Equation (5.3), and Equation (5.4)) Plotted on an Arithmetic Scale (SEAW = Shielded Electric Arc Welds)

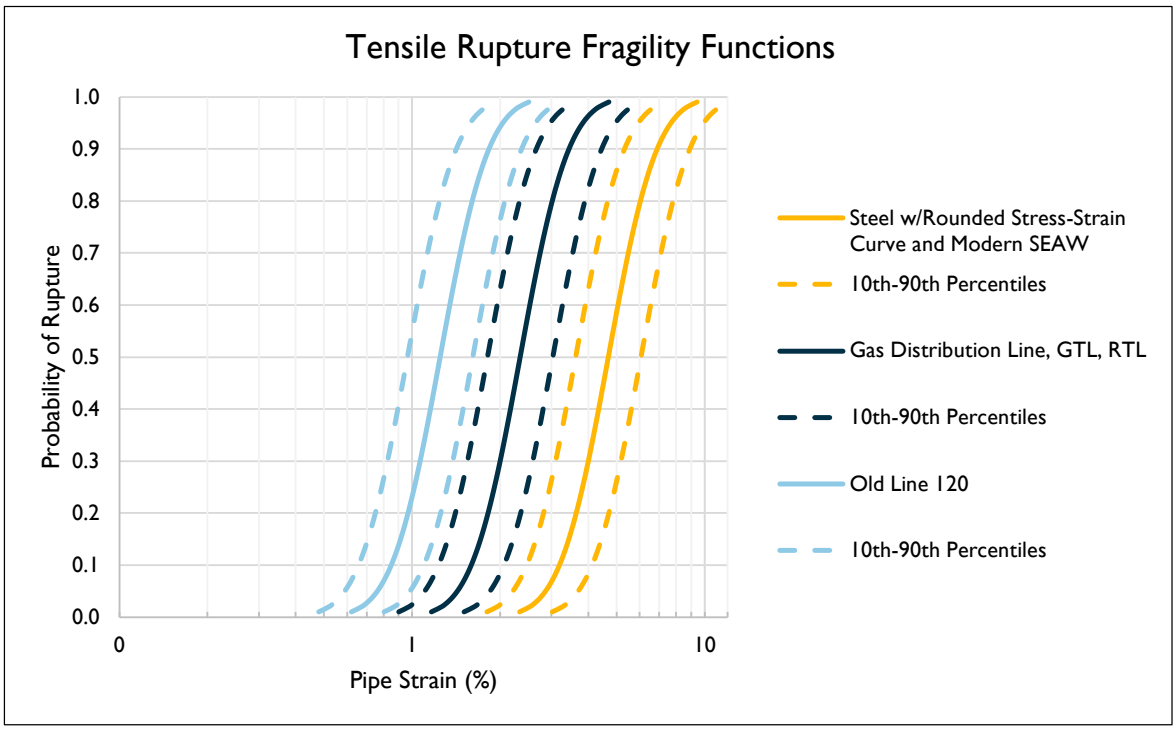

Figure 5.6: Tensile Rupture Fragility Functions (Equation (5.2), Equation (5.3), and Equation (5.4)) Plotted on a Logarithmic Scale (SEAW = Shielded Electric Arc Welds)

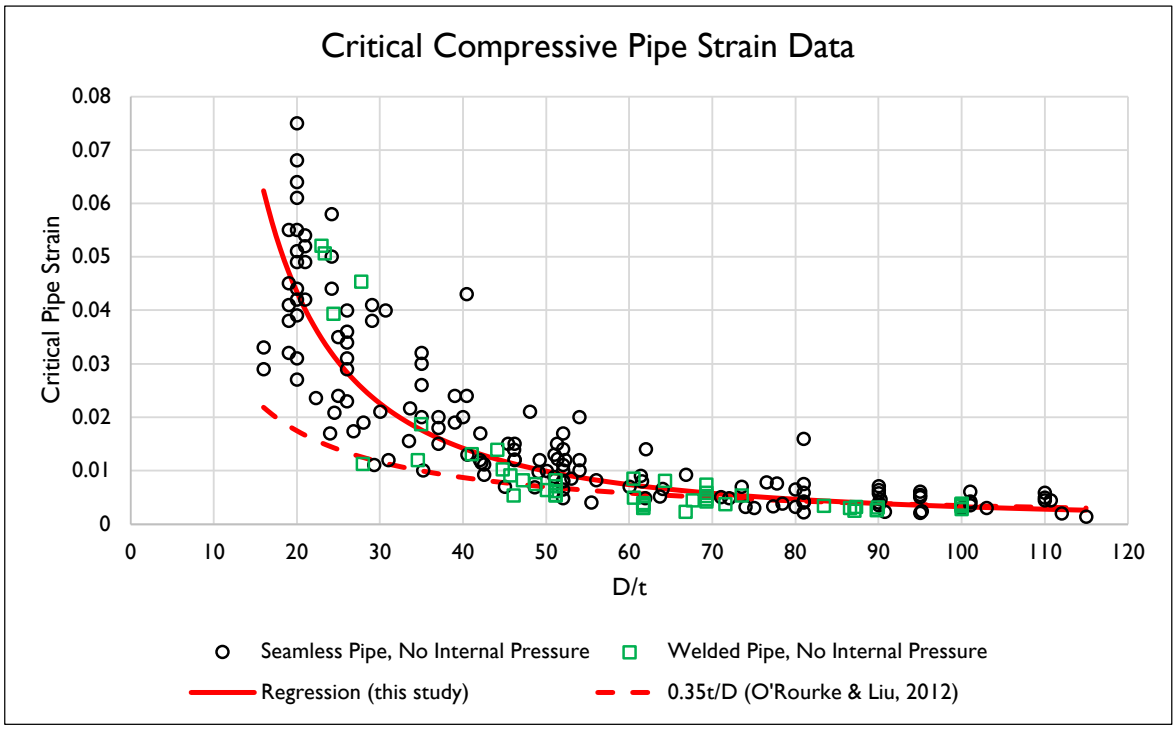

Figure 5.7: Critical Compressive Strain Data Corresponding to the Onset of Pipe Wall Wrinkling Plotted Against the Pipe Diameter to Wall Thickness (D/t) Ratio (Test Data Compiled by Mohr, 2003; Regression Equation (5.5) from this Study)

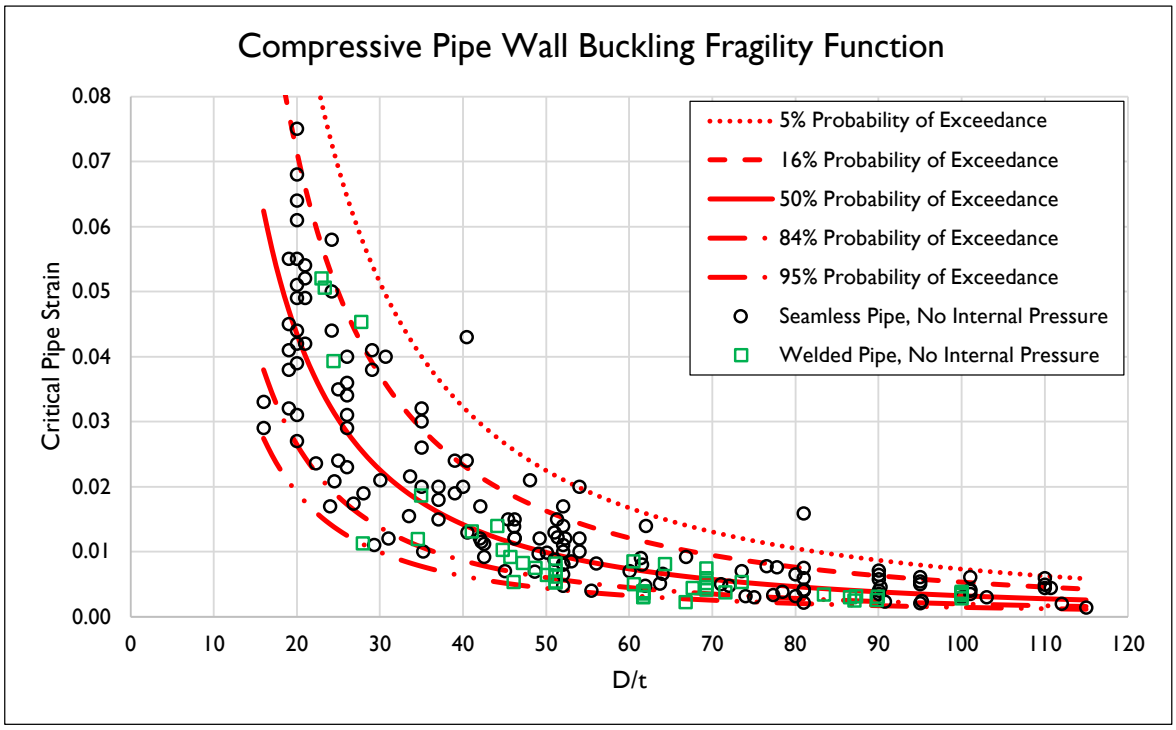

Figure 5.8: 95%, 84%, 50%, 16%, and 5% Probability of Exceedance Percentiles for the Compressive Pipe Wall Buckling Fragility Function Plotted on Arithmetic Scale (Test Data Compiled by Mohr, 2003; Fragility Function Equation (5.8) from this Study)

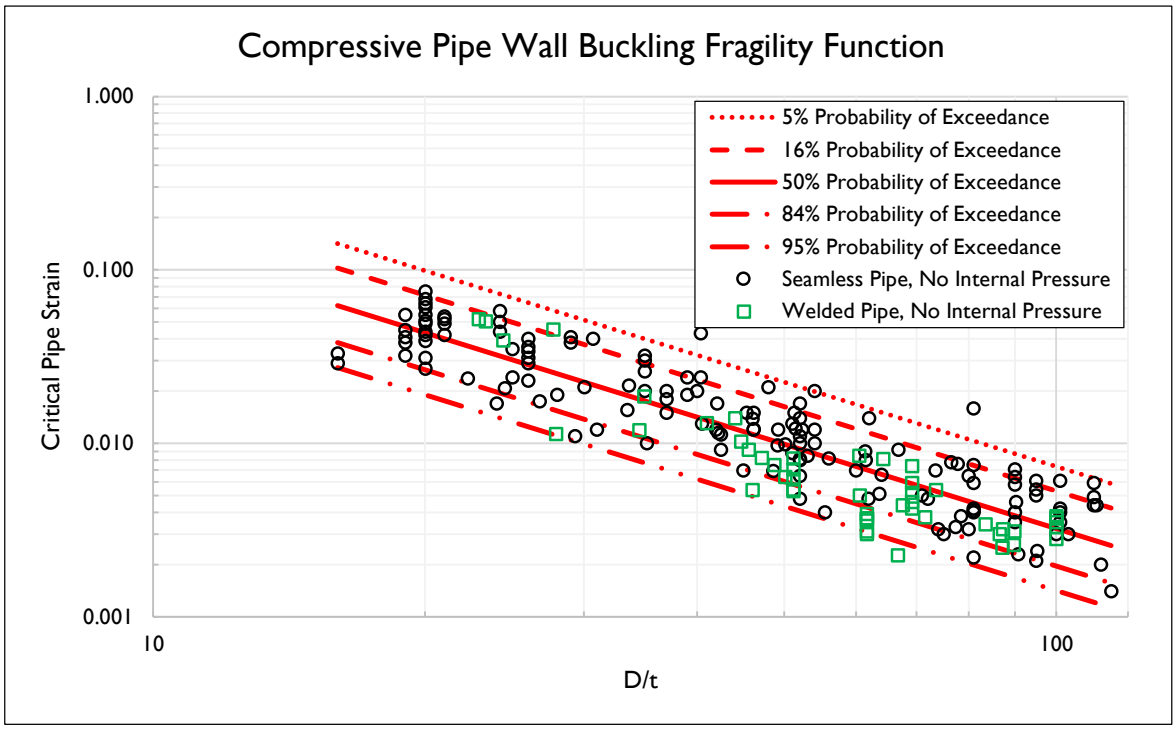

Figure 5.9: 95%, 84%, 50%, 16%, and 5% Probability of Exceedance Percentiles for the Compressive Pipe Wall Buckling Fragility Function Plotted on Logarithmic Scale (Test Data Compiled by Mohr, 2003; Fragility Function Equation (5.8) from this Study)

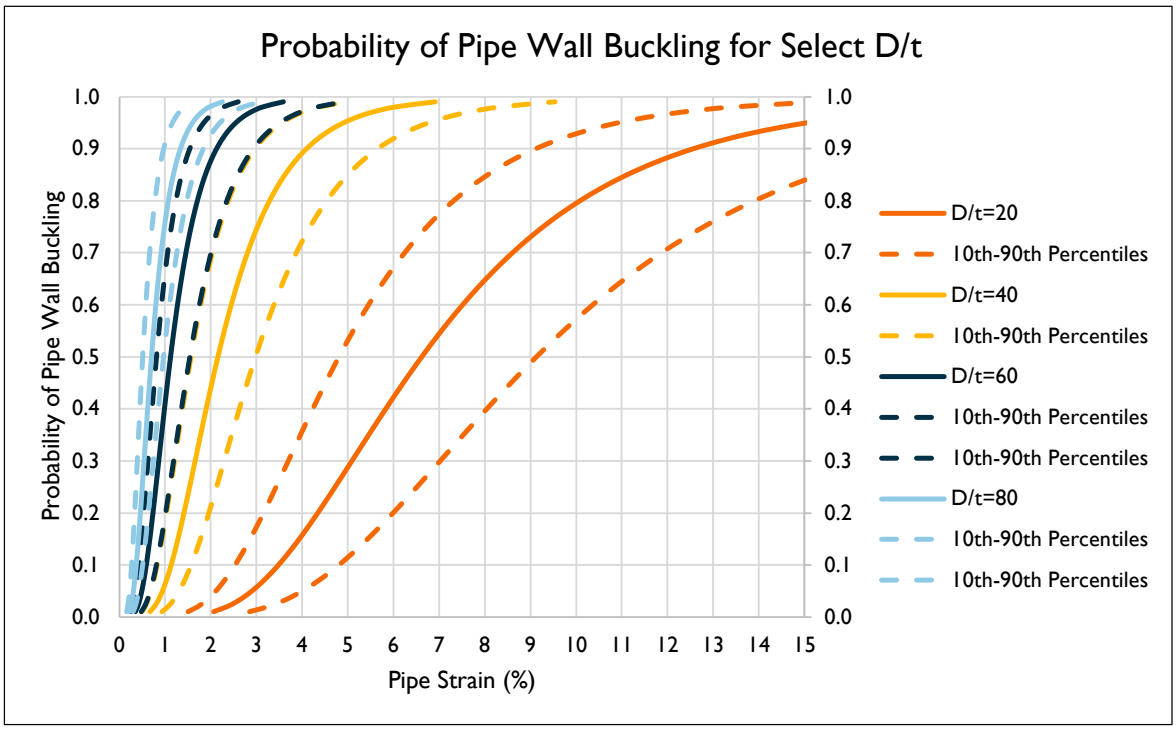

Figure 5.10: Compressive Pipe Wall Buckling Fragility Function (Equation (5.8)) Plotted for D/t Ratios of 80, 60, 40, and 20 on Arithmetic Scale

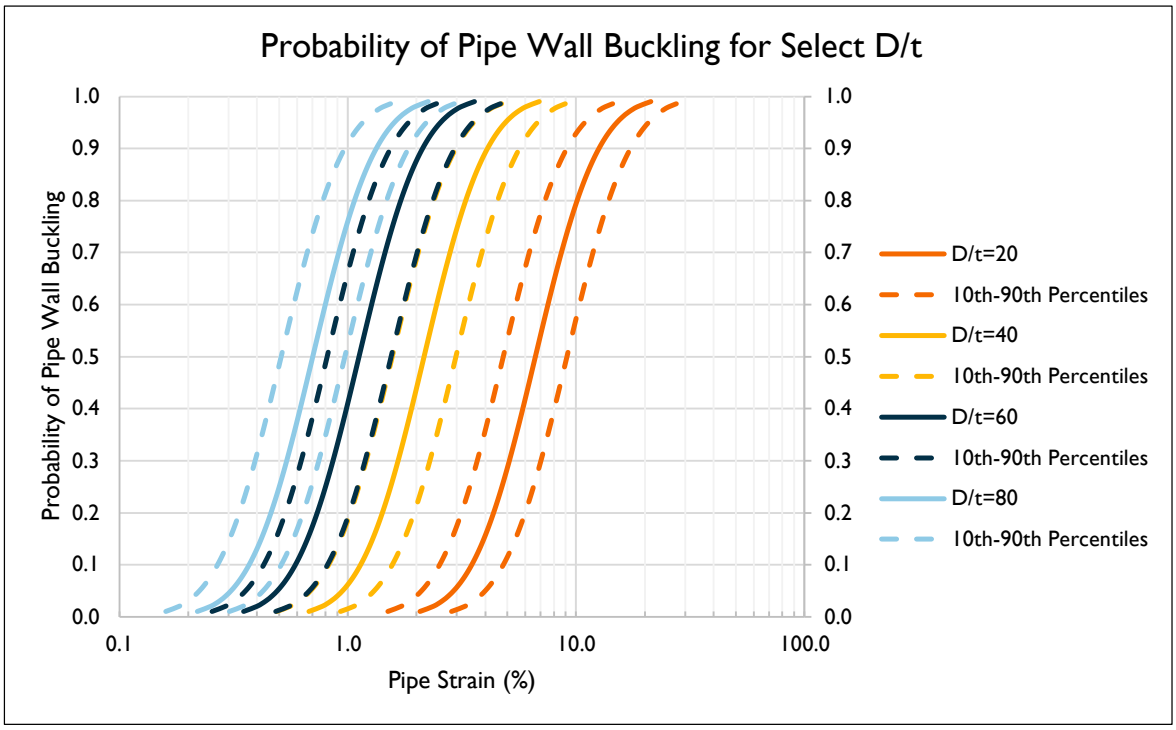

Figure 5.11: Compressive Pipe Wall Buckling Fragility Function (Equation (5.8)) Plotted for D/t Ratios of 80, 60, 40, and 20 on Logarithmic Scale

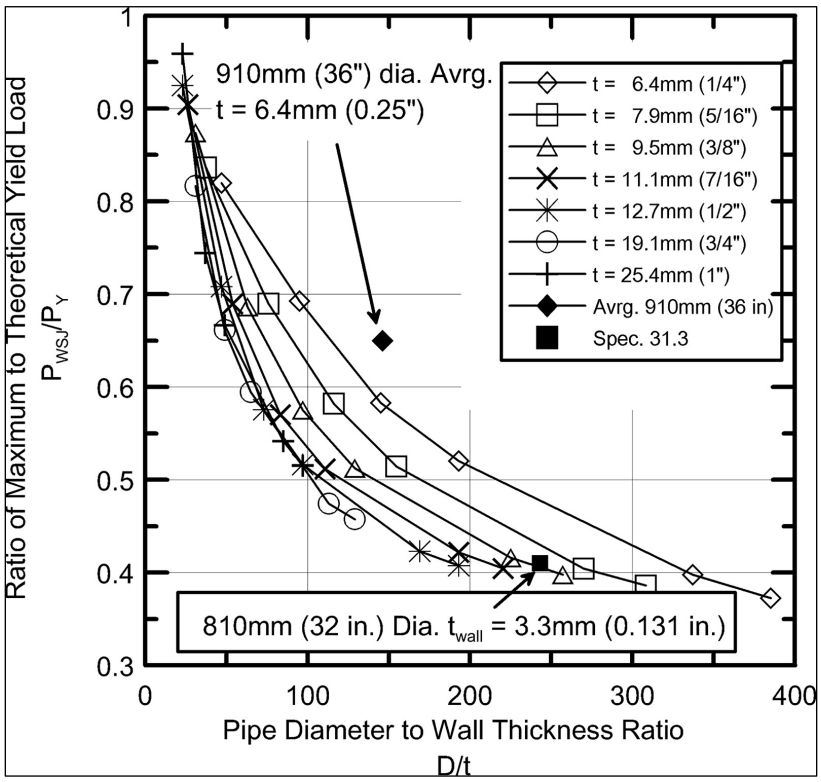

Figure 5.12: Design Chart to Estimate the Capacity of Welded Slip Joints with Internal Welds (from Mason et al., 2010)

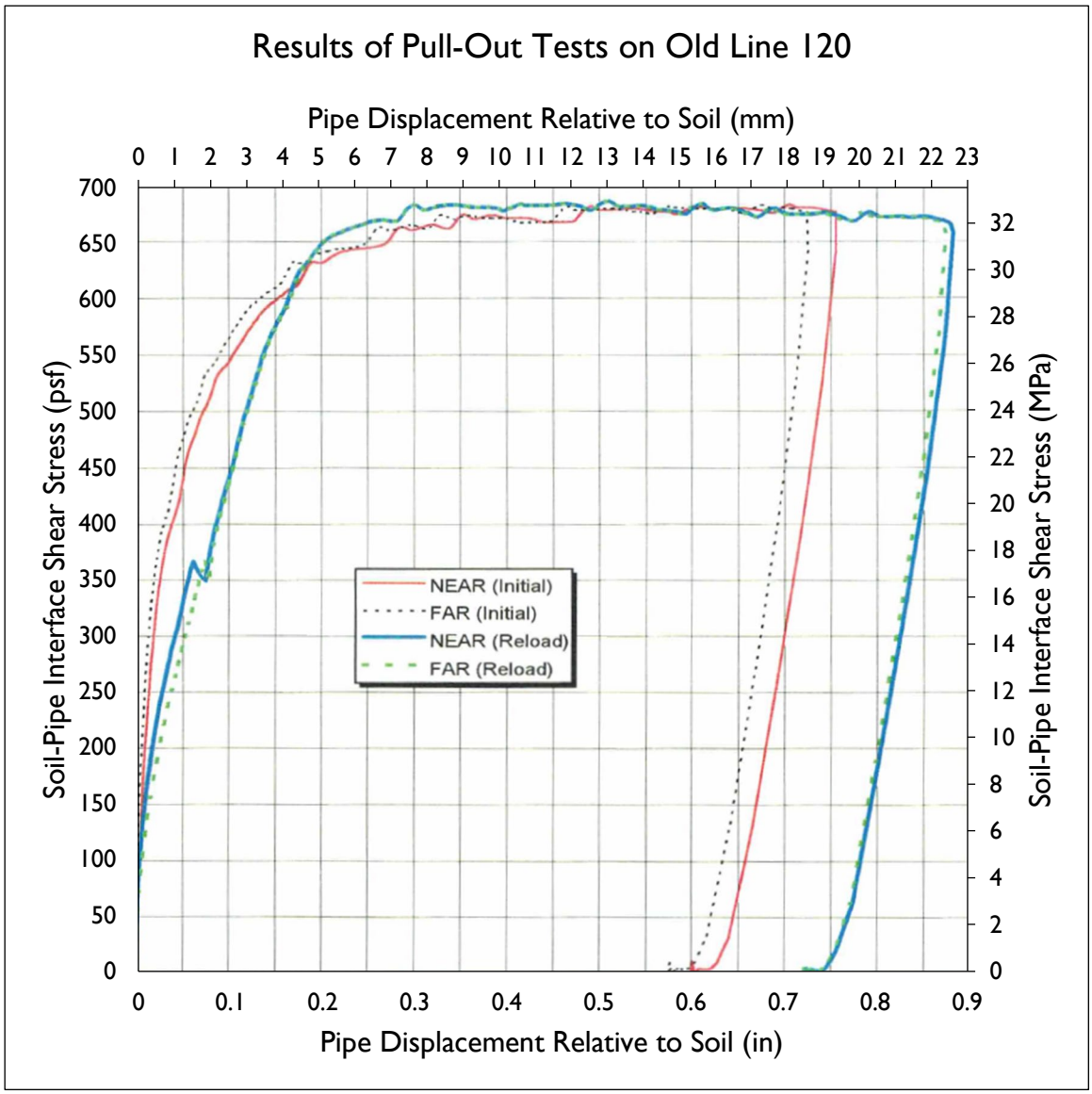

Figure 5.13: Results of the Pipe Jacking Tests on Old Line 120 at Balboa Boulevard (from SoCalGas & PG&E, 2000)

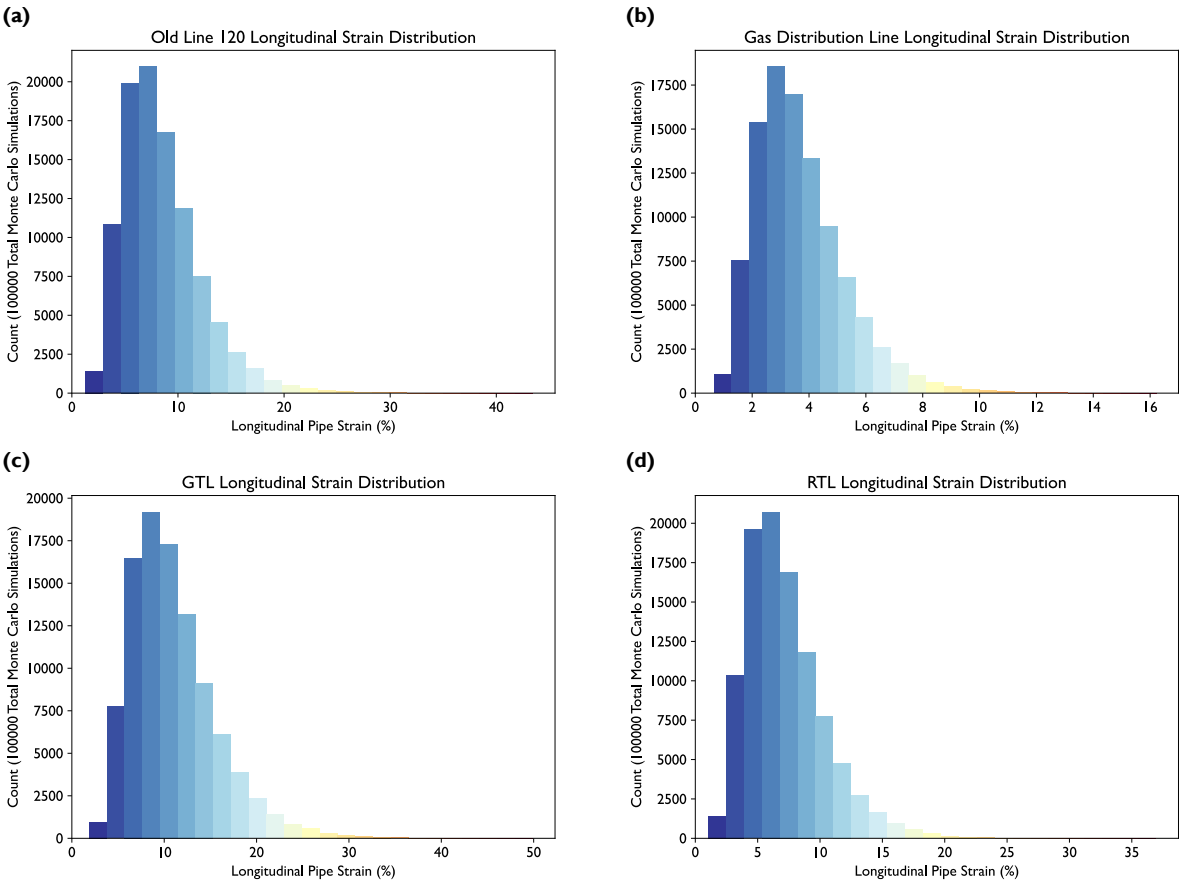

Figure 5.14: Distributions of Modeled Pipe Strain at the Tensile and Compressive Deformation Zones for (a) Old Line 120, (b) Gas Distribution Line, (c) the Granada Trunk Line, and (d) the Rinaldi Trunk Line

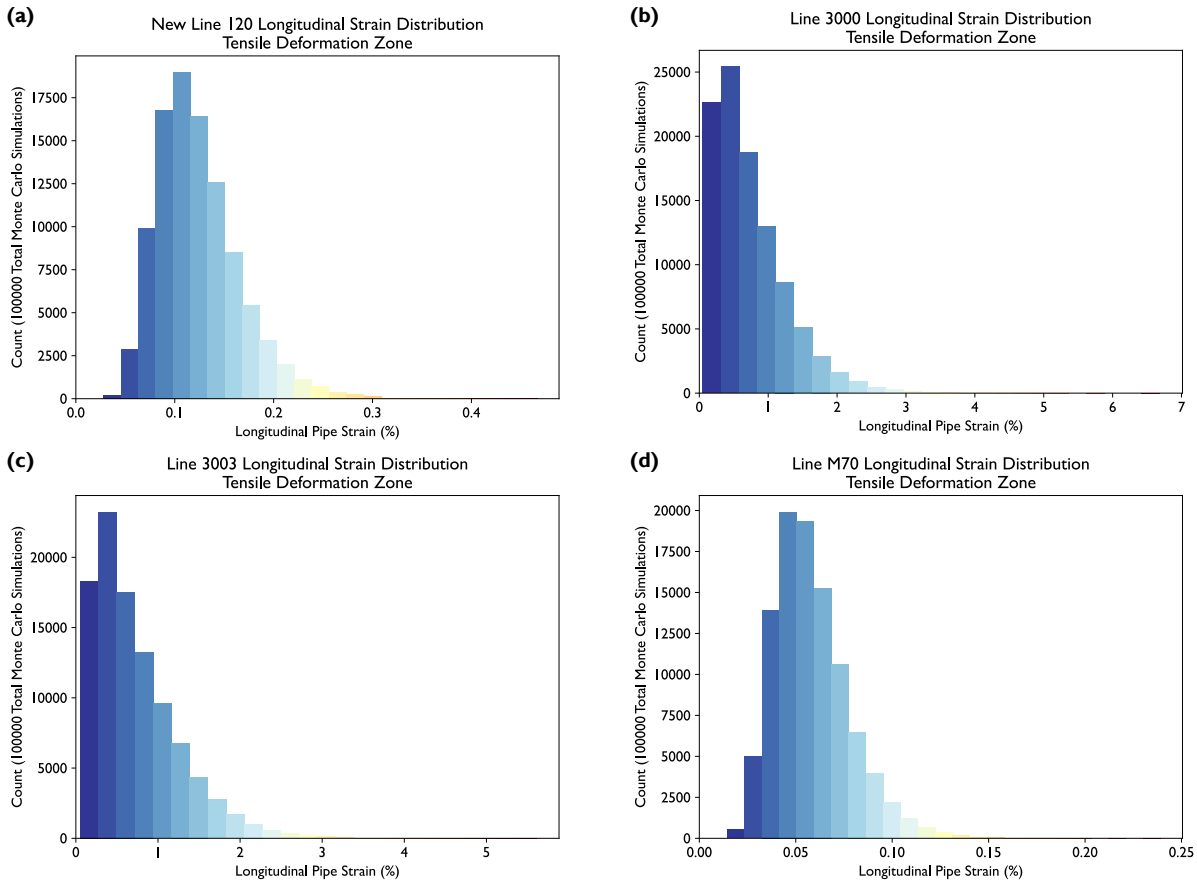

Figure 5.15: Distribution of Modeled Pipe Strain at the Tensile Deformation Zone for (a) New Line 120, (b) Line 3000, (c) Line 3003, and (d) Mobil Oil Line M70

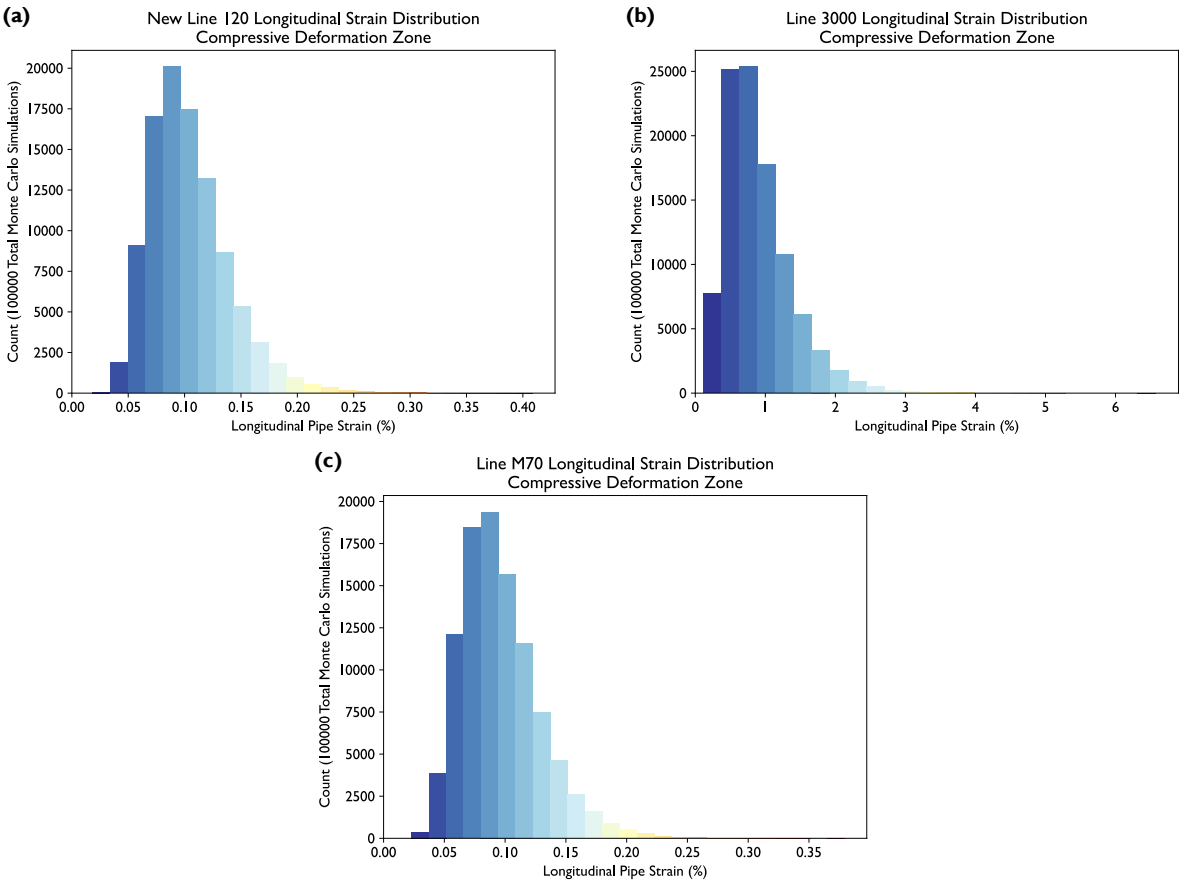

Figure 5.16: Distribution of Modeled Pipe Strain at the Compressive Deformation Zone for (a) New Line 120, (b) Line 3000, and (c) Mobil Oil Line M70

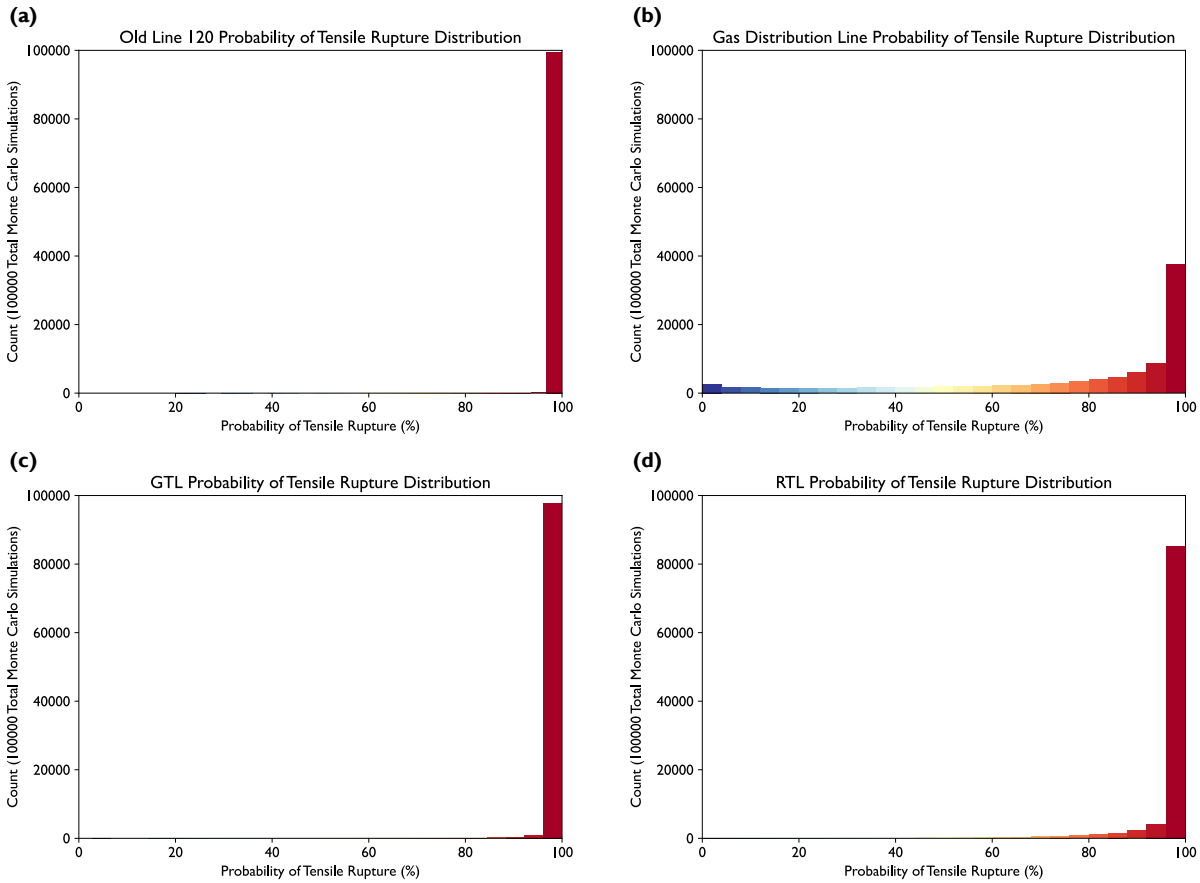

Figure 5.17: Distributions of Modeled Probability of Tensile Rupture at the Tensile Deformation Zone for (a) Old Line 120, (b) Gas Distribution Line, (c) the Granada Trunk Line, and (d) the Rinaldi Trunk Line

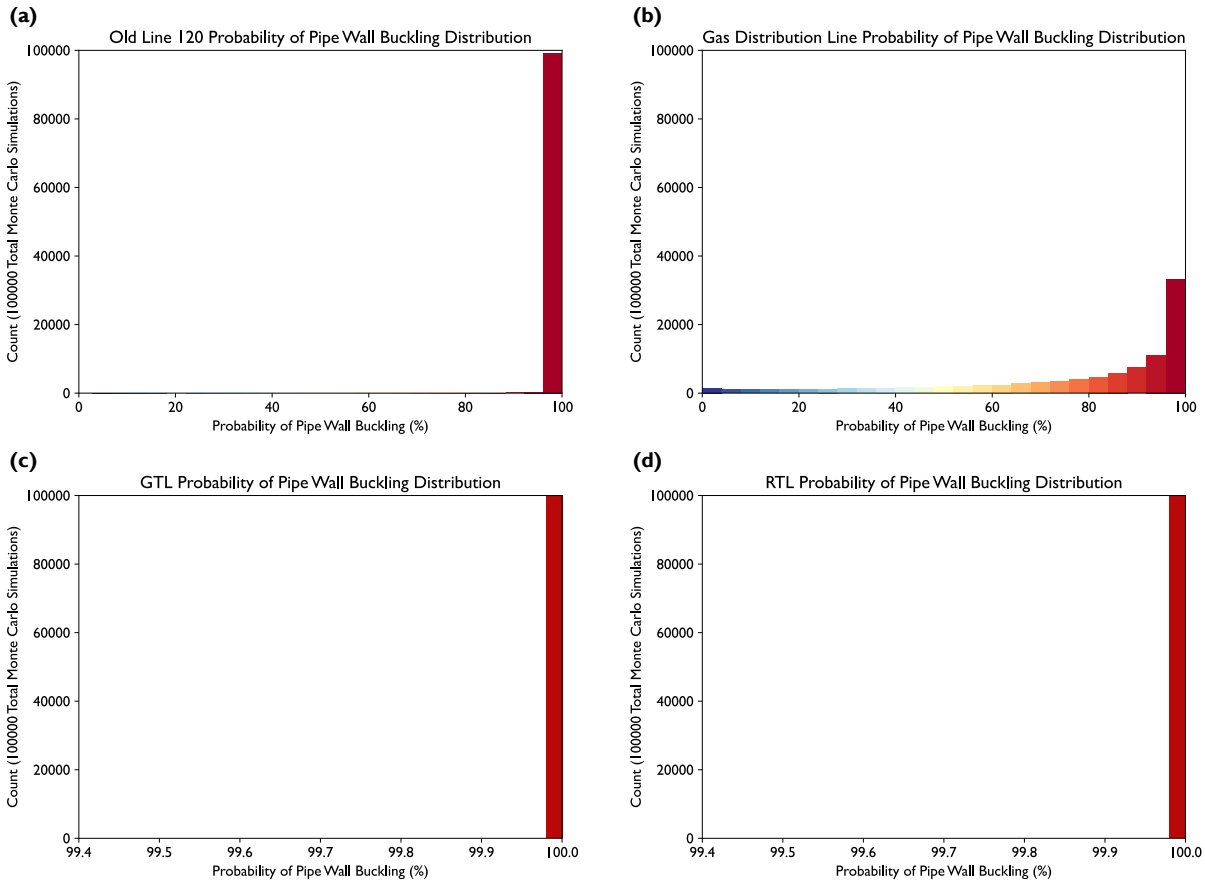

Figure 5.18: Distributions of Modeled Probability of Tensile Rupture at the Tensile Deformation Zone for (a) New Line 120, (b) Line 3000, (c) Line 3003, and (d) Mobil Oil Line M70

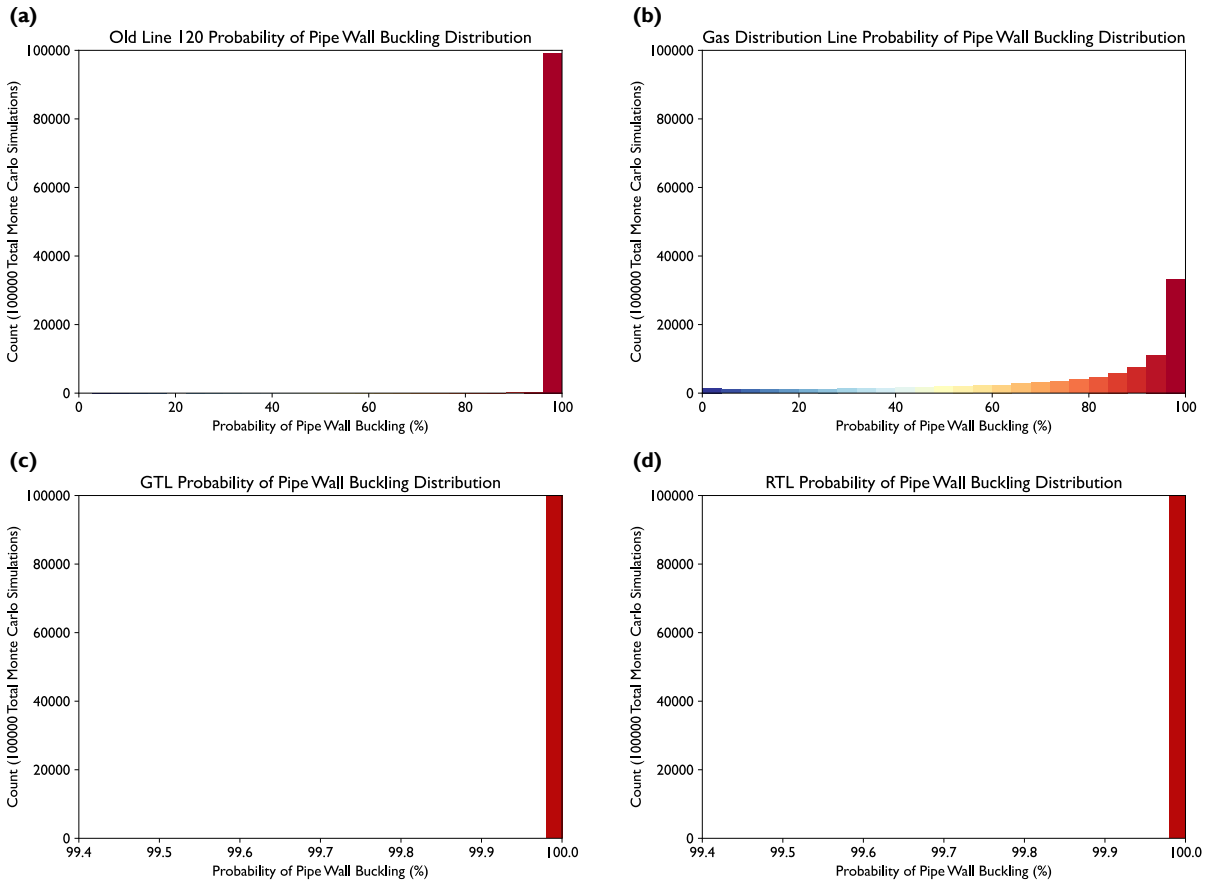

Figure 5.19: Distribution of Modeled Probability of Compressive Pipe Wall Buckling at the Compressive Deformation Zone for (a) Old Line 120, (b) Gas Distribution Line, (c) the Granada Trunk Line, and (d) Rinaldi Trunk Line

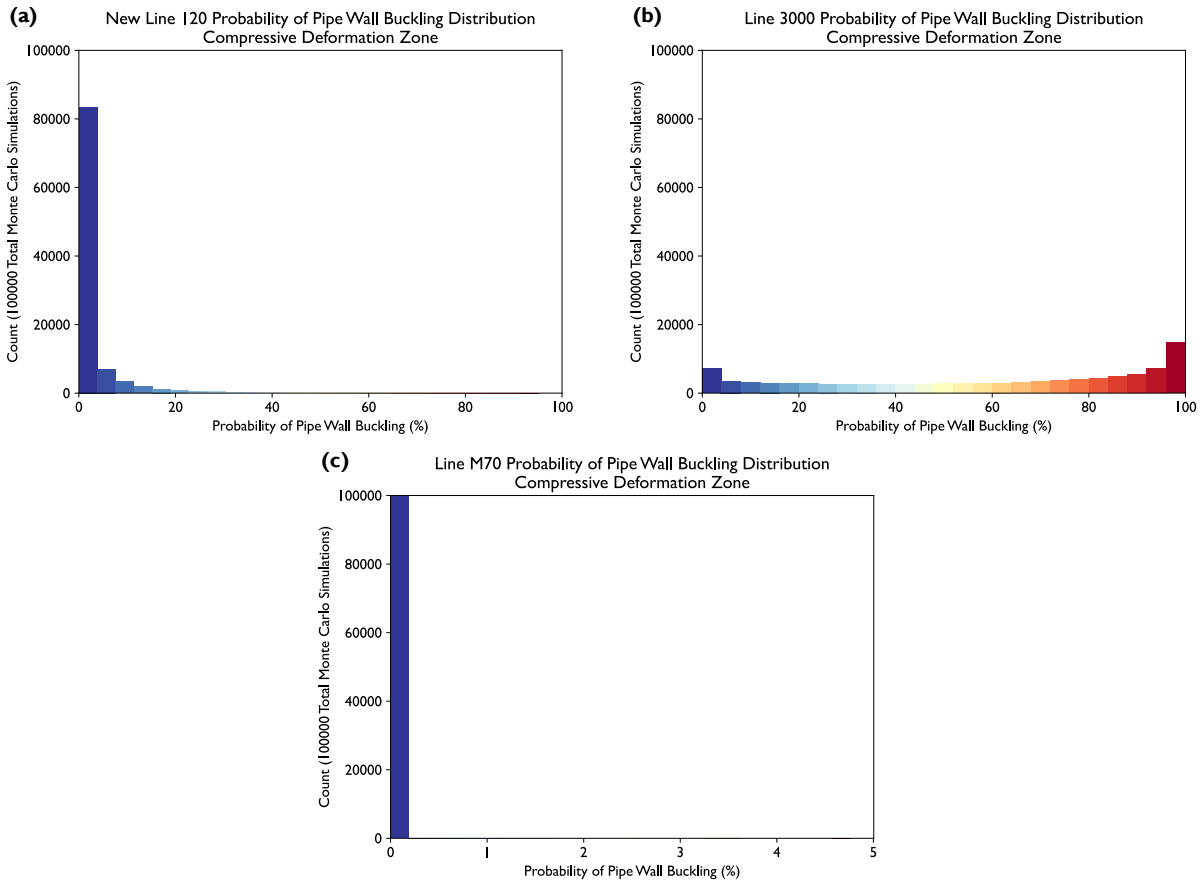

Figure 5.20: Distribution of Modeled Probability of Compressive Pipe Wall Buckling at the Compressive Deformation Zone for (a) New Line 120, (b) Line 3000, (c) Line 3003, and (d) Mobil Oil Line M70

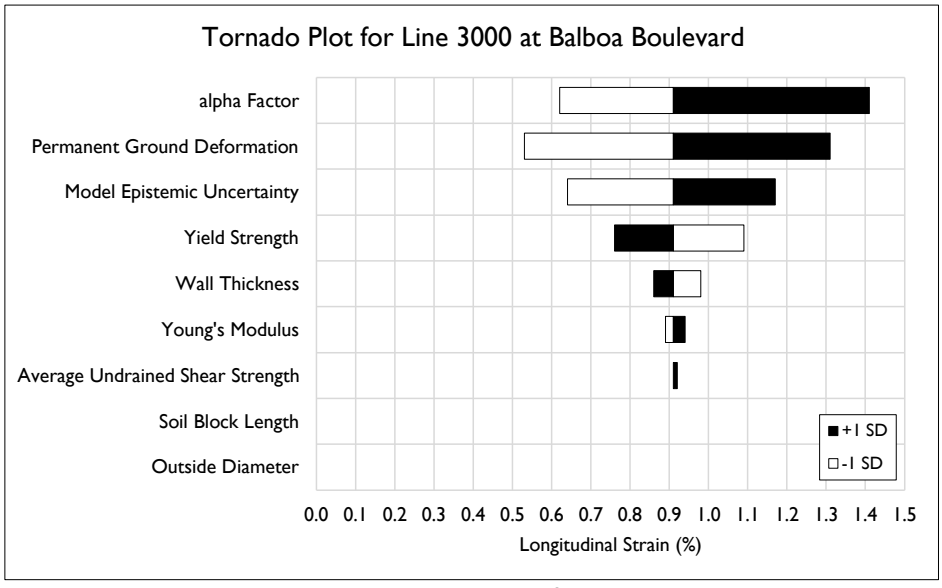

Figure 5.21: Tornado Plot for Line 3000

6 CONCLUSIONS

6.1 SUMMARY

The research described in this dissertation was performed during development of the Open Seismic Risk Assessment (*OpenSRA*) software tool. The *OpenSRA* tool implements the Pacific Earthquake Engineering Research (PEER) center's Performance-Based Earthquake Engineering (PBEE) risk assessment methodology. The tool is required to assess the seismic risk to natural gas infrastructure, including buried pipelines, at the statewide to site-specific scales. A comprehensive literature review was performed to identify methods for evaluating the seismic ground failure hazard from liquefaction-induced displacement and seismic slope instability. Gaps in the relevant literature were identified and were a focus of original research. Additional research focused on validating the *OpenSRA* tool at select demonstration sites including Balboa Boulevard in the San Fernando Valley.

OpenSRA implements data and methods for assessing seismic permanent ground deformation (PGD) at the statewide to site-specific scales. Due to differences in the types of data and methods available for estimating seismic displacement at the statewide versus the site-specific scale, four data and analysis levels were created: Level 1 analyses assess the seismic risk to natural gas transmission pipelines from ground failure at a uniform resolution across the state of California, Level 2 analyses utilize data available at regional scales at higher resolution compared to Level 1, Level 3 analyses utilize site-specific data including subsurface data, and Level 4 analyses employ state-of-the-art numerical simulations which require advanced laboratory testing to calibrate. Level 4 analyses are beyond the current scope of *OpenSRA*.

Through this research, a new method was developed for probabilistically evaluating the liquefaction-induced lateral spread displacement hazard at regional scales. The method uses site-specific cone penetration test (CPT) data to create models that estimate the probability that the lateral displacement index (LDI) is essentially zero (i.e., LDI < 3), and the mean, non-zero LDI given surficial geology, depth-to-groundwater (GWT), and peak ground acceleration (PGA). Combining maps of surficial geology, topography, GWT, and PGA with the model equations derived in this study, the lateral spread displacement hazard can be probabilistically assessed at regional scales. The method was applied in two regions: 1) the San Francisco Bay area of California and validated for the 1989 M_w 6.9 Loma Prieta earthquake, and 2) Christchurch, New Zealand and validated for the 2010 M_w 7.1 Darfield and 2011 M_w 6.2 Christchurch earthquakes. In both regions, the method provided reasonable estimates of both the spatial extent and magnitude of liquefaction-induced lateral spread displacements.

Validation of the *OpenSRA* tool was performed at several demonstration sites, the most important being the Balboa Boulevard site in the San Fernando Valley of Southern California. The site experienced strong ground motions during the 1971 San Fernando and 1994 Northridge earthquakes. Liquefaction-induced lateral spread displacement during the 1994 Northridge earthquake ruptured four pipelines, including a natural gas transmission pipeline. No seismic ground failure occurred in 1971 due to depressed groundwater at the time. The strain response of the pipelines was evaluated following two methodologies: 1) in a convention manner using mean estimates for the soil-pipeline system parameters including the pipe yield strength, the soil-pipeline interface shear strength, and the critical tensile and compressive strains, and 2) in a probabilistic framework that evaluated the aleatory variability and epistemic uncertainty of the soil-pipeline system with Monte Carlo simulations using the validated analytical models to calculate

longitudinal pipe strain. The results show generally good agreement between the expected and observed seismic performance of the buried pipelines. This good comparison provides confidence in the uncertainty estimates employed in the *OpenSRA* tool.

6.2 FINDINGS

6.2.1 Seismic Ground Failure Hazard Demands Affecting Buried Pipeline Performance

Data and methods for assessing seismic ground failure at the statewide to site-specific scales were identified and implemented in the *OpenSRA* software tool. Keys findings from the study include:

- Four data and analysis levels were created to assess the seismic ground failure hazard at the statewide to site-specific scales. Level 1 analyses assess seismic ground failure at the statewide scale, Level 2 analyses assess seismic ground failure at regional scales with data collected at a higher resolution compared to Level 1, and Level 3 analyses are informed by site-specific data. Level 4 analyses employ state-of-the-art numerical simulations which require advanced laboratory testing to calibrate the material constitutive models. Level 4 analyses are beyond the current scope of *OpenSRA*.
- A review of the relevant literature identified a lack of methods for estimating the liquefaction-induced lateral spread displacement at regional scales.

6.2.2 Regional Scale Probabilistic Procedure for Estimating Lateral Spread Displacements

A new method was developed for probabilistically estimating the liquefaction-induced lateral spread displacement hazard at regional scales. The method was applied in the San Francisco Bay area of California and in Christchurch, New Zealand. Validation of the method using data from three earthquakes demonstrates its proficiency in estimating the spatial extent and magnitude of potential lateral spread displacement and its uncertainty. Key findings from the study include:

- Other methods for assessing the liquefaction hazard at regional scales often do not include an assessment of the potential consequences of liquefaction (i.e., lateral spread displacement). There was a need for a method that quantitatively assesses the lateral spread displacement hazard and its uncertainty at regional scales that this research addressed.
- Two corrections are shown to reduce overestimation of the lateral spread displacement hazard: 1) a depth weighting factor (DWF) to limit the contribution of deep liquefiable layers to the liquefaction hazard, and 2) a factor equal to the proportion of a geologic unit estimated to be susceptible to surface manifestations of liquefaction. The second factor corrects for sites with non-zero LDI (i.e., LDI > 3) and topographic conditions conducive to lateral spread displacement (i.e., topographic slopes between 0.1% and 5% and free-face ratios between 1 and 50) that do not experience lateral spread displacement.
- Consideration of topography is essential to estimate reasonably the lateral spread displacement hazard. Topographic slope can be estimated reliably using digital elevation models (DEMs). A method to estimate the free-face ratio at regional scales was developed for sites near a free-face feature. Regional scale methods that do not consider topography (i.e., Hazus, 2020) are less reliable.

6.2.3 *Pipeline Response to Seismic Displacement at Balboa Boulevard during the 1994 Northridge Earthquake*

The performance of the pipelines at Balboa Boulevard undergoing seismic permanent ground displacement (PGD) during the 1994 Northridge earthquake was evaluated in a conventional manner (i.e., no uncertainty in the mean properties was considered). The Balboa Boulevard site experienced about 0.5 m of PGD due to the 1994 Northridge earthquake. Four pipelines ruptured in both tension and compression while four others were undamaged. The study evaluated the longitudinal strain response of the pipelines and shows good agreement between their expected and observed performance. No pipelines failed in 1971 because no PGD was observed at the site after the San Fernando earthquake. Key findings from the study include:

- The four pipelines that ruptured in tension and compression (the Old Line 120 natural gas transmission line, a gas distribution line, and the Granada and Rinaldi Water Trunk Lines) are estimated to have the highest longitudinal strains and consequently the highest likelihood of tensile and compressive failures.
- The expected performance of natural gas transmission line 3000 does not align with its observed performance in the compressive deformation zone. This may be due to several factors that have significant uncertainty, including: 1) the soil-pipeline interface shear stress, 2) the estimated critical compressive strain, 3) the pipe steel yield stress, and 4) the amount of ground displacement. Additionally, the model of O'Rourke & Liu (2012) considers abrupt displacements at the margins of the soil block, which may overestimate the strain.
- The pipelines buried in sandy backfill (i.e., New Line 120, Mobil Oil Line M70) are estimated to have experienced the lowest longitudinal strains due to their low interface shear stress. The pipelines buried in clayey backfill are estimated to have significantly higher interface shear stress.

6.2.4 *Probabilistic Assessment of the Pipeline Response to Seismic Displacement at Balboa Boulevard during the 1994 Northridge Earthquake*

The performance of the buried pipelines at Balboa Boulevard to the seismic PGD experienced during the 1994 Northridge earthquake was assessed in a probabilistic framework. The aleatory variability and epistemic uncertainty of the soil-pipeline system parameters is estimated. A distribution of the strain response for each pipeline is achieved through Monte Carlo simulations using a validated analytical model. New fragility functions for assessing the performance of the pipelines in response to tensile or compressive strains developed in them are proposed. The expected and observed performance of the pipelines during the 1994 Northridge earthquake shows good agreement. Key findings of the study include:

- There is significant uncertainty in the soil-pipeline interface shear stress, the critical tensile and compressive strains, the steel yield stress particularly for the lines constructed with X-grade steel, and the amount of PGD. Reducing the uncertainty in these variables is important for reducing the total uncertainty of the assessment.
- The assessment of Line 3000 in the compressive deformation zone shows significant uncertainty in the performance of this pipeline. The 5^{th} to 95^{th} probability of pipe wall buckling ranges from low (i.e., ~10%) to high (i.e., 100%). The seismic performance of

this pipeline is highly sensitive to the soil-pipeline interface shear stress, the critical compressive strain, the yield stress (assumed to equal its specified minimum value), and the magnitude of PGD. Additionally, the model of O'Rourke & Liu (2012) considers a soil block with abrupt displacements at the margins of the displacement, which may overestimate the longitudinal strain.

- New fragility functions consider the aleatory variability and epistemic uncertainty in the pipeline performance in response to longitudinal strain.
- This study demonstrates the value of probabilistic assessments. This framework properly considers all sources of uncertainty, shows the range of possible results, and highlights the data that can collected to reduce uncertainty and increase reliability. The results of this study confirm the viability of the way *OpenSRA* characterizes key sources of uncertainty.

6.3 FUTURE RESEARCH

Future research recommendations to advance the state-of-knowledge and engineering practice for regional scale assessments of the liquefaction-induced lateral spread displacement hazard and the evaluation of buried pipelines in response to seismic ground failure include:

- The proposed regional scale liquefaction-induced lateral spread displacement method requires CPT data across a region that will be assessed to be publicly available. These data are readily available in parts of the San Francisco Bay and are widely available in Christchurch. However, CPT data are not commonly available publicly in other regions, such as the Los Angeles basin. Further research should focus on collecting informative CPT data in other seismically active regions and sharing these data publicly.
- In the San Francisco Bay area, the method should also be evaluated for the 2014 M_w 6.0 South Napa earthquake. In the Christchurch area, the method should also be evaluated for the June 13, 2011 M_w 6.0 and the December 23, 2011 M_w 5.8 and M_w 5.9 earthquakes.
- The method should be applied in an analysis of the *HayWired* scenario (USGS, 2017) to examine how the simulated ground shaking from a major earthquake on the Hayward Fault affects ground failure and the seismic performance of the buried pipelines in the San Francisco Bay area.
- The complete strain response of the buried pipelines at Balboa Boulevard to the seismic PGD produced by the 1994 Northridge earthquake should be evaluated using numerical modeling tools such as Abaqus. In particular, the soil-pipeline interaction and the strain response at pipe elbows is complex and requires numerical modeling tools to evaluate well.

REFERENCES

American Lifelines Alliance (ALA). (2001). Seismic Fragility Formulations for Water Systems, Part 1 – Guideline. ASCE.

American Pipeline Institute (API). (2018). Specification 5L. 46th Edition.

American Society for Testing and Materials (ASTM). (2017). Standard A283 Specification for Low and Intermediate Tensile Strength Carbon Steel Plates. ASTM International, West Conshohocken, PA. https://doi.org/10.1520/A0283_A0283M-03.

American Society of Civil Engineers (ASCE). (1984). Guidelines for the Seismic Design of Oil and Gas Pipeline Systems. Committee on Gas and Liquid Fuel Lifeline, ASCE, Reston, VA.

Argyrou, C., Bouziou, D., O'Rourke, T. D., & Stewart, H. E. (2018). Retrofitting Pipelines with Cured-in-Place Linings for Earthquake-Induced Ground Deformations. Soil Dynamics and Earthquake Engineering, 115, 156–168. doi.org/10.1016/j.soildyn.2018.07.015.

Bain, C. A., & Bray, J. D. (2023). Regional Scale Probabilistic Procedure for Estimating Lateral Spread Displacements. Soil Dynamics and Earthquake Engineering, 171, 107928. https://doi.org/10.1016/j.soildyn.2023.107928.

Bain, C. A., O'Rourke, T. D., & Bray, J. D. (2023a). Pipeline Response to Seismic Displacement at Balboa Boulevard during the 1994 Northridge Earthquake. Under Review.

Bain, C. A., O'Rourke, T. D., & Bray, J. D. (2023b). Probabilistic Assessment of the Pipeline Response to Seismic Displacement at Balboa Boulevard during the 1994 Northridge Earthquake. In Preparation.

Bay Area Open Space Council (2008). Streams: San Francisco Bay Area, California, 2008. [Shapefile]. San Francisco Bay Area Upland Habitat Goals Project. Retrieved October 1, 2021, from https://maps.princeton.edu/catalog/stanford-km172ps5456.

Bedrossian, T. L., Roffers, P., Hayhurst, C. A., Lancaster, J. T., & Short, W. R. (2012). Geologic Compilation of Quaternary Surficial Deposits in Southern California (Special Report 217). Department of Conservation, California Geological Survey, Sacramento.

Befus, K. M., Barnard, P. L., Hoover, D. J., Finzi Hart, J. A., & Voss, C. I. (2020). Increasing Threat of Coastal Groundwater Hazards from Sea-Level Rise in California. Nature Climate Change, 10(10), 946–952. https://doi.org/10.1038/s41558-020-0874-1.

Bennett, M. J., Ponti, D. J., Tinsley, J. C., Holzer, T. L., & Conaway, C. H. (1998). Subsurface Geotechnical Investigations Near Sites of Ground Deformation Caused by the January 17, 1994, Northridge, California, Earthquake. Open-File Report. https://doi.org/10.3133/ofr98373.

Blevins, G. (2010). Explosion of 20" Gas Main and Rupture of 56" DWP Water Main. [Photograph]. Los Angeles Fire Department Historical Archive. LAFD. Retrieved March 19, 2023, from https://www.lafire.com/famous_fires/1994-0117_NorthridgeEarthquake/1994-0117_GleneBlevinsPhotos.htm (Originally photographed 17 January 1994).

Boulanger, R. W., & Idriss, I. M. (2014). CPT and SPT Based Liquefaction Triggering Procedures. Report No. UCD/CGM-14/01, Center for Geotechnical Modeling, Department of Civil and Environmental Engineering, University of California, Davis, CA.

Boulanger, R. W., & Idriss, I. M. (2016). CPT-Based Liquefaction Triggering Procedure. Journal of Geotechnical and Geoenvironmental Engineering, 142(2), 04015065. https://doi.org/10.1061/(asce)gt.1943-5606.0001388.

Boulanger, R. W., & Ziotopoulou, K. (2017). PM4Sand (version 3.1): A Sand Plasticity Model for Earthquake Engineering Applications. Rep. No. UCD/CGM-17/01. Davis, CA: Univ. of California.

Boulanger, R. W., & Ziotopoulou, K. (2018). PM4Silt (version 1): A Silt Plasticity Model for Earthquake Engineering Applications. Rep. No. UCD/CGM-18/01. Davis, CA: Univ. of California.

Boulanger, R. W., & Ziotopoulou, K. (2019). A Constitutive Model for Clays and Plastic Silts in Plane-Strain Earthquake Engineering Applications. Soil Dynamics and Earthquake Engineering, 127, 105832. https://doi.org/10.1016/j.soildyn.2019.105832.

Bradley, B. A., & Hughes, M. (2012). Conditional Peak Ground Accelerations in the Canterbury Earthquakes for Conventional Liquefaction Assessment. Technical Report for the Ministry of Business, Innovation and Employment.

Bradley, B., Maurer, B., Geyin, M., Green, R., & van Ballegooy, S. (2020). CPT-Based Liquefaction Case Histories Resulting from the 2010-2016 Canterbury, New Zealand, Earthquakes: A Curated Digital Dataset (Version 2). DesignSafe-CI. https://doi.org/10.17603/ds2-tygh-ht91.

Bray, J. D. (2007). Simplified Seismic Slope Displacement Procedures. In Earthquake Geotechnical Engineering: 4th International Conference on Earthquake Geotechnical Engineering: Invited Lectures (pp. 327–353). Springer.

Bray, J. D., & Macedo, J. (2019). Procedure for Estimating Shear-Induced Seismic Slope Displacement for Shallow Crustal Earthquakes. Journal of Geotechnical and Geoenvironmental Engineering, 145(12). https://doi.org/10.1061/(asce)gt.1943-5606.0002143.

Bray, J. D., & Macedo, J. (2021). Closure to 'Procedure for Estimating Shear-Induced Seismic Slope Displacement for Shallow Crustal Earthquakes'. Journal of Geotechnical and Geoenvironmental Engineering, 147(5). https://doi.org/10.1061/(ASCE)GT.1943-5606.0002143.

Bray, J. D., & Travasarou, T. (2007). Simplified Procedure for Estimating Earthquake-Induced Deviatoric Slope Displacements. Journal of Geotechnical and Geoenvironmental Engineering, 133(4), 381–392. https://doi.org/10.1061/(asce)1090-0241(2007)133:4(381)

Bray, J. D., Macedo, J., & Travasarou, T. (2018). Simplified Procedure for Estimating Seismic Slope Displacements for Subduction Zone Earthquakes. Journal of Geotechnical and Geoenvironmental Engineering, 144(3). https://doi.org/10.1061/(asce)gt.1943-5606.0001833.

California Department of Fish and Wildlife (CDFW). (n.d.). Average Annual Precipitation (Inches): California, 1981-2010 (800m). [GIS Raster Image Dataset]. California Department of Fish and Wildlife. Retrieved June 15, 2020, from http://purl.stanford.edu/cp513wz4565.

CERA (2014). Verification of LiDAR Acquired Before and After the Canterbury Earthquake Sequence. Technical Specification 03. Canterbury Earthquake Recovery Authority. Retrieved September 22, 2022, from https://www.nzgd.org.nz/.

Cetin, K. O., Bilge, H. T., Wu, J., Kammerer, A. M., & Seed, R. B. (2009). Probabilistic Model for the Assessment of Cyclically Induced Reconsolidation (Volumetric) Settlements. Journal of Geotechnical and Geoenvironmental Engineering, 135(3), 387–398. https://doi.org/10.1061/(asce)1090-0241(2009)135:3(387).

Cetin, K. O., Seed, R. B., Der Kiureghian, A., Tokimatsu, K., Harder, L. F., Kayen, R. E., & Moss, R. E. (2004). Standard Penetration Test-Based Probabilistic and Deterministic Assessment of Seismic Soil Liquefaction Potential. Journal of Geotechnical and Geoenvironmental Engineering, 130(12), 1314–1340. https://doi.org/10.1061/(asce)1090-0241(2004)130:12(1314).

Cetin, K. O., Seed, R. B., Kayen, R. E., Moss, R. E. S., Bilge, H. T., Ilgac, M., & Chowdhury, K. (2018). SPT-Based Probabilistic and Deterministic Assessment of Seismic Soil Liquefaction Triggering Hazard. Soil Dynamics and Earthquake Engineering, 115, 698–709. https://doi.org/10.1016/j.soildyn.2018.09.012.

CGS (2010). Geologic Map of California. [Shapefile]. California Geological Survey, Retrieved June 1, 2020, from https://maps.conservation.ca.gov/cgs/gmc/.

Cornell, C. A. (1968). Engineering Seismic Risk Analysis. Bulletin of the Seismological Society of America, 58(5), 1583–1606. https://doi.org/10.1785/bssa0580051583.

Coutu, T. B. (2017). Development of a Performance-Based Procedure for Assessment of Liquefaction-Induced Lateral Spread Displacements using the Cone Penetration Test (thesis). Brigham Young University, Provo, UT.

Cubrinovski, M., & Robinson, K. (2016). Lateral Spreading: Evidence and Interpretation from the 2010–2011 Christchurch Earthquakes. Soil Dynamics and Earthquake Engineering, 91, 187–201. https://doi.org/10.1016/j.soildyn.2016.09.045.

Cubrinovski, M., Robinson, K., Taylor, M., Hughes, M., & Orense, R. (2012). Lateral Spreading and its Impacts in Urban Areas in the 2010–2011 Christchurch Earthquakes. New Zealand Journal of Geology and Geophysics, 55(3), 255–269. https://doi.org/10.1080/00288306.2012.699895.

Davis, C. A. (1999). Case Study of the Granada Trunk Line During Two Near-Field Earthquakes. Proceedings of the 7th US-Japan Workshop on Earthquake Resistant Design of Lifeline Facilities and Countermeasures for Soil Liquefaction, Seattle, WA, T. D. O'Rourke, J. P. Bardet, and M. Hamada, Eds., Tech. Rep. MCEER-99-0019, pp. 415-430.

Duncan, J. M. (2004). Strength of Sands and Gravels. Kenneth L. Lee Memorial Seminar. Long Beach, CA. April 28, 2004.

ESRI (2019a). USA Detailed Streams. [Shapefile]. Retrieved June 15, 2020, from https://www.arcgis.com/home/item.html?id=1e29e33360c8441bbb018663273a046e.

ESRI (2019b). USA State Boundaries. [Shapefile]. Retrieved June 15, 2020, from https://www.arcgis.com/home/item.html?id=44c9104ea1a94aeeadcca551b7749cc0.

Fan, Y., & Miguez-Macho, G. (2010). A Simple Hydrologic Framework for Simulating Wetlands in Climate and Earth System Models. Climate Dynamics, 37(1-2), 253-278. doi:10.1007/s00382-010-0829-8.

Faris, A. T., Seed, R. B., Kayen, R. E., & Wu, J. (2006). A Semi-Empirical Model for the Estimation of Maximum Horizontal Displacement Due to Liquefaction-Induced Lateral Spreading. Proceedings of the 8th U.S. National Conference on Earthquake Engineering. San Francisco, CA, 18 April 2006. Earthquake Engineering Research Institute (EERI).

FEMA (2020). Hazus 4.2 SP3 Technical Manual. Federal Emergency Management Agency. https://www.fema.gov/sites/default/files/2020-10/fema_hazus_earthquake_technical_manual_4-2.pdf.

Franke, K. W., & Kramer, S. L. (2014). Procedure for the Empirical Evaluation of Lateral Spread Displacement Hazard Curves. Journal of Geotechnical and Geoenvironmental Engineering, 140(1), 110–120. https://doi.org/10.1061/(asce)gt.1943-5606.0000969.

Fregoso, T. A., Wang, R-F., Altejevich, E., & Jaffe, B. E. (2017). San Francisco Bay-Delta Bathymetric/Topographic Digital Elevation Model (DEM). U.S. Geological Survey. https://doi.org/10.5066/F7GH9G27.

Gillins, D. T., & Bartlett, S. F. (2014). Multilinear Regression Equations for Predicting Lateral Spread Displacement from Soil Type and Cone Penetration Test Data. Journal of Geotechnical and Geoenvironmental Engineering, 140(4). https://doi.org/10.1061/(asce)gt.1943-5606.0001051.

Grant, A., Wartman, J., & Abou-Jaoude, G. (2016). Multimodal Method for Coseismic Landslide Hazard Assessment. Engineering Geology, 212, 146–160. doi: 10.1016/j.enggeo.2016.08.005.

Hatch, M. S. (2017). Development of a Performance-Based Procedure to Predict Liquefaction-Induced Free-Field Settlements for the Cone Penetration Test (thesis). Brigham Young University, Provo, UT.

Hecker, S., Ponti, D. J., Garvin, C. D., Powers, T. J., Fumal, T. E., Hamilton, J. C., Sharp, R. V., Prentice, C. S., & Cinti, F. R. (1995). Ground Deformation in Granada Hills and Mission Hills Resulting from the January 17, 1994, Northridge, California, Earthquake. Open-File Report. doi:10.3133/ofr9562.

Holzer, T. (1998). The Loma Prieta, California, Earthquake of October 17, 1989 – Liquefaction. U.S. Geological Survey Professional Paper 1551-B. https://doi.org/10.3133/pp1551B

Holzer, T. L., Bennett, M. J., Ponti, D. J., & Tinsley III, J. C. (1999). Liquefaction and Soil Failure During 1994 Northridge Earthquake. Journal of Geotechnical and Geoenvironmental Engineering, 125(6), 438-452. doi:10.1061/(asce)1090-0241(1999)125:6(438).

Holzer, T. L., Noce, T. E., & Bennett, M. J. (2011). Liquefaction Probability Curves for Surficial Geologic Deposits. Environmental and Engineering Geoscience, 17(1), 1–21. https://doi.org/10.2113/gseegeosci.17.1.1.

Hutabarat, D., & Bray, J. D. (2021). Seismic Response Characteristics of Liquefiable Sites with and without Sediment Ejecta Manifestation. Journal of Geotechnical and Geoenvironmental Engineering, 147(6). https://doi.org/10.1061/(asce)gt.1943-5606.0002506.

Idriss, I. M., & Boulanger, R. W. (2008). Soil Liquefaction During Earthquakes. EERI Publication, Monograph MNO-12, Earthquake Engineering Research Institute, Oakland. https://www.eeri.org/.

Ishihara, K., & Yoshimine, M. (1992). Evaluation of Settlements in Sand Deposits Following Liquefaction During Earthquakes. Soils and Foundations, 32(1), 173–188. https://doi.org/10.3208/sandf1972.32.173.

Iwasaki, T., Arakawa, T., & Tokida, K. (1982). Simplified Procedures for Assessing Soil Liquefaction During Earthquakes. Proceedings of the Conference on Soil Dynamics and Earthquake Engineering, Southampton, UK, 925−939.

Jamiolkowski, M., Lo Presti, D. C. F., & Manassero, M. (2001). Evaluation of Relative Density and Shear Strength of Sands from Cone Penetration Test (CPT) and Flat Dilatometer Test (DMT). ASCE Geotechnical Special Publication No. 119: 201–238.

Jefferies, M., & Been, K. (2006). Soil liquefaction: A Critical State Approach (1st Edition). CRC Press. https://doi.org/10.4324/9780203301968.

Jibson, R. W. (2007). Regression Models for Estimating Coseismic Landslide Displacement. Engineering Geology, 91(2-4), 209-218. https://doi:10.1016/j.enggeo.2007.01.013.

Joyner, W. B., & Boore, D. M. (1988). Measurement, Characterization, and Prediction of Strong Ground Motion. Proceedings of Earthquake Engineering & Soil Dynamics II, 43- 102. Park City, Utah, 27 June 1988. New York: Geotechnical Division of the American Society of Civil Engineers.

Juang, C. H., Ching, J., Wang, L., Khoshnevisan, S., and Ku, C.-S. (2013). Simplified Procedure for Estimation of Liquefaction-Induced Settlement and Site-Specific Probabilistic Settlement Exceedance Curve using Cone Penetration Test (CPT). Canadian Geotechnical Journal, 50(10), 1055–1066. https://doi.org/10.1139/cgj-2012-0410.

Kramer, S. L., & Mayfield, R. T. (2007). Return Period of Soil Liquefaction. Journal of Geotechnical and Geoenvironmental Engineering, 133(7), 802–813. https://doi.org/10.1061/(asce)1090-0241(2007)133:7(802).

Ku, C.-S., Juang, C. H., Chang, C.-W., & Ching, J. (2012). Probabilistic Version of the Robertson and Wride Method for Liquefaction Evaluation: Development and Application. Canadian Geotechnical Journal, 49(1), 27–44. https://doi: 10.1139/t11-085.

Kulhawy, F. H., & Mayne, P. W. (1990). Manual on Estimating Soil Properties for Foundation Design. Cornell University. Prepared for Electric Power Research Institute.

LABE (1995). Northridge Earthquake1532 Horizontal Movement Study. Los Angeles Bureau of Engineering.

Los Angeles Daily News. (2019). Damage from Ruptured Pipelines along Balboa Boulevard During the Northridge Earthquake. [Photograph]. Retrieved March 19, 2023, from https://www.dailynews.com/2019/01/13/25-years-after-the-northridge-earthquake-another-one-could-hit-any-time-are-we-safer/ (Originally photographed 17 January 1994).

Mason, J. A. (2006). Earthquake Response and Seismic Strengthening of Welded Steel Pipelines (Ph.D. thesis, Cornell University, 2006). Ithaca, N.Y.: Cornell University.

Mason, J. A., O'Rourke, T. D., Jones, S., & Tutuncu, I. (2010). Compression Performance of Steel Pipelines with Welded Slip Joints. Journal of Pipeline Systems Engineering and Practice, 1(1), 2-10. https://doi:10.1061/(ASCE)PS.1949-1204.0000043.

Maurer, B. W., Green, R. A., van Ballegooy, S., & Wotherspoon, L. (2019). Development of Region-Specific Soil Behavior Type Index Correlations for Evaluating Liquefaction Hazard in Christchurch, New Zealand. Soil Dynamics and Earthquake Engineering, 117, 96–105. https://doi.org/10.1016/j.soildyn.2018.04.059.

McCrink, T., & Frost, E. (2021). Personal Communication.

Mohr, W. (2003). Strain-Based Design of Pipelines. Edison Welding Institute. Submitted to U.S. Dept. of Interior, Minerals Management Service, Herndon, VA and U.S. Dept of Transportation, Research and Special Programs Administration, Washington, DC. Retrieved March 16, 2022, from https://www.bsee.gov/sites/bsee.gov/files/tap-technical-assessment-program/434aa.pdf.

Moss, R. E., Seed, R. B., Kayen, R. E., Stewart, J. P., Kiureghian, A. D., & Cetin, K. O. (2006). CPT-Based Probabilistic and Deterministic Assessment of In Situ Seismic Soil Liquefaction Potential. Journal of Geotechnical and Geoenvironmental Engineering, 132(8), 1032–1051. https://doi: 10.1061/(asce)1090-0241(2006)132:8(1032).

Newmark, N. M. (1965). Effects of Earthquakes on Dams and Embankments. Géotechnique, 15(2), 139-160. https://doi:10.1680/geot.1965.15.2.139.

NZGD (2021). New Zealand Geotechnical Database. https://www.nzgd.org.nz/.

O'Rourke, M. J., & Liu, J. X. (2012). Seismic Design of Buried and Offshore Pipelines. Monograph MCEER-12-MN04, Multidisciplinary Center for Earthquake Engineering Research, Buffalo, NY.

O'Rourke, T. D. & Palmer, M. C. (1994). The Northridge, California Earthquake of January 17, 1994: Performance of Gas Transmission Pipelines. Technical Report NCEER-94-0011, National Center for Earthquake Engineering Research, Buffalo, NY. ISSN: 1088-3800.

O'Rourke, T. D. (2020). Pipeline Fragilities for Natural Gas Pipelines. Memorandum.

O'Rourke, T. D., & Druschel, S. J. (1989). Improved Anchoring Practices for Plastic Gas Distribution Pipelines. Technical Report 89-2. Cornell University, Ithaca, N.Y.

O'Rourke, T. D., & O'Rourke, M. J. (1995). Pipeline Response to Permanent Ground Deformation: A Benchmark Case. Proceedings of the Fourth U.S. Conference of Lifeline Earthquake Engineering. Technical Council on Lifeline Earthquake Engineering Monograph No. 6. August 10-12, 1995, San Francisco, CA.

O'Rourke, T. D., Wang, Y., & Shi, P. (2004). Advances in Lifeline Earthquake Engineering, Keynote Paper. Proceedings of the 13th World Conference on Earthquake Engineering, Vancouver, B.C., Canada. August 1-6, 2004. Paper No. 5003.

O'Rourke, M. J., & Hmadi, K. E. (1988). Analysis of Continuous Buried Pipelines for Seismic Wave Effects. Earthquake Engineering & Structural Dynamics, 16(6), 917–929. https://doi.org/10.1002/eqe.4290160611.

O'Rourke, T. D., Druschel, S. J., & Netravali, A. N. (1990). Shear Strength Characteristics of Sand-Polymer Interfaces. Journal of Geotechnical Engineering, 116(3), 451–469. doi.org/10.1061/(asce)0733-9410(1990)116:3(451).

Paolella, L., Modoni, G., Spacagna, R. L., & Baris, A. (2022). A Generalized Severity Number to Predict Liquefaction Damage with Lateral Spreading. Géotechnique, 1–22. https://doi.org/10.1680/jgeot.21.00006.

Peterson, B. D. (2016). Development of a Performance-Based Procedure for Assessment of Liquefaction-Induced Free-Field Settlements (thesis). Brigham Young University, Provo, UT.

Phoon, K.-K., & Kulhawy, F. H. (1999). Characterization of Geotechnical Variability. Canadian Geotechnical Journal, 36(4), 612–624. https://doi.org/10.1139/t99-038.

Pipelines Research Council International (PRCI). (2004). Seismic Guidelines for the Design and Assessment of Natural Gas and Liquid Hydrocarbon Pipelines. PRCI.

Pretell, R., Ziotopoulou, K., & Davis, C. A. (2021). Liquefaction and Cyclic Softening at Balboa Boulevard During the 1994 Northridge Earthquake. Journal of Geotechnical and Geoenvironmental Engineering, 147(2). doi.org/10.1061/(asce)gt.1943-5606.0002417.

Rashidian, V., & Baise, L. G. (2020). Regional Efficacy of a Global Geospatial Liquefaction Model. Engineering Geology, 272, 105644, https://doi.org/10.1016/j.enggeo.2020.105644.

Rathje, E. M., & Antonakos, G. (2011). A Unified Model for Predicting Earthquake-Induced Sliding Displacements of Rigid and Flexible Slopes. Engineering Geology, 122(1-2), 51–60. https://doi.org/10.1016/j.enggeo.2010.12.004.

Rathje, E. M., Secara, S. S., Martin, J. G., van Ballegooy, S., & Russell, J. (2017). Liquefaction-Induced Horizontal Displacements from the Canterbury Earthquake Sequence in New Zealand Measured from Remote Sensing Techniques. Earthquake Spectra, 33(4), 1475–1494. https://doi.org/10.1193/080816eqs127m.

Robertson, P. (2009). Performance Based Earthquake Design Using the CPT. Performance-Based Design in Earthquake Geotechnical Engineering. https://doi.org/10.1201/noe0415556149.ch1.
Robertson, P. (2009). Performance Based Earthquake Design Using the CPT. Performance-Based Design in Earthquake Geotechnical Engineering. https://doi.org/10.1201/noe0415556149.ch1.
Robertson, P. K., & Cabal, K. L. (2015). Guide to Cone Penetration Testing for Geotechnical Engineering (6th ed.). Gregg Drilling & Testing Inc.
Robertson, P. K., & Campanella, R. G. (1983). Interpretation of Cone Penetration Tests. Part I: Sand. Canadian Geotechnical Journal, 20(4), 718–733. https://doi.org/10.1139/t83-078.
Robertson, P. K., & Wride, C. E. (1998). Evaluating Cyclic Liquefaction Potential using the Cone Penetration Test. Canadian Geotechnical Journal, 35(3), 442–459. https://doi: 10.1139/t98-017.
Robinson, K. M. (2016). Liquefaction-Induced Lateral Spreading in the 2010-2011 Canterbury Earthquakes (thesis). University of Canterbury, New Zealand. http://dx.doi.org/10.26021/1749.
Robinson, K., Cubrinovski, M., & Bradley, B. A. (2013). Lateral Spreading Displacements from the 2010 Darfield and 2011 Christchurch Earthquakes. International Journal of Geotechnical Engineering, 8(4), 441–448. https://doi.org/10.1179/1939787913y.0000000032.
Rodriguez-Marek, A., & Song, J. (2016). Displacement-Based Probabilistic Seismic Demand Analyses of Earth Slopes in the Near-Fault Region. Earthquake Spectra, 32(2), 1141–1163. https://doi.org/10.1193/042514eqs061m.
Russell, J., van Ballegooy, S., & Ogden, M. (2017). Influence of Geometric, Geologic, Geomorphic and Subsurface Ground Conditions on the Accuracy of Empirical Models for Prediction of Lateral Spreading. In 3rd International Conference on Performance-Based Design in Earthquake Geotechnical Engineering. Vancouver.
Sadigh, K., Egan, J. A., & Youngs, R. R. (1986). Specification of Ground Motion for Seismic Design of Long Period Structures. Earthquake Notes, vol. 57, no. 1: 13, relationships are tabulated in Joyner and Boore (1988) and Youngs and others (1987).
San Francisco Estuary Institute and Aquatic Science Center (SFEI ASC) (2017). Bay Area Aquatic Resource Inventory (BAARI) Version 2.1 GIS Data. [Shapefile]. Retrieved October 1, 2021, from http://www.sfei.org/data/baari-version-21-gis-data.
Sano, Y. (1998). GIS Evaluation of Northridge Earthquake Ground Deformation and Water Supply Damage. (Master's thesis, Cornell University, 1998). (pp. 103-108). Ithaca, N.Y., Cornell University.
Schmidt, K. M., Roering, J. J., Stock, J. D., Dietrich, W. E., Montgomery, D. R., & Schaub, T. (2001). The Variability of Root Cohesion as an Influence on Shallow Landslide Susceptibility in the Oregon Coast Range. Canadian Geotechnical Journal, 38(5), 995–1024. https://doi.org/10.1139/t01-031.
Seed, H. B., & Idriss, I. M. (1971). Simplified Procedure for Evaluating Soil Liquefaction Potential. Journal of the Soil Mechanics and Foundations Division, 97(9), 1249–1273.
Seed, R. B., Dickenson, S. E., & Idriss, I. M. (1991). Principal Geotechnical Aspects of the 1989 Loma Prieta Earthquake. Soils and Foundations, 31(1), 1–26. https://doi.org/10.3208/sandf1972.31.1.

Shinozuka, M. & Koike, T. (1979). Estimation of Structural Strains in Underground Lifeline Pipes. Lifeline Earthquake Engineering – Buried Pipelines, Seismic Risk, and Instrumentation, PVP-34, ASME, pp. 31-48.
SoCalGas & PG&E (2000). Gas Pipeline Performance in the Northridge Earthquake – Geologic, Geotechnical, and Pipeline Investigations. Southern California Gas Company & Pacific Gas and Electric Company.
Stoker, J., & Miller, B. (2022). The Accuracy and Consistency of 3D Elevation Program Data: A Systematic Analysis. Remote Sensing, 14(4), 940. https://doi.org/10.3390/rs14040940.
Timoshenko, S. (1976). Strength of Materials. Krieger.
Tomlinson, M. J. (1957). The Adhesion of Piles Driven in Clay. Proceedings of the 4th International Conference of Soil Mechanics. Vol. 2: London, 66-71.
Toprak, S., & Holzer, T. L. (2003). Liquefaction Potential Index: Field Assessment. Journal of Geotechnical and Geoenvironmental Engineering, 129(4), 315–322. https://doi.org/10.1061/(asce)1090-0241(2003)129:4(315).
Toprak, S., & Holzer, T. L. (2003). Liquefaction Potential Index: Field Assessment. Journal of Geotechnical and Geoenvironmental Engineering, 129(4), 315–322. https://doi: 10.1061/(asce)1090-0241(2003)129:4(315).
Toprak, S., Nacaroglu, E., Koc, A. C., O'Rourke, T. D., Hamada, M., Cubrinovski, M., & van Ballegooy, S. (2018). Comparison of Horizontal Ground Displacements in Avonside Area, Christchurch from Air Photo, Lidar and Satellite Measurements Regarding Pipeline Damage Assessment. Bulletin of Earthquake Engineering, 16(10), 4497–4514. https://doi.org/10.1007/s10518-018-0317-9.
USGS (2017). The HayWired Earthquake Scenario – Earthquake Hazards. (2017). U.S. Geological Survey. https://doi.org/10.3133/sir20175013v1.
USGS (2020a). Map of CPT Data: All Regions. U.S. Geological Survey. Retrieved June 1, 2020, from https://earthquake.usgs.gov/research/cpt/data/.
USGS (2020b). 3D Elevation Program 10-Meter Resolution Digital Elevation Models (published 2020). U.S. Geological Survey. Retrieved October 1, 2021, from https://apps.nationalmap.gov/downloader/#/.
USGS (2021a). Coastal Storm Modeling System (CoSMoS). U.S. Geological Survey. Retrieved October 1, 2021, from https://www.usgs.gov/centers/pcmsc/science/cosmos-groundwater#overview.
USGS (2021b). M 6.9 – Loma Prieta, California Earthquake ShakeMap (updated July 7, 2020). U.S. Geological Survey. Retrieved October 1, 2021, from https://earthquake.usgs.gov/earthquakes/eventpage/nc216859/executive.
USGS (2022). MODFLOW 6 Modular Hydrologic Model (version 6.3.0). U.S. Geological Survey. https://doi.org/10.5066/P97FFF9M.
USGS (2023a). M 6.6 – 10km SSW of Agua Dulce, CA ShakeMap (updated July 7, 2020). U.S. Geological Survey. Retrieved February 1 at: https://earthquake.usgs.gov/earthquakes/eventpage/ci3347678/executive.
USGS (2023b). M 6.7 – 1km NNW of Reseda, CA ShakeMap (updated July 7, 2020). U.S. Geological Survey. Retrieved February 1 at: https://earthquake.usgs.gov/earthquakes/eventpage/ci3144585/executive.
van Ballegooy, S. (2021). Personal Communication.

van Ballegooy, S., Cox, S. C., Thurlow, C., Rutter, H. K., Reynolds, T., Harrington, G., Fraser, J., & Smith, T. (2014b). Median Water Table Elevation in Christchurch and Surrounding Area after the 4 September 2010 Darfield Earthquake: Version 2. GNS Science Report 2014/18, April 2014. ISBN 978-1-927278-41-3.

van Ballegooy, S., Malan, P., Lacrosse, V., Jacka, M. E., Cubrinovski, M., Bray, J. D., O'Rourke, T. D., Crawford, S. A., & Cowan, H. (2014a). Assessment of Liquefaction-Induced Land Damage for Residential Christchurch. Earthquake Spectra, 30(1), 31–55. https://doi.org/10.1193/031813eqs070m.

Wechsler, S. P. (1999). 1999 Esri User Conference. In 1999 Esri User Conference Proceedings. Earth Systems Research Institute, Inc. Retrieved September 22, 2022, from https://proceedings.esri.com/library/userconf/proc99/navigate/proceed.htm.

Wijewickreme, D., Honegger, D., Mitchell, A., & Fitzell, T. (2005). Seismic Vulnerability Assessment and Retrofit of a Major Natural Gas Pipeline System: A Case History. Earthquake Spectra, 21(2), 539–567. https://doi.org/10.1193/1.1898273.

Wills, C. J., Gutierrez, C. I., Perez, F. G., & Branum, D. M. (2015). A Next Generation VS30 Map for California Based on Geology and Topography. Bulletin of the Seismological Society of America, 105(6), 3083-3091. doi:10.1785/0120150105.

Wilson, R. C., & Keefer, D. K. (1985). Predicting Areal Limits of Earthquake-Induced Landsliding. Evaluating Earthquake Hazards in the Los Angeles Region-An Earth-Science Perspective: U.S. Geological Survey Professional Paper 1360, pgs. 317-345.

Witter, R. C., Knudsen, K. L, Sowers, J. M., Wentworth, C. M., Koehler, R. D., Randolph, C. E., Brooks, S. K., & Gans, K. D. (2006). Maps of Quaternary Deposits and Liquefaction Susceptibility in the Central San Francisco Bay Region, California: U.S. Geological Survey Open-File Report 06-1037, http://pubs.usgs.gov/of/2006/1037/.

Yerkes, R. F., & Campbell, R. H. (2005). Preliminary Geologic Map of the Los Angeles 30' x 60' Quadrangle, Southern California. U.S. Geological Survey Open-File Report 2005-1019. https://doi.org/10.3133/ofr20051019.

Youd, T. L., & Perkins, D. M. (1978). Mapping Liquefaction-Induced Ground Failure Potential. Journal of the Geotechnical Engineering Division, 104(4), 433–446. https:// 10.1061/ajgeb6.0000612.

Youd, T. L., & Perkins, D. M. (1987). Mapping of Liquefaction Severity Index. Journal of Geotechnical Engineering, 113(11), 1374–1392. https://doi.org/10.1061/(asce)0733-9410(1987)113:11(1374).

Youd, T. L., Hansen, C. M., & Bartlett, S. F. (2002). Revised Multilinear Regression Equations for Prediction of Lateral Spread Displacement. Journal of Geotechnical and Geoenvironmental Engineering, 128(12), 1007-1017, doi:10.1061/(asce)1090-0241(2002)128:12(1007).

Youd, T. L., Idriss, I. M., Andrus, R. D., Arango, I., Castro, G., Christian, J. T., Dobry, R., Finn, W. D., Harder, L. F., Hynes, M. E., Ishihara, K., Koester, J. P., Liao, S. S., Marcuson, W. F., Martin, G. R., Mitchell, J. K., Moriwaki, Y., Power, M. S., Robertson, P. K., Seed, R. B., & Stokoe, K. H. (2001). Liquefaction Resistance of Soils: Summary Report from the 1996 NCEER and 1998 NCEER/NSF Workshops on Evaluation of Liquefaction Resistance of Soils. Journal of Geotechnical and Geoenvironmental Engineering, 127(10), 817–833, https://doi.org/10.1061/(asce)1090-0241(2001)127:10(817).

Zhang, G., Robertson, P. K., & Brachman, R. W. I. (2002). Estimating Liquefaction-Induced Ground Settlements from CPT for Level Ground. Canadian Geotechnical Journal, 39(5), 1168–1180, https://doi.org/10.1139/t02-047.

Zhang, G., Robertson, P. K., & Brachman, R. W. I. (2004). Estimating Liquefaction-Induced Lateral Displacements Using the Standard Penetration Test or Cone Penetration Test. Journal of Geotechnical and Geoenvironmental Engineering, 130(8), 861–871. https://doi: 10.1061/(asce)1090-0241(2004)130:8(861).

Zhu, J., Baise, L. G., & Thompson, E. M. (2017). An Updated Geospatial Liquefaction Model for Global Application. Bulletin of the Seismological Society of America, 107(3), 1365–1385, https://doi: 10.1785/0120160198.

Zhu, J., Daley, D., Baise, L. G., Thompson, E. M., Wald, D. J., & Knudsen, K. L. (2015). A Geospatial Liquefaction Model for Rapid Response and Loss Estimation. Earthquake Spectra, 31(3), 1813–1837, https://doi.org/10.1193/121912eqs353m.

Ziotopoulou, K. & Boulanger, R. W. (2016). Plasticity Modeling of Liquefaction Effects Under Sloping Ground and Irregular Cyclic Loading Conditions. Soil Dynamics and Earthquake Engineering, 84, 269–283. doi.org/10.1016/j.soildyn.2016.02.013.

Ziotopoulou, K., Davis, C. A., & Pretell, R. (2022). Investigation of Water Pipeline Failures at Balboa Boulevard during the 1994 Northridge Earthquake. Lifelines 2022. doi.org/10.1061/9780784484449.032.

APPENDIX A: DATA MATRIX AND GEOSPATIAL DATA

The *OpenSRA* Data Matrix lists the methods and datasets used in *OpenSRA* to estimate seismic displacements from landsliding and liquefaction at Levels 1 – 3 and a description of Level 4 methods, which are outside the scope of *OpenSRA*. The data matrix also lists methods for evaluating transient ground strains and underground pipeline performance in response to transient ground strains and permanent ground deformations. Appendix A also includes the geospatial datasets for the methods implemented in *OpenSRA* for assessing seismic permanent ground deformation.

OpenSRA Data Matrix				
	Level 1	**Level 2**	**Level 3**	**Level 4**
Description	Level 1 analyses utilize data that are geospatially continuous at a uniform resolution over the entire state of California. With its lower level of resolution and without site-specific or subsurface data, the state-wide data lead to very high uncertainty.	Level 2 analyses utilize data produced at regional scales collected at higher resolution than level 1 data. Level 2 data are not necessarily geospatially continuous over the entire state of California. There is minimal, generic subsurface data or estimated engineering properties. Use of level 2 data leads to high uncertainty, but less uncertainty than with level 1 data.	Level 3 analyses utilize site-specific geologic and topographic mapping and includes subsurface data through CPTs, borings with SPT, and soil/rock index tests. Subsurface data can be used in performance-based liquefaction, lateral spreading, slope displacement, and settlement procedures. Level 3 data enable assessment with medium uncertainty.	Level 4 analyses utilize high-quality laboratory test data with the Level 3 site-specific geologic, topographic, and geotechnical data. Use of Level 4 data enable the performance of advanced numerical analyses. Level 4 analyses will have the least uncertainty in estimating the effects of earthquake-induced ground deformation on buried pipes. Due to the high level of data required they will not be employed commonly.
Topographic Data	Statewide 10 m DEM.	Regional 1 m DEM.	Site-specific high-resolution topography from SfM or lidar.	Site-specific high-resolution topography from SfM or lidar.
Geologic Data	Statewide geologic maps generally produced at scales of 1:250,000 or smaller or regulatory maps: **A)** Wills et al. (2015) 1:250,000 to 1:24,000 statewide compilation of geologic maps. Population centers of the San Francisco Bay area and Los Angeles basin covered by the larger scale mapping. **B)** Digital Geologic Map of CA (CGS 2010) at 1:750,000. **C)** CGS Deep-Seated Landslide Susceptibility Map, GIS based.	Geologic maps produced at scales of 1:100,000 to 1:24,000: **A)** Bedrossian et al. (2012) 1:100,000 GIS based map of Quaternary geologic units in Southern California. **B)** Yerkes & Campbell (2005) 1:100,000 maps, some digital, incomplete coverage. **C)** Dibblee maps at 1:24,000, incomplete coverage. **D)** CGS Regional Geologic Maps at 1:100,000 and 1:24,000, incomplete coverage, some maps preliminary.	**A)** Detailed geologic maps produced at scales of 1:24,000 or larger. **B)** Level 2 maps at 1:24,000 scale, when available.	Detailed geologic maps produced at scales of 1:24,000 or larger.
Geotechnical Data	Not available. May use modeled V_{S30} and similar geotechnical data.	Limited subsurface data available (e.g., CGS borehole database). May use estimated soil or rock mass properties (e.g., CGS Seismic Hazard Reports).	CPTs or borings with SPTs. Soil index test data (e.g., Atterberg limits or grain-size distributions).	CPTs or borings utilizing SPTs. Extensive, high-quality, site-specific laboratory test data (e.g., TX, CSS tests).

Groundwater Data	No measurements available. May use statewide depth to groundwater model.	Limited data such as historic high-water table depths, regional maps of depth to groundwater, or regional groundwater models.	Groundwater depth measurements.	Groundwater depth measurements.
Output	Probabilistic analysis of ground failure hazard and effects to infrastructure with very high uncertainty.	Probabilistic analysis of ground failure hazard and effects to infrastructure with less uncertainty than at Level 1, but still high uncertainty.	Probabilistic analysis of ground failure hazard and effects to infrastructure with medium uncertainty.	Probabilistic analysis of ground failure hazard and effects to infrastructure with less uncertainty than at Level 3.
Liquefaction Triggering				
Preferred Liquefaction Triggering Procedures and Model Inputs & Outputs	**A)** Zhu et al. (2017) coastal (<20 km to coast and within coastal basin) and non-coastal models Inputs: PGV, modeled V_{S30}, precip, d_c, d_r, d_w, modeled GWT Outputs: P_L	**A)** Youd & Perkins (1978) and Witter et al. (2006) geologic based assessments used with HAZUS methodology to estimate probability of liquefaction triggering Inputs: Surficial Quaternary geologic maps, PGA, M_w, GWT Outputs: Liquefaction susceptibility converted to P_L **B)** Bain & Bray (2023) probabilistic lateral spread displacement procedure Inputs: Surficial Quaternary geologic maps, PGA, M_w, GWT Outputs: Probabilistic assessment of liquefaction triggering and lateral spread displacement	**A)** Boulanger & Idriss (2016) probabilistic liquefaction triggering procedure Inputs: CPT, PGA, M_w, GWT Outputs: P_L **B)** Probabilistic modification to Robertson & Wride (1998) procedure as updated by Robertson (2009) from Ku et. al. (2012) Inputs: CPT, PGA, M_w, GWT Outputs: P_L **C)** Moss et al. (2006) probabilistic liquefaction triggering procedure Inputs: CPT, PGA, M_w, GWT Outputs: P_L	Level 3 methods and: **A)** FLAC analyses with PM4Sand and PM4Silt **B)** FLAC analyses with UBCSAND **C)** PLAXIS analyses with PM4Sand **D)** OpenSees analyses with multiple soil models
Alternative Liquefaction Triggering Procedures and Model Inputs & Outputs	No Alternatives Available or Considered	**AA)** CA Earthquake Zones of Required Investigation Maps Inputs: 1:24,000 scale map Outputs: Delineates areas where liquefaction may occur converted to broad categories of effects	**AA)** Kramer & Mayfield (2007) PBEE Inputs: Cetin et al. (2004) model coefficients, boring with $(N_1)_{60,cs}$, FC, r_d, PSHA Outputs: FS_L, N_{req} hazard curves **BB)** Franke & Kramer (2014) PBEE Inputs: r_d, MSF, K_σ per Idriss & Boulanger (2008), boring with $(N_1)_{60,cs}$, PSHA Outputs: FS_L, N_{req} hazard curves	No Alternatives Available or Considered

Lateral Spreading				
Preferred Lateral Spreading Procedures and Model Inputs & Outputs	**A)** Zhu et al. (2017) coastal (<20 km to coast and within coastal basin) and non-coastal models combined with Hazus methodology to estimate lateral spread displacement Inputs: PGV, modeled V_{S30}, precip, d_c, d_r, d_w, modeled GWT Outputs: Liquefaction susceptibility class converted to settlement estimate	**A)** Youd & Perkins (1978) and Witter et al. (2006) geologic based assessments used with HAZUS methodology to estimate lateral spread displacement Inputs: Surficial Quaternary geologic maps, PGA, M_w, GWT Outputs: Liquefaction susceptibility converted to lateral spread displacement **B)** Bain & Bray (2023) probabilistic lateral spread displacement procedure Inputs: Surficial Quaternary geologic maps, PGA, M_w, GWT Outputs: Probabilistic assessment of liquefaction triggering and lateral spread displacement	**A)** Zhang et al. (2004) Inputs: CPT, PGA, M_w, GWT, topographic slope or free-face ratio Outputs: Estimate of lateral spread displacement **AA)** Idriss & Boulanger (2008) procedure for calculating maximum and limiting shear strains combined with Zhang et al. (2004) or Faris et al. (2006) procedure Inputs: CPT or boring Outputs: Estimate of lateral spreading displacement **B)** Youd et al. (2002) Inputs: Boring with $(N_1)_{60}$, W, S, T_{15}, F_{15}, $D50_{15}$ Outputs: Estimate of lateral spread displacement **C)** Faris et al. (2006) Inputs: CPT, PGA, M_w, GWT, topographic slope or free-face ratio Outputs: Estimate of lateral spread displacement	Level 3 methods and: **A)** FLAC analyses with PM4Sand and PM4Silt **B)** FLAC analyses with UBCSAND **C)** PLAXIS analyses with PM4Sand **D)** OpenSees analyses with multiple soil models
Alternative Lateral Spreading Procedures and Model Inputs & Outputs	No Alternatives Available or Considered	**AA)** CA Earthquake Zones of Required Investigation Maps Inputs: 1:24,000 scale map Outputs: Delineates areas where liquefaction and hence, lateral spreading, may occur if slightly sloping ground or adjacent to a free-face	**AA)** Franke & Kramer (2014) PBEE Inputs: Youd et al. (2002) model coefficients, boring with $(N_1)_{60}$, W, S, T_{15}, F_{15}, $D50_{15}$, PSHA Outputs: D_H hazard curve **BB)** Coutu (2017) incorporation of Zhang et al. (2004) into PBEE Inputs: CPT, PSHA Outputs: Lateral spread displacement hazard curves	No Alternatives Available or Considered

Liquefaction-Induced Settlement				
Preferred Liquefaction-Induced Settlement Procedures and Model Inputs & Outputs	**A)** Zhu et al. (2017) coastal (<20 km to coast and within coastal basin) and non-coastal models combined with Hazus methodology to estimate liquefaction-induced settlement Inputs: PGV, modeled V_{S30}, precip, d_c, d_r, d_w, modeled GWT Outputs: Liquefaction Susceptibility Class Converted to Settlement Estimate	**A)** Zhu et al. (2017) coastal (<20 km to coast and within coastal basin) and non-coastal models combined with Hazus methodology to estimate liquefaction-induced settlement Inputs: PGV, modeled V_{S30}, precip, dc, dr, dw, GWT Outputs: Liquefaction Susceptibility Class Converted to Settlement Estimate **B)** Youd & Perkins (1978) and Witter et al. (2006) geologic based assessments combined with Hazus methodology to estimate liquefaction-induced settlement Inputs: Surficial Quaternary geologic maps, GWT Outputs: Estimate of liquefaction-induced settlement	**A)** Cetin et al. (2009) Inputs: Boring with SPT, PGA, M_w, GWT Outputs: Estimate of free-field, level-ground settlement **B)** Ishihara and Yoshimine (1992) Inputs: Boring with SPT, PGA, M_w, GWT Outputs: Estimate of free-field, level-ground settlement **C)** Zhang et al. (2002) Inputs: CPT, PGA, M_w, GWT Outputs: Estimate of free-field, level-ground settlement	Level 3 methods and: **A)** FLAC analyses with PM4Sand and PM4Silt **B)** FLAC analyses with UBCSAND **C)** PLAXIS analyses with PM4Sand **D)** OpenSees analyses with multiple soil models
Alternative Liquefaction-Induced Settlement Procedures and Model Inputs & Outputs	No Alternatives Available or Considered	**AA)** CA Earthquake Zones of Required Investigation Maps Inputs: 1:24,000 scale map Outputs: Delineates areas where liquefaction and hence, liquefaction-induced settlement may occur	**AA)** Peterson (2016) PBEE based on Cetin et al. (2009) Inputs: Boring with $(N_1)_{60,cs}$, N_{req}^{Cetin}, M_w, K_{md}, K_{Mw}, K_σ, D_R, PSHA Outputs: ε_v, settlement hazard curves **BB)** Peterson (2016) PBEE based on Ishihara and Yoshimine (1992) Inputs: Boring with $(N_1)_{60,cs}$ per Idriss and Boulanger (2008), $N_{req}^{B\&I}$, D_R, PSHA Outputs: ε_v, settlement hazard curves **CC)** Hatch (2017) PBEE based on probabilistic adaption of Ishihara & Yoshimine (1992) from Juang et al. (2013) Inputs: CPT, PGA, M_w, GWT Outputs: Post-liquefaction free-field settlement hazard curves	No Alternatives Available or Considered

Seismic Slope Stability				
Preferred Slope Stability/ Displacement Procedures and Model Inputs & Outputs	**A)** Infinite slope analysis using strength distributions developed from CGS database for generalized geologic units Inputs: Statewide Geologic Map Outputs: Estimate of Seismic Slope Displacement	**A)** Grant et al. (2016) multimodal method for coseismic landslide hazard assessment Inputs: DEM, φ, γ, c, c_r, S, h, H, α, k_y, M_w, PGA, T_{PGA} Outputs: Model predicts the type of slope movement (rock-slope failures, disrupted soil slides, coherent rotational slides, and lateral spreads) and estimates seismic slope displacement distribution **B)** Modified Bray & Macedo (2019) & Bray et al. (2018) using k_y from Grant et al. (2016) Inputs: k_y, T_s from slide depth estimate, Sa($1.3T_s$), M_w Outputs: Seismic Slope Displacement Distribution	**A)** Bray & Macedo (2019) Inputs: k_y, T_s, Sa($1.3T_s$), M_w, PGV Outputs: Seismic Slope Displacement Distribution **B)** Rathje & Antonakos (2011) Inputs: k_y, PGA, T_s, T_m, PGV Outputs: Seismic Slope Displacement Distribution **C)** Jibson (2007) Inputs: k_y, PGA, M_w Outputs: Seismic Slope Displacement Distribution **D)** Bray et al. (2018) PBEE Inputs: k_y, T_s, Sa($1.5T_s$), Mw Outputs: Seismic Slope Displacement Distribution **E)** Block theory analyses Inputs: Strike and dip measurements, rock mass properties, slope/block geometry Outputs: FS rock slope failures converted to displacement estimate	Level 3 methods and: **A)** FLAC analyses **B)** PLAXIS analyses **C)** OpenSees analyses
Alternative Slope Stability/ Displacement Procedures and Model Inputs & Outputs	**AA)** CGS Deep-Seated Landslide Susceptibility Map Inputs: Statewide map Outputs: Indicates the relative likelihood of deep-seated landsliding	**AA)** Hazus methodology based on Wilson & Keefer (1985) Inputs: Surficial Quaternary geologic maps, d_{wt}, M_w, a_{is}, slope angle Outputs: Estimate of landslide displacement **BB)** CA Earthquake Zones of Required Investigation Maps Inputs: 1:24,000 scale map Outputs: Delineates areas where earthquake-induced landsliding may occur **CC)** CGS landslide inventory map Inputs: GIS based inventory map Outputs: Spatial extent, type, and age of known or suspected landslides	No Alternatives Available or Considered	No Alternatives Available or Considered

Transient Ground Strains				
Preferred Transient Ground Strain Procedures and Model Inputs & Outputs	**A)** Newmark (1967) Inputs: PGV, modeled V_s, estimated γ_s, modeled C_R Outputs: ε_g, which is assumed to be equal to ε_p (no soil-pipe interface slippage)	**A)** Newmark (1967) Inputs: PGV, modeled V_s, estimated γ_s, modeled C_R Outputs: ε_g, which is assumed to be equal to ε_p (no soil-pipe interface slippage) **B)** Shinozuka & Koike (1979) Inputs: A, E, K_g, t, modeled G, λ, estimated t_u, D, q, ε_g from Newmark's Approach Outputs: ε_p	**A)** Newmark (1967) Inputs: PGV, V_s, γ_s, C_R Outputs: ε_g, which is assumed to be equal to ε_p (no soil-pipe interface slippage) **B)** Shinozuka & Koike (1979) Inputs: A, E, K_g, t, G, λ, t_u, D, q, ε_g from Newmark's Approach Outputs: ε_p **C)** O'Rourke and El Hmadi (1988) Inputs: A, E, K_g, t_u, U_g, U_p, L_s, H, D Outputs: ε_g, ε_p	Level 3 methods and: **A)** FLAC analyses **B)** PLAXIS analyses **C)** OpenSees analyses
Alternative Transient Ground Strain Procedures and Model Inputs & Outputs	No Alternatives Available or Considered	No Alternatives Available or Considered	No Alternatives Available or Considered	No Alternatives Available or Considered

Underground Pipeline Performance				
Preferred Pipeline Performance Model Inputs & Outputs	**A)** O'Rourke (2020) response to transient ground strain Inputs: Geomean PGV & pipe type Outputs: RR	**A)** O'Rourke (2020) response to transient ground strain Inputs: Geomean PGV & pipe type Outputs: RR **B)** O'Rourke (2020) response to permanent ground deformation Inputs: Ground deformation & pipe type Outputs: RR	**A)** Soil-pipeline spring model Inputs: Soil deformation magnitude and pattern, soil spring stiffness (Kg), and pipe material (D, t, E, and joints) Outputs: ε_p	**A)** FLAC SSI analyses **B)** PLAXIS SSI analyses **C)** OpenSees SSI analyses
Alternative Preferred Pipeline Performance Model Inputs & Outputs	No Alternatives Available or Considered	No Alternatives Available or Considered	No Alternatives Available or Considered	No Alternatives Available or Considered

Abbreviations:

PGV	Peak ground velocity
V_{S30}	Time-averaged shear-wave velocity in upper 30 meters of subsurface
precip	Precipitation
d_c	Distance to nearest coast for use in Zhu et al. (2017)
d_r	Distance to nearest river for use in Zhu et al. (2017)
d_w	Distance to nearest water body for use in Zhu et al. (2017)
P_L	Probability of liquefaction triggering
GWT	Depth of the water table
FC	Fines content
PSHA	Probabilistic seismic hazard analysis
FS_L	Factor of safety against liquefaction triggering
N_{req}	Corrected SPT blow counts required to resist liquefaction triggering
MSF	Magnitude scaling factor. Procedure for computing MSF varies for different authors.
K_σ	Overburden correction factor
CPT	Cone penetration test
PGA	Peak ground acceleration
M_w	Moment magnitude
$\bar{V}_{s,12}$	Average shear wave velocity in upper 12 meters of subsurface profile
P_{LAT}	Probability of lateral spreading
DEM	Digital elevation model
φ	Friction angle of soil or rock
γ	Unit weight of soil or rock
c	Cohesion of soil or rock
c_r	Root cohesion for Grant et al. (2016)
S	Ground slope angle
h	Vertical height of failure mass for Grant et al. (2016)
H	Local relief for Grant et al. (2016)
α	Critical angle of slope for Grant et al. (2016)
k_y	Yield acceleration
T_{PGA}	PGA thresholds for liquefaction triggering used in Youd and Perkins (1978) and Witter et al. (2006) procedures
W	Free-face ratio
T_{15}	Cumulative thickness (in upper 20 meters) of all saturated soil layers susceptible to liquefaction initiation with $(N_1)_{60}$ > 15 blows per 0.3 meters
F_{15}	Average fines content of the soil comprising T_{15}
$D50_{15}$	Average mean grain size comprising T_{15}
D_H	Lateral spread displacement
T_s	Natural period of sliding mass
$Sa(1.3T_s)$	Spectral acceleration at 1.3 times T_s
T_m	Mean period of earthquake motion
$Sa(1.5T_s)$	Spectral acceleration at 1.5 times T_s
P_{LS}	Probability of liquefaction-induced settlement
K_{md}	Correction factor to convert multidirectionally applied CSR_{field} to unidirectionally applied CSR_{lab}
K_{Mw}	Magnitude correction factor
K_σ	Correction factor to account for nonlinear increase in cyclic resistance to shear stresses with increasing confining effective stresses

D_R	Relative density
ε_v	Vertical strain
V_s	Shear wave velocity
γ_s	Angle between direction of wave propagation and orientation of pipeline
C_R	Propagation or phase velocity of the R-wave
ε_g	Ground strain
ε_p	Pipe strain
A	Cross-sectional area of pipeline
E	Young's modulus of pipeline
D	Pipeline diameter
t	Pipe wall thickness
K_g	Linear soil stiffness per unit length
G	Shear modulus of soil
λ	Wavelength
t_u	Maximal frictional resistance
q	Factor that ranges from 1 to $\pi/2$ and quantifies the degree of slippage at the pipe-soil interface
a_{is}	Induced acceleration (equal to a_{max} for rockslides or shallow, disrupted soil slides but less than a_{max} for deep-seated, coherent slides)
RR	Repair rate (typically per km)

OpenSRA Geospatial Datasets

Figure A.1: Statewide 30 m Digital Elevation Model (DEM)

Figure A.2: Statewide 30 m Slope Model

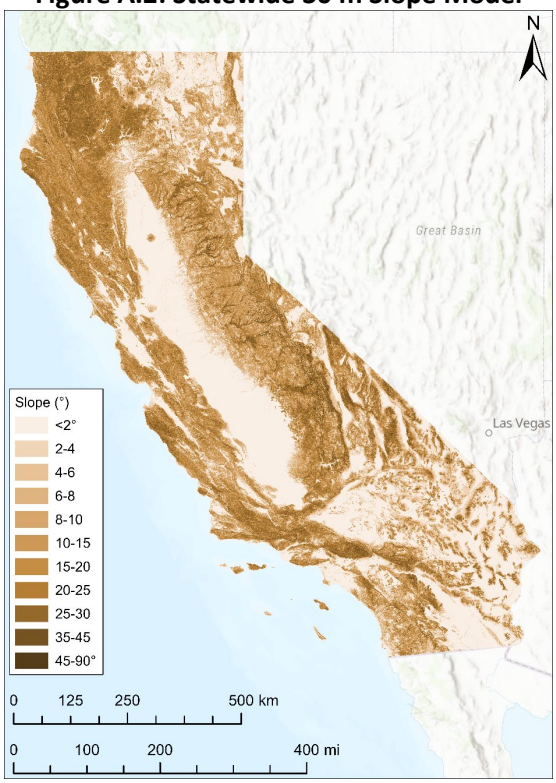

Figure A.3: Statewide Geologic Map from Wills et al. (2015)

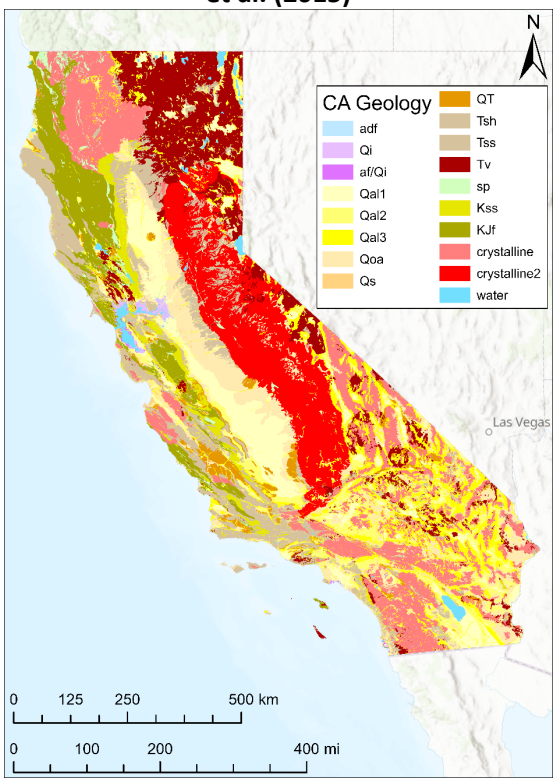

Figure A.4: ESRI USA Detailed Streams GIS Layer (ESRI, 2019a)

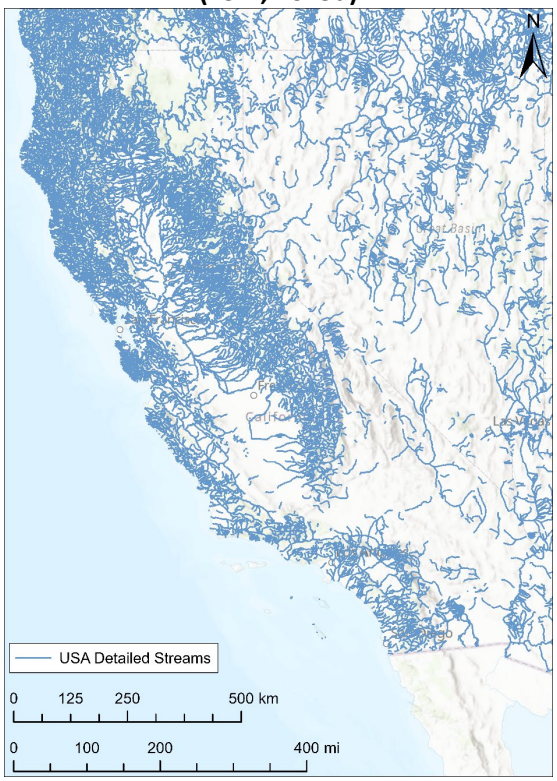

Figure A.5: Distance to Nearest River for Zhu et al. (2017) Method

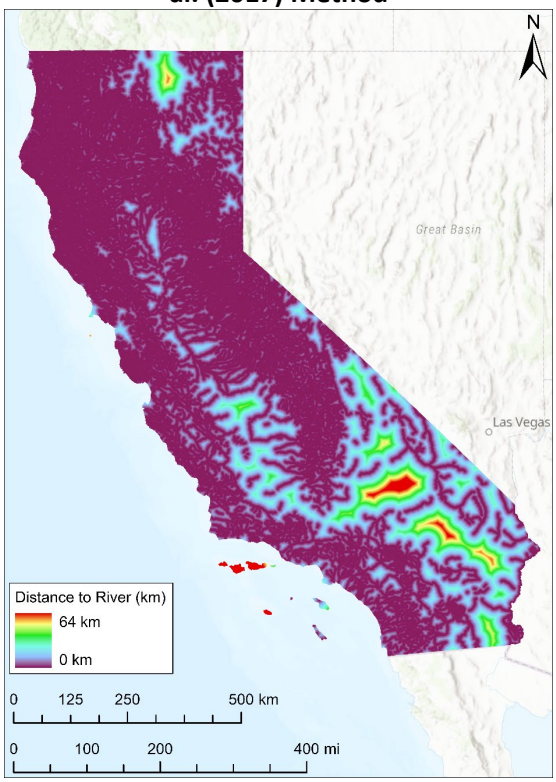

Figure A.6: Distance to the Coast for Zhu et al. (2017) Method

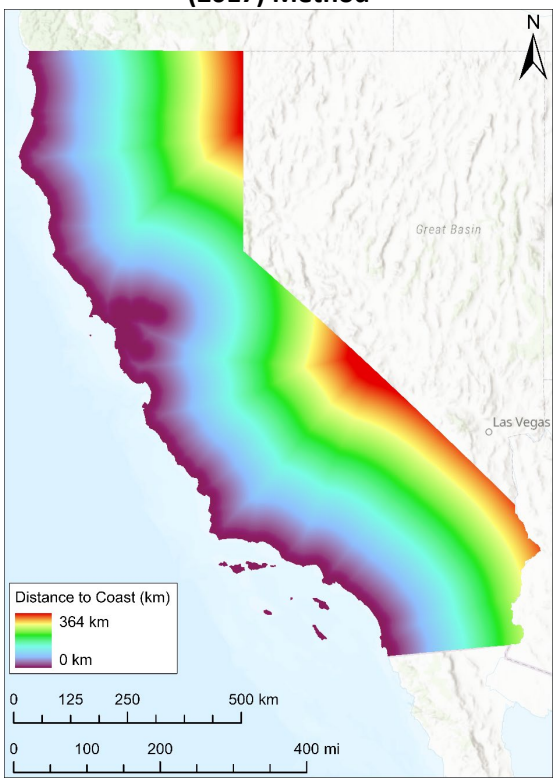

Figure A.7: Distance to the Nearest River or to the Coast for Zhu et al. (2017) Method

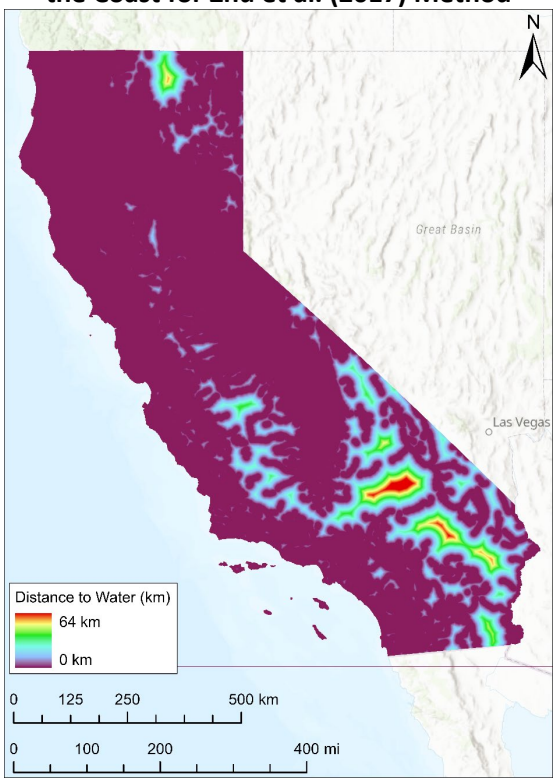

Figure A.8: Statewide Precipitation Map for Zhu et al. (2017) Method from CDFW (n.d.)

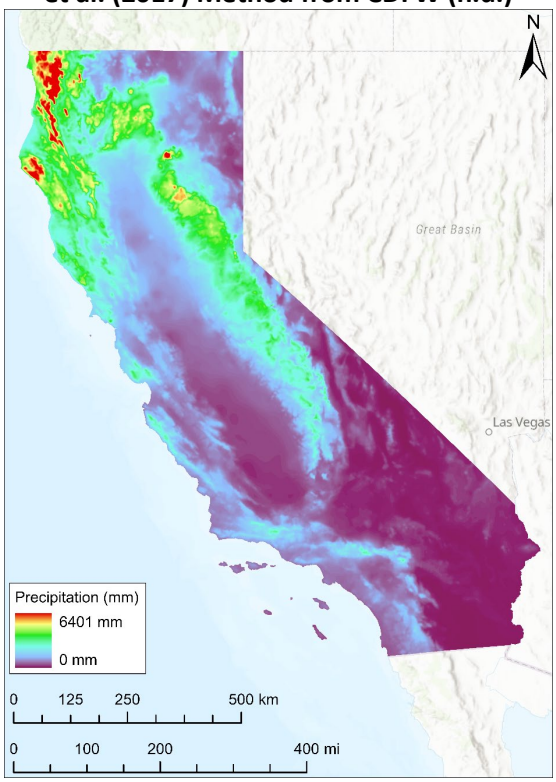

Figure A.9: Depth to Groundwater Model for Zhu et al. (2017) Method Described by Fan & Miguez-Macho (2010)

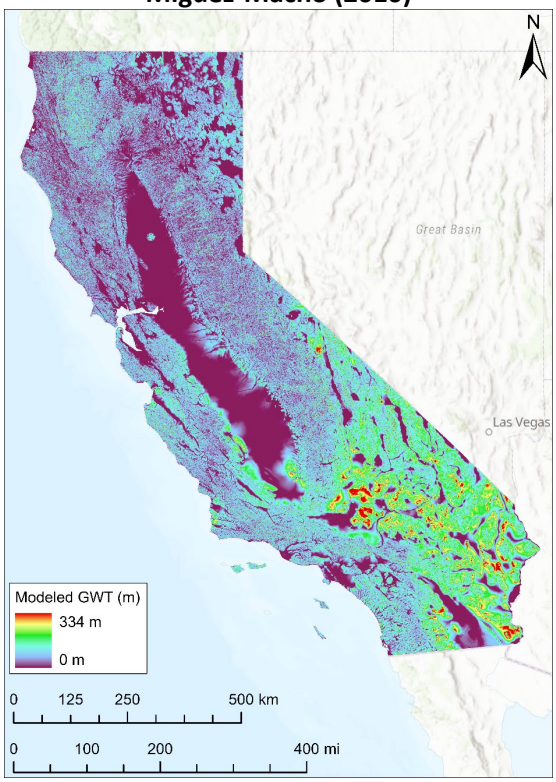

Figure A.10: Statewide VS30 Model from Wills et al. (2015)

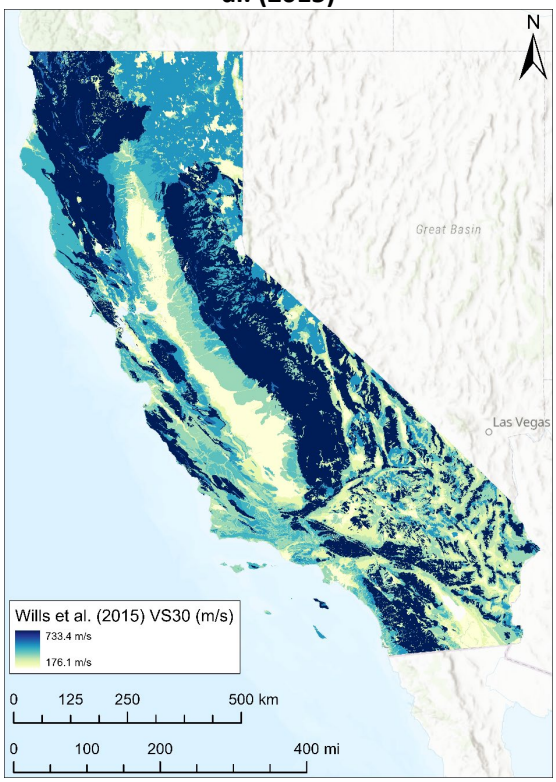

Figure A.11: Statewide Compound Topographic Index (CTI) for Zhu et al. (2015) Method

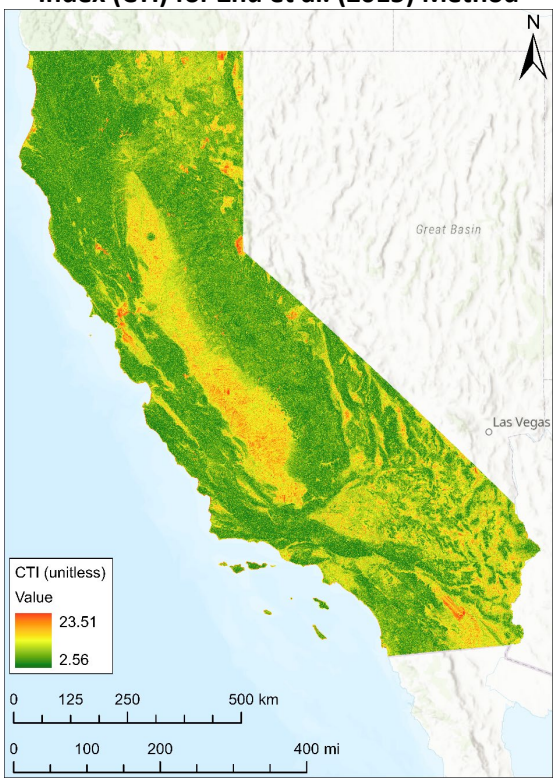

APPENDIX B: DATA FOR THE PROBABILISTIC REGIONAL SCALE LATERAL SPREAD DISPLACEMENT METHOD

Appendix B presents data used in the probabilistic regional scale lateral spread displacement method (Bain & Bray, 2023). Data in Appendix B includes:

1. CPT data from the United States Geological Survey (USGS) sorted into simplified geologic deposits. All raw CPT data is available at: https://earthquake.usgs.gov/research/cpt/data/.
2. Surficial geologic units in the 1:24,000 scale geologic map from Witter et al. (2006), available at: https://pubs.usgs.gov/of/2006/1037/, sorted into simplified geologic deposits.
3. 10 m resolution digital elevation model (DEM) with terrestrial and bathymetric elevations from Fregoso et al. (2017), available at: https://doi.org/10.5066/F7GH9G27.
4. Free-face features in the San Francisco Bay area from the Bay Area Aquatic Resources Inventory (BAARI) shapefile dataset, available at: https://www.sfei.org/baari, and a shapefile dataset of streams in the San Francisco Bay area, available at: https://maps.princeton.edu/catalog/stanford-km172ps5456.

Table B.1: USGS CPTs in the San Francisco Bay Area Sorted into Simplified Geologic Deposits

Artificial Fill over Estuarine Mud (afem) CPTs (89)				
ALC001	ALC019	ALC043	OAK039	OAK060
ALC002	ALC020	ALC063	OAK040	OAK063
ALC003	ALC025	ALC064	OAK041	OAK064
ALC004	ALC026	ALC065	OAK042	OAK065
ALC005	ALC027	ALC067	OAK043	OAK066
ALC006	ALC028	ALC072	OAK044	OAK067
ALC007	ALC030	ALC085	OAK045	OAK079
ALC008	ALC031	OAK001	OAK048	OAK080
ALC009	ALC033	OAK002	OAK050	OAK081
ALC010	ALC034	OAK003	OAK051	OAK082
ALC011	ALC035	OAK004	OAK052	SCC003
ALC012	ALC036	OAK005	OAK053	SCC004
ALC013	ALC037	OAK006	OAK054	SCC006
ALC014	ALC038	OAK013	OAK055	SCC007
ALC015	ALC039	OAK019	OAK056	SCC047
ALC016	ALC040	OAK031	OAK057	SMC009
ALC017	ALC041	OAK037	OAK058	SMC010
ALC018	ALC042	OAK038	OAK059	
Latest Holocene Alluvial Fan Levee and other, Highly and Very Highly Susceptible Deposits (Qhly) CPTs (41)				
SCC013	SCC081	SCC140	SCC149	SCC159
SCC045	SCC089	SCC141	SCC150	SCC165
SCC046	SCC092	SCC142	SCC151	SCC166
SCC057	SCC120	SCC143	SCC152	SCC167
SCC066	SCC135	SCC144	SCC154	SMC018
SCC073	SCC136	SCC145	SCC155	
SCC076	SCC137	SCC146	SCC156	
SCC077	SCC138	SCC147	SCC157	
SCC079	SCC139	SCC148	SCC158	
Holocene Alluvial Fan and other, Moderately Susceptible Deposits (Qhf) CPTs (177)				
ALC046	OAK033	OAK125	SCC054	SCC132
ALC049	OAK047	OAK126	SCC055	SCC134
ALC050	OAK049	SCC001	SCC056	SCC153
ALC051	OAK071	SCC002	SCC060	SCC160
ALC052	OAK072	SCC005	SCC061	SCC161
ALC053	OAK073	SCC008	SCC064	SCC162
ALC054	OAK074	SCC009	SCC067	SCC163
ALC055	OAK075	SCC010	SCC069	SCC164
ALC056	OAK076	SCC011	SCC082	SCC168
ALC057	OAK083	SCC012	SCC084	SCC179
ALC058	OAK084	SCC014	SCC085	SCC180
ALC059	OAK085	SCC015	SCC086	SCC182
ALC060	OAK086	SCC016	SCC088	SCC183
ALC061	OAK088	SCC017	SCC093	SCC184

ALC062	OAK089	SCC018	SCC095	SCC185
ALC073	OAK090	SCC019	SCC096	SCC186
ALC074	OAK091	SCC021	SCC097	SCC187
ALC075	OAK092	SCC022	SCC098	SCC188
ALC076	OAK093	SCC023	SCC099	SCC189
ALC077	OAK094	SCC026	SCC102	SCC190
ALC078	OAK097	SCC028	SCC103	SCC191
ALC079	OAK098	SCC030	SCC104	SCC192
ALC080	OAK099	SCC032	SCC106	SCC193
ALC081	OAK100	SCC033	SCC109	SCC194
ALC082	OAK103	SCC034	SCC111	SCC195
ALC083	OAK104	SCC035	SCC112	SCC196
ALC084	OAK105	SCC036	SCC117	SCC197
OAK008	OAK106	SCC037	SCC118	SCC198
OAK009	OAK107	SCC039	SCC119	SCC199
OAK011	OAK108	SCC042	SCC123	SMC001
OAK014	OAK119	SCC048	SCC124	SMC015
OAK015	OAK120	SCC049	SCC125	SMC016
OAK016	OAK121	SCC050	SCC126	SMC017
OAK018	OAK122	SCC051	SCC128	
OAK027	OAK123	SCC052	SCC129	
OAK028	OAK124	SCC053	SCC130	

Table B.2: Simplified Geologic Deposits from the Units in Witter et al. (2006)

Simplified Geologic Deposit	Unit in Witter et al. (2006)	Area (km^2)
Artificial Fill over Estuarine Mud (afem)	afem	180.6
	Total afem Area:	**180.6 km^2**
Latest Holocene Alluvial Fan Levee and other, Highly and Very Highly Susceptible Deposits (Qhly)	Qhly	36.2
	Qhc	64.2
	Qhfy	43.5
	Qhty	43.9
	Qhty1	0.2
	Qhty2	6.3
	Qhty?	12.9
	Qhay	23.7
	Qhbs	2.2
	alf	61.1
	acf	1.0
	Qhc	64.2
	ac	9.7
	Qhed	1.9
	Qhfe	4.7
	Total Qhly Area:	**376.0 km^2**
Holocene Alluvial Fan and other, Moderately Susceptible Deposits (Qhf)	Qhf	760.0
	Qhf?	645.1
	Qhf1	13.6
	Qhf2	16.2
	Qhf3	21.2
	Qhff	223.1
	Qhl	121.8
	Qhl1	6.5
	Qhl2	0.0
	Qhl3	10.6
	Qhds	0.1
	Qhb	20.2
	Qht	66.0
	Qht1	1.4
	Qht2	1.3
	Qha	215.1
	Qha?	47.6
	Qds	23.3
	Qf	138.3
	Qt	10.2
	Qt?	0.1
	Qt1	0.0
	Qt2	0.0
	Qa	72.8
	Qa?	0.1
	Total Qhf Area:	**2414.7 km^2**

Figure B.1: Bathymetric and Terrestrial Elevations in the San Francisco Bay Area (from Fregoso et al., 2017)

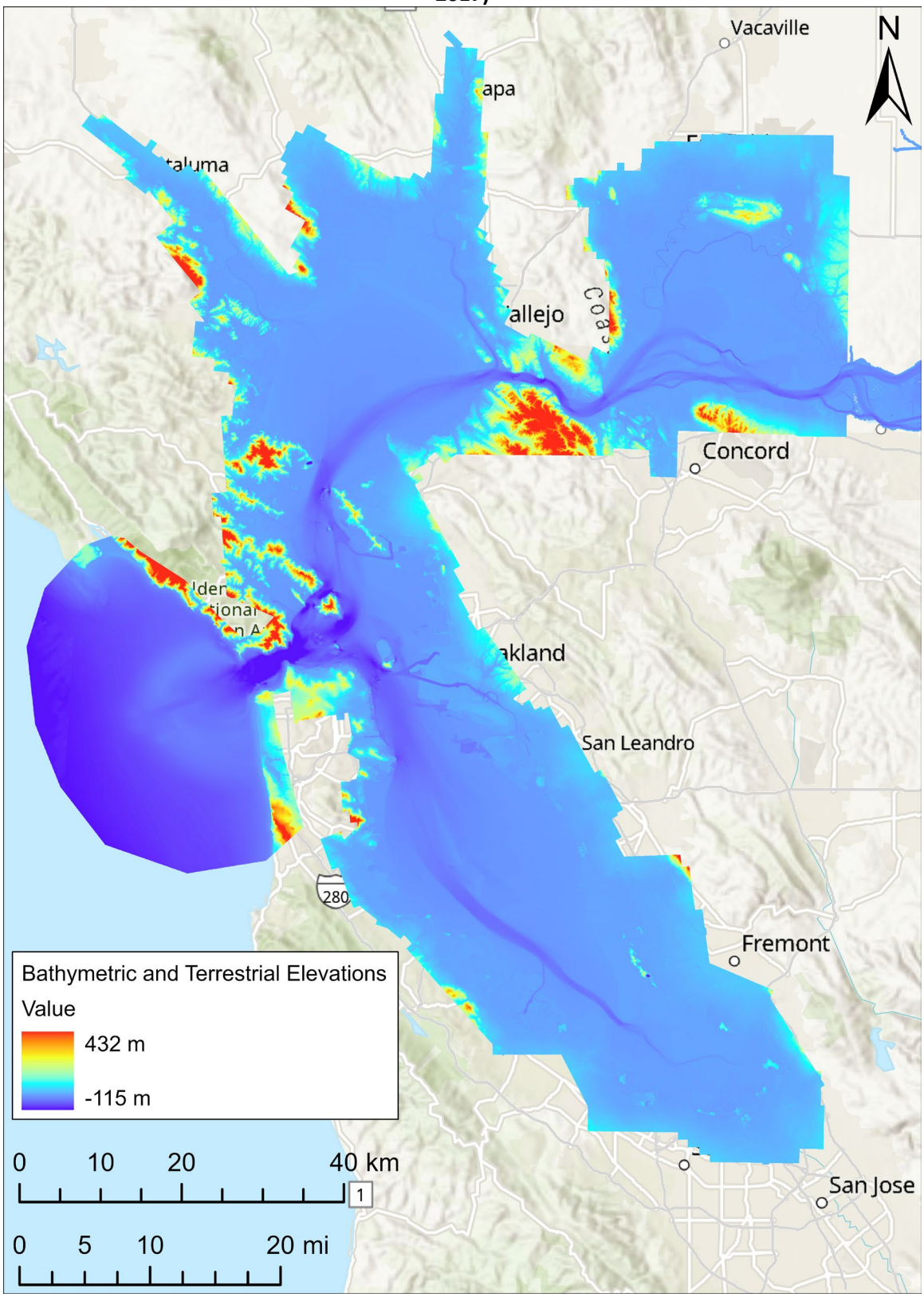

Figure B.2: Free-Face Features in the San Francisco Bay Area (from SFEI, 2017; Bay Area Open Space Council, 2008)

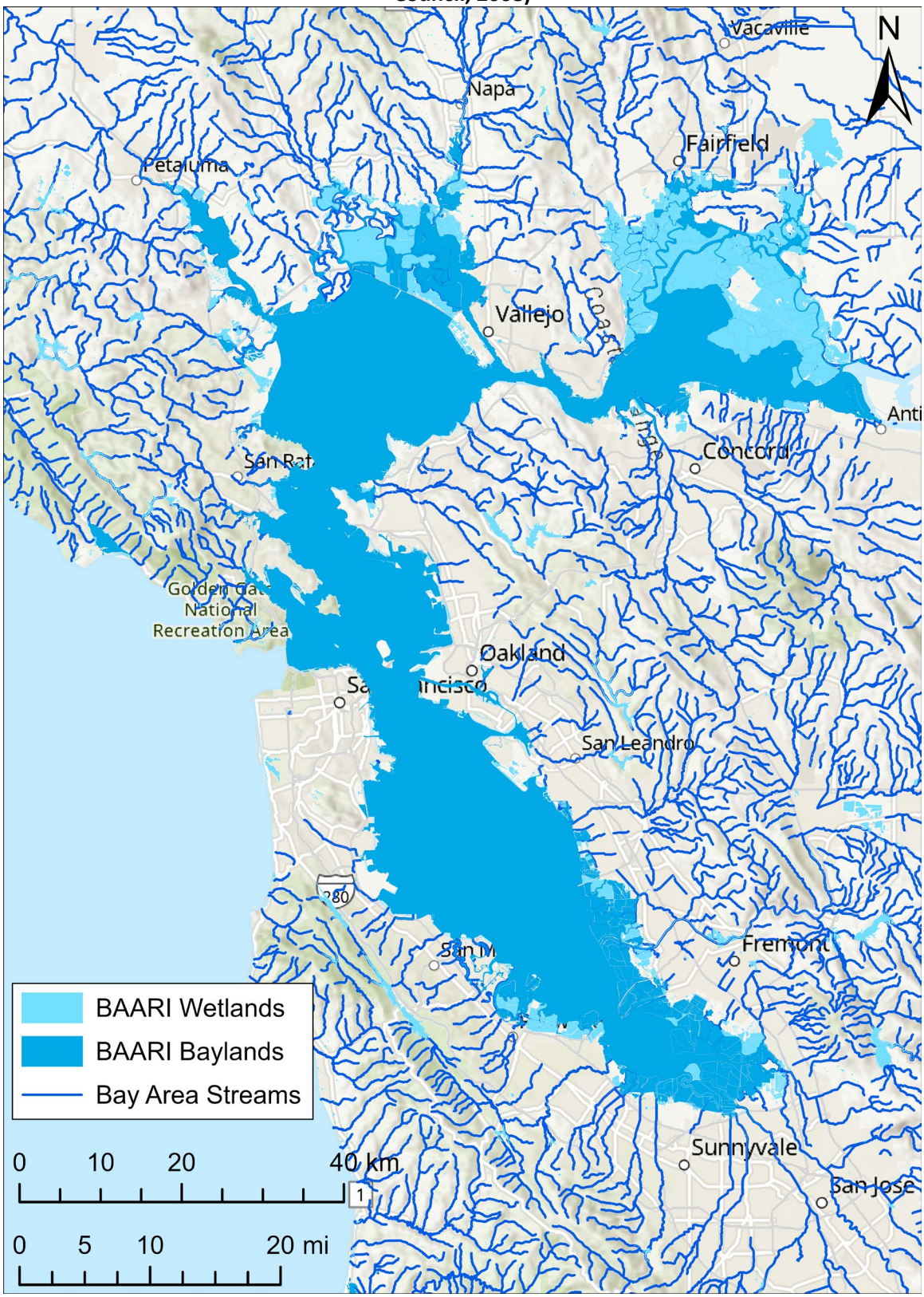

APPENDIX C: DATA FOR THE CONVENTIONAL AND PROBABILISTIC ANALYSES AT BALBOA BOULEVARD

Appendix C presents data used in the conventional and probabilistic analyses of the pipeline response to permanent ground deformation during 1994 M_w 6.7 Northridge earthquake (Bain et al., 2023a; Bain et al., 2023b). Data in Appendix C includes:

1. Summary of a compressive pipe tests compiled by Mohr (2003), available at: https://www.bsee.gov/sites/bsee.gov/files/tap-technical-assessment-program/434aa.pdf. This data was used to derive the fragility function for pipes subjected to compressive longitudinal strain.

Table C.1: Summary of Critical Compressive Pipe Strain Data Compiled by Mohr (2003)

Diameter/Wall Thickness (D/t)	Plain or Welded Pipe	Critical Strain
50.08	Plain	0.0099
90.71	Plain	0.0023
90.24	Plain	0.0046
52	Plain	0.008
28	Plain	0.019
30	Plain	0.021
31	Plain	0.012
40	Plain	0.02
40.5	Plain	0.013
42	Plain	0.012
45	Plain	0.007
48	Plain	0.021
51	Plain	0.013
52	Plain	0.01
53	Plain	0.0085
54	Plain	0.01
60	Plain	0.007
62	Plain	0.014
71	Plain	0.005
72	Plain	0.0048
73.5	Plain	0.007
74	Plain	0.0032
75	Plain	0.003
95	Plain	0.0021
100	Plain	0.003
103	Plain	0.003
112	Plain	0.002
115	Plain	0.0014
81	Plain	0.0041
81	Plain	0.0042
101	Plain	0.0042
101	Plain	0.0035
19	Plain	0.055
19	Plain	0.045
19	Plain	0.041
19	Plain	0.038
19	Plain	0.032
20	Plain	0.075
20	Plain	0.068
20	Plain	0.064
20	Plain	0.061
20	Plain	0.055
20	Plain	0.051

20	Plain	0.049
20	Plain	0.044
20	Plain	0.042
20	Plain	0.039
20	Plain	0.031
20	Plain	0.027
21	Plain	0.049
21	Plain	0.042
26	Plain	0.04
26	Plain	0.036
26	Plain	0.034
26	Plain	0.031
26	Plain	0.029
29	Plain	0.041
29	Plain	0.038
35	Plain	0.032
35	Plain	0.03
35	Plain	0.026
35	Plain	0.02
37	Plain	0.02
37	Plain	0.018
37	Plain	0.015
39	Plain	0.024
39	Plain	0.019
52	Plain	0.017
52	Plain	0.014
52	Plain	0.011
52	Plain	0.0081
52	Plain	0.0065
52	Plain	0.0048
54	Plain	0.02
54	Plain	0.012
81	Plain	0.0075
81	Plain	0.004
81	Plain	0.0022
90	Plain	0.0071
90	Plain	0.0064
90	Plain	0.0058
90	Plain	0.004
90	Plain	0.0035
95	Plain	0.0061
95	Plain	0.0054
95	Plain	0.005
110	Plain	0.0059
110	Plain	0.0049

110	Plain	0.0044
81	Plain	0.0159
81	Plain	0.0059
95.2	Plain	0.0024
101	Plain	0.004
101	Plain	0.0061
48.6	Plain	0.0069
55.4	Plain	0.004
77.3	Plain	0.0033
110.7	Plain	0.0044
30.7	Plain	0.04
46.1	Plain	0.0139
61.5	Plain	0.008
78.4	Plain	0.0038
42.5	Plain	0.0092
35.2	Plain	0.01
80	Plain	0.0032
49.1	Plain	0.0097
51	Plain	0.0088
56	Plain	0.0082
64	Plain	0.0066
80	Plain	0.0065
45.4	Plain	0.015
29.3	Plain	0.011
26.8	Plain	0.0174
22.3	Plain	0.0236
24	Plain	0.017
25	Plain	0.024
26	Plain	0.023
16	Plain	0.029
16	Plain	0.033
25	Plain	0.035
42.5	Plain	0.0112
63.7	Plain	0.0051
42.2	Plain	0.0115
24.2	Plain	0.044
24.2	Plain	0.05
24.2	Plain	0.058
21	Plain	0.052
21	Plain	0.054
40.4	Plain	0.024
40.4	Plain	0.043
42.1	Plain	0.017
46.2	Plain	0.015
46.2	Plain	0.0121

46.2	Plain	0.012
51.3	Plain	0.015
51.4	Plain	0.0122
61.4	Plain	0.009
66.8	Plain	0.0092
76.5	Plain	0.0078
77.8	Plain	0.0076
52.3	Plain	0.012
33.5	Plain	0.0155
33.65	Plain	0.0216
24.5	Plain	0.0208
49.2	Plain	0.012
61.9	Plain	0.0048
50.08	Welded	0.0064
64.3	Welded	0.0081
87.09	Welded	0.0025
48.68	Welded	0.0075
89.75	Welded	0.0026
60.48	Welded	0.0085
83.42	Welded	0.0034
87.26	Welded	0.0032
41.01	Welded	0.0131
69.23	Welded	0.0046
69.23	Welded	0.0042
100	Welded	0.0028
100	Welded	0.0038
61.64	Welded	0.0031
69.23	Welded	0.0074
69.23	Welded	0.0059
69.23	Welded	0.0052
100	Welded	0.0037
100	Welded	0.0033
100	Welded	0.0037
100	Welded	0.0035
61.64	Welded	0.003
61.64	Welded	0.0037
51.13	Welded	0.0071
51.13	Welded	0.0062
51.13	Welded	0.0082
61.64	Welded	0.0039
61.64	Welded	0.0036
51.13	Welded	0.0053
51.13	Welded	0.0054
61.64	Welded	0.0037
24.41	Welded	0.039331

27.73	Welded	0.04533
34.94	Welded	0.018667
46.09	Welded	0.005384
66.74	Welded	0.002253
73.52	Welded	0.00536
71.55	Welded	0.003743
47.17	Welded	0.008241
89.89	Welded	0.003112
23.35	Welded	0.050592
22.93	Welded	0.052058
27.94	Welded	0.011293
34.54	Welded	0.011931
45.65	Welded	0.009156
67.60	Welded	0.004389
44.73	Welded	0.01026
44.07	Welded	0.013921
86.57	Welded	0.002998
60.56	Welded	0.004987